NORTHWESTERN UNIVERSITY

Nucleation and Growth of Metastable Phases in Thin Films

A DISSERTATION

SUBMITTED TO THE GRADUATE SCHOOL IN PARTIAL FULFILLMENT OF THE REQUIREMENTS

for the degree

DOCTOR OF PHILOSOPHY

Field of Materials Science and Engineering

By

Quan Li

EVANSTON, ILLINOIS

December 2001

UMI Number: 3033521

ProQuest Information and Learning Company
300 North Zeeb Road
P.O. Box 1346
Ann Arbor, MI 48106-1346

ABSTRACT

Nucleation and Growth of Metastable Phases in Thin Films

Quan Li

This research focuses on the synthesis of metastable phases in thin films away from their thermal equilibrium conditions. The goal of this study is not only to achieve the desirable metastable phases, but also to understand their nucleation and growth process, so that the principles employed in this study may be applied to other material systems.

Several material systems have been used, including aluminum nitride, aluminum oxide, boron nitride and diamond. Different factors, which affect the formation of the metastable phases, have been studied. The first three materials, AlN, Al_2O_3 and BN were deposited using magnetron sputter techniques, while diamond was grown by direct ion-beam deposition.

The metastable phases can be obtained by different routes. B1-AlN was stabilized in epitaxial AlN/VN (001) superlattices with an AlN layer thickness less than 4.0 nm, a so-called epitaxial stabilization effect, taking advantage of the material system itself --- stabilizing the metastable phase based on the small interfacial energy between B1-AlN and VN.

Another method to achieve metastable phases in thin films is to modify the conventional deposition techniques, i.e., increasing the ion-bombardment of the growing films. Crystalline alumina was obtained using an intensified ionized magnetron

sputtering, where an increased ion-flux to the substrate was obtained using a magnetic trap generated by an external solenoid.

Cubic boron nitride (cBN) was synthesized using a similar method, i.e. ion-bombardment assisted magnetron sputtering. Factors affecting the cubic phase formation were investigated, including pre-deposition vacuum, film stoichiometry, deposition temperature, and substrate bias. Study of the micro-environments of tBN prior to the cBN nucleation disclosed different types of cBN nucleation and growth associated with different film internal stress levels.

In order to precisely control the ion-bombardment during film deposition, direct ion-beam deposition was employed to study diamond nucleation on silicon. Ion beam nucleation of diamond using different reactive gas ratios leads to different nuclei qualities, which may be explained by the ion-solid interaction and the effect of several competing nucleation mechanisms.

Approved:

Professor Laurence D. Marks
Department of Materials Science & Engineering
Northwestern University

ACKNOWLEDGMENTS

Unlike most people, my PhD study is unusual. I spent two years and a half in Northwestern University and the rest of my PhD study in City University of Hong Kong. I am very grateful for the unusual circumstances that allow me to complete a PhD outside Northwestern University. I would like to thank the department of materials science and engineering in Northwestern University for giving me this chance. I would also like to thank the two supervisors of mine in City University of Hong Kong, Professor Suit-Tong Lee and Professor Igor Bello, for their guidance and kind support. I am extremely grateful to the three of my thesis advisors, Professor Laurence D. Marks, Professor Scott A. Barnett and Professor Yip-wah Chung in Northwestern University. Without their help, support and encouragement, I can never finish this degree. I especially want to thank Professor Chung for creating me the opportunity to continue my study in Hong Kong and for his father-like guidance and care for me; Professor Marks for his great effort in preparing me many things to enable my study in HK and his patient instruction all through these years. I also like to thank the outside committee member of my dissertation, Dr. Mike Graham.

I would like to thank Ilwon Kim with whom I have collaborated in the research on AlN/VN superlattice, Yuan-hsin Yu with whom I collaborated in the research on AlO_x film growth, and Professor Xiaofeng Duan, Dr. Naigui Shang and Fanyu Meng, with whom I collaborated in the research on diamond epitaxial nucleation. I would also like to thank Professor Y. Lifshitz for his great instruction and many valuable discussions during

my study in City University of Hong Kong. I acknowledge the following people for teaching me TEM sample preparation: Dr. Wenan Chiou, Dr. Yanguo Wang and Dr. Zhenquan Liu. I especially thank Dr. Grozea for teaching me almost everything I need to know in the TEM lab.

I am grateful for being able to join Professor Marks', Professor Barnett's, Professor Chung's, and Professor Lee's groups, and would like to thank the members of the group for all kinds of help and support through my PhD study.

I especially want to thank my parents and my husband for their love and support throughout my study.

Finally, I gratefully acknowledge the financial support of the MRSEC program of the National Science Foundation (DMR-9632472) at the Materials Research Center of Northwestern University and financial support from the project funds in Professor Lee's group.

TABLE OF CONTENTS

FIGURES

LIST OF TABLES

CHAPTER 1. INTRODUCTION

Thin film coatings have been widely used in many industries, including electronic devices, optical materials and as decorative and protective layers. Solid thin films are different from bulk materials in at least two ways: (i) thin films are often nanocrystalline, leading to interesting properties; (ii) the deposition process may be performed under highly non-equilibrium conditions, leading to formation of abnormal phases [Wasa, 1992]. Various deposition techniques have been developed to meet the requirements of different materials and applications. Although the detailed growth process of individual film materials may differ from one to another, there are general principles that all follow.

For decades, scientists have been trying to understand the nucleation and growth of thin films in order to extend applications of thin film technology. Several theoretical principles have been developed to explain the thin film process, including the adsorption theory [London, 1930; Lennard-Jones, 1937] steady-state nucleation theory [Pound et al., 1954; Lothe et al., 1962; Hirth et al., 1967], time-dependent nucleation [Zinsmeister, 1966; Lewis et al., 1967], coalescence process [Lewis, 1970], and the growth of continuous films. It is now generally understood that the formation of thin films follows several steps: (i) *adsorption*. There are two main processes involved in adsorption, i.e., arrival of atoms at the surface and motion of atoms on the surface. Once the atoms arrive at the substrate surface, they may not stay there permanently. They have a finite probability of acquiring sufficient energy to overcome the attractive force and leave the substrate. If condensation (aggregation of the adatoms) does not

occur, they will eventually re-evaporate. Therefore, the adsorption energy, the sublimation energy and condensation energy are the three important factors, which determine the characteristics of the adsorption process. Adatoms migrate on the substrate surface, they may join with other adatoms and form clusters. These clusters may capture other migrating monomers to form larger clusters or go through a decay process by releasing monomers. Real surfaces usually contain imperfections, such as dislocations, vacancies, steps etc. When adatoms are absorbed in these specific defect sites, the number of nearest-neighbor atoms will be increased compared with adsorption on the perfect surface, and hence the absorption energy increased. Preferential adsorption on a surface step or ledge lead to an increased lifetime of the adatom before desorption. Moreover, the adatom's probability of meeting another atom in one-dimensional migration along the step is very high. (ii) *Formation of critical sized nuclei.* The stability of clusters of atoms decreases with decreasing cluster size. Only clusters larger than a critical size are likely to grow than to decay. (iii) *Growth of nuclei and coalescence.* When the substrate is covered with stable clusters of the deposited material, these clusters further grow and coalescence to form larger ones, which finally leads to the formation of large patches of deposited materials. Coalescence may occur either by growth of neighboring immobile nuclei until they meet, or by cluster migration and collision. Small nuclei islands tend to coalescence with each other in order to reduce the surface area, thus the surface energy. This process can be enhanced by increase the mobility of the surface species, for instance increasing the substrate temperature. When the disappearance of one island into another

leaves bare area on the substrate, secondary nucleation on the substrate can occur. (iv)Thin film formation. As nuclei growth and coalescence continues, the film reaches a network stage with unfilled channels or holes, and the final continuous film is obtained by channel filling.

Three modes of nucleation are generally described as (Figure 1-1): (i) three-dimensional island growth (Volmer-weber type); (ii) layer-by layer growth (Frank-van der Merwe type); and (iii) combination of an initial layer-by layer growth followed by three-dimensional island growth (Stranski-Krastanov type). A quasi two-dimensional growth is commonly observed for films grown on single crystal substrates, where the lattice mismatch between the film and substrate is small. In fact, the AlN/VN superlattice growth at low AlN layer thickness in chapter 4 resembles a quasi two-dimensional growth, where the lattice mismatch between the B1-AlN and VN is only 1.5%.

The microstructural and the topographical details of thin films depend on the kinetics of growth. Deposition parameters, including the substrate temperature, the flux and energy of the incident species, chemical nature, topography of the substrate surface, and the gas ambient, influence the surface mobility of absorbed species, thus affecting the final microstructure and morphology of thin films.

Many materials when prepared as thin films exhibit metastable structures, which are not found or are difficult to synthesize in the corresponding bulk materials. These structures may be formed due to the substrate effect (see below), or the non-equilibrium nature of the deposition process.

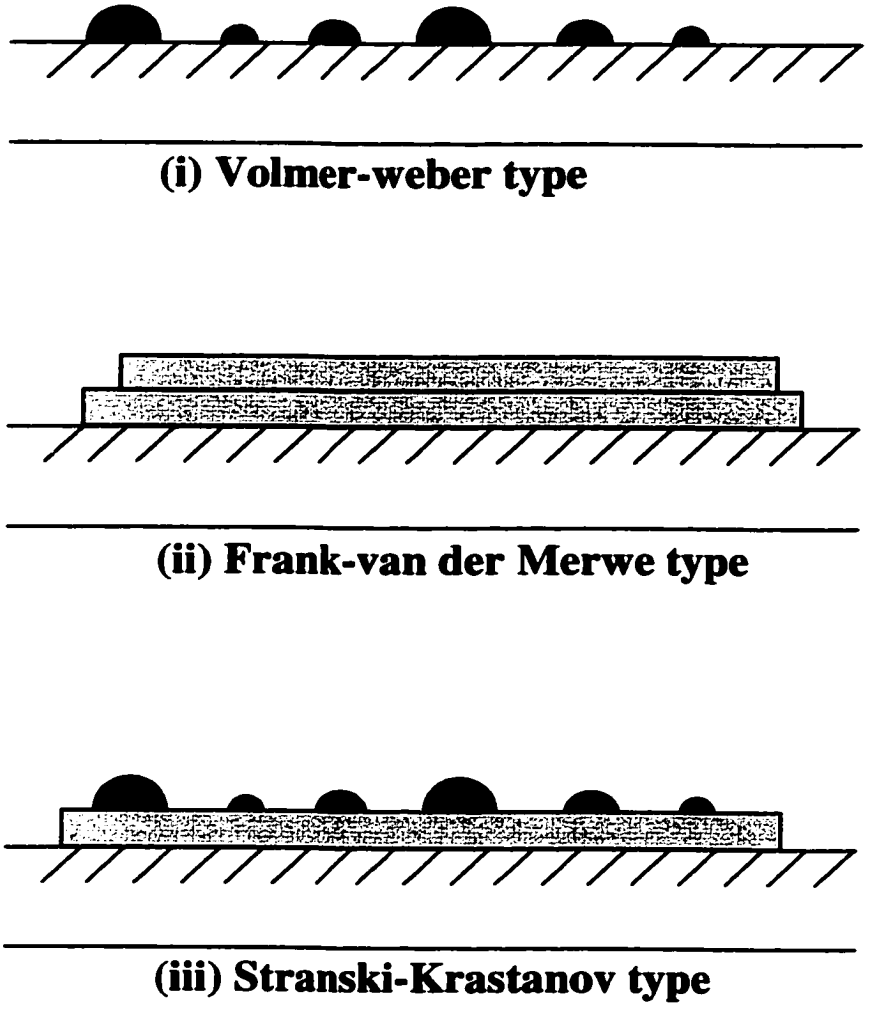

Figure 1-1. Three modes of thin film growth process [Wasa, 1992]

Four different material systems are investigated in the current work. They were synthesized using different methods. The deposition techniques are explained in Chapter 2. Based on the understanding of the nucleation and growth process of thin films stated above, the current work focuses on the nucleation and growth process of metastable phases in thin films. The two factors, substrate effect and the non-equilibrium nature of the deposition techniques are studied in different material systems. The kinetics of growth, which affects the structure of the films, also plays an important role in the formation of metastable phases. Usually, more than one phase is encountered in each individual system, which makes the nucleation and growth process more complicated. Structural characterization becomes very important due to thenature of the current work. The major characterization methods and the principles are stated in detail in chapter 3.

Chapter 4 focuses on the substrate effect (epitaxial stabilization) in obtaining the metastable B1-AlN, a high-pressure phase, in AlN/VN superlattice. It belongs to a special case of nucleation and growth—epitaxial nucleation and growth, i.e., B1-AlN forms an epi-layer on the underlying VN at the initial nucleation stage. This is different from another widely used term "epitaxial growth", which may refer to nuclei reorientation during growth. In epitaxial nucleation, the occurrence of oriented nuclei is explained by the dependence of nucleation rate on interfacial energy between the nuclei and the substrate [Walton, 1962]. Similarly, the discrimination between two different phases can be differentiated by the interfacial energy as well. This is demonstrated by the formation

of B1-AlN/VN instead of w-AlN/VN superlattice under specific conditions, although the wurtzite phase of AlN is the stable one.

Chapter 5, 6, and 7 focus on the other factor, namely, the formation of metastable phases under non-equilibrium deposition conditions. This is investigated by varying different deposition parameters in the film growth process. Chapter 5 demonstrates how increased mobility of surface species can lead to the formation of metastable phase. Crystalline aluminum oxides, including the alpha, theta, gamma and kappa alumina, are normally synthesized using high-temperature techniques. Modification of the conventional magnetron sputter deposition leads to significantly increased ion flux to the substrate during deposition, thus increased mobility of the surface species, which results in the formation of crystalline alumina at reduced substrate temperatures. The ion bombardment affects the film nucleation and growth process in more than one way. On one hand, it increases the mobility of surface species and enables the migration of adatoms on the substrate surface, through which the adatoms may find their equilibrium location and initiate nucleation. On the other hand, excessive ion bombardment rapidly increases the defect density and can result in an entrapment of processing gas atoms. It also contributes to the small grain size and high compressive stress in the films. An interesting point made in chapter 5 is that control of ion-bombardment together with other deposition parameters can lead to equilibrium between the secondary nucleation and growth. Since ion bombardment helps to initiate nucleation and prevent the nuclei from growing, nanocrystalline films can be achieved by this route.

Chapter 6 continues the research on ion-bombardment effect in nucleation and growth of the metastable phase. It is a little inappropriate to define the cubic phase of boron nitride as a metastable phase. The original pressure-temperature phase diagram of BN [Bundy et al., 1963] indicates that hBN is stable at ambient temperature and pressure, whereas the cubic phase is only stable at high pressures. However, recent experiments and calculations [Solozhenko et al., 1993] suggest that the P-T boundary line between cBN and hBN should be shifted to low pressure, which make the cBN thermodynamically stable under ambient conditions. Nevertheless, a significant kinetic barrier hinders the direct transition from sp^2 to sp^3 bonding under ambient conditions. The nucleation and growth process of cBN is fairly complicated. It is shown in chapter 6 that the formation of cBN only takes place within a certain range of the deposition parameters and ion-bombardment is one crucial factor. However, the significant compressive stress in the films introduced by ion bombardment cause film delamination at larger thickness. In order to understand how ion bombardment affects cBN nucleation and growth from a microstructure point of view, the local atomic environments of cBN nucleation and growth using different ion impacts during deposition are compared. In this way, the internal relationship among ion bombardment, film microstructure, and internal stress can be built.

Chapter 7 studies the effect of gas ambients and the substrate surface topography on the nucleation of diamond on silicon substrate. Diamond is well known to be a high-pressure phase, and synthesis of diamond in bulk form requires high-temperature and

high-pressure techniques. Studies of diamond in thin films have been ongoing for several decades. However, the initial nucleation stage of diamond, especially the hetero-epitaxial nucleation is far from being well understood. Since ion bombardment is known to be an important factor in the formation of diamond nuclei, direct ion beam deposition was employed, where the ion current and energy can be independently controlled. Chapter 7 demonstrates that epitaxial diamond nuclei can be achieved using this deposition technique. The nucleation mechanisms are discussed.

CHAPTER 2 DEPOSITION TECHNIQUES

2.1. Sputtering

Sputtering is a process by which ion impacts establish a series of collision events in the target leading to the ejection of matrix atoms. The ejected material is then transported through the vacuum chamber and condenses on a substrate surface. The ejection of material from the target surface is accomplished typically using a glow-discharge plasma. A simplified sputtering chamber is shown in Figure 2-1. The plasma is initiated by applying a large negative potential between a cathode and an anode across the working gas. The cathode is also known as the target, the material from which films are synthesized. The substrate that faces the cathode can be grounded, electrically floating, biased, and heated. The chamber is filled with a working gas. Positive ions in the discharge are accelerated towards the negative electrode (cathode). When the accelerated ions collide with the cathode surface, most of their kinetic energy is lost in the form of heat. Only a small part of their incident energy is transferred to cathode atom displacements, which may result in eject ion of neutral atoms from the cathode surface. The sputtering process can only occur when the incident ion energy is greater than the surface binding energy of the target material. These ejected atoms enter and pass through the discharge region and eventually deposit on the substrate. In addition, secondary electrons are also emitted from the target due to the energetic ion bombardment. These electrons can cause more ionization events, hence sustain the discharge. The number of atoms ejected from a target surface per incident ion is defined as the sputter yield. It is a measure of the efficiency of sputtering.

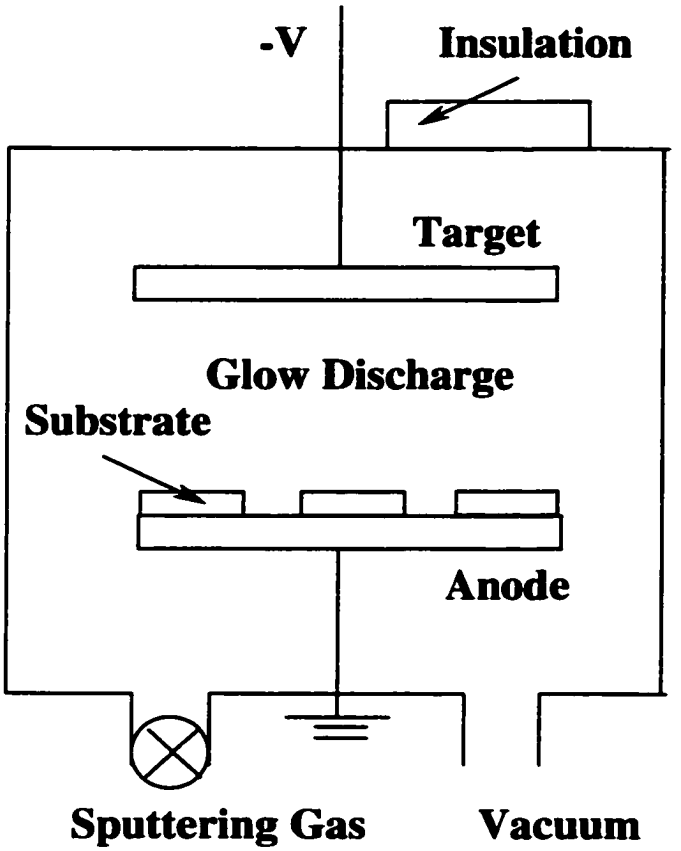

Figure 2-1. Schematics of a simplified sputtering chamber [Ohring, 1991]

The sputtering can be categorized as direct current (dc) sputtering and radio frequency (rf) sputtering, depending on the power supply used. For insulating materials such as boron nitride, rf sputtering is needed to avoid charge build-up on the target surface.

The geometric configuration of the deposition system affects film deposition. It is generally known that shorter target-substrate separation distance results in higher film deposition rate. Another factor, which is easily ignored, is that the energy distributions of the sputtered atoms change as they travel from the target to the substrate. Figure 2-2 illustrates this phenomenon by showing the change in Nb energy distribution with distance from target with argon pressure at 10 mTorr [Meyer et al., 1981].

Other than the geometric configuration, the discharge environment, the intrinsic sputter yield, and the sputtering pressure also affect the film deposition rate and morphology. At low pressures, the ionization efficiency is low due to the large mean free path of atoms and ions. If the pressure is too high, the sputtered atoms undergo increased scattering and cannot be efficiently deposited as well. In general, there is always an optimal operating condition, which can be different from system to system.

2.1.1. Magnetron Sputtering

By employing a magnetic field oriented parallel to the target and perpendicular to the electric field, ideally one can trap the electrons near the. Figure 2-3 shows a typical planar magnetron electrode. Electrons within the dual field environment experience the well-known Lorentz force in addition to the force from the electric field. After emission from the cathode, electrons are initially accelerated toward the anode, executing a helical motion in the process; when they encounter the region of the parallel magnetic

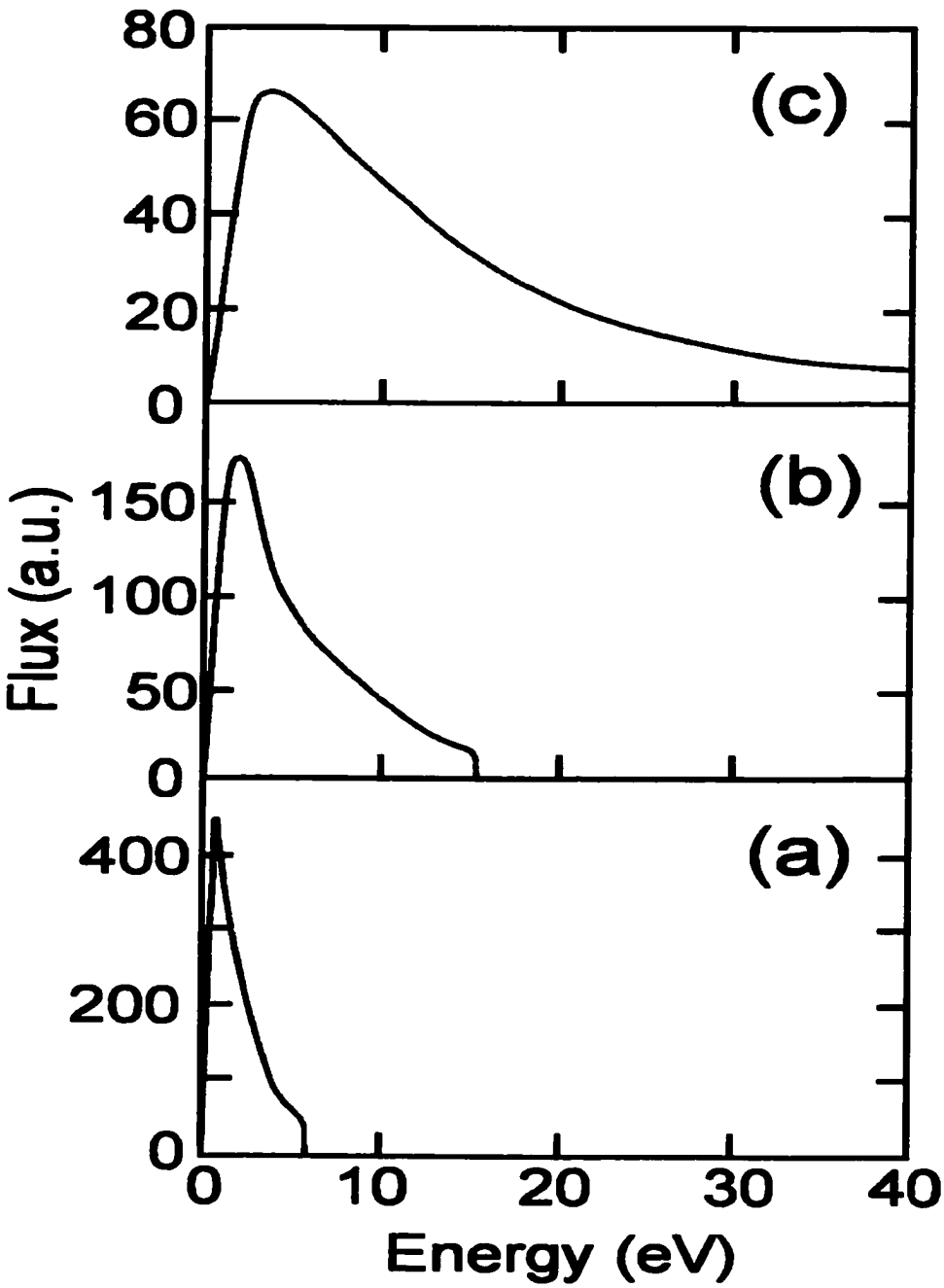

Figure 2-2 Change in Nb energy distribution as a function of distance from target with Ar pressure at 10 mTorr. (a) 0 cm (b) 3 cm (c) 6 cm [Meyer et al., 1981]

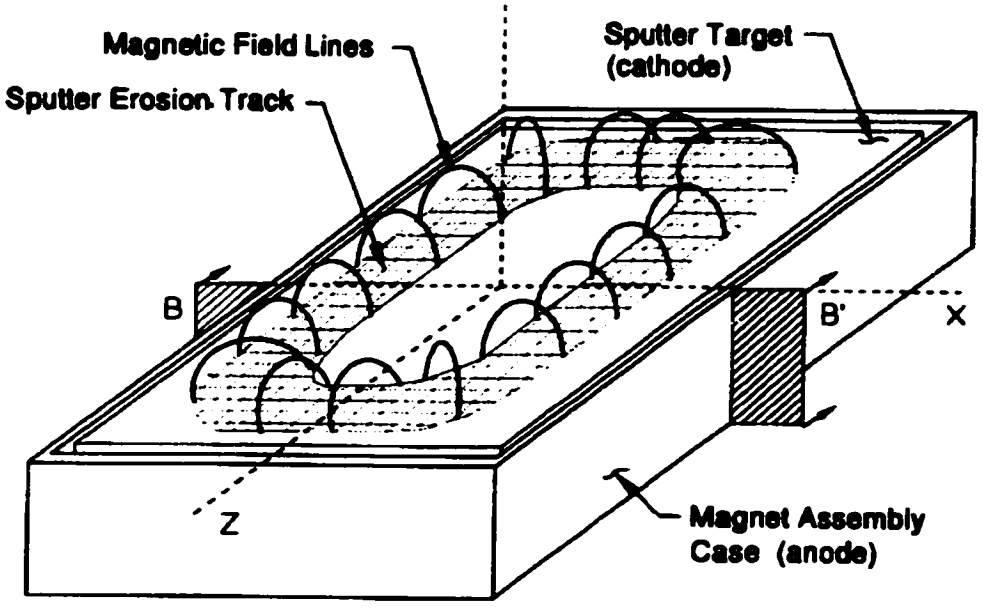

Figure 2-3. Schematic diagram of a typical planar magnetron [Konuma, 1992]

field, they are bent into an orbit back to the target. Magnetic fields prolong the electron residence time in the plasma and thus enhance the probability of collisions with neutrals to produce ions. This leads to larger discharge currents and increased sputter deposition rates, compared with normal diode- sputtering configurations. Therefore, applied magnetic fields have the desirable effect of reducing electron bombardment of substrates and extending the operating vacuum range.

Magnetron sputtering is presently the most widely practiced sputtering method in industry due to its high deposition rates, which are typically an order of magnitude higher than deposition rates obtained from conventional sputtering techniques.

2.1.2. Reactive Magnetron Sputtering

In reactive sputtering, thin films of compounds are deposited by sputtering from metallic targets in mixtures of a reactive gas and an inert work gas, typically argon. The deposition rates of reactive sputtering at a given applied power are very much dependent on the reactive gas pressure. As the reactive gas pressure increases, sputtering rate of metals drops tremendously because the metal target begins to form a compound with the reactive gas. The decrease in deposition rate is due to the lower sputter yield of the compounds relative to metals. On the other hand, the reactive gas pressure must be high enough to ensure the correct stoichiometry.

To visualize the condition required to yield stoichiometric compound films at reasonable deposition rates, a hysteresis test of the system is needed. Figure 2-4 shows hysteresis loops for the reactive sputtering of TiN thin films. At point A, the nitrogen partial pressure remains low as the nitrogen flow is increased, because the nitrogen

introduced to the chamber reacts with the sputtered Ti metal and is removed from the gas phase. At point B on the curves, the nitrogen partial pressure begins to increase, as there is slightly more nitrogen gas present than is necessary to react with the sputtered Ti metal. At point C, the nitrogen partial pressure jumps to a very high value, while the deposition rate drops to a very low value. This is due to the large excess of nitrogen gas present, which reacts with not only the sputtered Ti metal but the Ti metal on the target to form a layer of TiN on the target surface as well. Once this equilibrium is established, further increase of nitrogen flow will only cause the linear increase of the nitrogen partial pressure, while the deposition rate remains low and relatively constant. To achieve both high deposition rates and stoichiometric films, one must operate at regions near point B on the hysteresis loop.

The most common problem for dc reactive sputtering of low conductivity compounds is arcing, which can cause instability in the deposition process, and result in large fluctuations of film thickness, and possibly damaging the power supply. Other than changing the power supply system to rf-power or a pulsed dc-power supply, one can either increase the inert working gas flow or reduce the target power to eliminate arcing to some extent. However, this is achieved at the expense of the deposition rate.

2.2. Ion Beam Process

Large range of ion energies can be used in ion beam applications. The classification of processes induced by ion beams is summarized in Figure 2-5. All the ion beam applications employ an ion beam generating system and a beam transporting

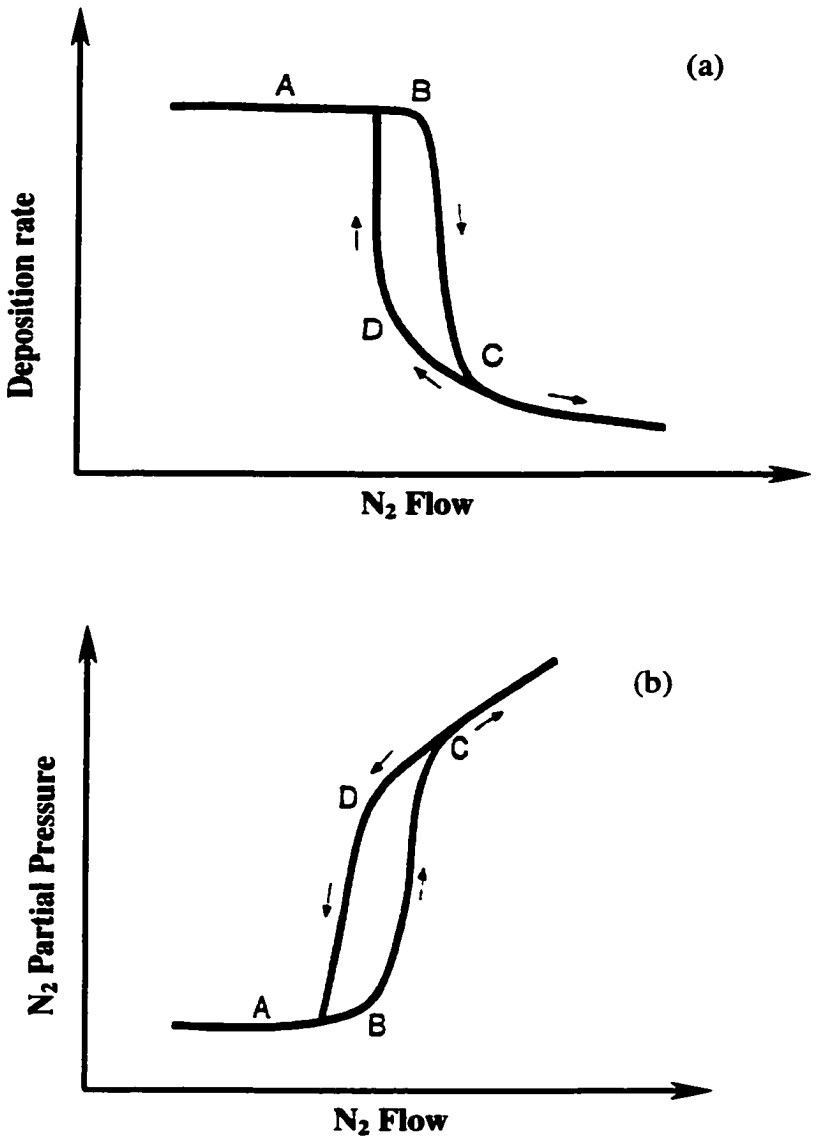

Figure 2-4. (a)Deposition rate and (b) Nitrogen partial pressure vs. nitrogen flow hysteresis loops for the reactive sputtering of TiN [Sproul et al. 1987]

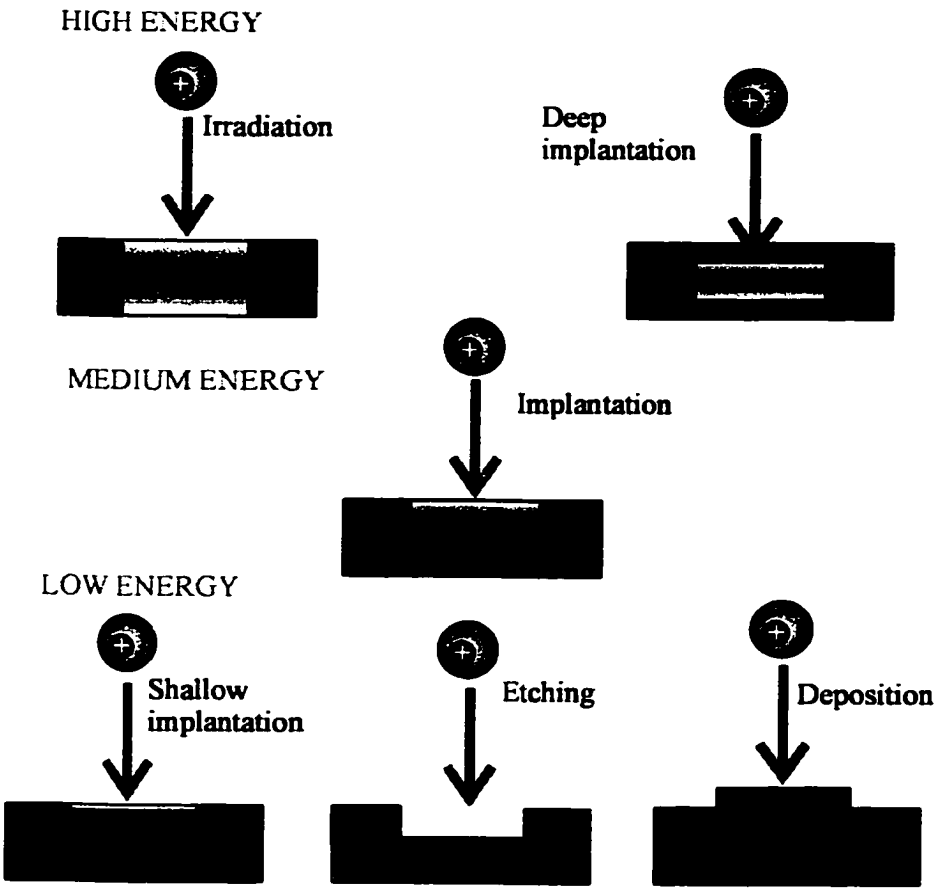

Figure 2-5 Summary of the ion beam process [Bello, 2000]

system. The schematic of a mass-selected ion beam system is illustrated in Figure 2-6 as an example. The ions are generated by ion sources. There are more than 100 types of ion sources and their modifications. They are different in the types of ions generated, method of ionization, working conditions, etc. Extraction electrodes are placed in front of the ion generator to extract ions after they are generated. After that, the ion beam may go through a series of focusing, mass selecting, deflecting and neutralizing process and finally transport to the target.

There are many ways to generate ions inside an ion source, such as electron impact ionization, thermal ionization, chemical ionization, laser ionization and field ionization. The majority of ion source employs electron impact ionization, where an electron beam from a simple diode gun is injected into the ionization chamber containing the processing gases. Once generated, the ions are extracted from the ion source by applying the appropriate bias between the ion source and the extracting electrode. The extracted ion beam is affected by several parameters including the applied field strength, the shape of the emitter surface as well as the extraction electrode geometry. Influence of the applied field on the ion beam trajectories is illustrates in Figure 2-7 under following conditions: (a) No acceleration voltage, (b) low acceleration voltage, (c) medium acceleration voltage, and (d) normal acceleration voltage.

2.2.1. Direct Ion Beam Deposition Using a Kaufman Ion Source

The Kaufman ion source was developed in 1960 as a mercury ion source for propulsion applications. The operation of the ion source is based on the application of .

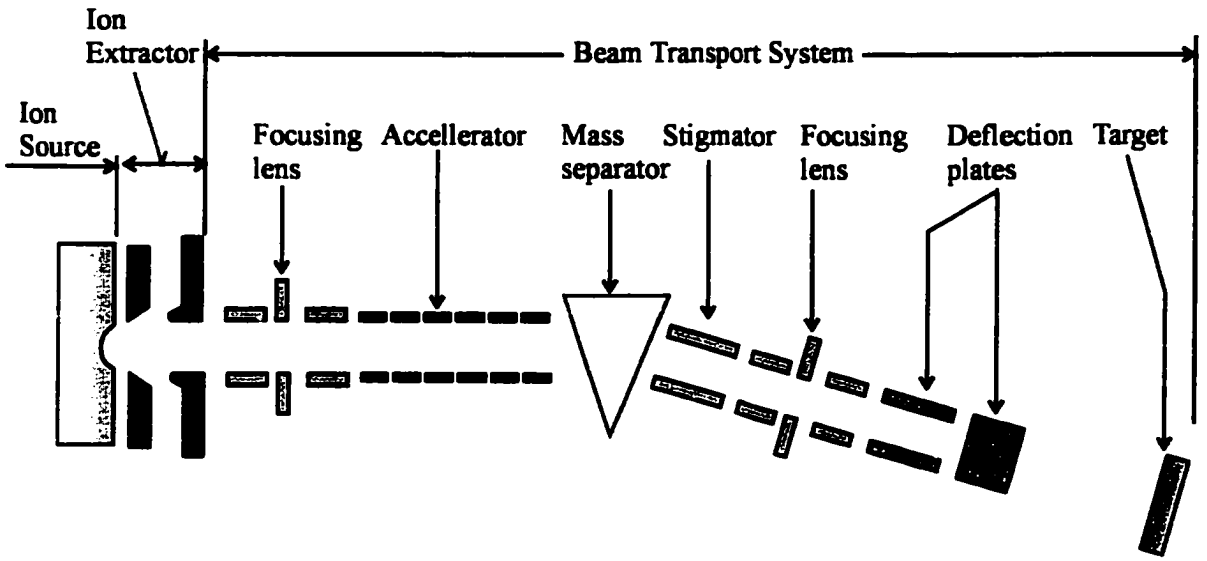

Figure 2-6. Schematic of the mass-selected ion beam system. [Bello, 2000]

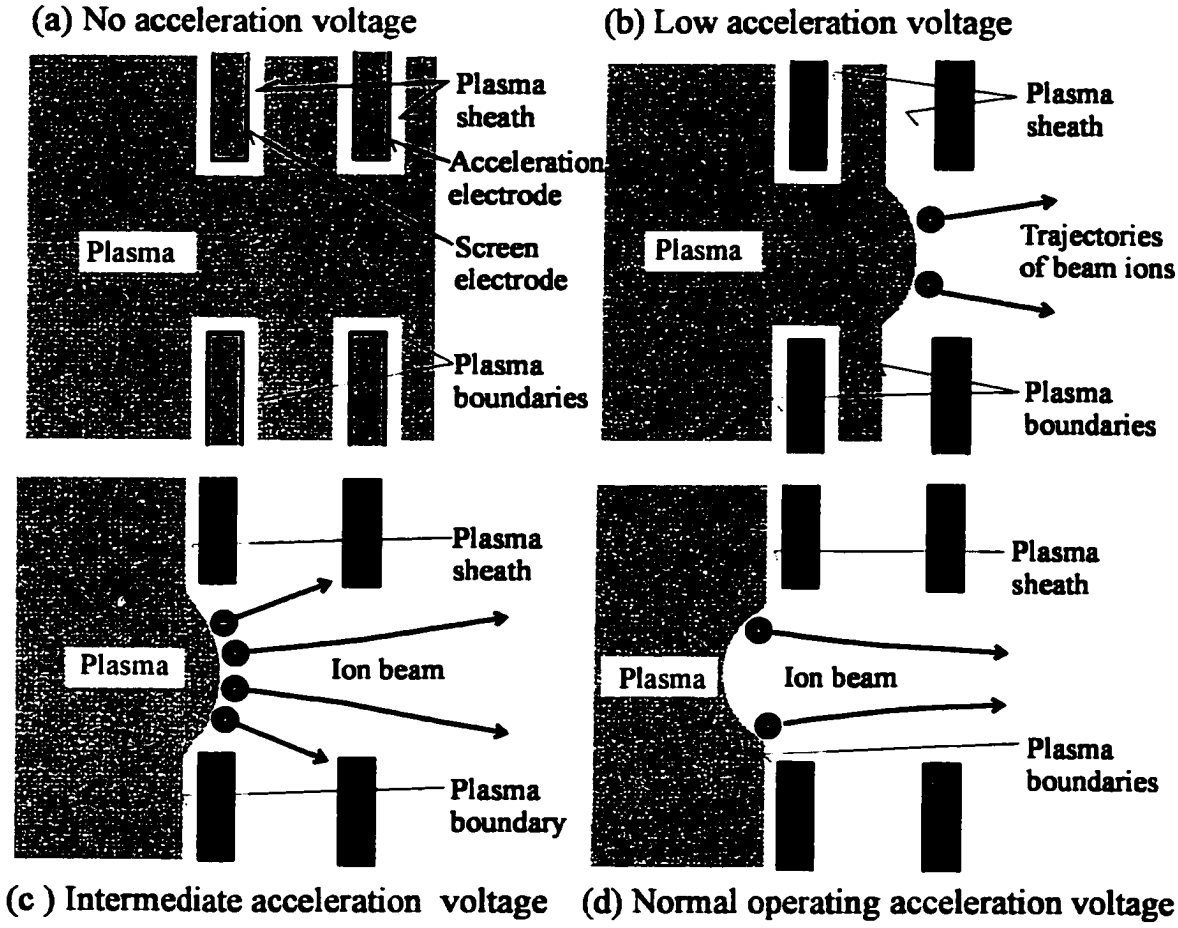

Figure 2-7 Plasma boundaries with respect to the extraction voltage [Bello, 2000]

trapped oscillating electrons from a thermionic emitter with ions extracted in the direction of magnetic field lines. There are numerous variants of the Kaufman source. For example, permanent magnets in place of magnet coil and variety of cathodes are commonly used. This type of ion source has been widely used in ion beam milling and sputter deposition of thin film. A schematic of the Kaufman ion source is shown in the Figure 2-8. The working pressure of the ion source is below 5×10^{-4} Torr, and argon is usually introduced to stabilize the ion source. The extraction grids are usually made of low-sputter yield materials, such as graphite and molybdenum to reduce contamination. One common problem during ion beam deposition is shorting between the extraction grids. This problem becomes serious when using carbon-containing gases, as solid flakes can easily cause shorting during deposition. Therefore, experiments operated at high concentration of carbon-containing gases usually have low reproducibility.

The usable ion energy of a Kaufman ion source ranges from tens of eV to 1000 eV. Nevertheless, in direct ion beam deposition, the useful energy range of the beam is limited at low energies. As the ion beam current increases with beam energy almost linearly [Fair, 1969], the deposition rate at low beam energy is usually low. Space charge spreading occurs at high energies by self-sputtering of the growing film or sputtering of the substrate. Therefore, the maximum deposition rate occurs when approximately half of the depositing material is being sputtered away.

One advantage of direct ion beam deposition is variable ion beam current independently of the beam energy. Compared to the conventional bias-assisted deposition

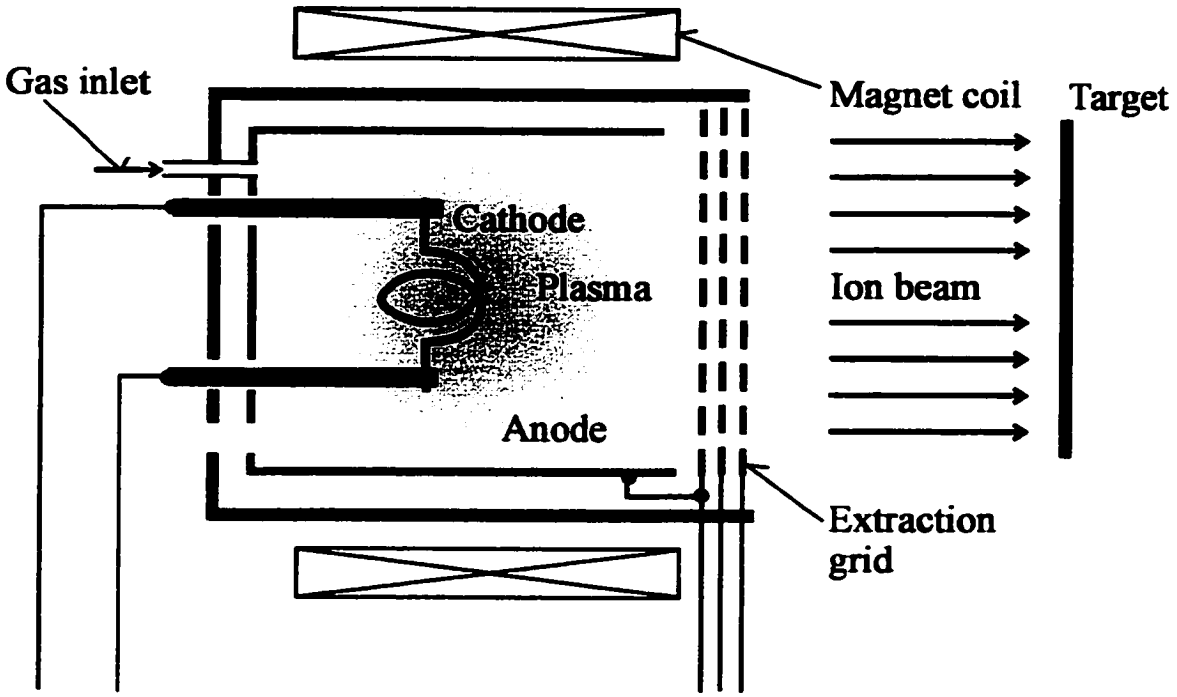

Figure 2-8 Schematic of the Kaufman ion source

method, direct ion beam deposition allows better isolation of the substrate from the ion generation process, thus gives more accurate control over the deposition conditions.

CHAPTER 3. STRUCTURAL CHARACATERIZATION OF THIN FILMS

Different characterization methods are needed when studying different aspects of thin films. As the present work focuses on the nucleation and growth of metastable phases in thin films, structural characterization is the most important analytical method.

3.1 X-ray Diffraction (XRD)

X-rays are electromagnetic radiation, which can be treated as waves in accordance with classical theory. X-rays will be scattered while traveling through material. The wavelength (λ) of the scatter x-ray beam would not be modified most of the time (coherent scattering), although incoherent (inelastic) Compton scattering may occur [Cullity, 1978]. The important characteristic of the incoherently scattered beam is that the phase has no fixed relation to the phase of the incident beam, and thus only gives a background rather than sharp peaks.

X-ray diffraction is essentially a coherent scattering phenomenon in which a large number of atoms cooperate. It is known that the differences in the path length traveled by the scattered beams lead to differences in their phases. For a crystalline structure where atoms are arranged periodically on a lattice, the rays scattered by the atoms have definite phase relationships. In most directions, destructive interference occurs, but in a few directions, constructive interference takes place and diffracted beams are formed. This is known as the Bragg law in kinematical diffraction:

$$\lambda = 2d \sin\theta \qquad 3.1$$

where d is the lattice spacing and θ is the Bragg angle. Not all coherent scattering that satisfies the Bragg law can produce diffraction. Sometimes no diffraction may occur due

to a particular arrangement of the atoms within the unit cell. The Intensity of the beam diffracted by all the atoms of a unit cell is proportional to the square of the amplitude (**F**), which is known as the structure factor. In order to obtain the intrinsic intensity distribution, given by $|F|^2$, the experimentally observed intensity has to be corrected for various instrumental factors including polarization, Lorentz terms, absorption and the temperature factor.

So far only the kinematical approximation has been addressed. However, a Bragg-diffracted x-ray beam may be diffracted again when it passes through another part of a crystal, which is aligned at the right angle for Bragg reflection. Multiple scattering processes give rise to dynamical diffraction. This becomes important in thick perfect crystals, where the atomic planes are sufficiently ordered to give well-defined diffracted beams.

3.1.1 XRD of Superlattice Films

The principle of x-ray diffraction of a superlattice film is similar to that of a single crystal and the kinematical approximation is employed. Diffraction occurs when the scattering vector ($\mathbf{q} = \mathbf{k_s}-\mathbf{k_i}$, $\mathbf{k_s}$ and $\mathbf{k_i}$ are the scattered and the incident wave vectors, respectively) coincides with the superlattice period in the reciprocal lattice ($\Lambda^* = 1/\Lambda$). Detailed theories can be found in the literatures [Fujii, 1987]. The kinematical diffraction theory is widely used to analyze the observed intensity data of superlattice. The intensity of an ideal superlattice is calculated as

$$I(q) = L_N(q) \, | F(q) |^2 \qquad 3.2$$

$$L_N(q) = [\mathrm{Sin}\,(N\Lambda q/2)/\mathrm{Sin}\,(\Lambda q/2)]^2 \qquad 3.3$$

$$F(q) = f_{\upsilon}(q)\, T_{\upsilon}(q) \exp(iqz_{\upsilon}) \qquad 3.4$$

Where N is the total number of unit layers, Λ is the superlattice period, Q is the magnitude of the scattering vector, $f_{\upsilon}(Q)$ is the atomic scattering factor times atomic density in the υ-th plane, and $T_{\upsilon}(Q)$ is the Debye-Waller factor [Fujii, 1987]. Different one-dimensional models are used for different chemical ordering at the multiplayer interface, including the step model, the three-step model, the trapezoidal model, and the phonon model (Figure 3-1).

3.1.2 High-angle X-ray Diffraction Simulations of Metal Nitride Superlattice Structures

High-angle XRD simulations are performed for AlN/VN superlattices in chapter 4, using a kinematical calculation similar to what has been used for metallic superlattices [Fujii, 1987]. The simulation calculates the diffracted x-ray intensity by summing the scattered intensity from each plane in the crystal. The scattering factors and interplanar spacing are calculated by assuming trapezoidal composition waves, including a Gaussian variation of interplanar spacing and superlattice period. An R-squared (R^2) deviation of the simulated intensity from the experimental intensity is used in the fitting procedure.

The kinematical intensity (I) of diffracted x-rays at an angle θ is calculated as the summation of the wave scattered from each plane j,

$$I(\theta) = \left| \sum_{j=1}^{N} f(z_j) \exp(2\pi i q \cdot z_j) \right|^2 \qquad 3.5$$

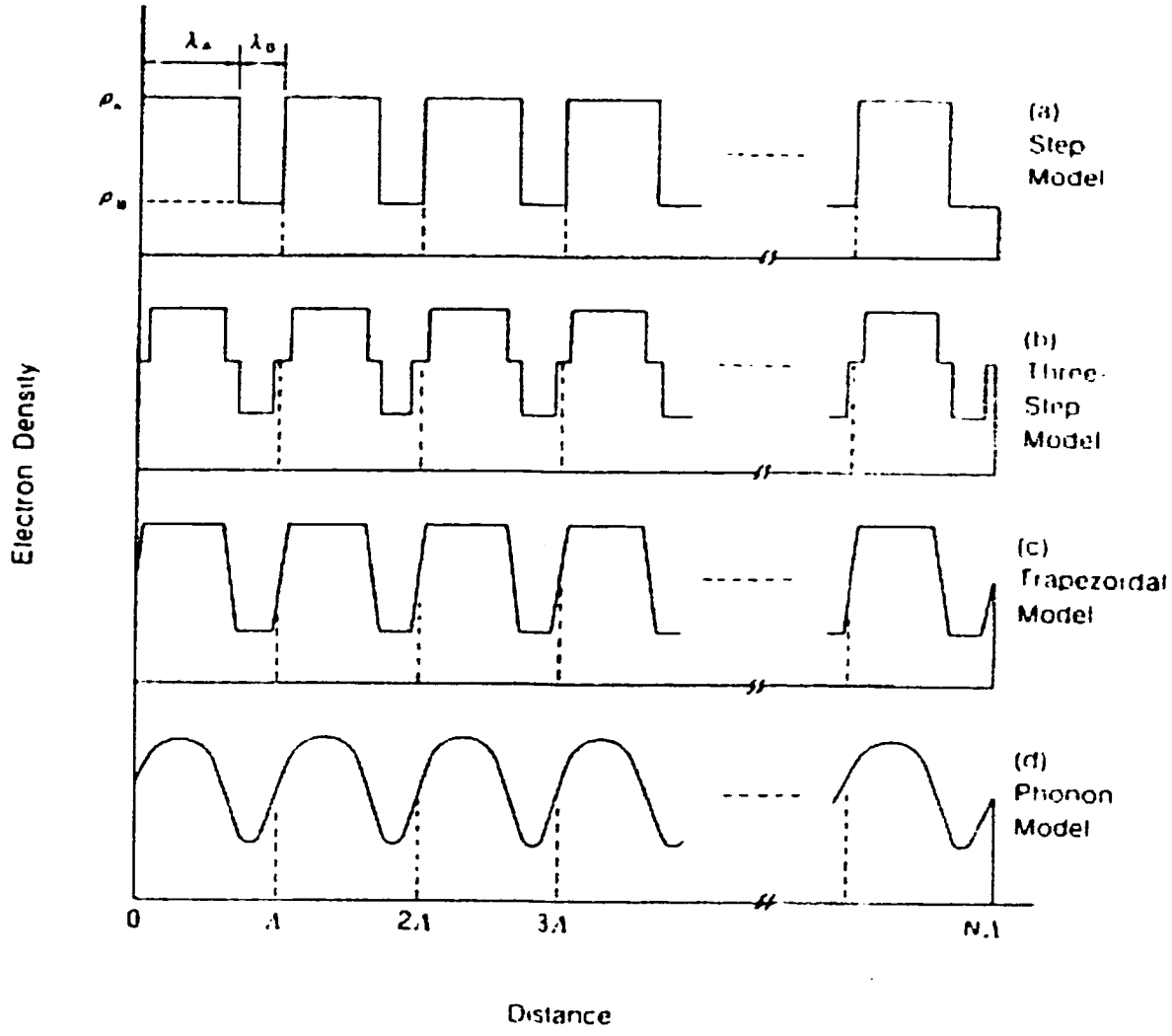

Figure 3-1 One-dimensional superlattice models with a perfectly periodic structure (period Λ). A charge-density contrast is shown schematically for N bilayers with four kinds of interfacial structures (a)-(d).

Where $\vec{z}_j$ is the position vector of the plane, $f(\vec{z}_j)$ is the average scattering factor per unit area of the plane, and $\vec{q} \cdot \vec{z}_j$ is a scalar product .

In an ideal crystal, the superlattice peaks have a FWHM [Guinier 1963] of about $\lambda/(2L\cos\theta)$, where L is the total thickness of the film. The intensity is calculated at FWHM/2 to ensure that the correct peak heights are obtained and no peaks are missed in the calculation. The x-ray intensities are corrected for the Debye-Waller factor, Lorentz factor, Polarization factor, and absorption using a standard procedure [Cook, 1969]. The simulated XRD patterns are convoluted with a Gaussian response function with a width corresponding to the resolution of the diffractometer. In this way, the instrumental broadening of the peaks is estimated from the width of a single crystal substrate peak.

In order to evaluate the x-ray intensity based on equation 3.6, a model of the superlattice structure is required. The superlattice is considered to be a stack of N atomic planes in the z-direction. The local lattice spacing d (z) and the scattering factors f (z) used in equation 3.6 vary with the composition c (z).

The simulation is carried out assuming interdiffusion in the superlattices. The composition modulation is approximated as having a constant average interface width (w) and amplitude (A). As w is less than both l_{VN} and l_{AlN}, the thickness of VN and AlN respectively, the composition modulation is trapezoidal.

The positions of the atomic planes fluctuate randomly via a Gaussian distribution of width (σ_d), which is assumed to be equal for the two materials. Layer thickness fluctuations, due to the deviations from perfect layer-by-layer growth and growth rate

fluctuations, are also simulated. The layer thicknesses l_{VN} and l_{AlN} fluctuate independently giving a Gaussian distribution of width $\sigma_\Lambda = \sigma_{VN} + \sigma_{AlN}$.

The fitting parameters are Λ, l_{AlN}/Λ, A, w, σ_d, σ_{VN} and σ_{AlN}. Since these seven parameters influence different aspects of the XRD patterns, they can be determined largely independently. The typical fitting procedure is described as following: firstly, l_{AlN}/Λ is varied to yield the correct Bragg peak position. Second, Λ is varied to match the correct satellite peak spacings. Third, the broadening of the x-ray peaks above the instrumental broadening, due to random disorder in the films, is fit. Increasing σ_{VN} and σ_{AlN} broaden only satellite peaks, not the Bragg peak, while increasing σ_d broadens all peaks. Fourth, the interface width w and the amplitude A are varied to fit the satellite peak intensities. These two parameters can be separated as they affect different satellite peaks. For a quantitative comparison of the fits, an R-squared R^2 deviation of the simulated I_s from the experimental I_m intensity ratios is evaluated.

$$R^2 = \sum_i [\log_{10}(I_m) - \log_{10}(I_s)]^2$$

Although this R-square factor has been used in many superlattice simulation fittings, and has been able to generate fairly reasonable fit, it is not a justified term [Grozea et al, 1998].

3.2 Transmission Electron Microscopy (TEM)

Although XRD is a very effective structural characterization method, it only provides average structural information on the films, as the size of the incident x-ray beam is

usually in the mm scale. Moreover, if the size of the crystal phase in the film is small (on the nanometer scale) and the crystals grow in a random orientation, the intensity of the x-ray peak can be low, and sometime no information is obtained using XRD. This problem is encountered in the research of both BN and diamond nucleation, as presented in chapter 5, 6 and 7. TEM is an ideal tool in these circumstances, as its probe size can be as small as several nanometers. Therefore, accurate structural information can be obtained from micro-areas.

The optics of a TEM is similar to those of transmission optical microscopes except that electron beams are used instead of visible light. Combining direct imaging and electron diffraction can provide fairly complete information of almost all the microscopic features in thin films. The TEM samples are required to be electron transparent, i.e., thinner than several tens of nanometers, for good TEM analysis.

3.2.1. TEM Sample Preparation

Sample preparation of thin film coatings is probably the most tedious part of TEM work. There are two types of sample preparation, plan-view, which provides information about the film surface, and cross-section, which provides information about substrate/film interface and film microstructure along the growth direction. The choice of TEM sample preparation technique depends upon the nature of the sample material and the information desired.

Conventional cross-section TEM (XTEM) sample preparation includes sample cutting, gluing, polishing, dimpling and ion-milling. A typical XTEM sample is shown in Figure 3-2 for both top-view and side-view.

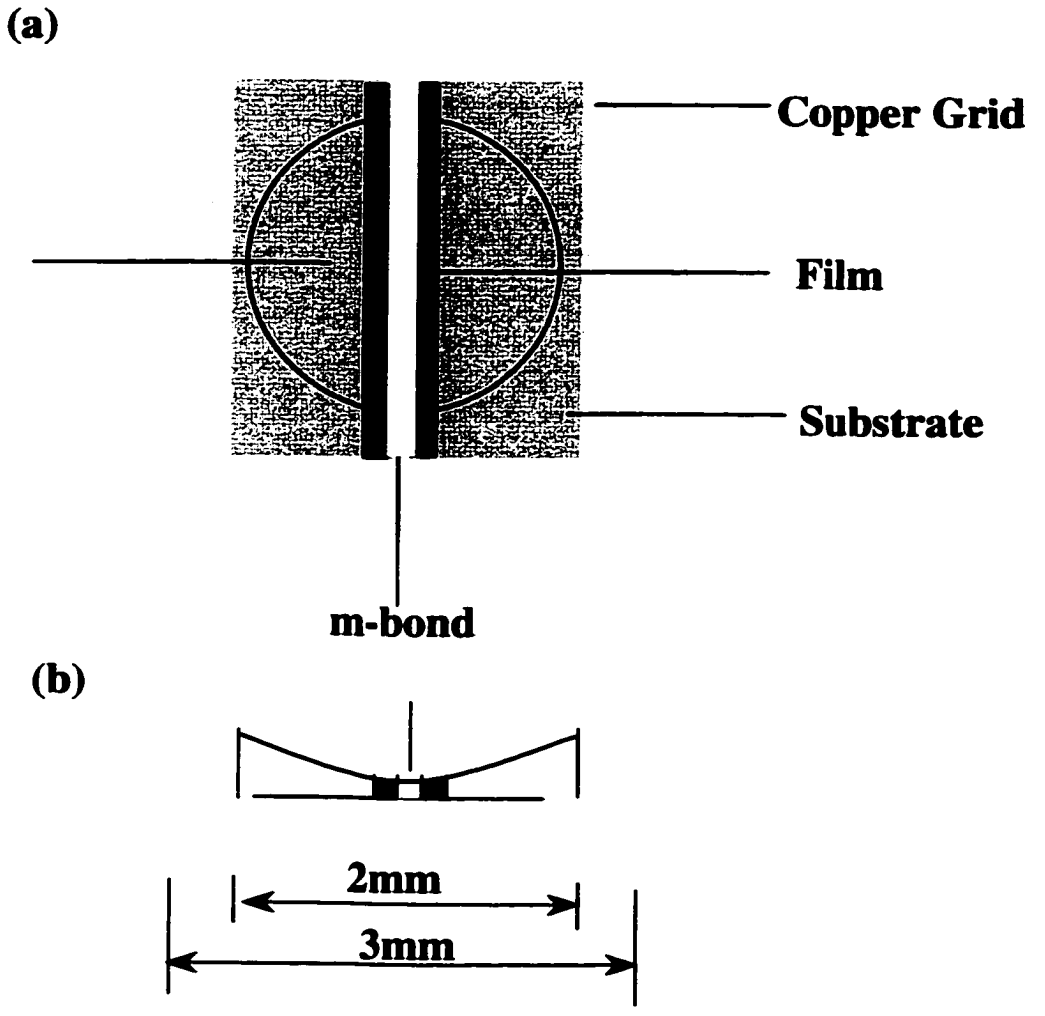

Figure 3-2 Schematic of (a) Top-view and (b) side-view of XTEM sample

Time-consuming is one major draw-back of the conventional sample preparation technique. It usually takes one day or two to prepare a good sample due to the long process of polishing, dimpling and ion-milling. Various techniques applicable to different types of materials have been developed in recent year to overcome this problem. Cleavage [McCaffrey, 2000] is capable of producing good TEM sample without ion-milling, and importantly, quickly. Unfortunately, cleavage requires crystalline samples with accessible cleavage planes. Information of the cleavage planes is required beforehand, and the information usually differs in materials with different crystalline structures.

Tripod polishing is another widely used technique in industries. Figure 3-3 shows the side-view schematic of the sample prepared by tripod polishing. It is commonly agreed that this method requires ion-milling process to achieve electron transparency in the sample. The current study demonstrates that with proper control, tripod polishing can produce good TEM sample for HREM study without ion-milling. Nevertheless, this is only valid when the film thickness on the substrate is less than 100 nm.

There are two ways to thin down the XTEM sample by tripod polishing, i.e. with the sample interface perpendicular to the wedge direction or parallel to the wedge direction. In the first case (shown in Figure 3-4 a), the sample has to be polished close to the interface and some ion-milling is required, as the sample may not be thin enough (depends on the wedge angle). The second case is totally different; as long as the sample is polished to the inner hole of the copper ring (Figure 3-4b), a thin area good for high-resolution TEM is guaranteed. This becomes important when ion-milling may change

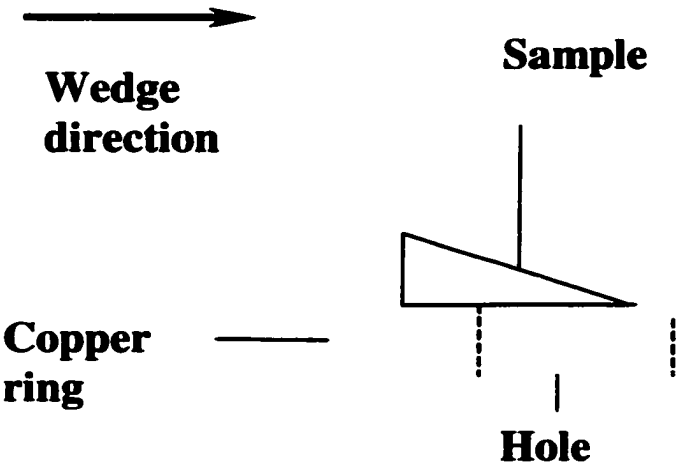

Figure 3-3 Schematic of the sample prepared by tri-pod polishing (side-view)

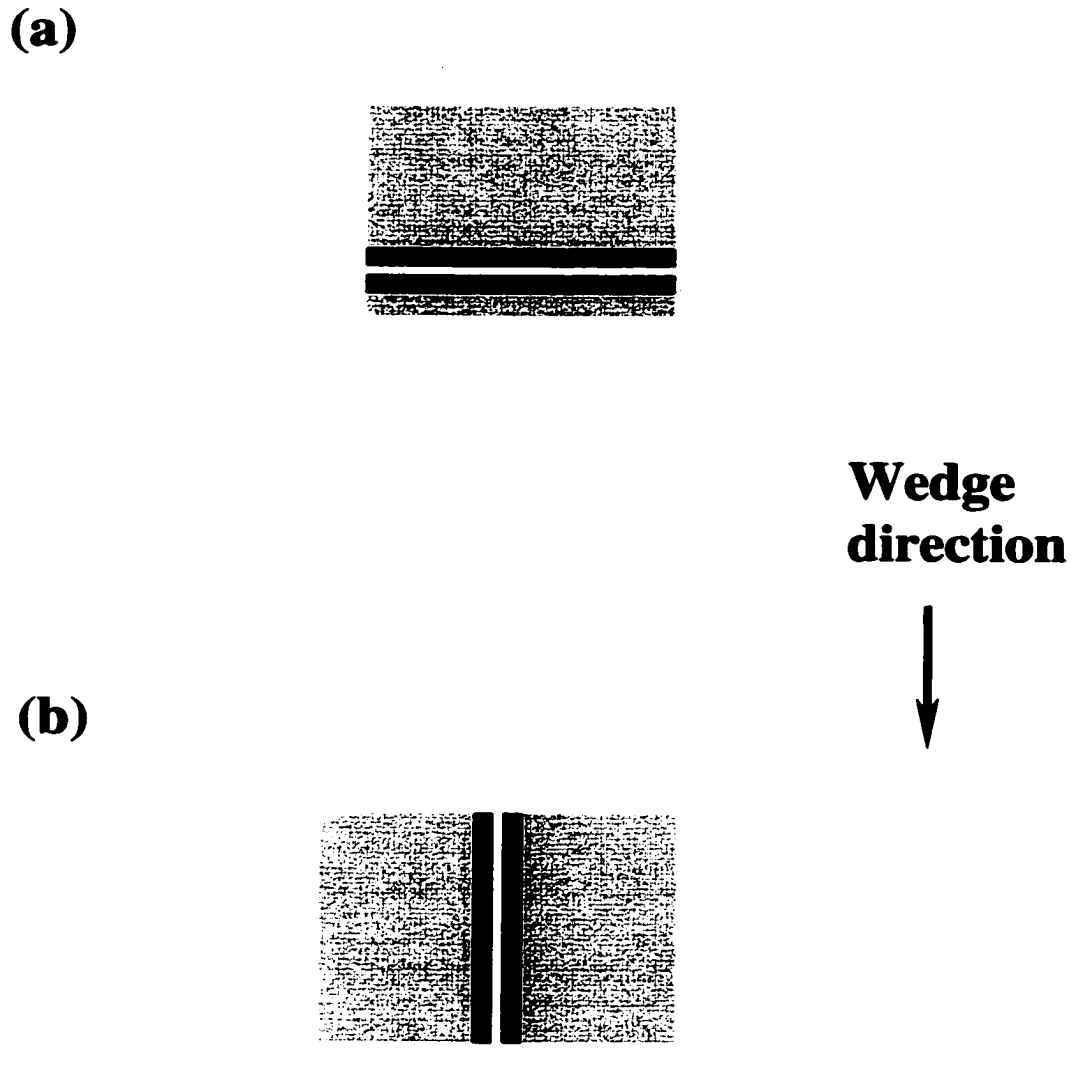

Figure 3-4 XTEM sample polished using tripod, the interface of the sample is (a) perpendicular and (b) parallel to the wedge direction

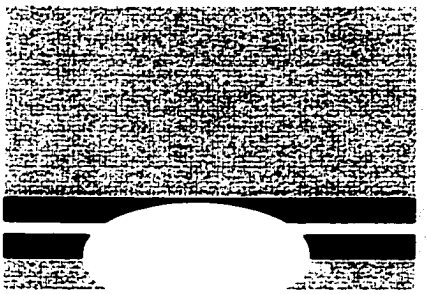

Figure 3-5 Ion milling result of the XTEM sample prepared using tri-polishing technique as shown in Figure 3-4 (a)

the original film composition by intensive ion bombardment (as in Chapter 7). Nevertheless, the thin area produced by this way is relatively small. Although the first case requires ion-milling, it could produce sample with large thin area (Figure 3-5)

No matter what kind of polishing technique is used, it is always important to determine the sample thickness at different polishing stages, so that a grinding paper with an appropriate grit can be chosen. There are different ways to determine the sample thickness, usually differing for different materials. Silicon is probably the easiest one, as it would display a series of colors in regions of less than 10 microns thickness and a series of interference fringes in the region of less than 2 microns backlit by an optical source [McCaffrey, 1998]. These colors and fringes result from the transmission, reflection, absorption and interference of light within the sample, and can be used to monitor the sample thickness during TEM sample preparation. The other method is generally used for transparent materials such as MgO. Optical microscope is used to measure the thickness of the sample by the difference between focusing on the front and the back surface (a fine polished sample surface is required).

Ion-milling is basically a sputtering effect. The sample is bombarded by argon ions until enough material is sputtered away and a small perforation is formed in the middle of the sample in the region of interest. Frequently damage occurs during the ion-milling process. An amorphous layer can be formed on both the top and the bottom surface of the sample, which contributes to a significant part of the entire sample thickness. This becomes especially problematic in HREM studies, when images are collected from the thinnest region of the sample. Moreover, ion-milling is known to

cause phase transformation in certain materials such as carbon, i.e., graphite or amorphous carbon can transform to diamond when the ion-milling voltage is high enough [Banhart, 1999].

3.2.2. Electron Diffraction and Diffraction Contrast

Electrons are treated as probability amplitude waves to explain their interaction with materials during the scattering process in a microscope. The wave function Ψ satisfies the time independent Schrödinger equation.

$$h^2/8\pi^2 m_0 e \nabla^2 \Psi + (E + V) \Psi = 0 \qquad 3.6$$

In the absence of a potential, the equation has plane waves solutions: $\Psi = A \exp(2\pi i \mathbf{kr})$, where $\mathbf{r}$ is the a point on the wave front, $\mathbf{k}$ is the wave vector. Similar to x-ray, only elastic scattering contributes to diffraction. Inelastic scattering, although relatively large, primarily gives background.

The image contrast can be explained using spherical wave and Bloch wave solutions to the Schrödinger equation using different potentials, and detailed explanations can be found in literatures [Hirsch et al., 1976; D. Williams et al., 1996]. Unlike x-ray, dynamical scattering is very important in TEM. The most important approximation made in the kinematical theory is that the amplitude of the incident beam at any point of the crystal is the same, so that the energy transmitted to the diffracted beam is neglected. Only single scattering processes are considered. However, in the most case, the diffracted wave will be scattered again by atoms when its amplitude becomes large.

3.2.3. Phase Contrast

Although electron diffraction provides direct information of the reciprocal lattice of crystalline structures, it cannot decide the relative positions of several co-existing phases in real space. For example, diffraction pattern taken from diamond-like-carbon film on silicon show the epitaxial relationships among silicon, silicon carbide, and diamond. However, it is impossible to determine whether the diamond is grown epitaxially on silicon or on silicon carbide just from the diffraction pattern (Figure 3-7). High-resolution electron microscopy (HREM) is very powerful in solving the problems mentioned above.

Although high-resolution image provides structural information of materials at the atomic level, it is not simply a projection of the specimen structure in the direction of the incident beam. In practice, there are many limitations in interpreting HREM images. For many instances, a one-to-one correspondence does not exist between the object and the image. The observed fringes do not necessarily correspond to the positions of atomic planes. Therefore, it is extremely important to understand the imaging conditions so that an accurate interpretation can be given.

Unlike the conventional medium/low resolution image contrast, which can be explained as the amplitude contrast, high-resolution images present details of the specimen comparable to the coherence width of the electron wave. Phase contrast becomes the dominant contrast mechanism. Interpretations of high-resolution images are usually based on theories of linear/non-linear imaging as well as various computational simulations, reference of which can be found elsewhere [Reimer, 1984, Buseck et al., 1988].

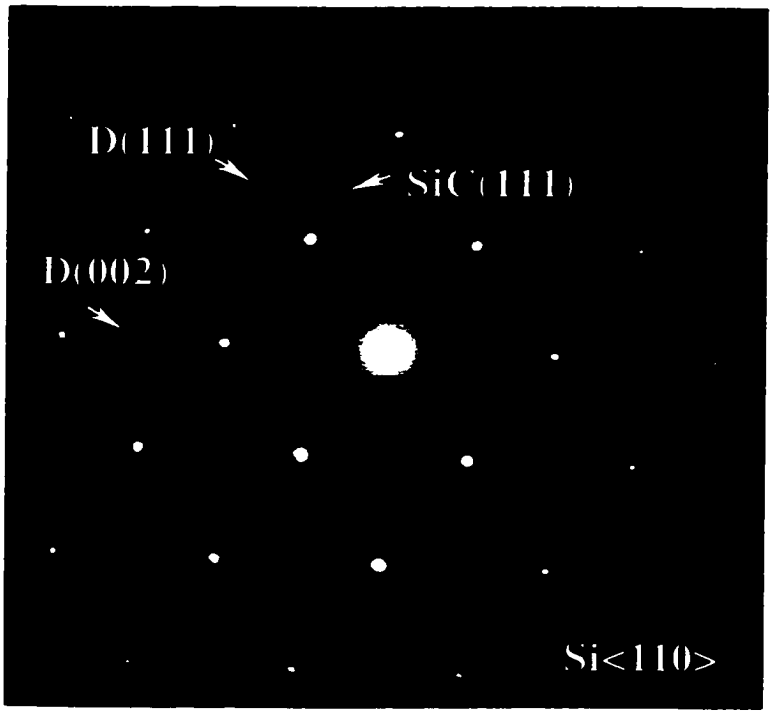

Figure 3-6 Transmission electron diffraction pattern taken from DLC/silicon interface with electron beam along the silicon <110> zone axis

CHAPTER 4. EPITAXIAL GROWTH AND PHASE TRANSFORMATION Of AlN IN AlN/VN SUPERLATTICES

4.1 Different Phases of AlN and Their Epitaxial Growth

AlN, as one of the III-V compounds, is characterized by high ionicity, short bond length, low compressibility, and high thermal conductivity greater than 100W/mK [Van Camp et al., 1991]. It also has a low thermal expansion coefficient, which is very close to that of silicon and GaAs. AlN has been considered a promising material for semiconductor devices applications since 1970, especially for the development of blue and UV light-emitting diodes. Together with other III-V nitrides such as InN and GaN, AlN is a candidate material for optoelectronic applications. These nitrides could form a continuous alloy system (InAlN, AlGaN, etc) whose direct optical bandgaps for the hexagonal wurtzite (w) phase range from 1.9 eV for α-InN to 6.3 eV for α-AlN [Van Camp et. al., 1991]. Other advantageous properties of AlN include high mechanical and thermal stability, large piezoelectric constants and the possibility of passivation by forming thin layers of Al_2O_3 with a band-gap of approximately 9eV [Ambacher, 1998].

In contrast to cubic III-V semiconductors such as GaAs, with a zinc-blende (zb) structure, the thermodynamically stable phase of AlN is the hexagonal wurtzite structure (w-AlN), which is called the α-phase. At ambient temperature and pressure, AlN can only crystallize in the wurtzite phase. However, it undergoes a pressure- induced phase transformation into a rocksalt (B1) structure (B1-AlN), which is predicted by an empirical ionicity concept [Phillips, 1973] as well as a first-principles calculation [Chelikowsky et. al, 1987]. It is also predicted that a phase transition would take place in

AlN from the rocksalt to zinc-blende structure (zb-AlN) [Phillips, 1973] when the pressure is further increased. The structures of these phases are shown in Figure 4-1.

Figure 4-2 shows the total energies as a function of the reduced volume for hexagonal and cubic AlN. The calculations are based on the local density functional formalism together with ab initio norm-conserving pseudopotentials [Van Camp. et. al. 1991]. The dashed line is the common tangent of the two curves and indicates the path of the pressure-induced phase transition. Microscopically, pressure-induced phase transformation belongs to the homogeneous phase transformation category, i.e., it occurs over the entire volume of the system simultaneously rather than near an interface. At no time during the homogeneous transformation does a part remain unaffected. The entire system changes and gradually approaches the final equilibrium state. This type of phase transformation always involves local bonding change .

Another means to achieve the metastable cubic phase of AlN is epitaxial stabilization. Epitaxial growth of AlN on most substrates yields the stable wurtzite structure, such as AlN (0001) on (0001) sapphire [Zhang et. al., 1992], AlN (0001) on NiAl (111) [Gaβmann et. al., 1995], AlN (0001) on Si (111) [Malengreau et. al., 1997], as well as Si (001) [Meng et al., 1993]. There have also been a few reports of cubic AlN layers grown on substrates with cubic symmetry, including a 12 nm thick zinc-blende AlN layer formed by a solid-state reaction between epitaxial Al (001) and TiN (001) layers [Petrov et. al., 1992]. Previous work in Barnett's group shows that zinc-blende AlN could be stabilized in an AlN/W superlattice with AlN layer thicknesses less than 1.5 nm, in which it transforms to w-AlN at larger thickness [Madan et. al., 1996].

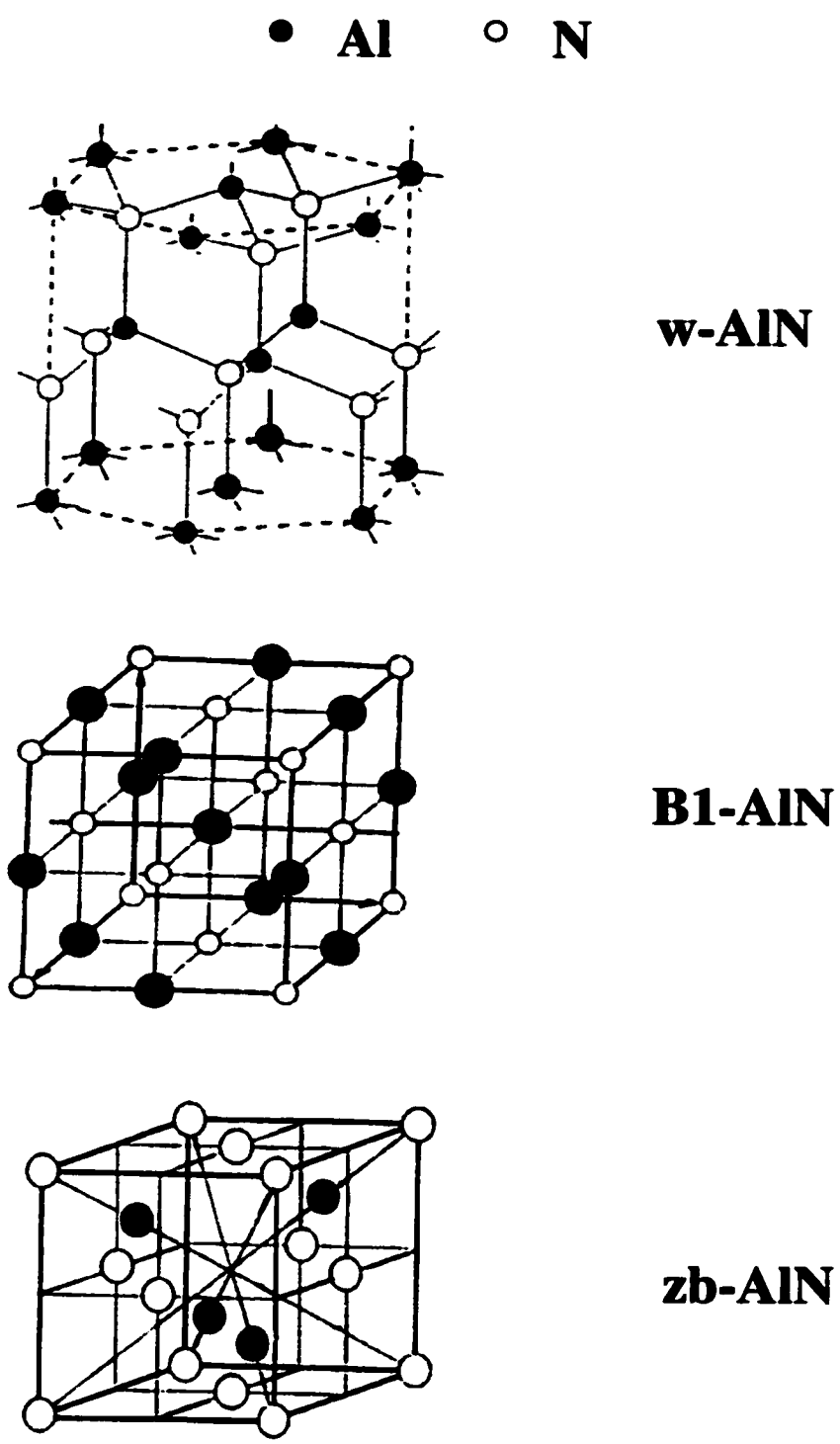

Figure 4-1 Schematic of three AlN crystal structures

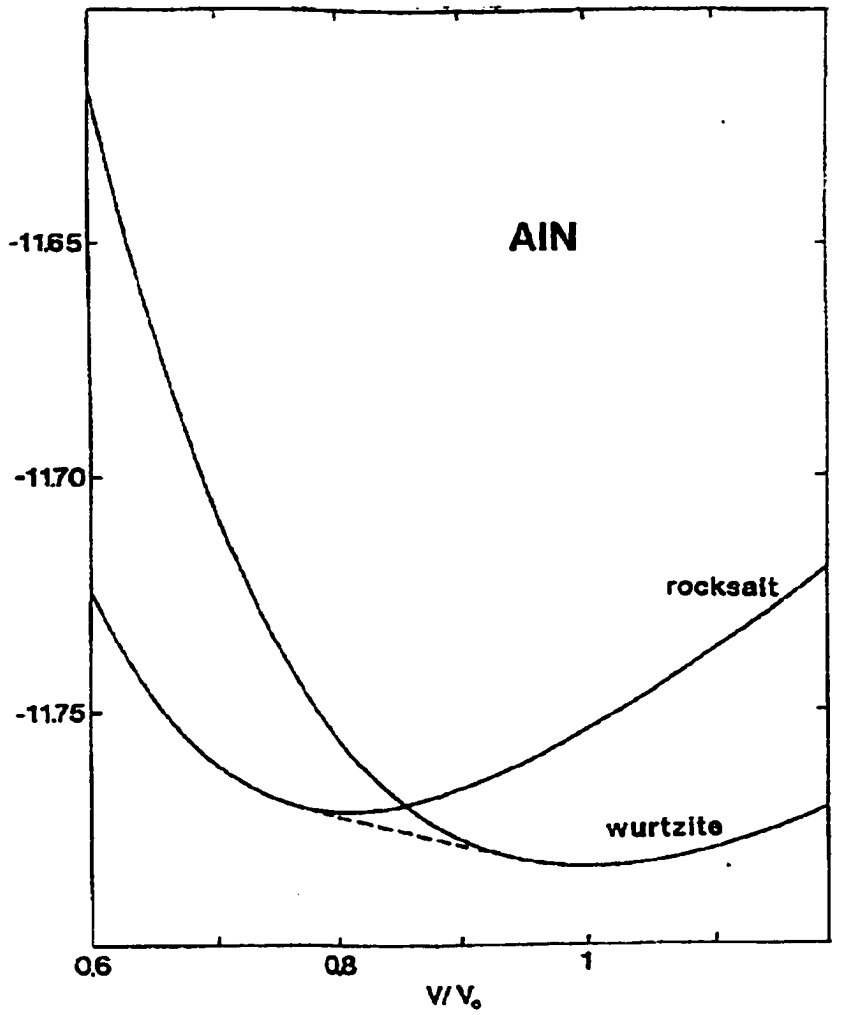

Figure 4-2. Total energies as a function of the reduced volume for hexagonal and cubic AlN. The dashed line is the common tangent of the two curves and indicates the path of the pressure-induced phase transformation [Van Camp et al., 1991]

B1-AlN is observed to be stabilized in both AlN/NbN [Madan et. al., 1996] and AlN/TiN [Madan et. al., 1997] superlattices with AlN layer thickness less than a certain thickness value.

Phase transformation of AlN from cubic to hexagonal is observed in all the superlattice systems for AlN layer thickness greater than a certain critical thickness value. This critical thickness varies in different superlattice systems. Figure 4-3 shows the evolution of the x-ray diffraction pattern from an AlN/TiN superlattice as a function of AlN thickness . For superlattices with layer thickness $l_{AlN} < 2.0$nm, strong satellite reflections are observed which confirms the presence of epitaxial cubic AlN. When l_{AlN} is about 2-3 nm, the satellite reflections either decrease (B) or are lost (C), and extra peaks near wurtzite AlN (0001) and TiN (111) positions appear. For superlattices with $l_{AlN} \sim 4.0$nm, no satellite reflections are observed and the predominant high-angle XRD peaks are due to w-AlN (0002).

In this chapter, results of AlN/VN superlattices will be presented. X-ray diffraction and TEM are the two major methods for structural characterization of the superlattices. Factors affecting epitaxial stabilization and the critical thickness of the metastable B1-AlN will be covered. The phase transformation from B1 to wurzite structure beyond the critical thickness value is analyzed. The phase transformation process will be discussed.

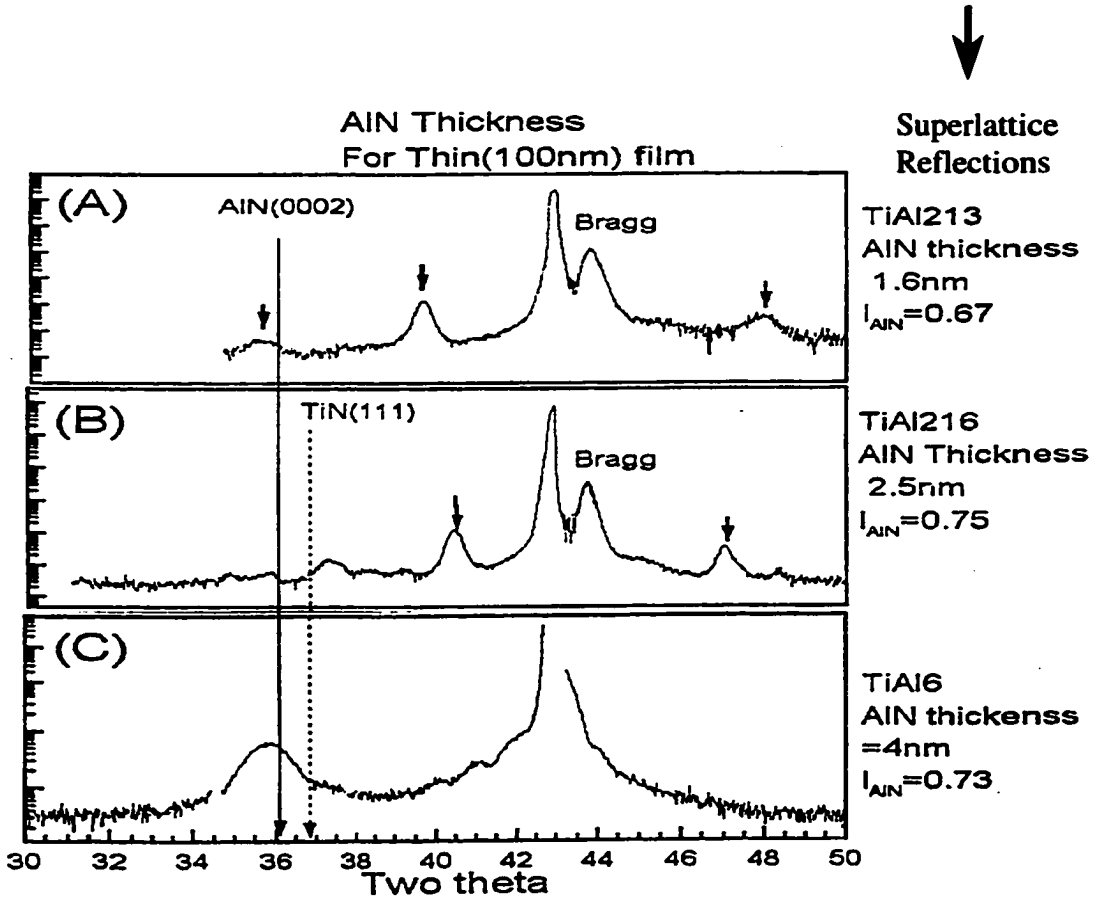

Figure 4-3. X-ray diffraction showing the phase transformation of AlN in AlN/TiN superlattices [Madan et al.1997]

4.2 Preparation of AlN/VN superlattices

AlN/VN superlattices were grown on MgO (001) substrates in an ultrahigh vacuum dc-magnetron sputtering system. A schematic of the chamber is shown in Figure 4-4. The sputtering targets were 99.95% pure V and 99.99% pure Al. Superlattices were deposited in mixtures of 12 mTorr Ar and 3.6 mTorr N_2. The MgO (001) substrates were first cleaned in organic solvents and then annealed at 750 ° C in vacuum for 0.5 h. After that, the substrate temperature was dropped to 630 ° C, which proved (from experiments at different temperatures) to be the optimal operating temperature. All buffer layers and superlattices were deposited at this temperature. In all cases, a 200 nm VN buffer –layer was deposited prior to superlattice deposition. A special multi-layer sample was grown for the TEM study that contained three consecutively-grown superlattices with different AlN layer thickness: [AlN (1.8 nm)/VN (6.2 nm)]$_3$, [AlN (4.0 nm)/VN (6.2 nm)]$_3$, and [AlN (14.8 nm)/VN (6.2 nm) $_3$, which enabled observation of both the stabilized B1-AlN and the w-AlN after the phase transformation in the same sample (Figure 4-5).

XRD scans were carried out in a double-crystal diffractometer equipped with a LiF focusing monochromator. Transmission electron diffraction (TED) and HREM were used to examine the superlattice structures of both the stabilized phase and the transformed phase. Two TEM samples were prepared with different orientations, which enabled high-resolution images to be taken with the electron beam along the MgO [100] and [110] directions, respectively. The high-resolution images were taken on a Hitachi H-9000 microscope operated at 300kV. The TED patterns were taken on a Hitachi H-8100 microscope using the smallest selected area aperture.

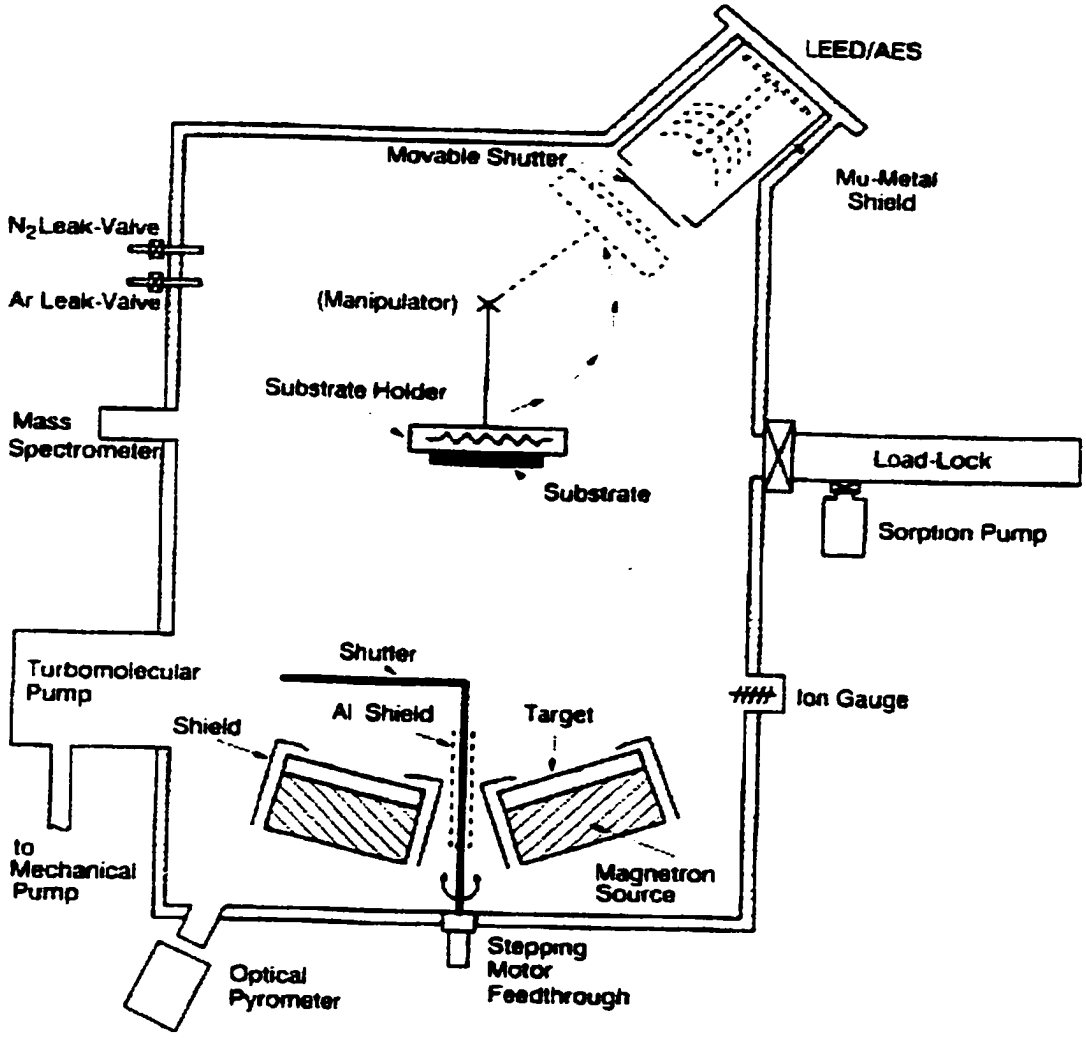

Figure 4-4. Schematic of the deposition chamber [Mirkarimi et al., 1992]

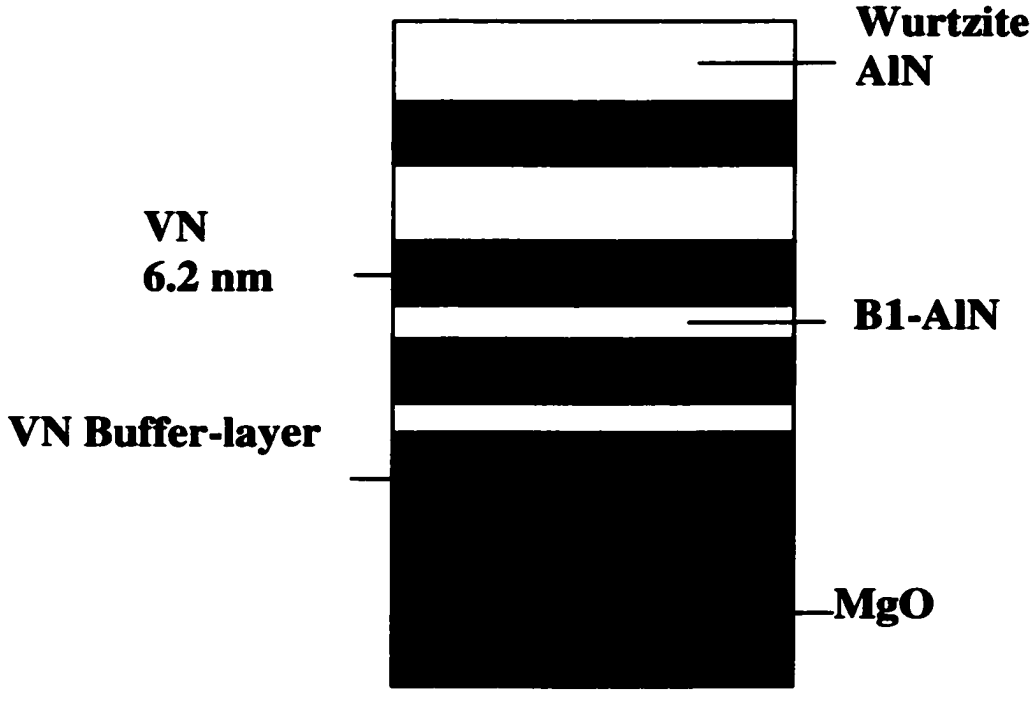

Figure 4-5. Schematic diagram of the period variation of TEM sample

4.3 Overview of AlN/VN Superlattice Growth

Figure 4-6 shows a low magnification image of the special TEM superlattice with the electron beam along the VN [100] zone axis. The layer thickness of the VN is 6.2 nm. There are two different periods shown in Figure 4-4: 10.2 nm with an AlN layer thickness of 4.0 nm, and 21.0 nm with an AlN layer thickness of 14.8 nm. The AlN layers appear slightly lighter than the VN layers because of the lower scattering factor of Al. When the AlN layers are thin (4.0 nm layer thickness), a relatively smooth layered structure is present. When the AlN layers grow thicker (14.8 nm layer thickness), the layered structure becomes wavy above the first AlN with 14.8 nm layer thickness.

4.4 Epitaxial Stabilization of B1-AlN in ALN/VN Superlattices

Figure 4-7 shows a higher magnification image of region (a) in Figure 4-6, with an inset diffraction pattern. Both the VN and AlN show square lattice fringes. The measured lattice fringe spacing of 2.05 ± 0.03 Å, agrees with the theoretical NaCl-type structure lattice parameters: a_{VN} = 4.14Å and $a_{B1\text{-}AlN}$ = 4.06Å, respectively. The small difference between the measured d-spacings and the theoretical ones is due to the strained coherent lattice. The diffraction pattern also shows a square symmetry. The diffraction spots are extended along the [002] (growth) direction, this is due to superlattice reflections arising from the artificial periodicity in the structure. The orientation relationship between the two materials is (001)VN//(001)B1-AlN and (010)VN//(010)B1-AlN. No misfit dislocations are observed, which indicates a strained coherent interface between B1-AlN and VN.

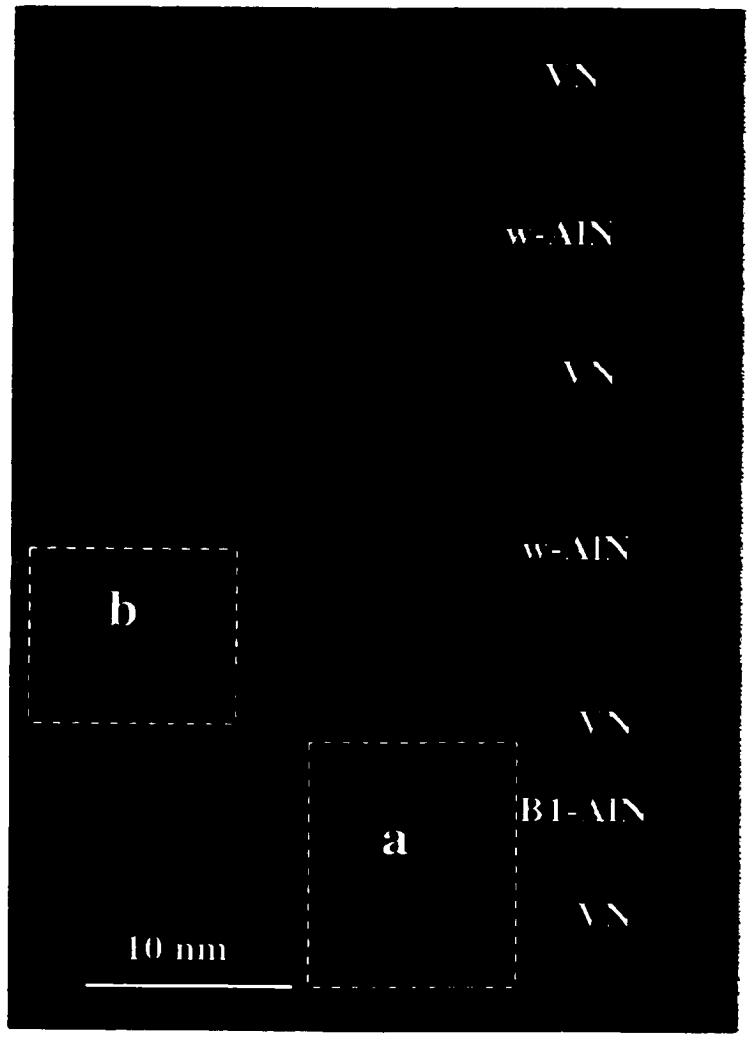

Figure 4-6 Image of AlN/VN taken with the electron beam along the MgO [100] direction. A smooth layered structure was observed when the AlN layer thickness is thin. The layered structure became wavy after the B1-wurtzite phase transformation took place.

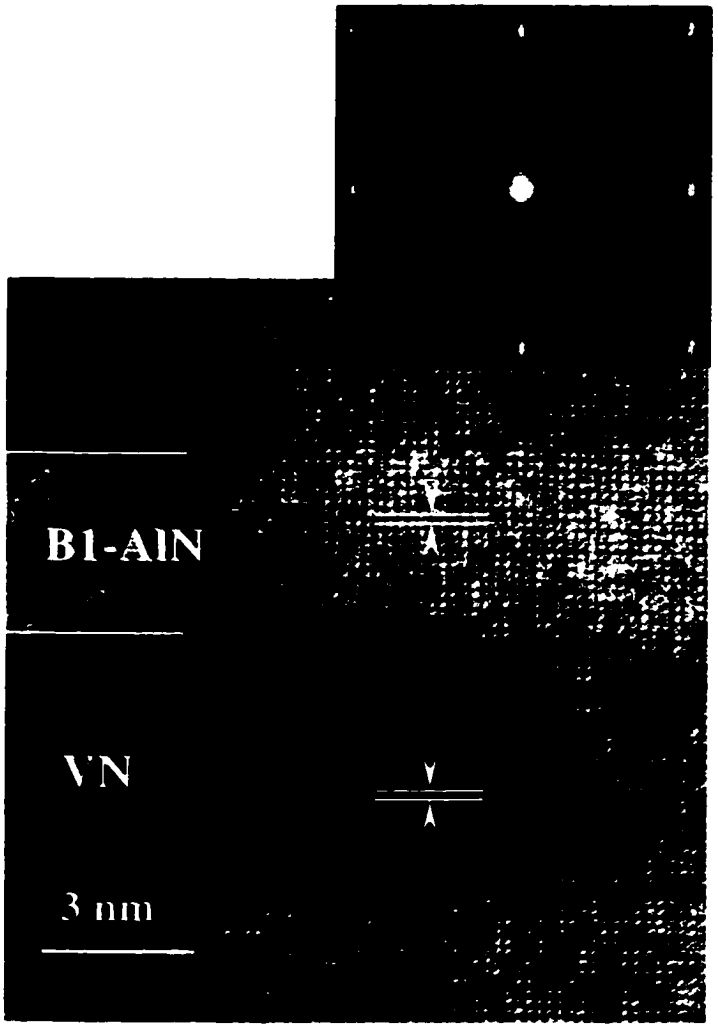

Figure 4-7 HREM image of ALN/VN taken several periods away from the MgO substrate with the electron beam along the MgO [100] direction. The layer thickness of AlN was 4.0 nm and the B1 structure was stabilized in the superlattice. The diffraction pattern in the inset confirmed the cubic structure

For superlattices with AlN layer thickness less than 4.0 nm, strong satellite reflections are observed for both low- and high-angle XRD scans. Figure 4-8 shows typical experimental low- and high-angle XRD patterns for a [AlN (1.3nm) /VN (2.5nm)] superlattice.

The high-angle XRD pattern shows a central Bragg peak (FWHM ~0.6°) surrounded by equally spaced reflections, which is typical in superlattice films. The (002) Bragg peak appears in a position between that expected for (002) VN and (002) B1-AlN. The experimental data are fitted using a kinematical model with a trapezoidal composition modulation, which has been described in detail in 3.1.2. The Λ and the l_{AlN} are estimated from deposition parameters and low-angle XRD patterns. The simulation did not match the superlattice peak positions when zinc-blende AlN structure was assumed. The best fit is obtained by assuming B1-AlN and B1-VN layers with interfacial widths of 0.3 nm and layer thickness fluctuations of 0.2-0.25 nm. The fits yield lattice spacings of 0.405 ± 0.002 nm for B1-AlN and 0.413 ± 0.003 nm for VN, slightly less than the bulk values. This suggests tensile stress in both layers, presumably due to the higher thermal expansion coefficient of the MgO substrate. A larger critical thickness of AlN before the B1/wuritzite phase transformation was achieved in this system, compared to the result in a previous study of AlN/TiN [Madan et. al., 1997].

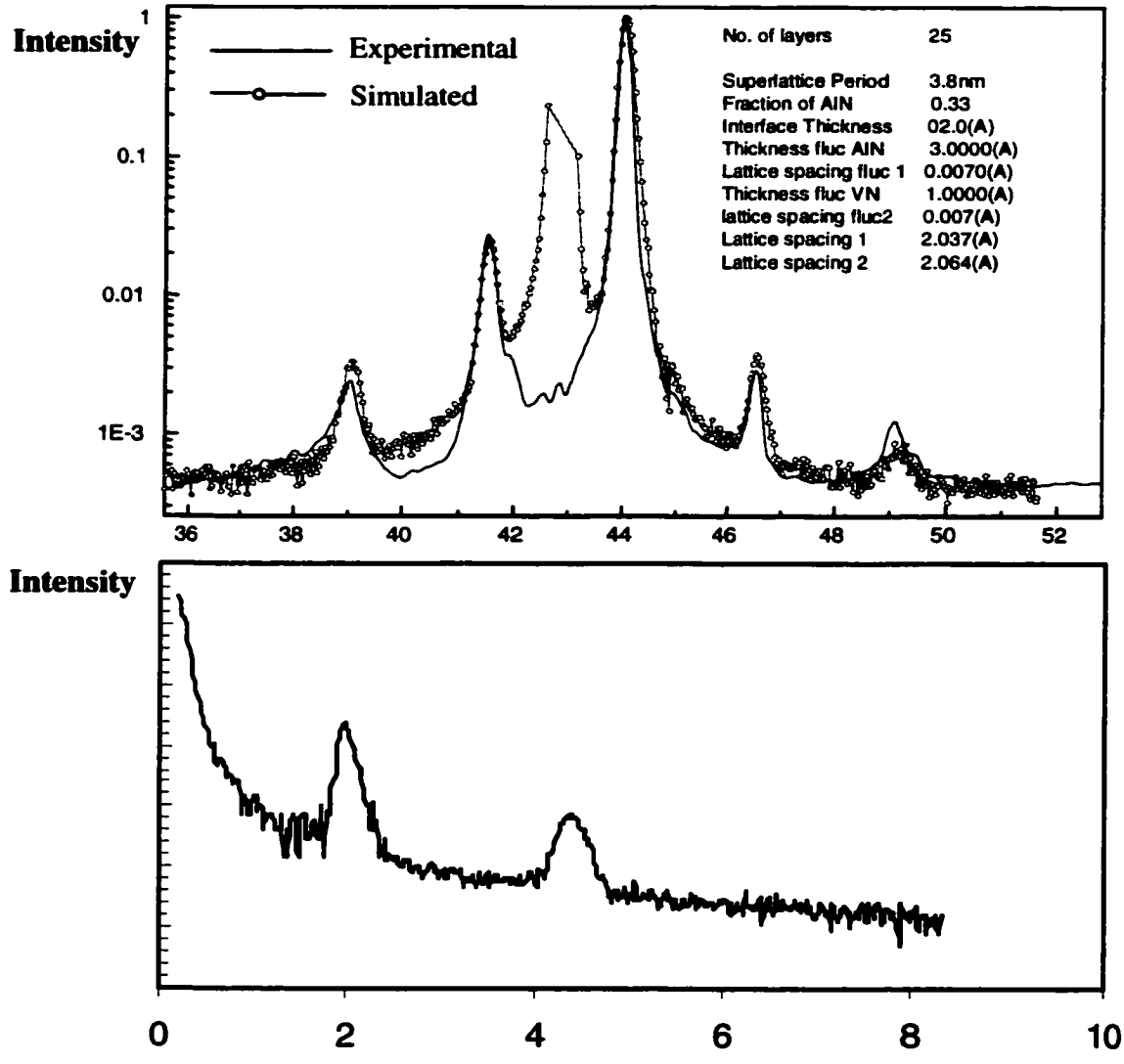

Figure 4-8 (a) Experimental and simulated high-angle XRD scans for a [AlN (1.3 nm)/VN (2.5nm)] superlattice. Simulation assuming out of plane lattice spacing of d_{AlN} = 2.037 Å, d_{VN} = 2.064 Å , and an interface width of 2.0 Å provide a reasonable fit. Random d-spacing fluctuations (Gaussian width ~ 0.007 Å) and layer thickness fluctuations (Gaussian width ~ 1 Å) were incorporated to match the observed broadening of the peaks. (b) Experimental low-angle XRD scans for a [AlN (1.3 nm)/VN (2.5nm)] superlattice

Figure 4-9 shows a θ-2θ x-ray diffraction scan from both [AlN (4.0 nm)/VN (6.2 nm)]$_{45}$ (a) and [AlN (2.6 nm)/TiN (4.5 nm)]$_{14}$ (b) superlattices. The lines with open circles are the experimental data of the superlattices, and the solid lines are the simulated patterns that would be expected for high quality epitaxial superlattices. Satellite reflections consistent with the simulated data are observed only in the AlN/VN superlattice. XRD results reveal that B1-AlN can be stabilized in the AlN/VN superlattice up to 4.0 nm critical thickness, higher than that in AlN/TiN superlattices (2.0-2.5 nm).

The dependence of critical thickness on lattice mismatch can be explained using a simple model accounting only for the AlN bulk and interfacial energies. The total energy per formula unit area of an AlN layer during growth can be written as

$$E_{Total} = (E_B + E_S) * l + E_I$$

where E_B is the strain-free bulk energy, E_s the coherency strain energy, E_I the interfacial energy and l the thickness of the growing AlN layer. The $(E_B + E_S)$ term of the three lowest-energy AlN structures (wurtzite, zinc-blende, and B1) are compared to understand the epitaxial stabilization effect. Figure 4-10 shows the predicted $E_B + E_S$ of an AlN layer versus the in-plane lattice spacing [Madan et. al., 1997]. As wurtzite AlN has a large lattice mismatch to the underlayer materials (either TiN or VN), it could be considered as totally relaxed, therefore the $E_B + E_S$ of w-AlN remains constant as the lattice spacing changes. The stress free energies E_B used in the total energy calculation are from the previous work of Christensen and Gotczyca [Christensen et. al. 1994]. For B1-AlN and zb-AlN, the biaxial elastic strain energy due to the lattice mismatch was

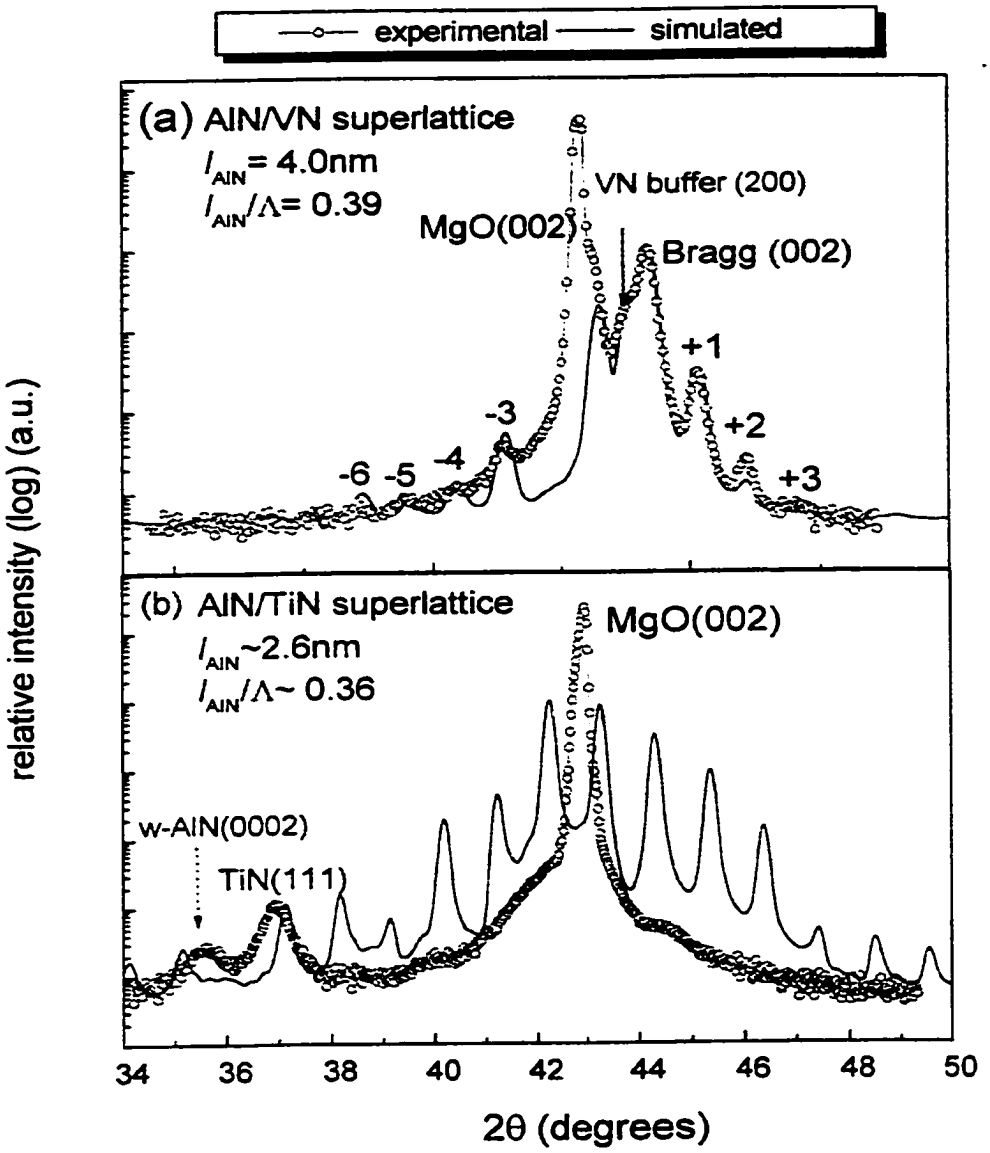

Figure 4-9 Experimental and simulated θ-2θ XRD pattern from a [AlN (4.0 nm)/VN (6.2 nm)]$_{45}$ superlattice with l_{AlN}/Λ = 0.39 (a), and a typical θ-2θ scan from a [AlN (2.6 nm)/TiN (4.5 nm)]14, l_{AlN}/Λ = 0.36 superlattice (b) (courtesy from Madan et al. 1997)

calculated assuming coherent layers using linear elastic theory and elastic stiffness tensor components calculated from first principles [Madan et. al. 1997].

In the case of AlN/TiN, although the bulk energy is much lower in both w-AlN and zb-AlN than in B1-AlN, B1-AlN still crystallizes as it forms a low energy coherent interface with TiN, while both w-AlN and zb-AlN do not. The B1-structure forms at smaller layer thickness where the interfacial energy term dominates the bulk energy. The formation of B1-AlN in AlN/VN superlattice follows the same principle. As shown in Figure 4-10, the strain energy of both B1-AlN and VN lattices is lower due to a smaller lattice mismatch of 2.4%, compared to 4.8% in the case of AlN/TiN. A larger critical thickness for the phase transformation is expected, which is consistent with experimental result.

Dependence of the critical thickness on the thickness of the underlying material is also found in AlN/VN superlattices. Figure 4-11 shows the XRD results from [AlN (2.7 nm) /VN (2.0 nm)]$_{45}$ superlattices. For l_{AlN} = 2.7 nm, the substrate, superlattice and the VN buffer layer Bragg reflections are present. For l_{AlN} = 3.0 nm, the predominant peaks are a broad w-AlN (002) reflection, a superlattice Bragg (002) reflection, and a cubic VN (002) reflection from the VN buffer layer. The disappearance of high-angle satellite reflections and weak superlattice Bragg peak suggest that AlN has at least partially transformed to wurtzite with a (0002) texture, and the layered structure has been lost. The critical thickness of AlN is 2.7 nm when the underlying VN layer is 2.0nm thick, while the critical thickness of AlN becomes 4.0nm when the VN layer thickness is increased to 6.2 nm.

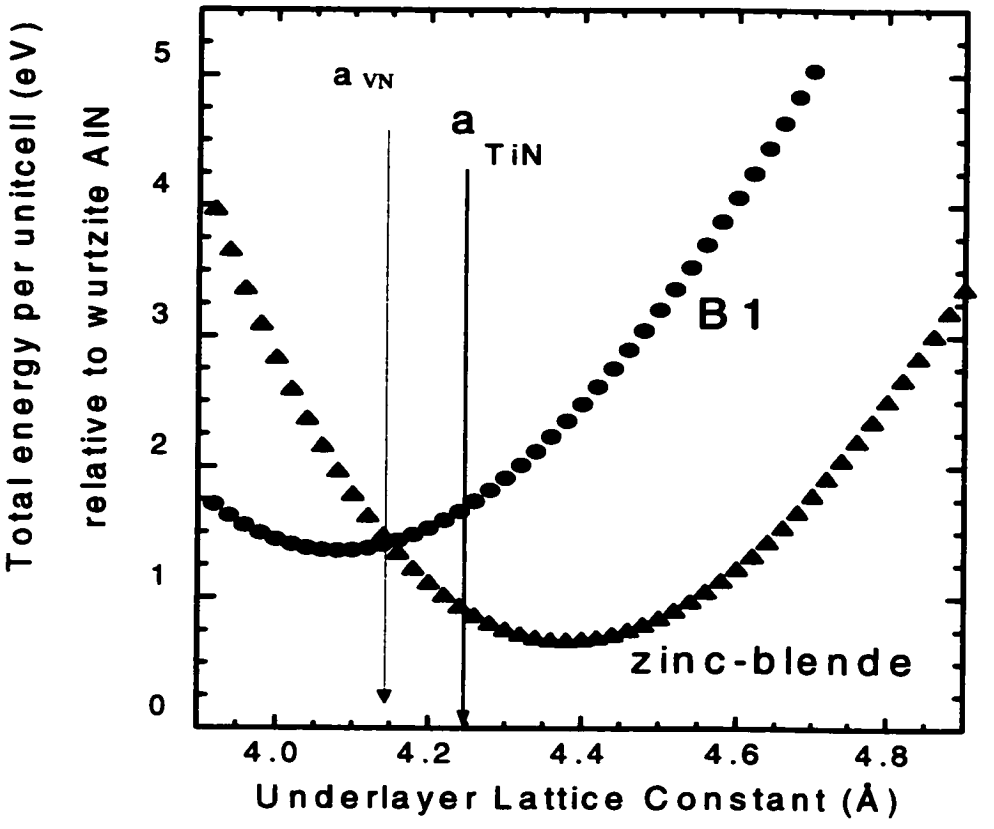

Figure 4-10. Bulk energy per formula unit for biaxially strained B1 and zinc-blende AlN as a function of the in-plane lattice spacing, excluding the interfacial energy.

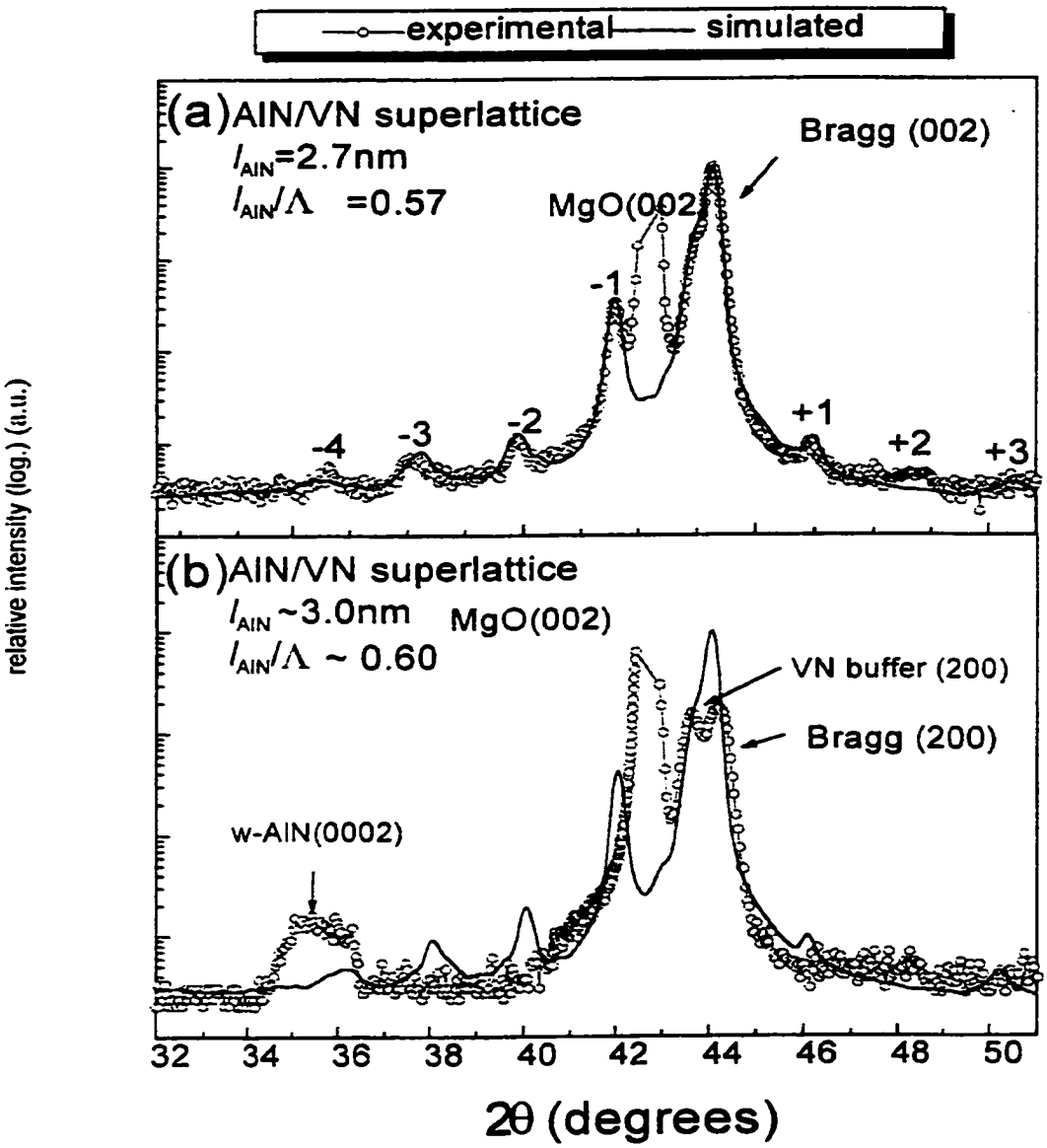

Figure 4-11 High-angle XRD pattern from AlN/VN with l_{AlN}/L = 0.57 ~0.60 with l_{AlN} = 2.7 nm (a) and l_{AlN} = 3.0 nm (b), respectively

This increase in AlN critical thickness with increasing VN layer thickness can be rationalized as follows. If the AlN layer exceeds the VN layer in thickness, there may be insufficient VN to maintain stabilization. In this case, rather than imposing its structure on the AlN, the VN may be deformed by the transforming AlN; note that there is a 23% volume expansion associated with the transformation. Indeed, in $CrN_{0.6}$/TiN superlattices deposited at low temperatures [Yashar et al., 1998], highly-deformed zones were observed in the TiN layers within ~ 5 nm of the interfaces after the CrN transformed from cubic to hexagonal. (The deformation was presumably not observed in Figure 4-12, as presented later in the chapter, because of the high growth temperature, which allowed annealing of defects.) Thus, decreasing the thickness of the VN layer decreases the amount of material that must be deformed during the transformation of AlN---the barrier to transformation and hence the critical thickness.

4.5 Phase Transformation of AlN from the Rocksalt to Wurtzite Structure

4.5.1. Overview of Phase Transformation

4.5.1.1. Experimental Evidence

Phase transformation from B1-AlN to w-AlN is first suggested by X-ray diffraction as shown in Figure 4-11 (b). The disappeared superlattice reflections as well as the dominant w-AlN (0002) peak at ~36 °indicates that the phase transformation has occurred.

Figure 4-12 shows a higher magnification image of region (b) in Figure 4-6. Comparing to Figure 4-7, although the lattice fringes within the VN layer retain a square

symmetry, parallel fringes appear in the AlN layer at 4° to the AlN/VN interface. The measured d-spacing in the AlN layer is 2.49 ± 0.03 Å, which matches d_{002} (2.49 Å) of the w-AlN [Schulz et. al., 1977], further confirming that phase transformation has occurred in the thicker AlN material.

Although almost all the AlN has transformed to the wurtzite structure, there does exist a small fraction of cubic material (< 5%). Figure 4-13 shows a high-resolution image taken at the interface of VN and AlN with an AlN layer thickness exceeding the critical thickness. It was taken with the electron beam along the MgO [100]//VN [100]//B1-AlN [100] direction. Although in the region away from the VN/AlN interface, fringes almost parallel to the interface with d spacing of 2.49 ± 0.03 Å are found, residuals of square fringes are observed near the film-substrate interface in this particular region. Moiré fringes are also observed in the same region. The square fringes at the VN/AlN interface indicate that there is some residual cubic AlN left untransformed after the phase transformation. The Moiré fringes suggest the co-existence of multiple structures of B1-AlN and w-AlN. As the (002) planes of w-AlN are at a small angle to the film interface, a mixed Moiré pattern is formed due to overlapping w-AlN and B1-AlN in a [010] orientation and a small relative twist of the w-AlN (002) planes. The measured d-spacings from the power spectrum in this region are 2.03 ± 0.04 Å (A), 2.05 ± 0.04 Å (B), and 2.50 ± 0.04 Å (C), which match the d-spacing of the (002) planes (2.03 Å) of B1-AlN (A, B) and the d-spacing of the (002) planes (2.49 Å) of w-AlN (C) respectively.

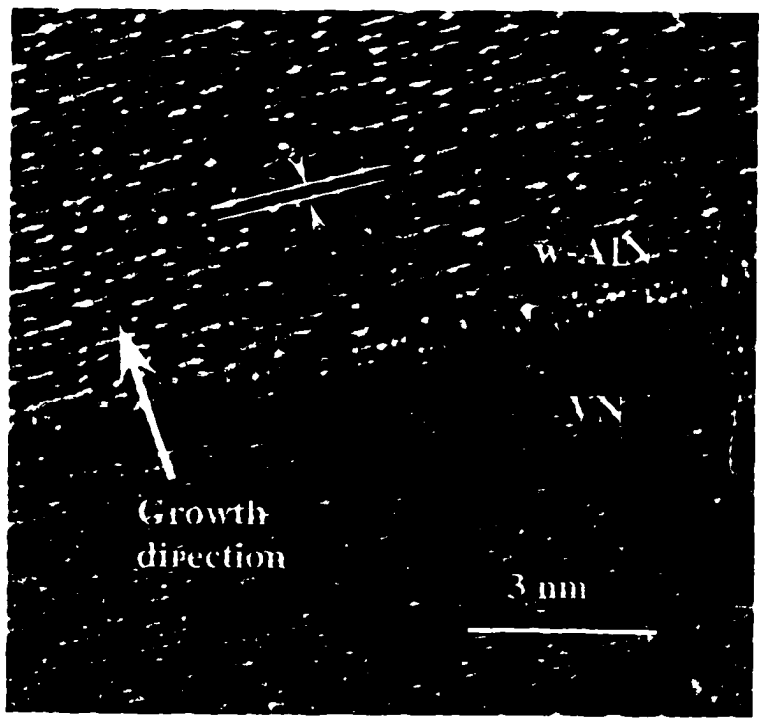

Figure 4-12. HREM image of AlN/VN taken at the interface of w-AlN/VN with electron beam along the MgO [100] direction. Parallel fringes representing the w-AlN (002) planes are seen throughout w-AlN layer. The image was high-pass filtered to improve clarity

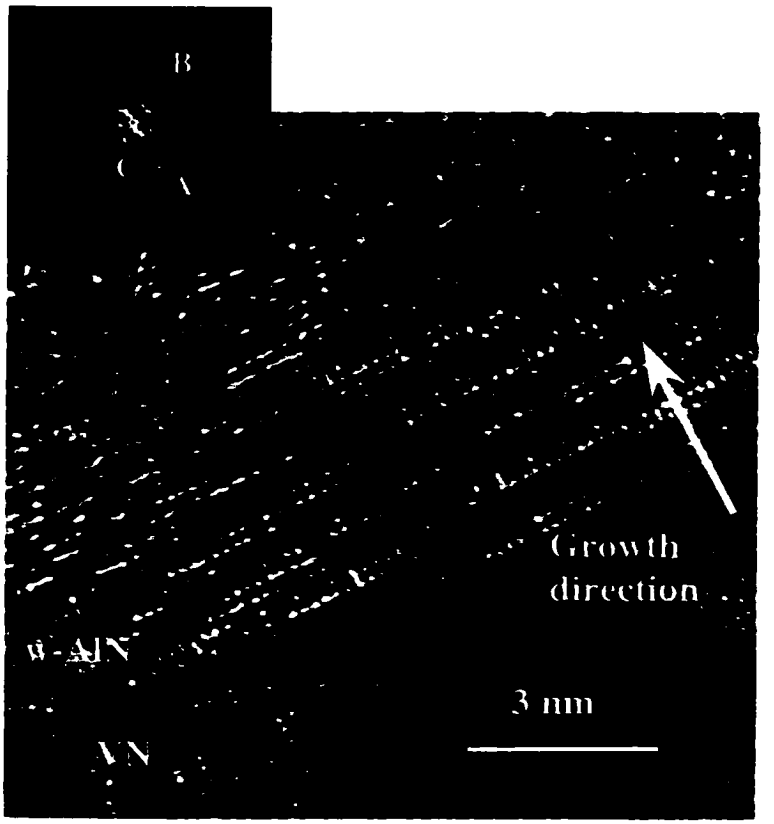

Figure 4-13 HREM image of AlN/VN taken at the interface of w-AlN/VN with electron beam along the MgO [100] direction. Cubic residuals of AlN are observed at the interface and Moiré fringes suggest the co-existence of multiple structures. The power Spectrum inset in the upper left of the image was taken from the region of Moiré fringes

4.5.1.2. Orientation of AlN Following the Phase Transformation

Figure 4-14 shows a selected area diffraction pattern taken from an area which includes the MgO substrate, the B1-AlN/VN (cubic) multilayers, and the w-AlN/VN multilayers. It was taken with the electron beam along the MgO [110] // [B1-AlN/VN] [110] zone axes. In addition to diffraction spots from the pseudomorphic cubic AlN/VN described above, there are two other sets of spots coming from w-AlN [100] and [120] zone axes respectively.

The orientation relationships are:

I. MgO (002) // [B1-AlN/VN] (002) // w-AlN (002);

MgO ($\bar{1}$10) // [B1-AlN/VN] ($\bar{1}$10) // w-AlN (010);

MgO (110) // [B1-AlN/VN] (110) // w-AlN ($\bar{1}$20)

II. MgO (002) // [B1-AlN/VN] (002) // w-AlN (002);

MgO ($\bar{1}$10) // [B1-AlN/VN] ($\bar{1}$10) // w-AlN ($\bar{1}$20);

MgO (110) // [B1-AlN/VN] (110) // w-AlN (010)

There are also diffraction spots from a rotated VN layer above the w-AlN layer (not marked here), which will be discussed later.

Images in Figures 4-15, 4-16and 4-17 were taken from different sample regions with the electron beam along the MgO [110] direction. There are three types of fringes in the w-AlN layer. Those perpendicular to the AlN/VN interface with a d-spacing of 2.70 ± 0.03 Å, which matches a calculated d_{010} (2.69 Å) for w-AlN; those parallel to the interface with a d-spacing of 2.49 ± 0.03 Å, which matches d_{002} (2.49 Å) of w-AlN; and

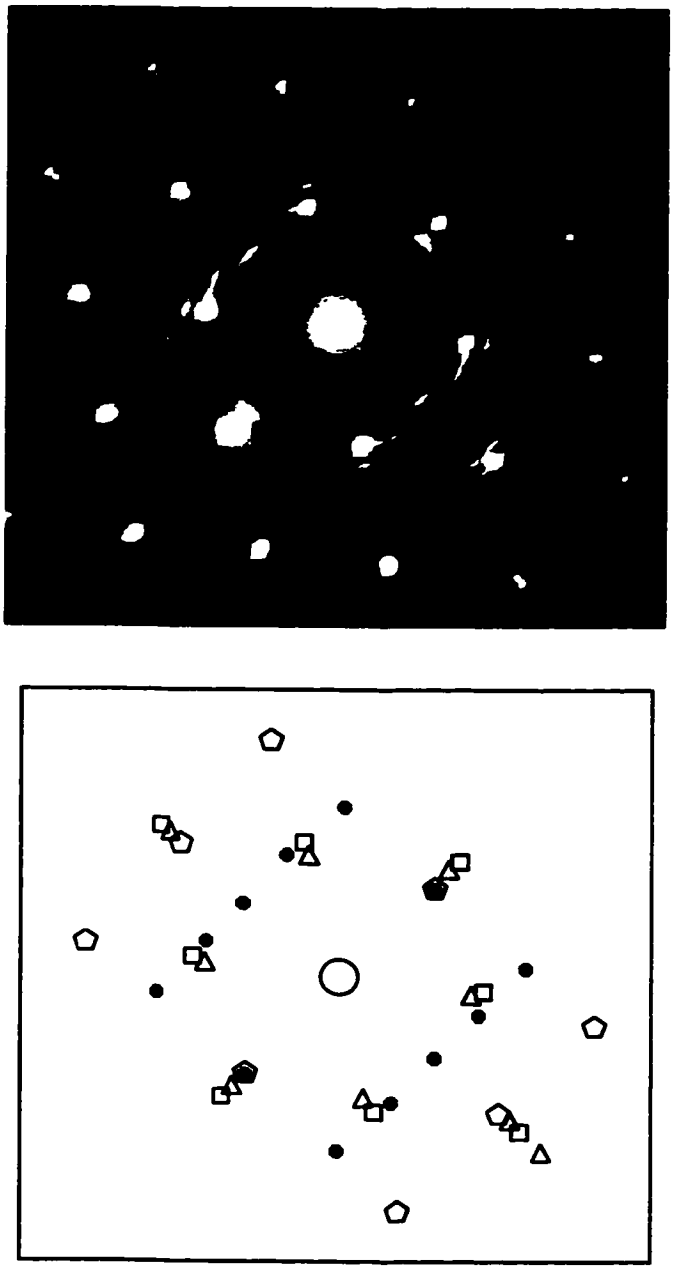

Figure 4-14 TED pattern taken from the superlattice film. Different symbols are used in the schematic to illustrate the TED pattern.

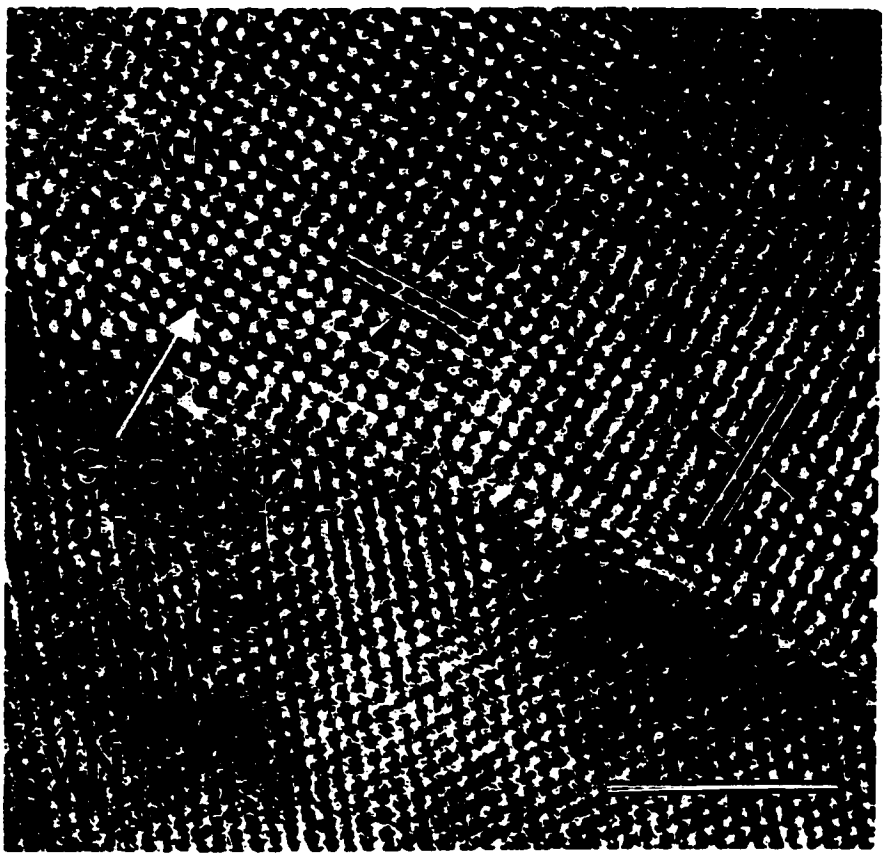

Figure 4-15 HREM image of AlN/VN superlattice taken at the interface of the first transformed layer of w-AlN and VN with electron beam along the MgO [110] direction. There are two types of fringes showed in the w-AlN layer—the ones that are perpendicular to the w-AlN/VN interface and the ones that are parallel to the interface.

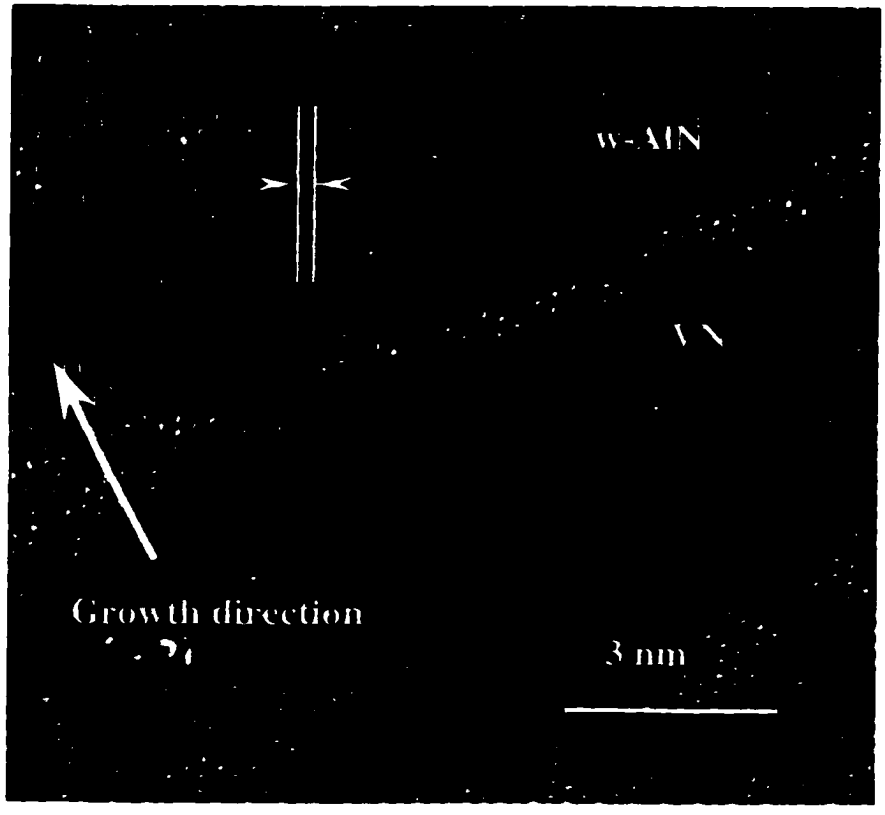

Figure 4-16 HREM image of AlN/VN superlattice taken with the same imaging condition as Figure 4-11. There is another type of fringe showed in the w-AlN layer—the ones that are at 63 degrees to the interface.

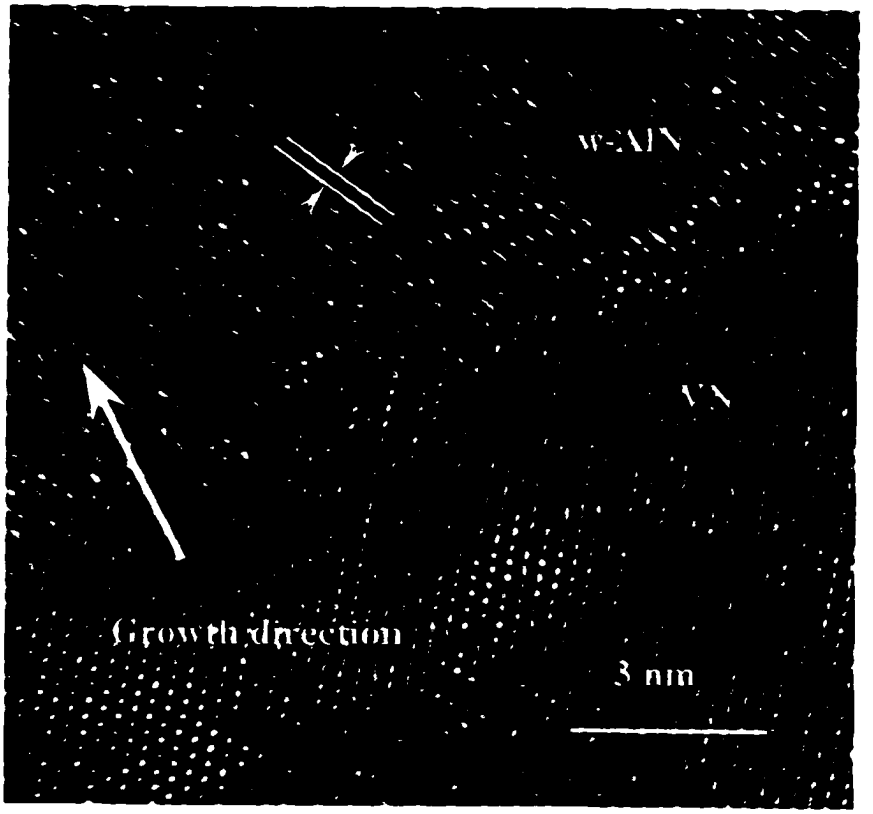

Figure 4-17 HREM image of AlN/VN superlattice taken with the same imaging condition as Figure 4-11. There is another type of fringe showed in the w-AlN layer—the ones that are at 117 degrees to the interface.

those at 63/117 degrees to the interface with a d-spacing of 2.35 ± 0.03 Å, which matches d_{011} (2.37 Å) of w-AlN.

4.5.2. Phase Transformation Model

The experimental evidence demonstrates that metastable B1-AlN is stabilized in AlN/VN superlattices when the AlN layers are sufficiently thin. A phase transformation from B1 to w-AlN takes place when the thickness of AlN exceeds a critical thickness of ≈ 3.0 - 4.0 nm, depending on the VN layer thickness. In our model of thicker AlN layer growth (explained via a simple cartoon in Figure 4-18), AlN grows in the B1 structure initially. The phase transformation starts by forming hexagonal wurtzite nuclei when the B1-AlN grows to its critical thickness value. Once the hexagonal nuclei are formed, they continue the phase transformation until the whole B1-AlN layer becomes hexagonal.

4.5.2.1. Nucleation of hexagonal wurtzite phase

The particular orientations of the w-AlN on the initially-grown B1-AlN can be understood via simple interface symmetry and lattice matching arguments. There are two plausible orientations for the transformed w-AlN, the one we observed or one with a common close-packed N plane (i.e. (111) in the B1 and the basal plane in the w-AlN), as shown in Figure 4-19 (The later would correspond to a dislocation driven phase transformation as discussed later).

Taking the observed lattice parameter of the AlN/VN cubic multilayer (4.1 Å), the observed orientation has a smaller misfit of 6.8% (along the w-AlN [120] // B1-AlN $[\bar{1}10]$ direction) compared to 7.9% (along the w-AlN [120] // B1-AlN $[\bar{1}12]$ direction) in

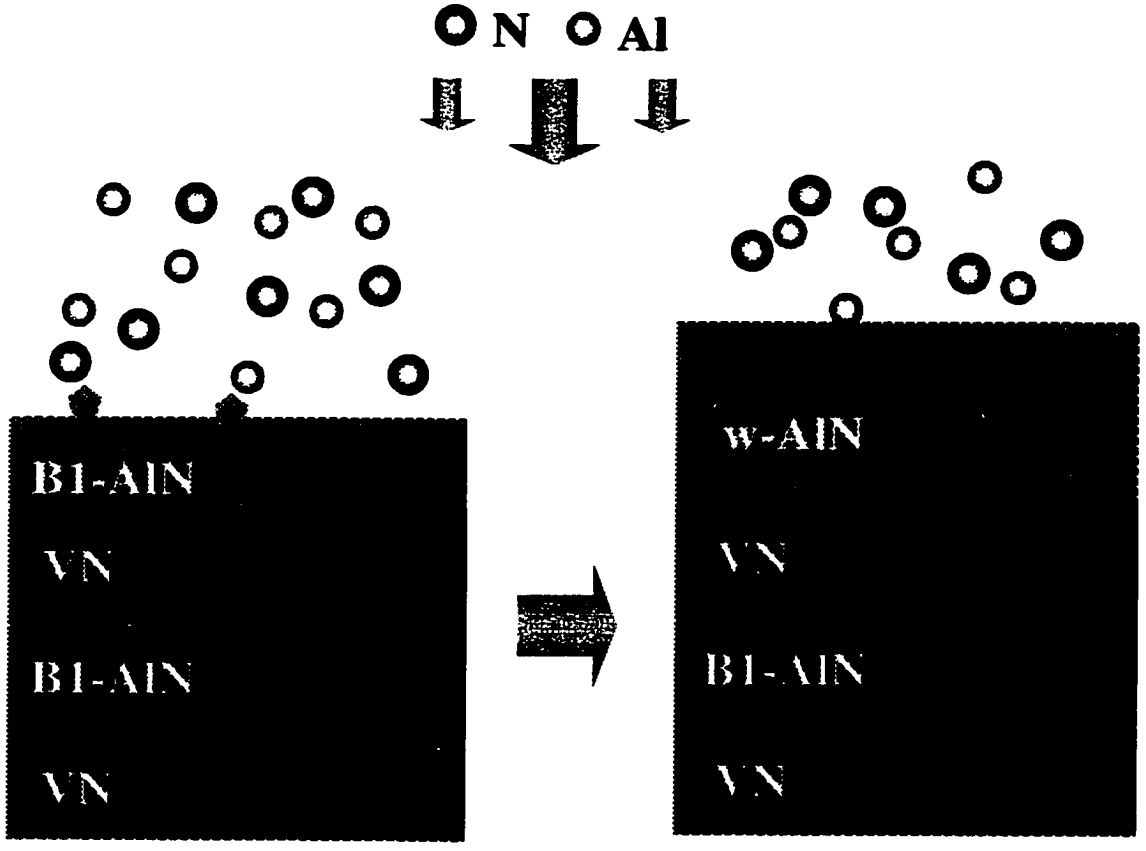

Figure 4-18 The phase transformation process

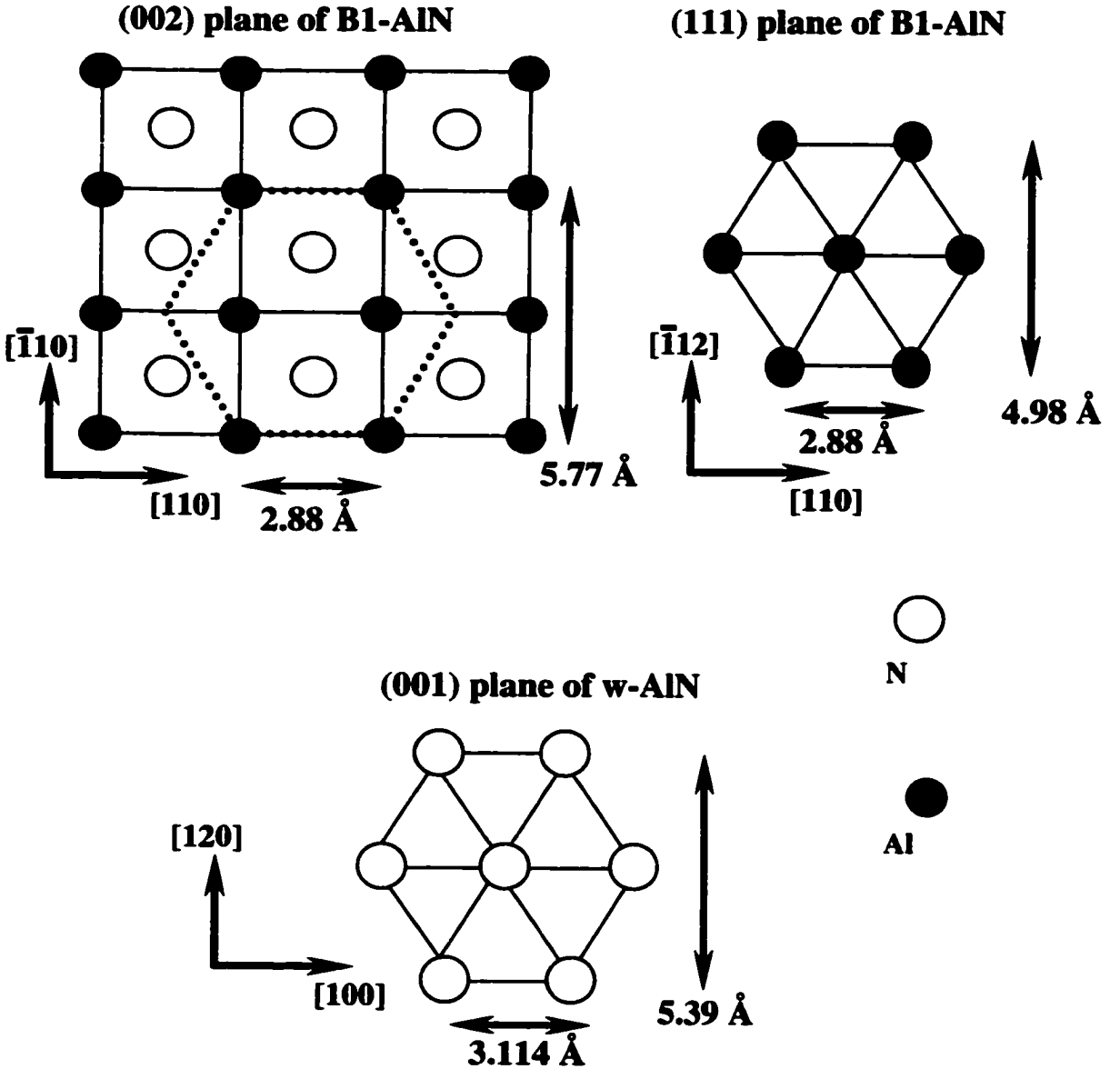

Figure 4-19 Comparison of B1-AlN (002) plane, (111) plane and w-AlN (002) plane.

Table 4-1. Comparison of the in-plane lattice mismatch of B1-AlN/w-AlN interface

		Lattice constant along different directions (Å)	
		x	Y
1	Strained B1-AlN (002)	[110] 2.88	2 [$\bar{1}$10] 5.77
2	Strained B1-AlN (111)	[110] 2.88	[$\bar{1}$12] 4.98
3	w-AlN (001)	[100] 3.11	[120] 5.39

the other orientation. (Table 4-1); N-N distances are smaller in B1-AlN than they are in w-AlN. Another possible explanation for the nucleation orientation is that the (002) B1-AlN plane is the only exposed free surface during the film growth process, thus becomes the only choice for w-AlN to nucleate on. If this is true, it will support the "free surface hexagonal phase nucleation" argument, which will be discussed in later paragraphs.

There are two equivalent orientations for this epitaxy, at ninety degrees to each other (as shown in Figure 4-20). There is a tilt of the w-AlN (002) plane to the w-AlN/VN interface (about 4 degrees) that probably helps to accommodate of the misfit. The two domains in nucleation orientation are due to different symmetry of the (002) B1-AlN planes and the (002) w-AlN planes.

While it is not possible to state in atomistic detail exactly what takes place during the phase transition from B1-AlN to w-AlN, a reasonable model can be generated based upon the observations of the orientations before and after the transition as well as the

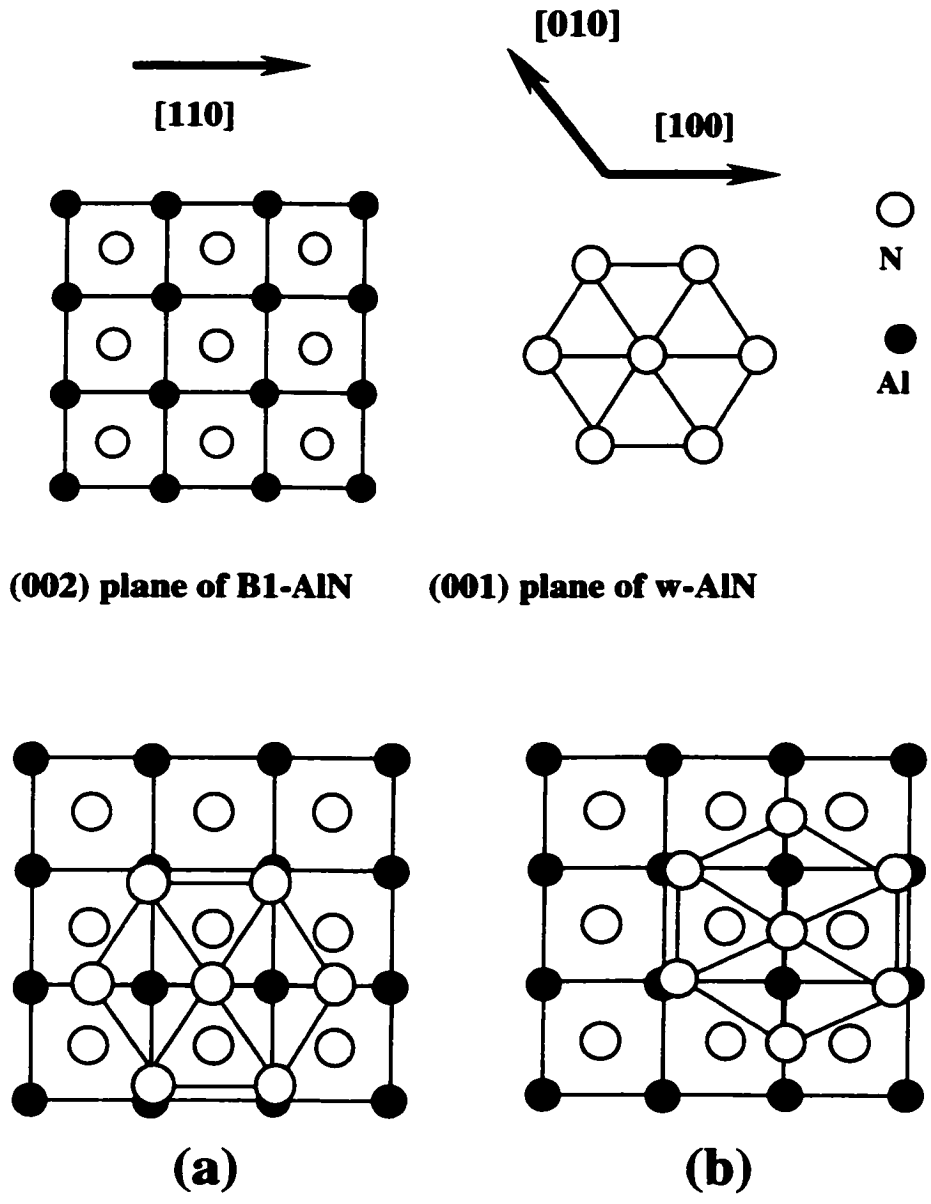

Figure 4-20 Two-dimensional model showing one type of epitaxy in w-AlN nucleation on B1-AlN. w-AlN takes the B1-AlN (002) plane as its (002) plane. Its (010) planes match the $(\bar{1}10)$ planes of B1-AlN (a), or its (010) planes match the (110) planes of B1-AlN (b).

presence of retained untransformed material. Microscopically, the phase transformation observed herein can take place in two ways. One is by heterophase nucleation of w-AlN on the B1-AlN phase during the film growth process, with atoms forming the nuclei coming from the vapor phase. The other is through atomic movements in the B1-AlN itself, a homophase nucleation. Whether the phase transformation starts with a homophase atomic movement or a heterophase nucleation is not clear.

If we have heterophase nucleation, the phase transformation would most likely start at the free surface of B1-AlN. With homophase nucleation the phase transformation could start at the free surface, the B1-AlN/VN interface, or (unlikely) within the AlN layer. The observation of cubic AlN residuals and Moiré fringes at the B1-AlN/VN interface suggests that the phase transformation started at the free surface.

Cubic AlN residuals and Moiré fringes were only found in rare regions near the interface of AlN/VN, and complete transformation to the interface was observed in most parts of the sample. Considering the configurations of the two (Figure 4-21), one can tell that Fig. 4-21a is a more stable configuration as the total energy of the system is only consisted of a bulk energy of w-AlN, a bulk energy of VN and an interfacial energy form w-AlN/VN interface. While in Fig. 4-21b, the total energy of the system is consisted of bulk energies of w-AlN, B1-AlN, VN and interfacial energies from w-AlN/B1-AlN and B1- AlN/VN interfaces. Therefore, thermodynamically, the transformation would proceed until it reaches the most stable final configuration (4-21a).

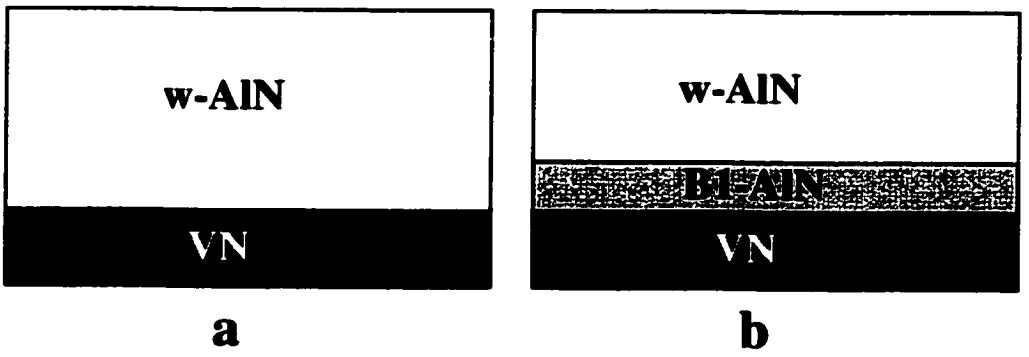

Figure 4-21 Two possible configurations during the B1-AlN/w-AlN phase transformation

However, the shape of the cubic residual might affect the total energy state. Compare the energy difference between figure 4-22 a and b, assuming the residual is half spherical shape and R is the radius of the sphere, E_t is the transformation energy from hexagonal to cubic AlN:

$$\Delta E = 2/3\pi R^3 E_t + \pi R^2\gamma_1 + 2\pi R^2\gamma_2 - \pi R^2\gamma_3$$

$$= \pi R^2 (2/3\ R\ E_t + 2\ \gamma_2 + \gamma_1 - \gamma_3)$$

If γ_3 is comparable with γ_1, ΔE is positive. Thermodynamically, the phase transformation would be complete and there wouldn't be any B1-AlN phase left. If γ_3 is much greater than γ_1, ΔE becomes negative, there might be some cubic residuals left.

4.5.2.2. Phase Transformation Process

Once a hexagonal nucleus is formed, the phase transition will proceed until almost all the AlN has transformed. Unlike the pressure-induced phase transformation, the characteristic of this transition is that part of the system has transformed whereas the rest has not. As time progresses, the volume fraction of the transformed portion increases, and, simultaneously, the volume fraction of the untransformed portion decreases.

Generally speaking, this type of phase transformation is initiated by the appearance of a small volume of the product phase at identifiable locations in the parent phase. Such initiation is known as nucleation. Progress of the transformation occurs by the migration of the interface between the nuclei of the product phase and the untransformed parent phase. This process is known as growth. There are two types of growth. One is common in liquid-solid and many solid-solid transformations. It is a diffusion-controlled

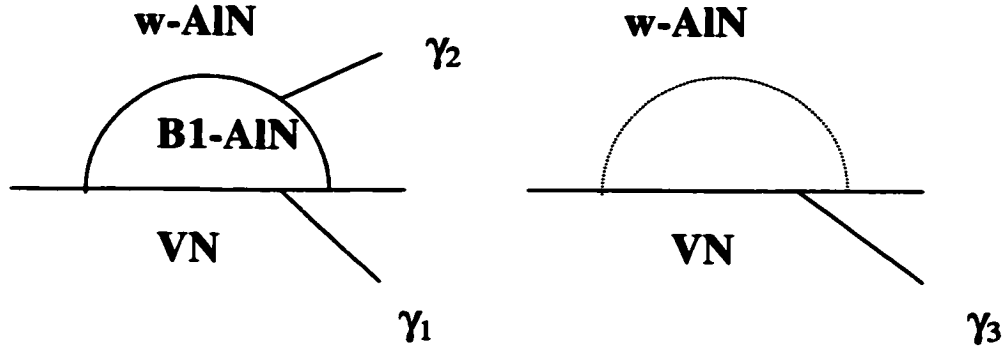

Figure 4-22 Un-transformed cubic AlN residual left at the interface. b. No cubic residual left. γ is the interfacial energy per unit area of different interfaces.

process, and the growth rate is strongly temperature-dependent. The other one is known as martensitic transformation. The growth rate is independent of temperature.

When an atom acquires higher vibrational energy by interacting with other atoms, it breaks away from its lattice site and moves through non-equilibrium high-energy positions to another site. Such atomic movements generate atomic fluxes and are known as diffusion. There are several mechanisms for the diffusion-controlled process, and the atomic process in phase transformation is realized by these mechanisms. They are known as vacancy mechanism, interstitial mechanism, interstitialcy mechanism and structural defect mechanism. All are temperature-dependent.

A number of nucleation and growth transformations exhibit growth rates that are temperature independent. During such a transformation, a single-phase reactant transforms into a single-phase product with a change of shape and without any change in composition. These transformations are known as martensitic transformations. The driving force of the transformation usually comes from homogeneous deformation.

The atomic process of martensitic transformation at the interface is different from that in the diffusional process. One example is the fcc-hcp martensitic transformation in cobalt [Jena et al. 1992]. The parent planes are the {111} planes of fcc-Co, which consists of three kinds of close packed layers of atoms in stacking sequence. The stacking sequence is described as abcabc.. The hcp structure consists of stacking of close packed layers in the sequence ababab.. In this structure the close packed planes constitute the (0001) planes of hcp. The martensitic transformation involves changes of the abcabc ...type of stacking of fcc to the abab...type of stacking of hcp at the

transformation interface. The phase transformation takes place by the passage of a partial dislocation a/6<112> on the {111} FCC planes, with the (111) planes of the cubic structure the basal planes of the HCP structure.

This type of transformation is observed in the structural transformation induced by nitrogen implantation in thin metal films, such as Al-AlN, Gd-GdN etc [Ma et.al., 1986]. A similar phase transformation is also reported to be found in ZnS [Areshkin et. al., 1996]

However, in the B1-AlN/w-AlN phase transformation, the w-AlN hexagonal basal plane does not coincide with that of the cubic (111) plane, but with the B1-AlN (002) plane. Therefore the phase transformation does not take place through a comparable dislocation motion. It seems more reasonable that the phase transformation takes place through atomic movements in B1-AlN itself, i.e. a "shuffle dominant, displacive, diffusionless transformation occurring by nucleation and growth", a so-called martensitic transformation [Cohen et al., 1979; Christian et al., 1995].

4.6 VN Growth after AlN Phase Transformation

The VN layer deposited after the AlN phase transformation is observed to be re-oriented. Figure 4-23 is taken at VN/w-AlN interface with the electron beam along the MgO [110]//B1-AlN [110]//w-AlN [100] zone axes. It is observed that the VN nucleates by taking the w-AlN (002) plane as its (111) plane instead of the (002) plane. As the lattice mismatch is still relatively large, some tilting of these (111) planes should be expected. Microscopically, one can notice in Figure 4-23 that the (111) planes of VN are not perfectly parallel to the w-AlN (002) planes. This is consistent with the rotated

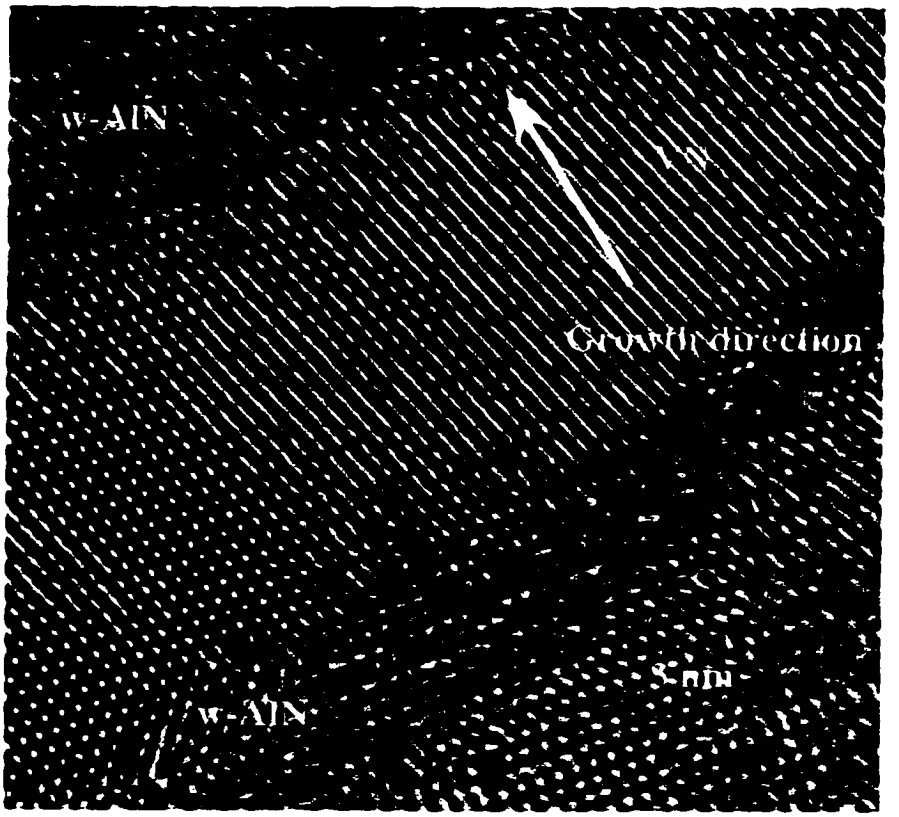

Figure 4-23 HREM images of w-AlN/VN/w-AlN taken with electron beam along the MgO [110] direction. The (002) plane of VN was re-orientated to where its (111) plane was in VN/B1-AlN multilayer.

diffraction spots observed in the TED patterns in Figure 4-14, where the (002) spots of VN move to the position of (111) spots in B1-AlN/VN superlattice diffraction pattern.

In fact, when the AlN phase transition occurs, further growth of VN onto the w-AlN is still epitaxial, but with a different orientation relative to the substrate VN. Because the w-AlN has two possible orientations with a slight tilt, in an x-ray diffraction measurement it might appear that the VN is completely misoriented and all epitaxial information lost, but this is not the case.

The subsequent growth of VN on the transformed w-AlN can be understood via the same interface symmetry and lattice matching arguments as in 4.5.2.1. (Figure 4-24) The observed VN orientation (common close-packed cation planes) has a smaller misfit of 6.1% (along the VN $[\bar{1}12]$ // w-AlN [120] direction) compared to that of 8.2% (along the VN $[\bar{1}10]$ // w-AlN [120] direction); as tabulated in Table 4-2, this orientation will also be favored by a hexagonal-hexagonal symmetry match. Unfortunately the experimental interfaces after the transformation are too rough for precise HREM to determine the atomistic interface structure or make statements about the possible presence of interface dislocations.

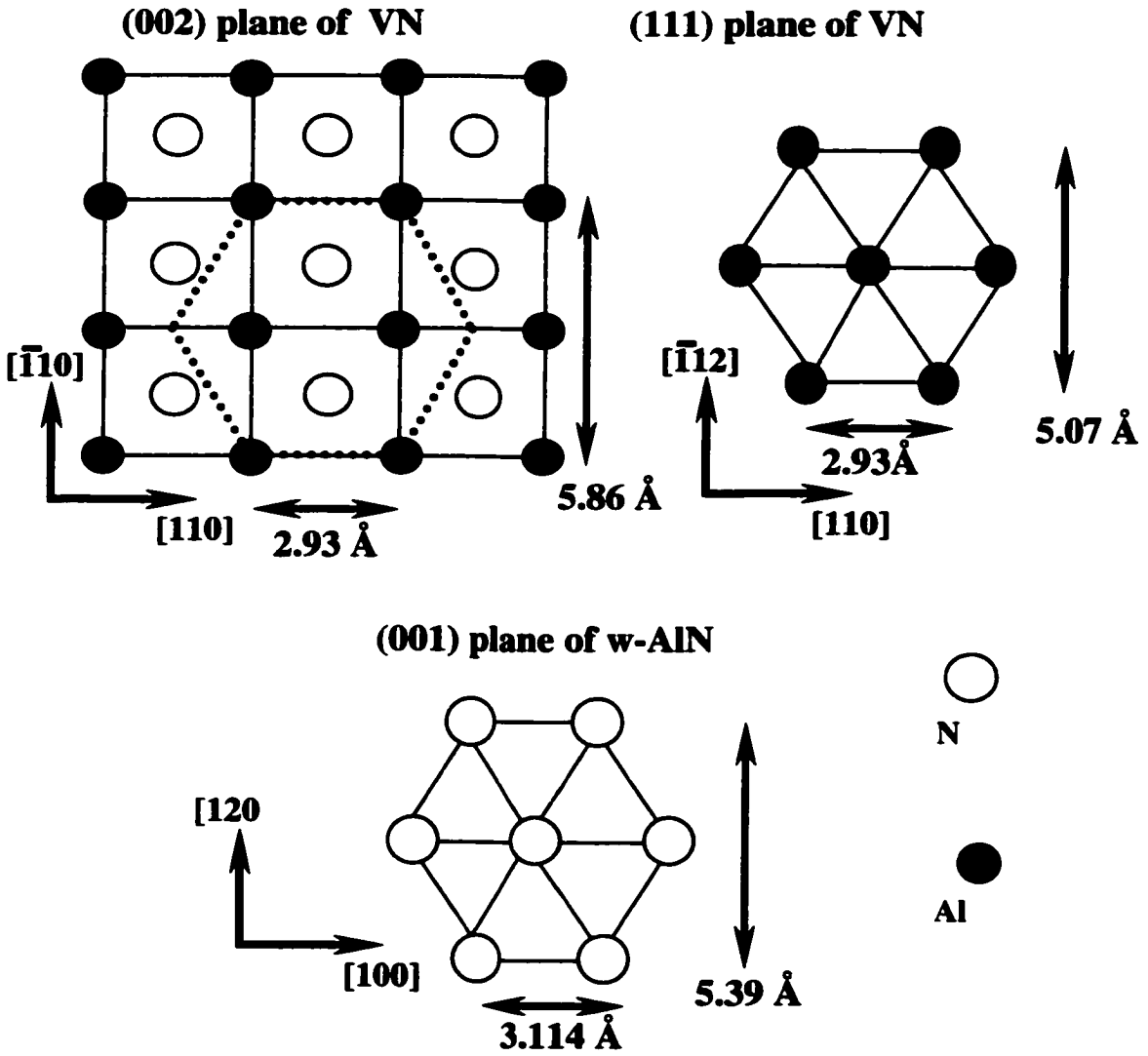

Figure 4-24 Comparison of VN (002) plane, (111) plane and w-AlN basal plane. There is a better match between VN (111) plane and w-AlN basal plane.

Table 4-2. Comparison of the in-plane lattice mismatch of w-AlN/VN interfaces.

		Lattice constant along different directions (Å)	
		x	Y
1	w-AlN (001)	[100] 3.11	[120] 5.39
2	VN (002)	[110] 2.93	2 [$\bar{1}$10] 5.86
3	VN (111)	[110] 2.93	[$\bar{1}$12] 5.07

4.7 Conclusion

The focus of this chapter is the epitaxial stabilization effect and the phase transformation mechanism of sputter deposited nitride superlattice. DC magnetron reactive sputtering was used to deposit AlN/VN superlattices. The superlattices were characterized by TEM and XRD. The high-angle XRD simulations gave quantitative estimates of period, layer thickness ratio, interface width and interface roughness.

B1-AlN can be epitaxially stabilized in AlN/VN superlattices using reactive magnetron sputtering without any substrate biasing. The non-ambient metastable B1 phase was able to form as it forms low energy coherent interface with the B1-VN, while the stable wurzite phase does not. The ion-bombardment was deliberately not introduced during the deposition in order to avoid ion-bombardment induced defects generation and ensure smooth layer growth. A larger critical thickness for B1-AlN was obtained in the

AlN/VN superlattices compared to that in AlN/TiN superlattices. The critical thickness depends on the underlayer VN thickness.

B1-AlN transformed to w-AlN at larger AlN layer thicknesses. There were two domains of the transformed w-AlN, i.e.

I. [B1-AlN/VN] (002) // w-AlN (002);

[B1-AlN/VN] ($\bar{1}$10) // w-AlN (010);

[B1-AlN/VN] (110) // w-AlN ($\bar{1}$20).

II.[B1-AlN/VN] (002) // w-AlN (002);

[B1-AlN/VN] ($\bar{1}$10) // w-AlN ($\bar{1}$20);

[B1-AlN/VN] (110) // w-AlN (010).

The VN layer deposited after the B1/w-AlN phase transformation was re-oriented compared to the VN in the B1-AlN/VN superlattice. The orientations of the w-AlN on the (strained) B1-AlN and the subsequent growth of (relaxed) VN on the transformed w-AlN were explained by the crystal symmetry and minimization of lattice misfit. The very small fraction of retained B1-AlN at the interface of VN and w-AlN suggested that the phase transformation started at the free surface of B1-AlN during deposition.

CHAPTER 5. SYNTHESIS OF CRYSTALLINE ALUMINA AT REDUCED SUBSTRATE TEMPERATURES

5.1 Efforts in Achieving Crystalline Alumina at Reduced Substrate Temperatures

Aluminum oxide thin films have many properties that are useful for applications in optical, electronics and cutting tool industries. Methods of synthesizing aluminum oxide thin films include chemical vapor deposition combined with ion-beam irradiation [Nakai et al., 1997], molecular beam epitaxy using a solid aluminum source and N_2O [Wado et al., 1995], laser-induced deposition from condensed layers of organoaluminum compounds and water [Moore et al., 1994] and magnetron sputter-deposition [Deshpandey et al., 1982].

Aluminum oxide has many crystalline phases, including alpha, gamma, theta, kappa, etc. In conventional deposition methods, one needs to use substrate temperatures higher than 700 C to obtain crystalline alumina [Hirschauer et al., 1997]. The high substrate temperature requirement limits the type of substrates that can be coated with alumina. Therefore, low-temperature synthesis of crystalline alumina is of great technological interest. One method to reduce the crystalline growth temperature is to enhance the mobility of surface species via low-energy ion bombardment. To explore this strategy, Schneider et al. [1997] incorporated an rf coil to enhance ionization in a standard magnetron sputter-deposition system. Together with pulsed dc substrate bias to enhance ion bombardment of the growing film, they demonstrated the growth of crystalline κ-alumina at relatively low substrate temperatures (400 C).

Chapter 4 showed that the high-pressure B1 phase of AlN can be achieved using

the epitaxial stabilization effect. Ion-bombardment is deliberately eliminated to avoid defects introduction. In this chapter, the metastable phases of alumina are obtained using a totally different approach, i.e., increasing the momentum of the surface species during deposition via low energy ion-bombardment, thus enabling the nucleation of the metastable phases at reduced temperatures. Effects of substrate temperature, bias, as well as the additional magnetic field above the substrate will be discussed. Structure and properties of alumina films synthesized under different conditions will be presented as well.

5.2 Deposition of Alumina Films

Aluminum oxide films were grown using pulsed dc magnetron sputtering in a single-cathode deposition chamber (Figure 5-1). The base pressure of the chamber was below 1 x 10^{-7} Torr. A two-inch aluminum target (99.99% purity) was used in an unbalanced magnetron. The target voltage was pulsed at 20 kHz (50% duty cycle), with the positive voltage set at 10% of the negative voltage (e.g., at a set target bias of -400 V, the actual target voltage is a rectangular wave cycling between –400 and +40 V). The sputtering gas was an argon-8% oxygen mixture at a total pressure of 7 mTorr. Si(100) wafers were used as substrates. They were first cleaned by acetone and 2-propanol, then transferred into the chamber and reverse-sputter-etched in an argon plasma at 60 mTorr. In selected runs, glass substrates were used to confirm visually the stoichiometry of alumina films (stoichiometric alumina films should be transparent). A 2 kHz pulsed dc bias (similar pulse shape as that applied to the target) was applied to the substrate during deposition for low-energy ion bombardment and eliminating charging. This bias was

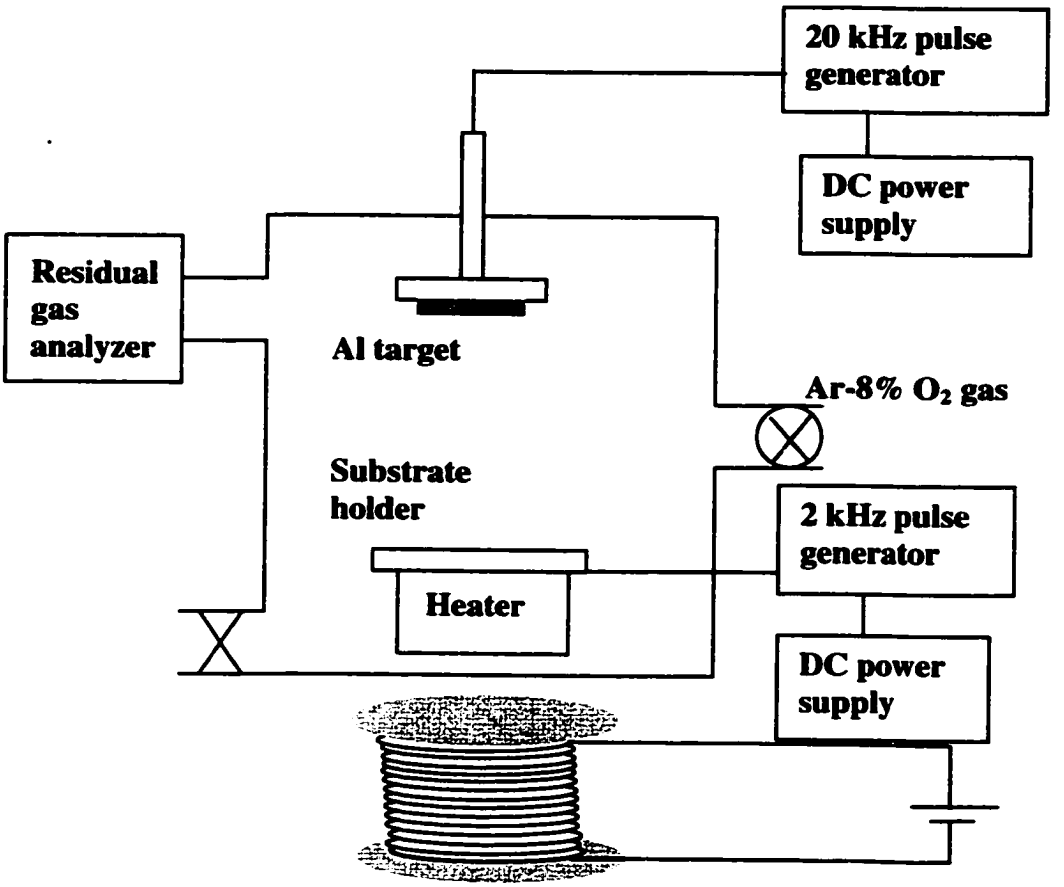

Figure 5-1 Schematic of the deposition system

varied from –200 to –400V. Substrate temperatures were maintained at or below 300 C, as measured by a thermocouple attached to the substrate holder. A magnetic field was applied (via an external solenoid) during deposition to further increase the substrate ion-current density. The field at the substrate surface was 42 G. Instead of using an rf coil to increase the ion concentration in the plasma, a magnetron sputter-source equipped with strong magnets was used instead. Together with proper substrate biasing, the additional magnetic field with the correct polarity near the substrate result in markedly improved ion currents to the substrate during film growth, as demonstrated by Petrov et al [1992] and Engstrom et al [2000]

.Auger electron spectroscopy was used to examine the chemical composition of the films. Film structure was characterized by standard x-ray diffraction using the Cu Kα line (0.154 nm) and transmission electron microscopy (TEM). The surface topography was obtained by atomic force microscopy (AFM). The film hardness was measured using a Hysitron nanoindentor, analyzed by the Pharr-Oliver method [Pharr et al., 1992]. In the latter case, the penetration was kept at less than 15% of the film thickness to minimize substrate effects. Film stress was measured using the wafer curvature method. Through-thickness dc electrical resistivity was also determined.

At a nominal target power of 100 W, deposition under conditions described above resulted in clear alumina films at 5 nm/min on substrates 13 cm from the target. Auger electron spectroscopy showed that the aluminum in the films gives an Auger peak at 51 eV, confirming that it is in an oxidized state (Fig. 5-2).

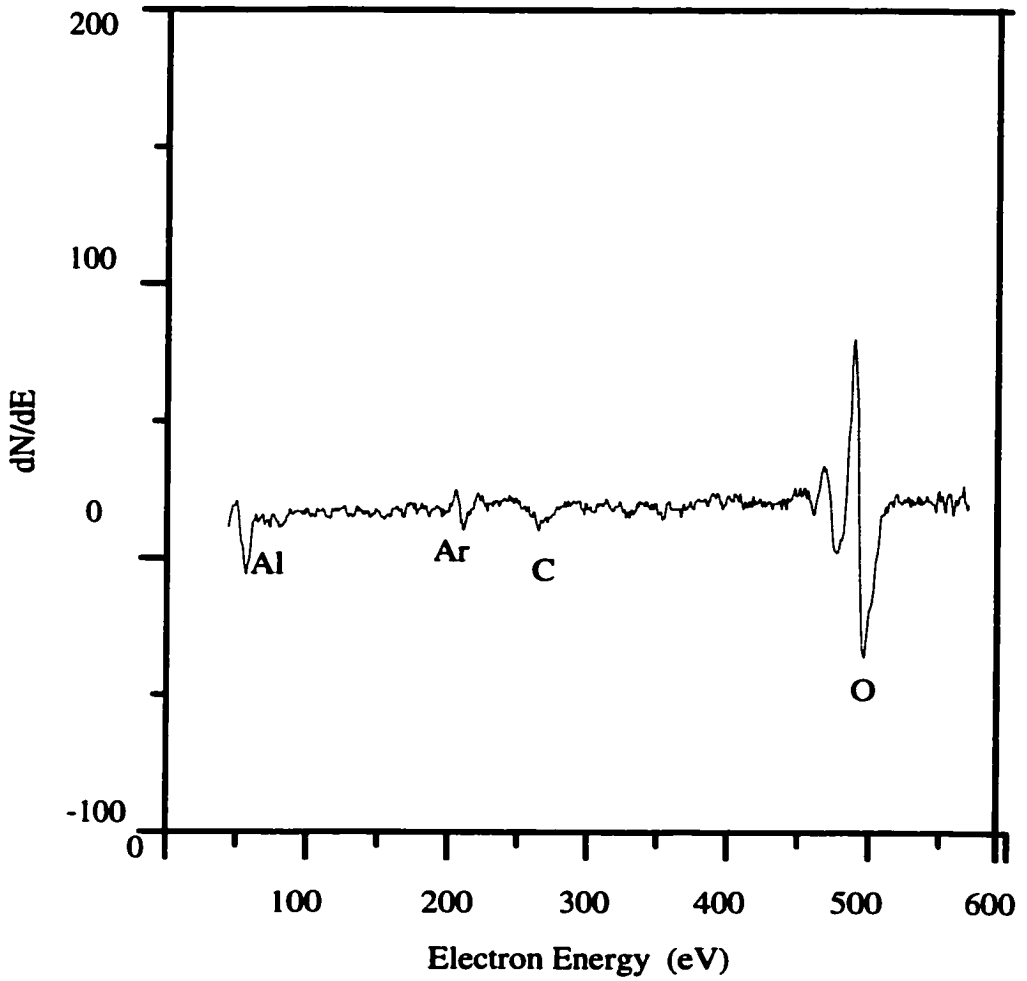

Figure 5-2 Auger electron spectrum of a typical alumina film deposited on Si. The Al Auger peak is 51 eV, characteristic of oxidized Al.

5.3 Substrate Temperature Effect

In order to investigate the effect of substrate temperature on the growth of alumina, three films were deposited at the same nominal power (100 W), pulsed substrate bias (-300 V) and with the external solenoid on, but with different substrate temperatures, *viz.*, 200, 250 and 300 C. X-ray diffraction in Figure 5-3 shows that crystalline alumina films can be grown at 250 and 300 C and appear to consist of mixed phases. For example, the peak at ~25° suggests the presence of α alumina, while the peak at ~30° can be due to either θ or κ phase. It is well known that the x-ray peak intensity and position will be largely affected by factors such as film internal stress, preferential crystalline texture etc. Detailed phase identification and film composition analysis would require more experiments and corresponding simulations. The goal of the current study is only to achieve crystalline alumina, thus we leave the part of specific phase identification to future work suggestions. The reference powder patterns for four typical alumina phases are included in this and other x-ray diffraction patterns. The alumina film grown at 200 C is amorphous (the Si(200) forbidden reflection appears because of growth-induced stress).

For the film grown at 300 C, high-resolution TEM images were taken at the Si substrate/film interface (Fig. 5-4), as well as regions away from the interface (Fig. 5-5) with the electron beam along the substrate [110] direction. Fringes in the aluminum oxide region are indicative of its crystalline nature. This is also confirmed by the ring diffraction pattern taken from the same region of the film.

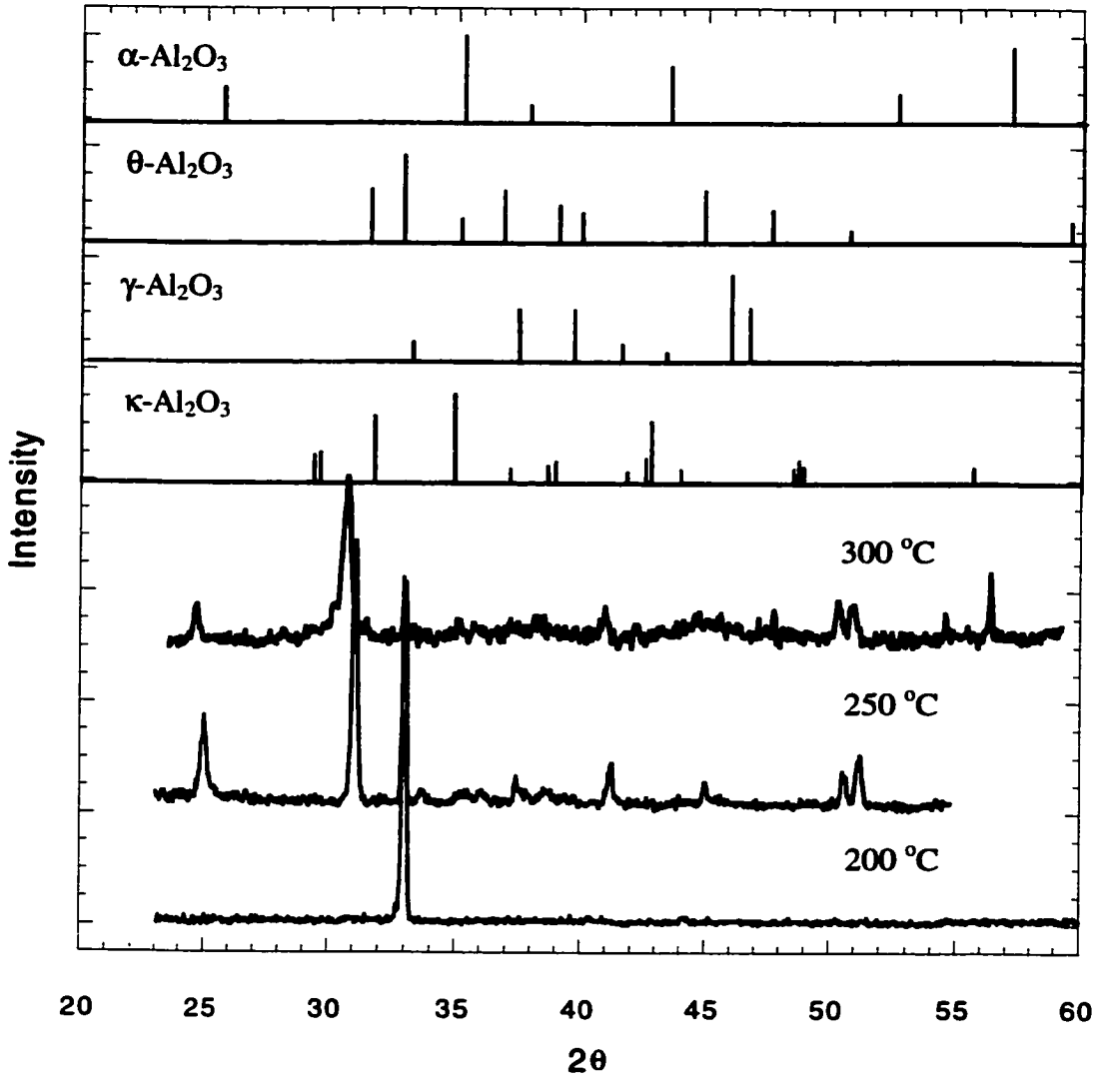

Figure 5-3 High-angle x-ray diffraction patterns of aluminum oxide films deposited at 200 C, 250 C and 300 C (nominal target power = 100 W, pulsed substrate bias = -300 V, magnetic field on). The Si (200) forbidden reflection at $2\theta = 33^{\circ}$ appears because of stress.

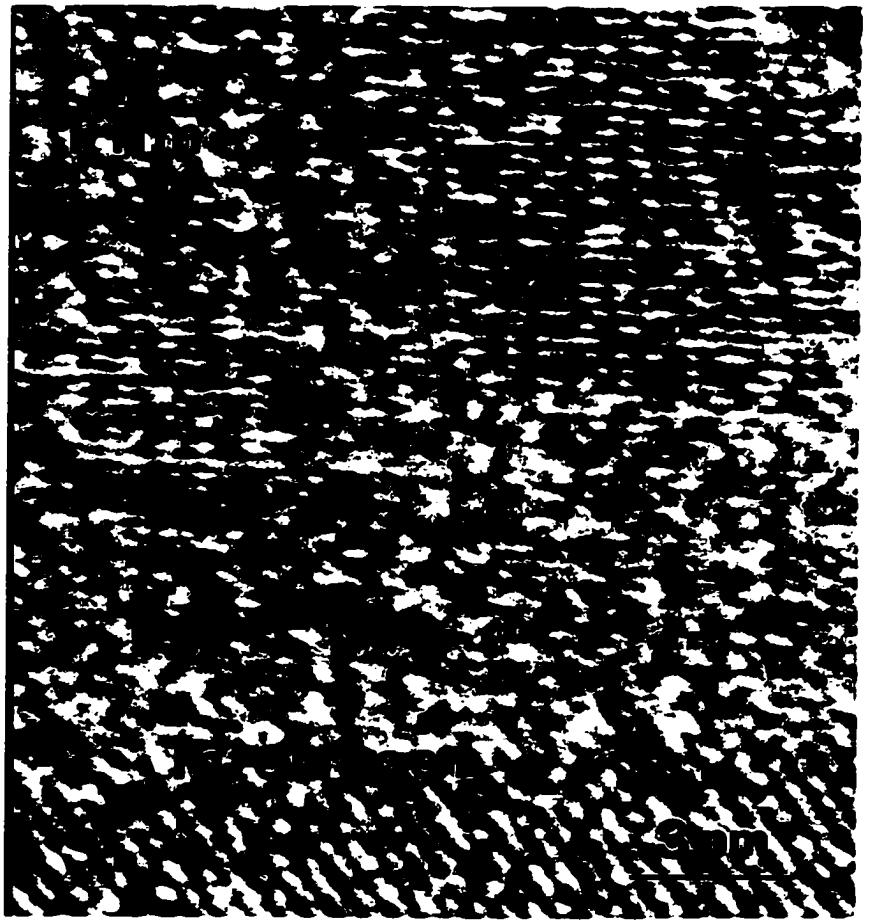

Figure 5-4 High-resolution TEM image taken at the interface of Si and aluminum oxide with the electron beam along the Si [110] direction for the film shown in Figure 5-3 (substrate temperature = 300 C). Fringes in the aluminum oxide region are evident, indicative of crystalline growth.

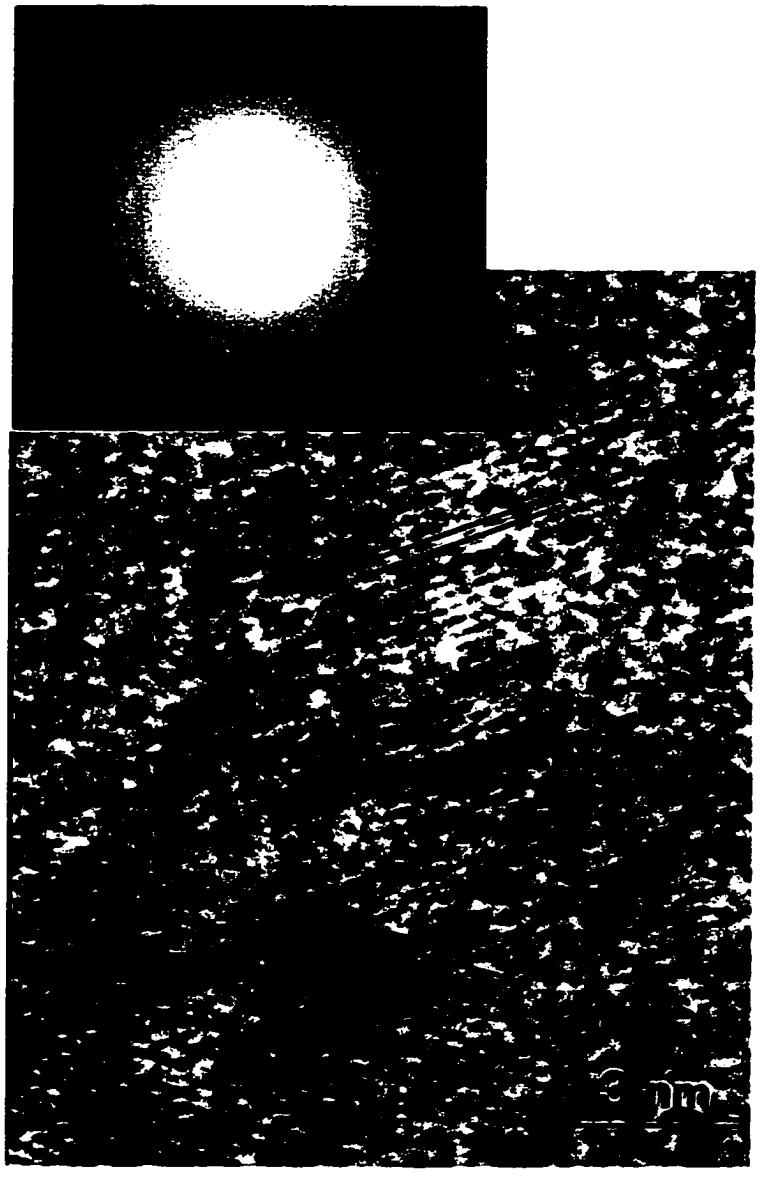

Figure 5-5 High-resolution TEM image taken at the film region away from the film/substrate interface for the film shown in Figure 5-3 (substrate temperature = 300 C). Randomly oriented aluminum oxide grains can be seen. The ring diffraction pattern in the inset shows a presence of polycrystalline aluminum oxide.

Figure 5-6 was taken from a different region of the film with the same imaging condition as the above two. Some amorphous regions exist. The size of the alumina crystallites ranges from 5 to 30 nm.

5.4 Substrate bias effect

In this series of experiments, the nominal target power and substrate temperature were kept constant (100 W and 300 C respectively), with the external solenoid on. The substrate bias was set at –200, –300 and –400 V. Crystalline alumina films were obtained at –300 and –400 V substrate bias, while films grown at –200 V were amorphous (Figure 5-7).

Alumina films grown at –300 V substrate bias appear to have better quality than those at –400 V. The diffraction peaks are stronger, and the films are harder (20.7 GPa vs. 17.6 GPa). Atomic force microscopy indicates (Figure 5-8) that films grown at –300V are smoother (rms surface roughness = 0.36 nm) than those grown at –400V (rms surface roughness = 1.78 nm).

Substrate bias has two opposing effects on crystal growth. On the one hand, substrate bias increases ion bombardment of the growing film, enhancing mobility of surface species. This makes it possible to grow crystalline alumina films at reduced temperatures. On the other hand, excessive ion bombardment can create defects at higher rates than can be repaired by enhanced mobility of surface species, resulting in worse crystallinity and the increased surface roughness. Further, excessive compressive stress can result. Therefore, some optimum bias must be found.

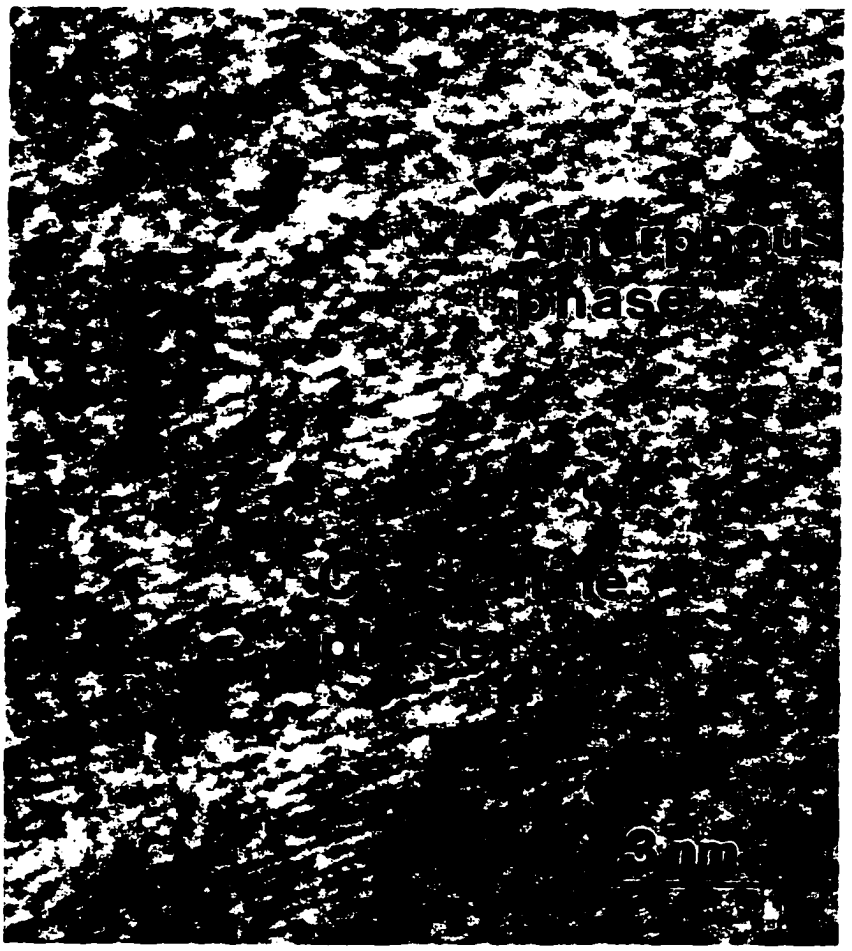

Figure 5-6 High-resolution TEM image taken at the film region away from the film/substrate interface for the film shown in Figure 5-3 (substrate temperature = 300 C). Both crystalline and amorphous phases are observed.

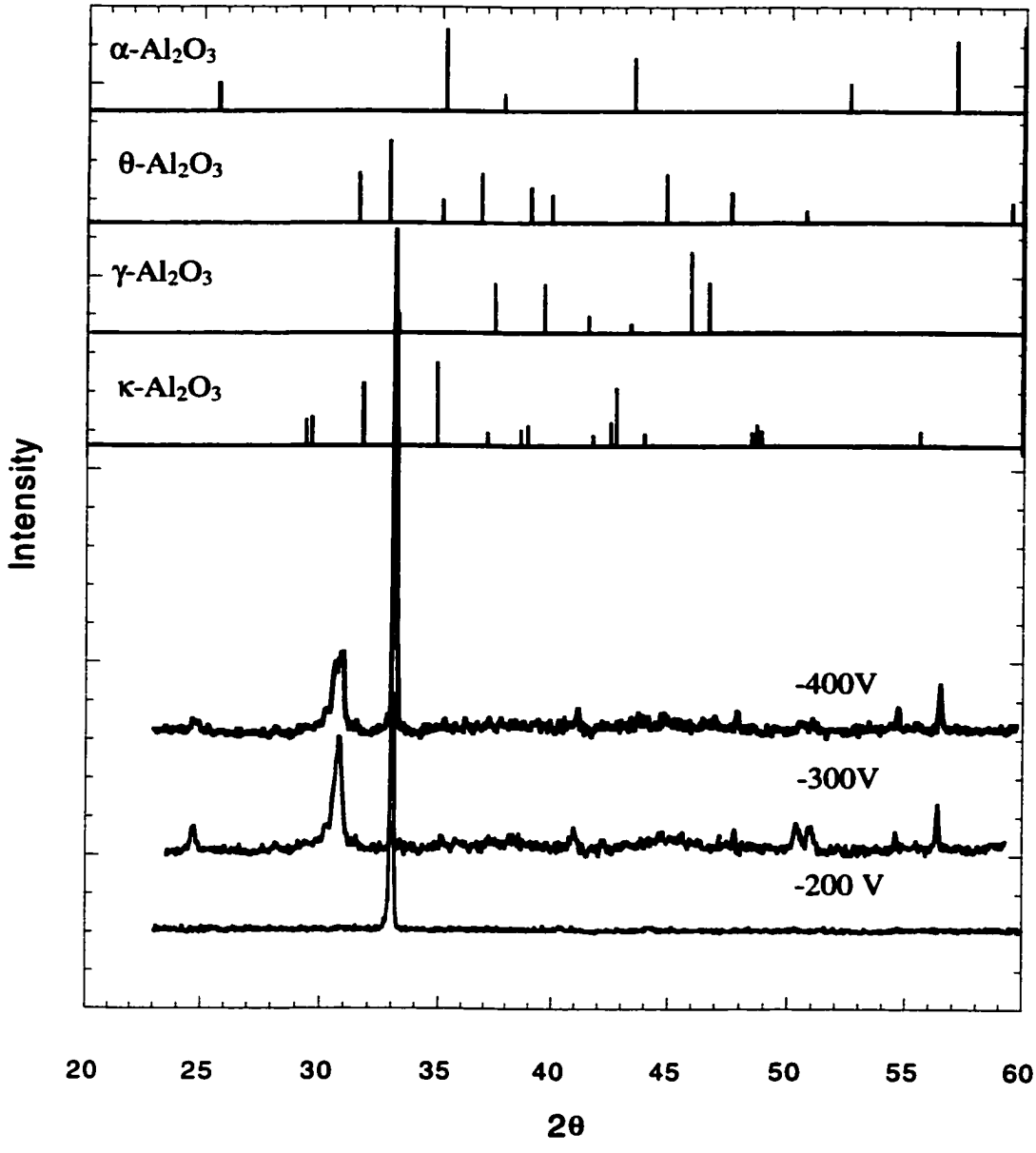

Figure 5-7 High-angle XRD patterns of aluminum oxide films deposited at -200 V, -300 V and -400 V substrate bias (nominal target power = 100 W, substrate temperature = 300 C, magnetic field on). Crystalline phases are obtained at -300 V and -400 V.

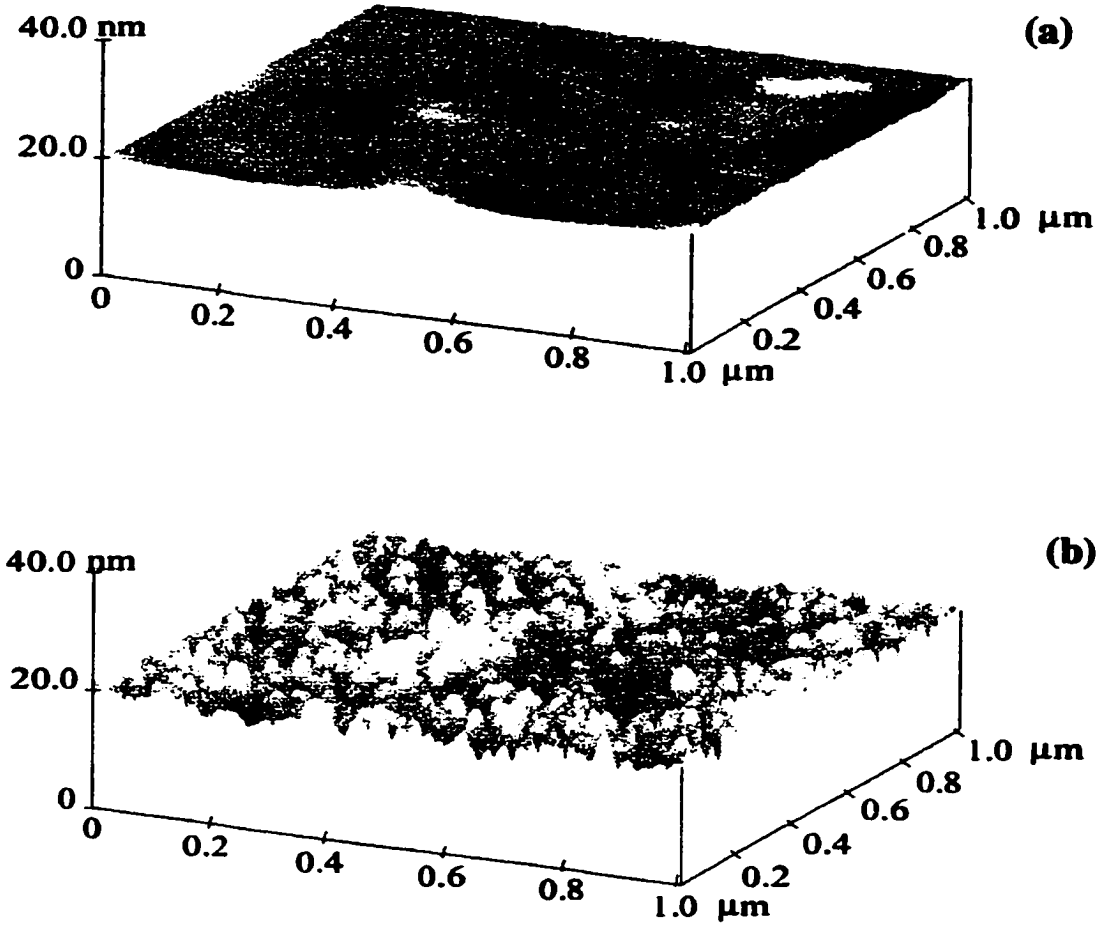

Figure 5-8 AFM images of aluminum films deposited at different substrate bias voltages (nominal target power = 100 W, substrate temperature = 300 C, magnetic field on).

(a) Substrate bias = -300 V, RMS surface roughness = 0.36 nm

(b) Substrate bias = -400 V, RMS surface roughness = 1.78 nm

The nanocrystalline nature of the films as described in section 5.3 is related to the substrate bias effect as well. This goes back to the old argument of nucleation and growth in thin films. The nucleation of many metastable phases (or stable phases with high energy barrier upon nucleation) may require intensive ion bombardment. However, once nucleated, their growth process needs less or no ion bombardment to maintain. Continuing the intensive ion-bombardment in the growth process will introduce secondary nucleation constantly and prevent the nuclei from growing to larger size. In fact, this argument applies to both cubic boron nitride and diamond growth, as will be demonstrated in the following two chapters. The two-step deposition process, i.e., separation of the nucleation and growth, has already been developed in both cBN and diamond growth. On the other hand, the equilibrium between the secondary nucleation and growth provides us a new area to explore---synthesis of nano-composite materials.

5.5 Magnetic Trap Effect

The next series of films were grown at a nominal target power of 100 W, substrate bias of –300 V and substrate temperature 300 C, one set with the solenoid off and one set with the solenoid on. The magnetic field applied via the external solenoid during deposition increases the substrate ion-current density. Separate measurements under the same process conditions showed that the ion-to-neutral arrival ratio at the substrate is 2.7 with the solenoid off and 5.2 on. The ion-to-neutral arrival ratio was calculated as follows. The deposition rate was 300 nm/hr, or 1000 monolayers/hr (assuming 0.3 nm = one monolayer). Assuming a surface atom density of 1×10^{15} atoms/cm^2, this is equivalent to an atom arrival rate of 2.78×10^{14} atoms/cm^2-sec. The substrate ion current

density was measured to be 0.12 mA/cm^2 with the solenoid off, and 0.23 mA/cm^2 with the solenoid on. Assuming singly charged ions, the ion arrival rates were calculated as 7.5×10^{14} and 1.44×10^{15} ions/cm^{2}sec respectively. The corresponding ion-to-neutral arrival rates were then 2.7 and 5.2. This approximate doubling of the ion-to-neutral arrival ratio had a dramatic effect on film crystallinity. Figure 5-9 demonstrates that without the magnetic field provided by the solenoid, there is no crystalline growth.

Together with the substrate bias, formation of a magnetic trap above the substrate surface increases ion bombardment of the growing film. As discussed earlier, this can enhance crystalline growth under optimum bias conditions. At the same time, such ion bombardment results in significantly increased film stress. For example, films grown with the solenoid on have internal compressive stress ~ 5 GPa, whereas films grown with the solenoid off have internal stress ~ 1 GPa. While thin crystalline alumina films appear to be stable (from electrical resistivity measurements), thick (> 100nm) crystalline films grown under these conditions experienced marked decrease of x-ray diffraction intensity 5-7 days after film deposition. This occurs even for films stored in a dessicator, suggesting that moisture is not a significant factor here.

5.6 Properties of Alumina thin films—Amorphous vs. Crystalline

5.6.1. Nano-indentation Hardness

The difference in the hardness of films deposited using different deposition parameters can be explained by the ion bombardment effect as well. Increasing ion bombardment of the growing film by increasing substrate bias or additional magnetic field leads to enhanced mobility of surface species. This results in reduction of the

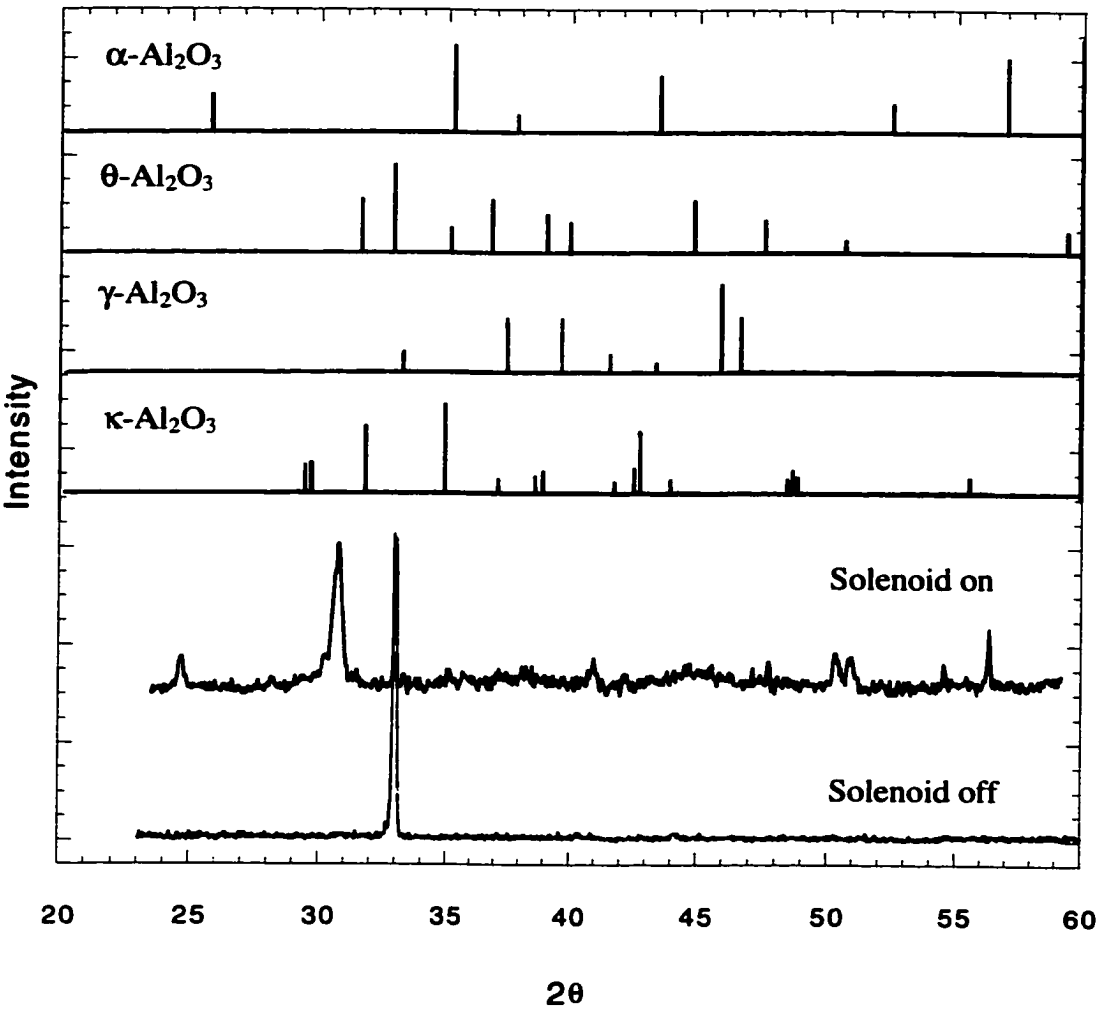

Figure 5-9 High-angle XRD patterns of aluminum oxide films grown with and without the extra magnetic field (nominal target power = 100 W, substrate bias = -300 V, substrate temperature = 300 C). Crystalline alumina appears only when the field is on.

defects in film structures, thus a denser film, which contributes to the high hardness. However, excessive ion bombardments can create defects at higher rates than can be repaired by enhanced mobility of surface species, which leads to films with higher vacancy or defect density. Crystalline films have nanoindentation hardness 18-21 GPa, in the same range as crystalline α alumina (sapphire)

Table 5-1 Nano-indentation hardness of alumina films deposited using differendeposition parameters

Substrate Bias(V)	Tempera-ture(°C)	Magnetic Field	Crystallinity	Hardness (GPa)
100	100	Off	Amorphous	10.96
200	100	Off	Amorphous	11.98
200	300	On	Amorphous	12.34
300	300	On	Crystalline	20.65
400	300	On	Crystalline	18.39

5.6.2. Electrical Resistivity

Through-thickness electrical resistivity of amorphous alumina films was measured as a function of the applied electric field, film thickness ranging from 10 to 50 nm (100 W nominal target power, –250 V substrate bias, and with the solenoid off).

There was no deliberate substrate heating. The substrate temperature was in the range of 100 C.

Fig. 5-10 shows two gneral trends. First, the resistivity decreases with increasing film thickness. This is most likely due to the classical size effect. Second, the resistivity decreases with increasing electric field. We speculate that this may be due to tunneling between conducting (defective) regions in the film. The detailed mechanism is beyond the scope of our investigation. Another way to view the data is that all alumina films exhibit no through-thickness breakdown and maintain resistivity > 10^9 ohm-cm upon application of 10 V.

Fig. 5-11 shows the resistivity data for three alumina films (10 nm amorphous, 3 nm crystalline and 10 nm crystalline). The crystalline films were grown at 100 W nominal target power, –300 V substrate bias, 300 C substrate temperature and with the solenoid on. Except at the lowest electric fields, crystalline alumina films generally have higher and more stable resistivity than amorphous ones with increasing electric field. This may be the result of crystalline alumina films having lower defect concentrations. These results indicate that ultrathin alumina films may be useful for low-voltage electrical isolation applications.

5.7 Conclusions

Stoichiometric alumina thin films can be synthesized by reactive magnetron sputtering with pulsed dc bias applied to the target and the substrate. Normally, amorphous films were produced with hardness < 12 GPa and high electrical resistivity. Intensified ionized magnetron sputtering can be achieved by forming a magnetic trap

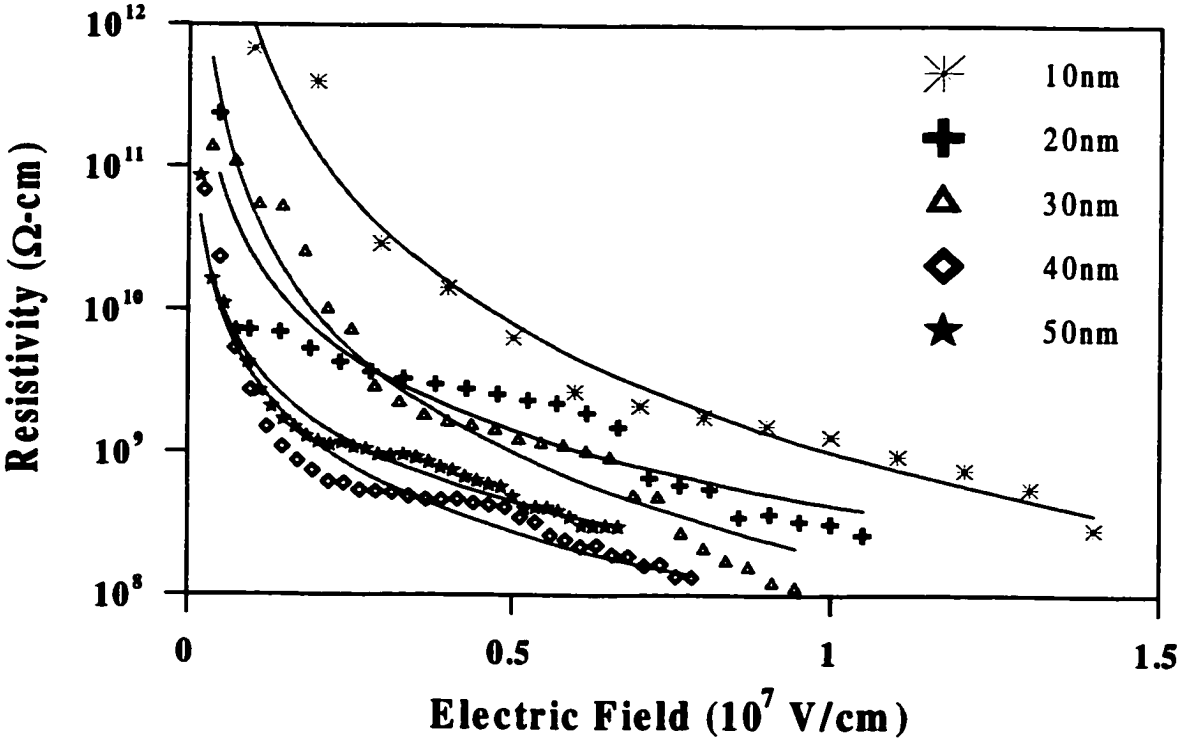

Figure 5-10 Variation of through-thickness electrical resistivity with applied electric field for amorphous alumina films (nominal target power = 100 W, substrate bias = -250 V, substrate temperature = 100 C, magnetic field off).

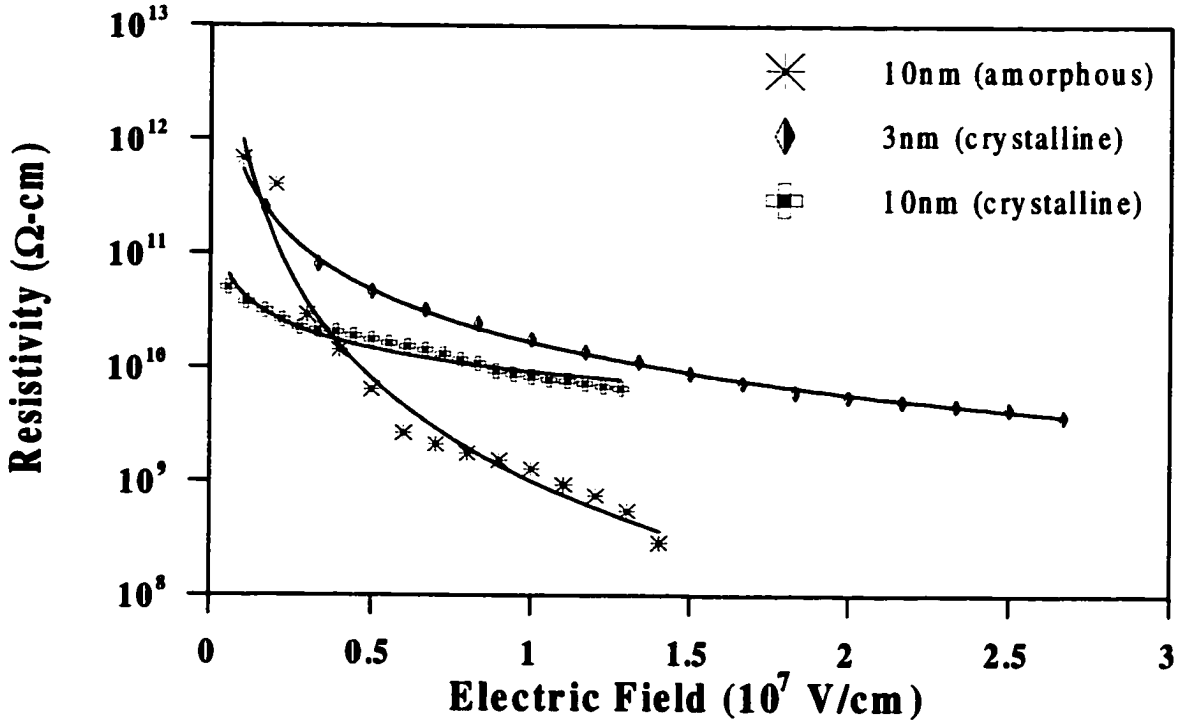

Figure 5-11 Variation of through-thickness electrical resistivity with applied electric field for amorphous and crystalline alumina films. The two crystalline films were grown at 100 W nominal target power, -300 V substrate bias, 300 C substrate temperature and with the magnetic field on.

between the target and the substrate during deposition. This technique enables the metastable phases of crystalline alumina to grow at substrate temperatures as low as 250 C. Unlike the stabilization of B1-AlN in AlN/VN superlattices, where the metastable phase is achieved due to a low interfacial energy between B1-AlN and VN, the crystalline alumina phases are obtained by increasing the mobility of surface species via low energy ion bombardment. However, excessive ion bombardment leads to high defect density and high internal stress in the film. In fact, the role of ion-bombardment will be further discussed in the next chapter of boron nitride film growth. Controlling the ion bombardment during deposition may lead to equilibrium between secondary nucleation and nuclei growth, which results in nanocrystalline film formation. The hardness of the crystalline alumina films is comparable to crystalline α alumina. Excellent electrical properties are maintained down to a thickness of 3 nm.

CHAPTER 6. NUCLEATION AND GROWTH OF cBN IN BN FILMS

6.1. Background of BN films Containing the Cubic Phase

Boron nitride is analogous to carbon in many ways. It can form both hard, diamond-like sp^3-bonded phases and soft, graphite-like sp^2-bonded phases. There are four primary crystalline boron nitride phases, i.e., hexagonal, wurtzite, rhombohedral, and cubic BN. The two common phases obtained in thin film growth are the hexagonal and the cubic phases. hBN has a layered structure similar to graphite with AA'AA'...stacking sequence. cBN has a zinc-blende structure, consisting of tetrahedrally coordinated boron and nitrogen atoms with the {111} planes arranged in an ABCABC...stacking sequence. The cubic BN has significant technological potential due to its many superior properties including high hardness, high thermal conductivity, chemical inertness, wide band gap and the ability to be both p-type and n-type doped [Holleck et al., 1986; Demazeau et al., 1991]. For specific applications such as hard protective coatings, cBN is superior to diamond because of its chemical inertness for Fe and Fe-based alloys at high temperatures.

Much effort has been made to understand cBN formation in the past decade. A wide range of deposition parameters [Inagawa et al., 1987; Ikeda et al., 1990; Kester et al., 1992; Mirkarimi et al., 1994; Reinke et al., 1994,1995; Mckenzie et al., 1995; Hackenberger et al., 1994; Hofsass et al., 1997; McCarty et al., 1996] including substrate material, deposition temperature, ion energy, ion flux, etc., have been investigated to determine the conditions for cBN formation. It is now fairly clear that ion bombardment is crucial for cBN nucleation. Although ion beam and ion-assisted techniques [Mirkarimi

et al., 1994; Reinke et al., 1994,1995; Mckenzie et al., Hofsass et al., 1997; Medlin et al., 1996; Cardinale et al., 1994; Yoshida et al., 1996] are able to produce ~100% cBN, the as-deposited BN films usually have high compressive stresses due to ion bombardment. The high compressive stress in these films limits the maximum thickness of these films to about 200 nanometers, beyond which cracking and delamination occurs. Therefore, synthesis of BN films with high cubic phase content and low internal stress is the most technological important issue in the field. Much effort [McKenzie et al., 1991; Hahn et al., 1996] has been made to reduce the stress level in c-BN films including separation of the nucleation and the growth stages during film deposition, i.e., reducing the ion-bombardment after c-BN nucleation. However, intensive ion-bombardment is still required to ensure c-BN nucleation. The stress levels in most c-BN films are higher than 5 GPa, which is too high for thick film growth.

In all previous studies of BN films containing the cubic phase, the nucleation of cBN is observed to follow the sequential formation of first amorphous boron nitride (aBN) then oriented tBN, on top of which cBN nucleates [McKenzie et al., 1991; Kester et al., 1993; Mirkarimi et al., 1997]. The tBN phase has a disordered sp^2-bonded BN structure. The two dimensional in-plane order of the hexagonal basal planes is largely retained, but these planes are stacked in a random sequence and with random rotations about the c-axis [Thomas et al., 1963]. Microscopically, most of the published works show that tBN layer grows with its (0002) basal planes perpendicular to the Si substrate surface. The cBN phase seems to nucleate on the edges of the tBN (0002) planes and

grow with its (111) planes parallel to the tBN (0002) planes [Kester et al., 1993; Mirkarimi et al., 1997].

Several growth mechanisms have been suggested, including the sputter model, quenching of the thermal spikes, stress model, and subplantation. The sputter model [Reinke et al., 1994, 1995] proposes that cBN grows by the preferential sputtering of cBN relative to graphitic BN. The facts that reasonable values of the sputter-yields are obtained from the model and the ion flux/deposition flux (J/a) boundary separating the tBN from cBN formation and the inverse sputter yield of silicon have essentially the same energy dependence support the argument. However, the experimental observation that low ion flux and energy are needed for cBN growth after nucleation makes the "phase selecting conditions" invalid. In the quenching model [Seitz et al., 1956], it is argued that thermal spikes can result in very high temperatures and pressures locally over a very brief period of time, and rapid quenching of the thermal spike region may allow the metastable cBN to be frozen in. One of the biggest questions about the quenching model is whether or not the thermal spike can permanently rearrange any atoms at all. Atomistic simulations of ion impacts [Mirkarimi et al., 1997] indicate that melting does not occur within the thermal spike of high-melting-point ceramics such as hBN and cBN. Colloza et al. [1999] investigated the possible atomic rearrangement of hBN using Xe ion bombardment, and concluded that the quenching of thermal spike by themselves is not able to account for the formation of cubic BN phase. The early compressive stress models for cBN growth can be defined as static stress model. McKenzie et al. [1994] suggest that cBN forms because the ion-induced stress places the BN material in the

cBN-stable region of the thermodynamic phase diagram. Alternatively, Mirkarimi et al. [1994] construct a kinetic model of stress. They note that strain is controlled by two factors, i.e., the dynamic concentration of interstitials and vacancies, which gives an "instantaneous stress", and the time-integrated accumulation of defects at sinks. They concluded that the maximum stress should scale approximately as ion momentum, and a critical stress is needed over some volume to induce the phase transformation in a stress mode. The major disagreement between their theoretical model and experimental results is the temperature effect. Higher temperatures allow more defect relaxation processes, thus decreasing the overall stress in the film. Therefore, one would expect cBN formation to be more difficult at higher temperatures if the compressive stress is the controlling factor. However, such a trend is not observed experimentally and cBN has been grown at temperatures higher than 1000 C [Litvnov et al, 1997, Zhang et al., 2000]. Lifshitz et al. [1987,1990] introduced the subplantation model in their explanation of sp^3-bonded carbon formation by ion irradiation. They propose that if ions of sufficient energy penetrate below the surface of sp^2-bonded carbon, the ions will displace more sp^2-bonded atoms than sp^3-bonded atoms, resulting in an accumulation of sp^3-bonded sites. However, the displacement energy difference is much smaller (< 10 eV) for BN than that for carbon (~45 eV). Apparently, none of the models describe a satisfying picture of cBN nucleation and growth process. Instead, each model focuses on a single aspect of a complicated process that involves significant ion damage, densification, and phase transformation.

The results in Chapter 5 suggest that substrate bias could increase the ion bombardment of the growing films, thus enhancing the mobility of the surface species.

At the same time, excessive ion-bombardment contributes to a high defect density, small grain size, and high internal stress in the films. In this chapter, the ion-bombardment effect is further explored. Results from BN films using different deposition parameters will be presented. The nucleation and growth of cubic boron nitride is studied at the atomic scale. Additional insight is given on the cBN nucleation and growth process.

6.2 Deposition of BN Films

Boron nitride thin films were deposited in a Kurt J. Lesker rf magnetron sputtering deposition system, shown in Figure 6-1 [Zhou et al., 2000]. The sputter target was a 99.99% pure hexagonal boron nitride disk one inch in diameter. The base pressure in the deposition chamber was on the order of 10^{-9} Torr.

The films were grown in 50%Ar/50%/N_2 mixtures at a total pressure of 10^{-2} mTorr. This parameter was one of the important conditions giving rise to stoichiometric BN films. Silicon (100) wafers were used as substrates. They were first ultrasonically cleaned in acetone and methanol, and then etched in a hydrofluoric acid solution in order to remove their native oxides and blow-dried with dry nitrogen. The hydrogen-passivated substrates were loaded into a load-lock chamber and then transferred into the deposition chamber. Prior to the deposition, the silicon substrates were reverse-sputter-cleaned in an argon atmosphere (~10^{-2} Torr) for 5 minutes in order to remove residual surface contaminants. The deposition temperature ranged from room temperature to 450 C, which was controlled by a halogen-lamp-heater. A high frequency pulsed dc bias at.

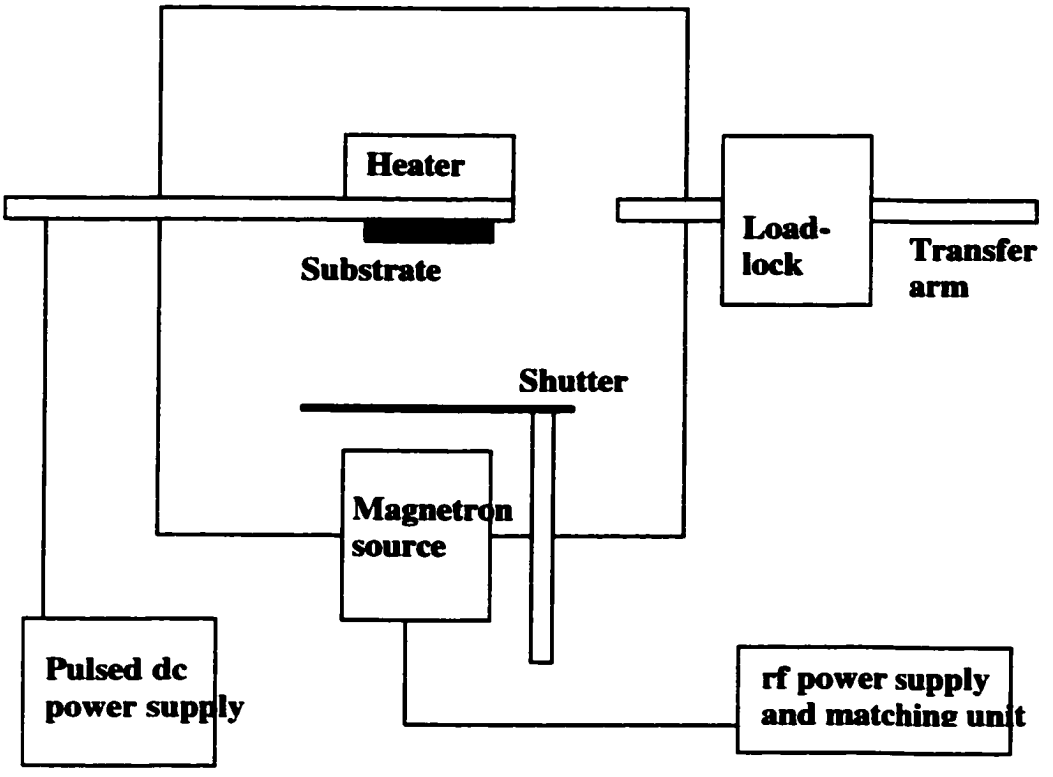

Figure 6-1 Schematic of the deposition system for BN

333 kHz was applied to the substrate during deposition. The bias voltage varied from – 30 V to – 180 V. The distance between the target and substrate varied from 2 cm to 5 cm in different depositions. The ion currents to the substrates were measured for each preset value of the target-substrate distance

6.3 Formation of Cubic Boron Nitride

6.3.1 Macro-environments Affecting the Formation of the Cubic Phase

6.3.1.1. Pre-deposition Vacuum Conditions

The normal base pressure of the deposition chamber is on the order of 10^{-9} Torr. However, the base pressure can be deliberately kept at ~10^{-7} Torr without baking the chamber after exposure to air. BN films were deposited using these two pre-deposition vacuum conditions, while keeping other deposition parameters exactly the same. The same specific range of substrate temperature and bias, which can yield cBN at a ~10^{-9} Torr base pressure, cannot produce any cubic phase at a base pressure of ~10^{-7} Torr. XPS of the films reveal that the films deposited with 10^{-7} Torr pre-deposition vacuum contain ~ 12% oxygen, a much higher value compared to <3% for films deposited with 10^{-9} Torr pre-deposition vacuum. It is generally understood that the cBN formation is affected by pre-deposition vacuum conditions, most likely by the oxygen content, as predicted by Marks et al. [1999]. They speculated that there is a very active "intermediary" for cubic BN nucleation. The presence of reactive gases such as oxygen may deactivate these precursor sites and terminate the nucleation process.

6.3.1.2. Substrate Temperature

cBN synthesis is relatively insensitive to substrate temperature. Formation of cBN has been reported at temperatures ranging from about 100 to over 1000C. Both the low- and high temperature thresholds are process-specific. It is generally believed that cBN nucleation and growth require different temperature conditions. While possibly making the initial nucleation of cBN more difficult, high-temperature growth holds promise for reducing intrinsic stresses and improving crystallinity [Kidner et al., 1994; McCarty et al., 1996; Mirkarimi et al., 1997].

In the current experimental setting, the low temperature threshold for the cubic phase formation is affected by ion bombardment during deposition. Similar to the alumina film growth described in Chapter 5, in BN film deposition, the thermal energy is one of the two energetic components improving the mobility of the adsorbed particles on the substrate surface, enhancing chemical bond formation, and annealing defects in the film. Ion bombardment provides another avenue for improving mobility of surface species, resulting in cBN formation at reduced temperatures. However, unlike alumina growth, no external magnetic trap was applied to further increase the ion-flux during film deposition. In the system described above, the low temperature threshold for cBN formation is relatively high (~400 C) compared to that in the literatures (~100C). The high temperature threshold was not observed due to limitation of the maximum temperature provided by the halogen lamp heater.

6.3.1.3. Substrate Bias

In the current experimental setting, the easiest way to examine the ion bombardment effect is to vary the substrate bias for different depositions. BN films,

designated as b1, b2, and b3, were deposited at 75 W target power, 450 °C substrate temperature with target-substrate separation distance of d_{ts} = 3 cm and at substrate bias voltage of – 30 V, - 120 V and – 180 V, respectively. Fourier transform infrared spectroscopy (FT-IR 1600, Perkin-Elmer) was used to characterize the phase distribution in both transmission and reflection modes in the 700 - 1600 cm^{-1} wavenumber range. The background spectrum of an uncoated Si substrate was subtracted from each spectrum.

Figure 6-2 gives their FTIR spectra for comparison. The FTIR spectrum taken from the BN film b1, deposited at – 30 V substrate bias, shows two peaks at 1370 cm^{-1} and 780 cm^{-1} (Figure 6-2a) characteristic of the sp^2 BN bonding. The 1370 cm^{-1} peak corresponds to the stretching of B-N bonds within the basal plane, and the 780 cm^{-1} mode corresponds to the bending of B-N-B bonds between the basal planes. The FTIR spectrum acquired from the BN film b2, deposited at – 120 V substrate bias, is dominated by a characteristic peak at ~1070 cm^{-1} (Figure 6-2b) implying a high content of sp^3 bonding in this film. However, the FTIR spectrum obtained from the BN film b3, deposited at – 180 V substrate bias, shows all three peaks with similar intensities, indicating that the cubic phase formation is hampered as the substrate bias increased from – 120 V to -180 V. Unlike film b1 and b2, film b3 delaminated right after being taken out from the deposition chamber. Therefore, the FTIR result of film b3 actually reflects the BN bonding state after its internal stress is relaxed, which explains the shift of the 1070 cm^{-1} peak to lower wavenumber. As far as ion bombardment is concerned, there are sharp thresholds for cBN formation in the experimental parameter space of (1) ion

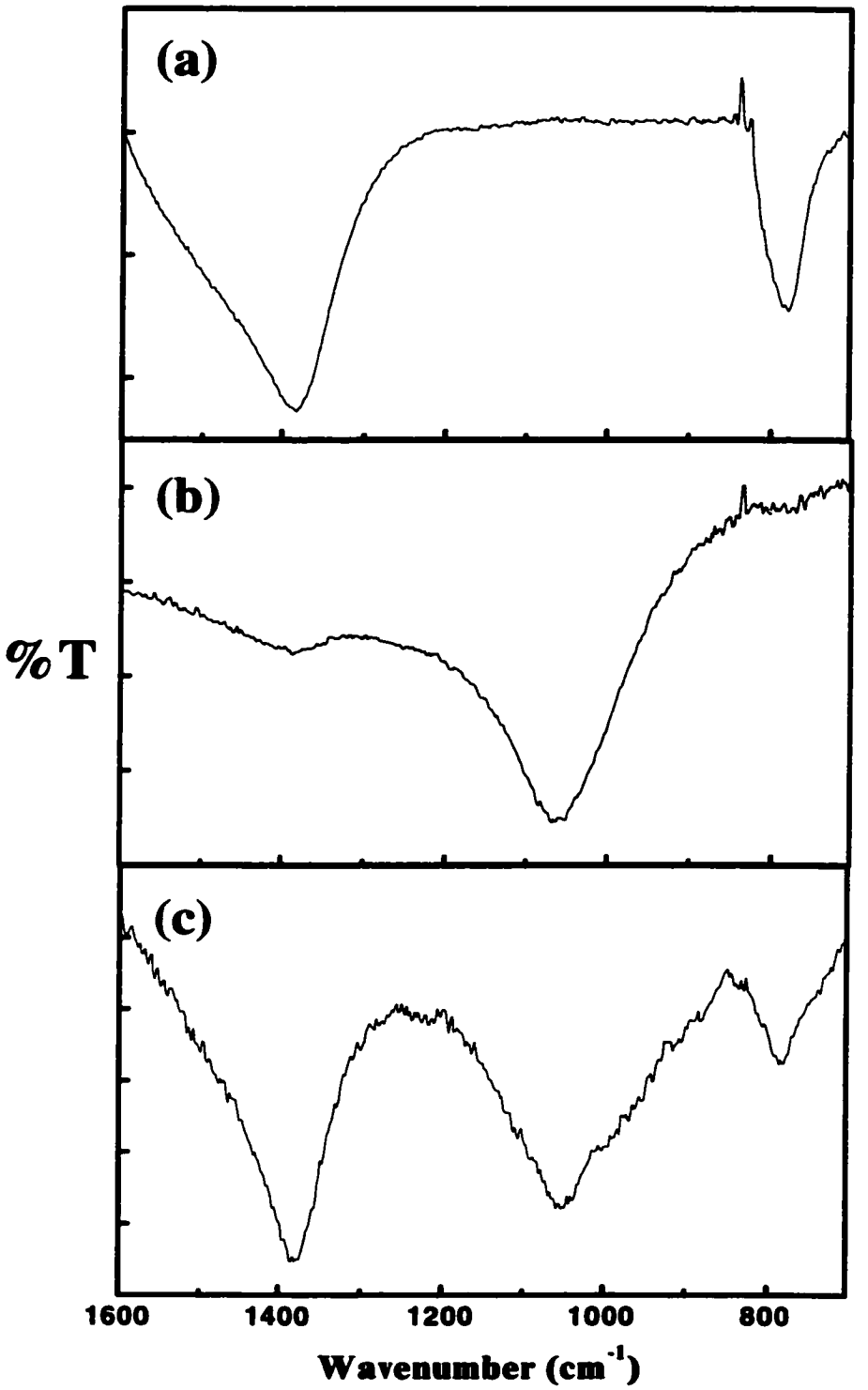

Fgiure 6-2 FTIR of three BN films deposited at (a) –30V , (b) -120V and (c) –180V substrate bias.

mass, (2) ion energy, (3) ion flux, (4) deposition flux. It is generally agreed that the sharp threshold can be described by a total momentum related parameter [D. J. Kester et al., 1992; P. B. Mirkarimi et al., 1994; S. Reinke et al., 1994,1995; D. R. Mckenzie et al., 1995; P. B. Mirkarimi et al., 1994].

$$(P_{Tot}/a) = \Sigma_i (J_i/a) (2 m_i E_i)^{1/2}$$

where J/a is the ratio of the ion flux to the deposition (atom) flux, m_i the mass of the ith ionic species, and E_i its energy. Varying the substrate bias mainly changes the ion energy term. However, the ion flux and the deposition flux will be affected as the substrate bias varies. Changing the substrate bias alone, while keeping all the other parameters constant, would define a specific region for cBN formation. The cubic phase only forms above some substrate bias value. With high bias, ion irradiation leads to a decrease of cBN content in the films.

6.3.1.4. Film Stoichiometry

The resputtering process was further examined by XPS using a VG ESCA LAB 220i-XL system equipped with a monochromatic Al Kα x-ray source operating at 1486.6 eV. The survey XPS spectrum of film b2 (Figure 6-3) shows that the B/N ratio is close to unity. Two minor components, oxygen and hydrocarbons, exist in amounts of less than 2 atomic % each.

The high resolution B 1s and N 1s XPS spectra, in Figure 6-4, with their maximum at binding energies of 190.4 and 398.1 eV, respectively, are corrected for 1.12 eV charging shift using the C 1s core level at 285 eV as a reference. Peaks at binding energies of 190.4 and 398.1 eV are associated with single B-N chemical states which can

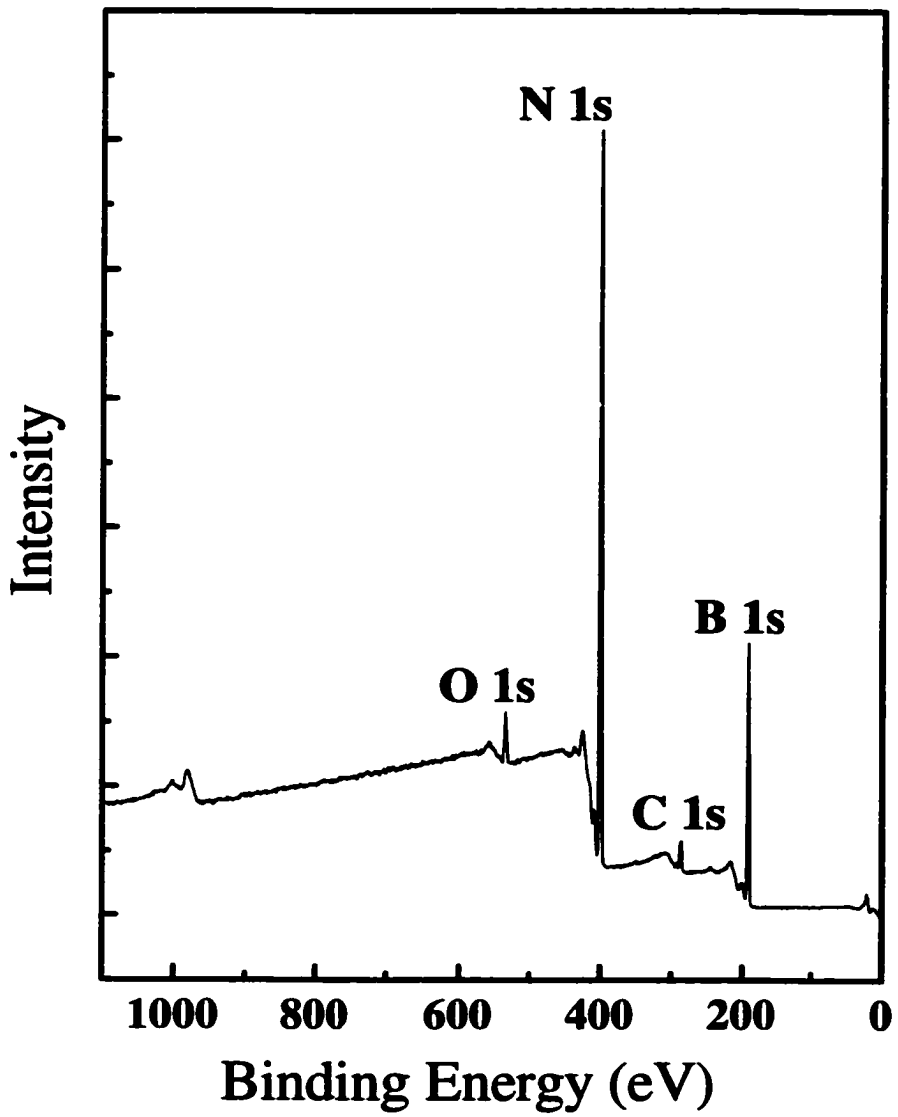

Figure 6-3 Survey XPS spectrum of BN film b2

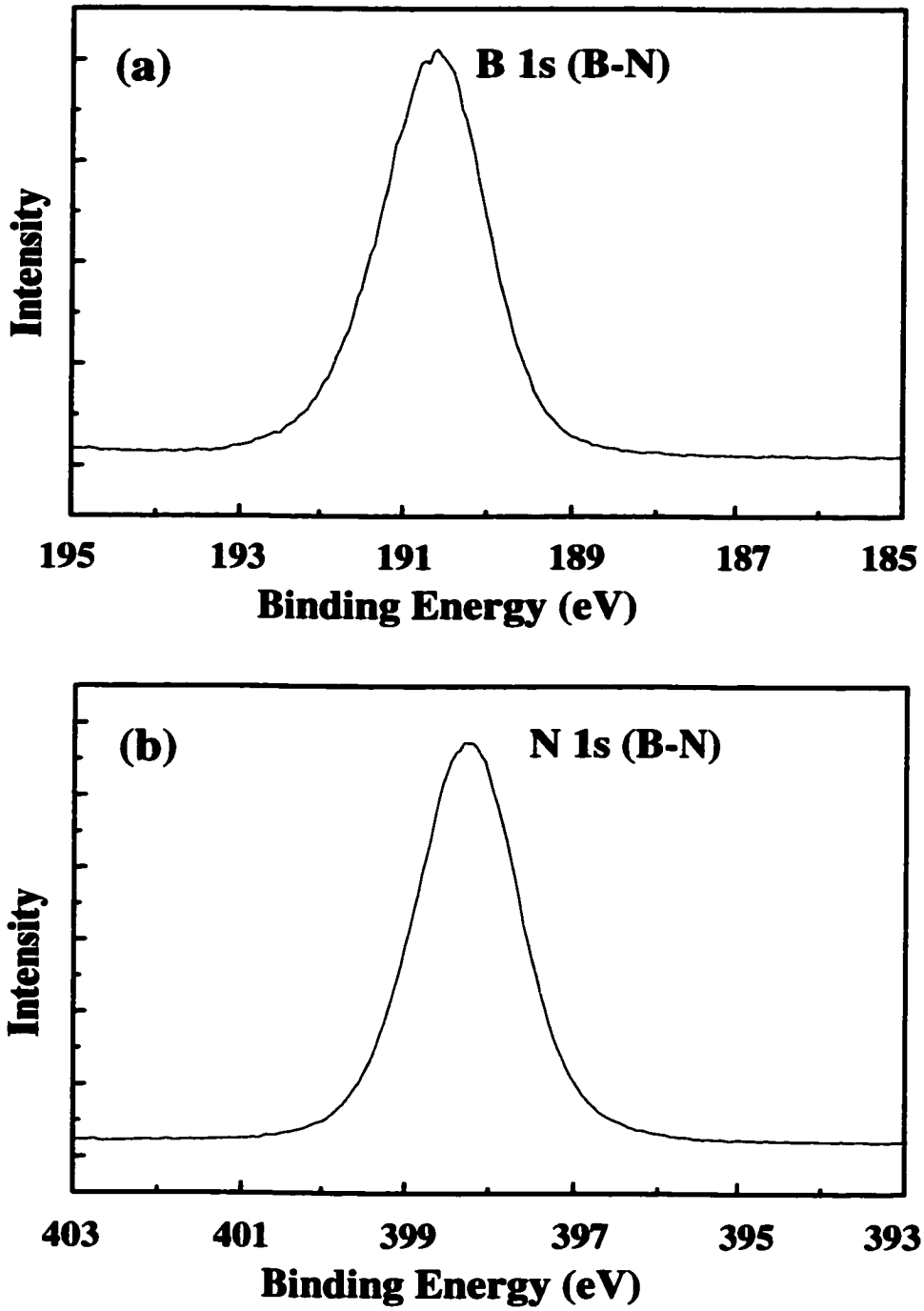

Figure 6-4 High resolution XPS spectra of B 1s core level (a) and N 1s core level (b) of BN film deposited at 75 W substrate bias, 450 °C substrate temperature, - 350 V substrate bias and using separation distance d_{ts} = 3 cm.

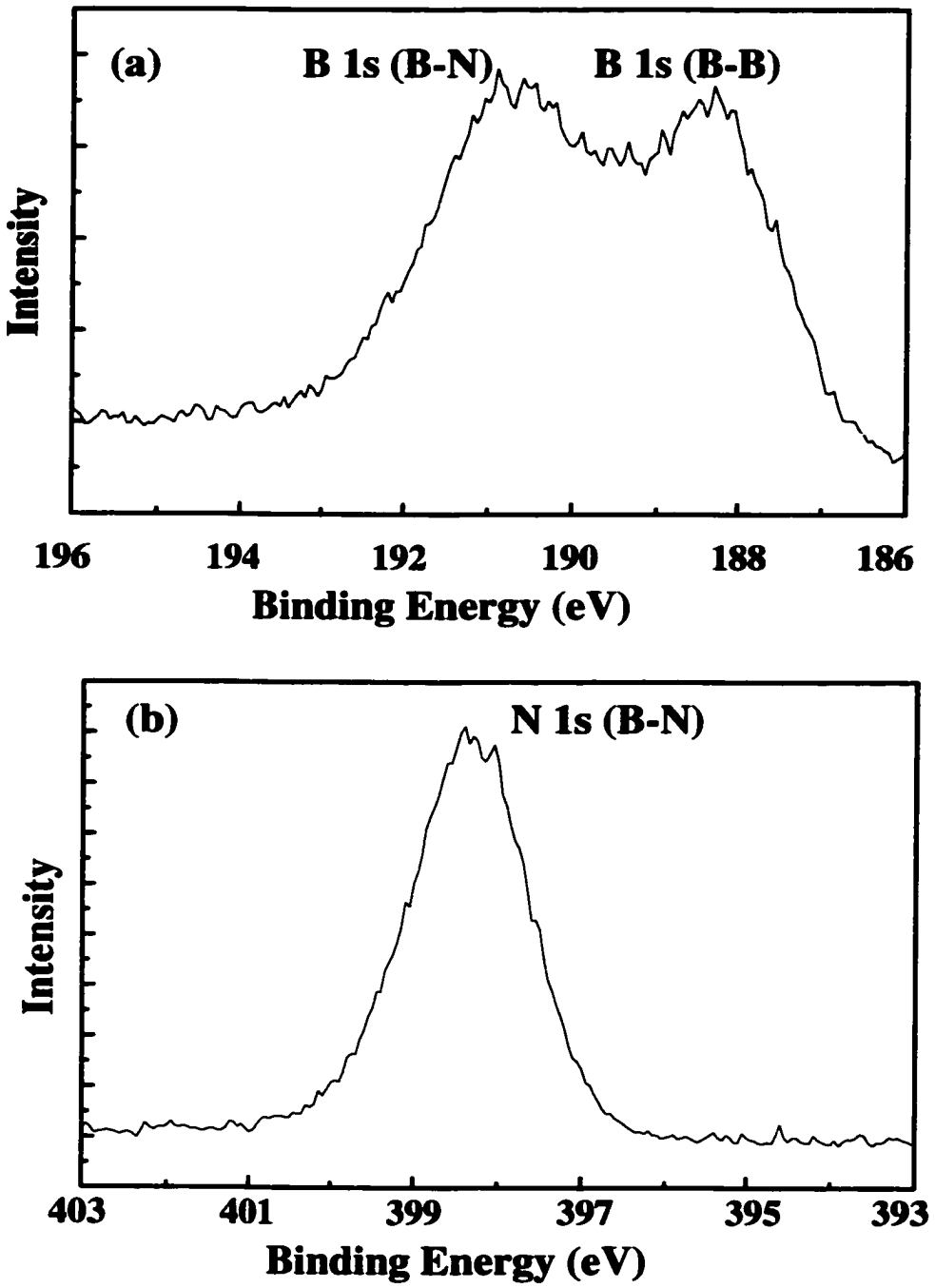

Figure 6-5 High resolution XPS spectra of B 1s core level (a) and N 1s core level taken from a BN film deposited at 75 W substrate bias, 450 °C substrate temperature, - 450 V substrate bias and separation distance d_{ts} = 3 cm.

also be deduced from the spectral symmetry and a relatively narrow FWHM of approximately 1.5 eV for both B 1s and N 1s core level spectra. The compositional analysis and high-resolution spectra taken from the BN film b1 is similar to those of film b2, as presented above. However, the compositional analysis of the film b3 yields a B/N ratio of 1.5. Excessive ion bombardment results in boron nitride films enriched in boron due to re-sputtering (detailed explanation see below). High resolution XPS analysis (Figure 6-5a), of the B 1s core level spectrum reveals at least two peaks indicating B-N and B-B bonding states [J. F. Moulder et al., 1992] at binding energies of 190.6 and 188.26 eV, respectively. The N 1s core level spectrum, in Figure 6-5b, shows its maximum at a binding energy of 398.13 eV, which is practically identical to that observed in films b1 and b2. However, a different chemical bonding induced peak broadening is observed in the high-resolution spectra of B 1s.

The kinetic energy of particles, driven by the substrate bias, is responsible for the displacement of boron and nitrogen constituents from the lattice sites, which results in the formation of lattice vacancies, and interstitials. Extensive defects may give rise to amorphous structures. The kinetic energy of impinging particles is also responsible for sputtering, of the film constituents. Since nitrogen is a volatile component, the broken B-N bonds may lead to a boron-nitride structure depleted in nitrogen. The inherent difference in the sputtering rates of film constituents alters the film composition and results in deposition of non-stoichiometric boron nitride films. Due to re-sputtering, the films suffer from low deposition rate, even no-growth conditions above certain thresholds of the kinetic energy and substrate temperature.

In summary, as nitrogen is more susceptible to ion bombardment and easier to be sputtered off (leave by forming N-N bonding—N_2 gas) compared to boron, the increase in ion-energy may enriched the film in boron, and the excessive boron atoms form bonds. The non-stoichiometry of BN due to the excessive ion-bombardment is well known to be detrimental to the cubic phase formation. Hackenberger et al. [1994] concluded that films with high cBN contents tended to have B/N ratios close to unity. However, whether the extra boron-boron bonding would affect the favorable environment for c-BN formation is unclear.

It is later on discovered that the hexagonal BN phases in the films deposited with different substrate bias have different microstructures (see 6.4). However, no difference is detected concerning the B and N 1s peaks in the XPS spectra of these films. The XPS analysis can be insensitive to different microstructures of the hexagonal BN phases [Bengu, 2000].

6.3.1.5. Substrate-Target Separation Distance (d_{ts})

Boron nitride films, designated as d1, d2, d3 and d4, were grown at variable target – substrate separation distances of 5, 4, 3 and 2 cm, respectively, while the 75 W target power, 450 °C substrate temperature, and – 120 V substrate bias were kept constant during depositions. Figure 6-6 shows the FTIR spectra of films d1 (5 cm), d2 (4 cm) and d3 (3 cm). The FTIR spectrum of the film d1, in Figure 6-6 a, shows two peaks at 1370 cm^{-1} and 780 cm^{-1} corresponding to the sp^2 B-N bonding. The three peaks observed in the spectrum of film d2 indicate that the film contains mixed phases of c-BN and t-BN

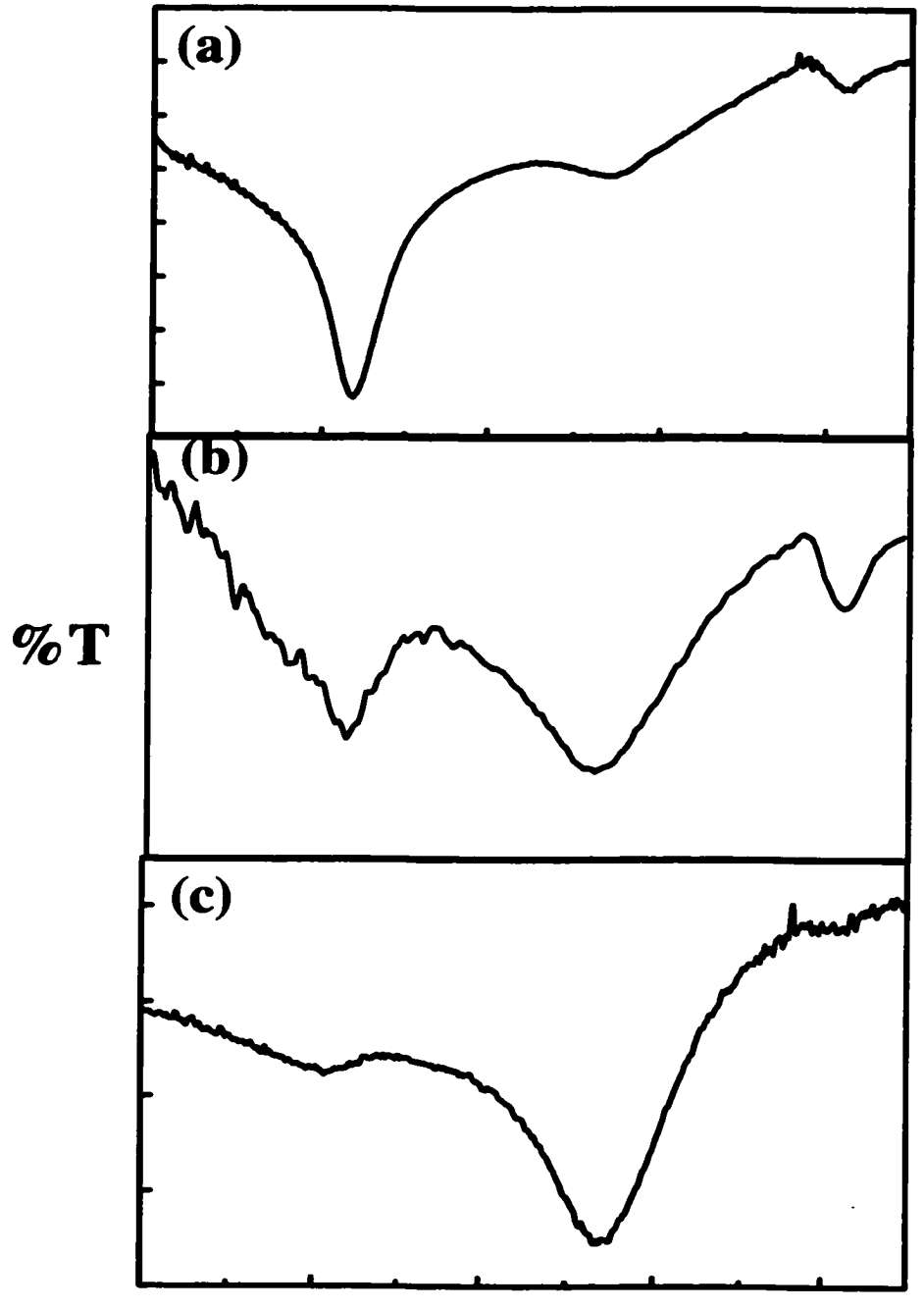

Figure 6-6 FTIR spectra collected from three films deposited with d_{ts} = 5cm (a), 4 cm (b), 3 cm (c).

(Figure 6-6b). The dominant peak at about 1070 cm^{-1} of film d3 implies boron nitride films with a high content of cubic phase (Figure 6-6c).

Although the deposition times for all films are identical, the BN film d4 is substantially thinner than the others. Therefore, FTIR analysis could not provide any useful information. The c-BN fraction is calculated as $I_{1070} / (I_{1070} + I_{1370})$ [Mirkarimi et al., 1994], where I_{1060} and I_{1370} are the normalized transmitted intensities of the IR absorbances at wavenumbers of approximately 1070 and 1370 cm^{-1}, respectively. The volume fraction of c-BN phase is plotted as a function of d_{ts} in Figure 6-7.

The ion-current density is also plotted as a function of the target – substrate distance, d_{ts}, in Figure 6-8. The ion-current density is low when the substrate is far away from the target, and it increases as d_{ts} is reduced until it reaches a maximum value of 4.3 mA/cm^2 at $d_{ts} = 3$ cm. The ion-current density declines with the further decrease in d_{ts}. Except for film d4, for which the deposition flux is severely changed, the deposition rates of the other three films do not vary significantly.

The ion-to-atom ratios (J/a) of the films deposited at different d_{ts} are estimated using the ion current density and deposition rate. The J/a ratios are estimated to be 24, 28 and 31 for separation distances of 5, 4 and 3 (see Table 6-1), respectively. In the estimation, only the deposited flux of particles is considered. The trend in ion-current density as well as ion-to-atom ratio is consistent with the FTIR results acquired from the three films. Since the arrival rate of energetic ions is reduced with the increase of target – substrate separation distance to 5 cm, t-BN is mainly formed at such condition. In contrast, moving the substrate closer to the sputtering target, the ion-current increases,

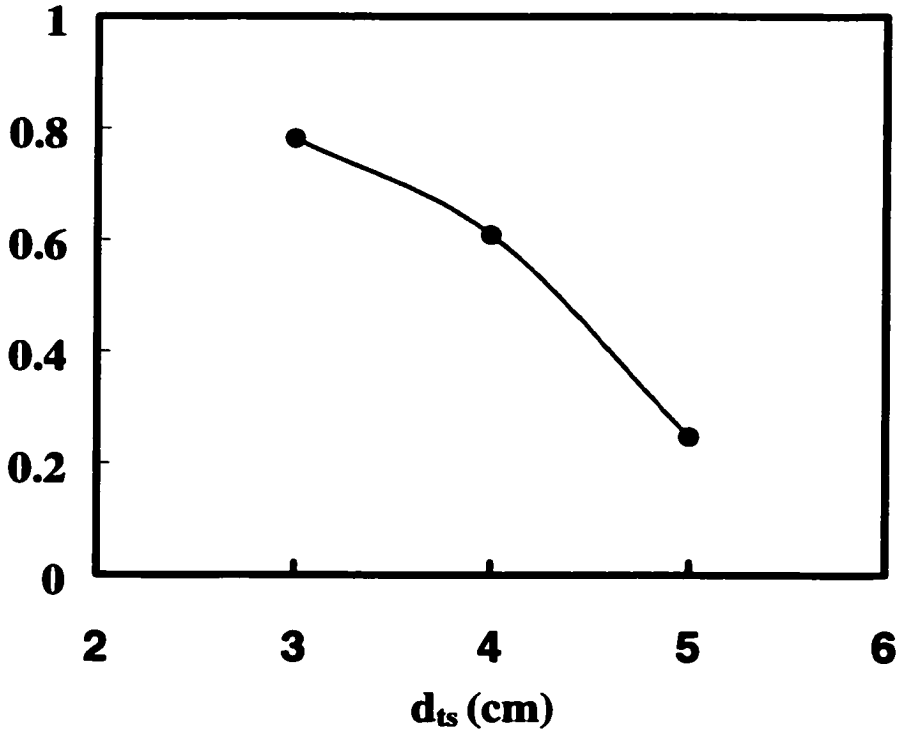

Figure 6-7 Volume fraction of the cubic phase in BN films versus target-substrate distance

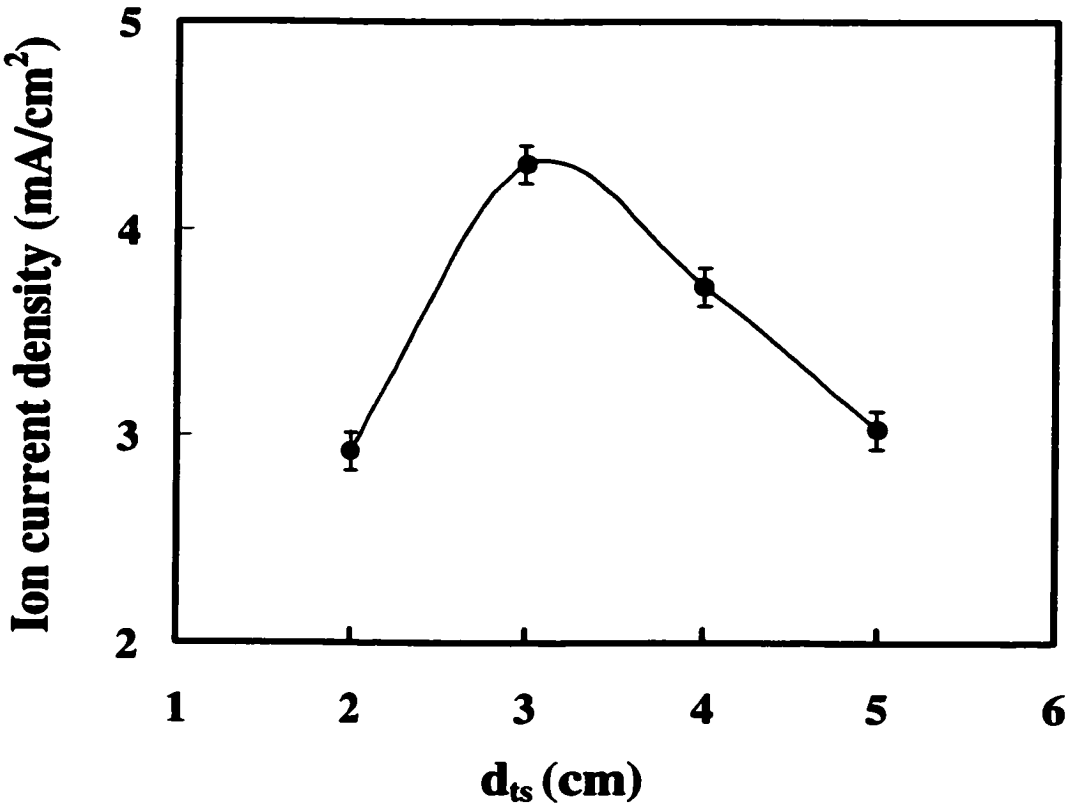

Figure 6-8 Ion current density corresponding to the arrival rate of energetic ions to the substrate with respect to variable separation distance between the target and the substrate

thus the arrival rate of energetic ions increases, which makes the c-BN formation more favorable. Therefore, optimizing the ion-current to the substrate without changing the deposition flux leads to boron nitride films with higher contents of the cubic phase. However, at very short d_{ts}, the electric field arising from the substrate biasing may interact with the plasma generated by magnetron, which gives rise to disturbed plasma. In addition, as a result of the disturbed plasma, the film appears to be non-uniform and experiences very low deposition rate. Basically, the observed trend is consistent with the literature when interpreting the change in d_{ts} as changing the J/a ratio. Nevertheless, changing the d_{ts} value also changes the energy distribution of impinging particles. This factor is expected to contribute to cBN formation as well.

Table 6-1 Deposition flux and ion flux of four BN films deposited with different target-substrate separation distance

Film No.	Ion-current density (mA/cm^2)	Deposition rate (nm/hr)	Ion-to-neutral ratio
d_1	3.0	178	24
d_2	3.7	190	28
d_3	4.3	200	31
D_4	2.9	N/A Extreme non-uniformity of the film	N/A

6.3.2. General Description of BN Films Containing the Cubic Phase

The microstructure of the as-deposited BN film is similar to those reported in literature [D. R. McKenzie et al., 1991; D. J. Kester et al., 1993; P. B. Mirkarimi et al., 1997]. Figure 6-9 shows a TEM images of the BN film deposited at 75 W target power,

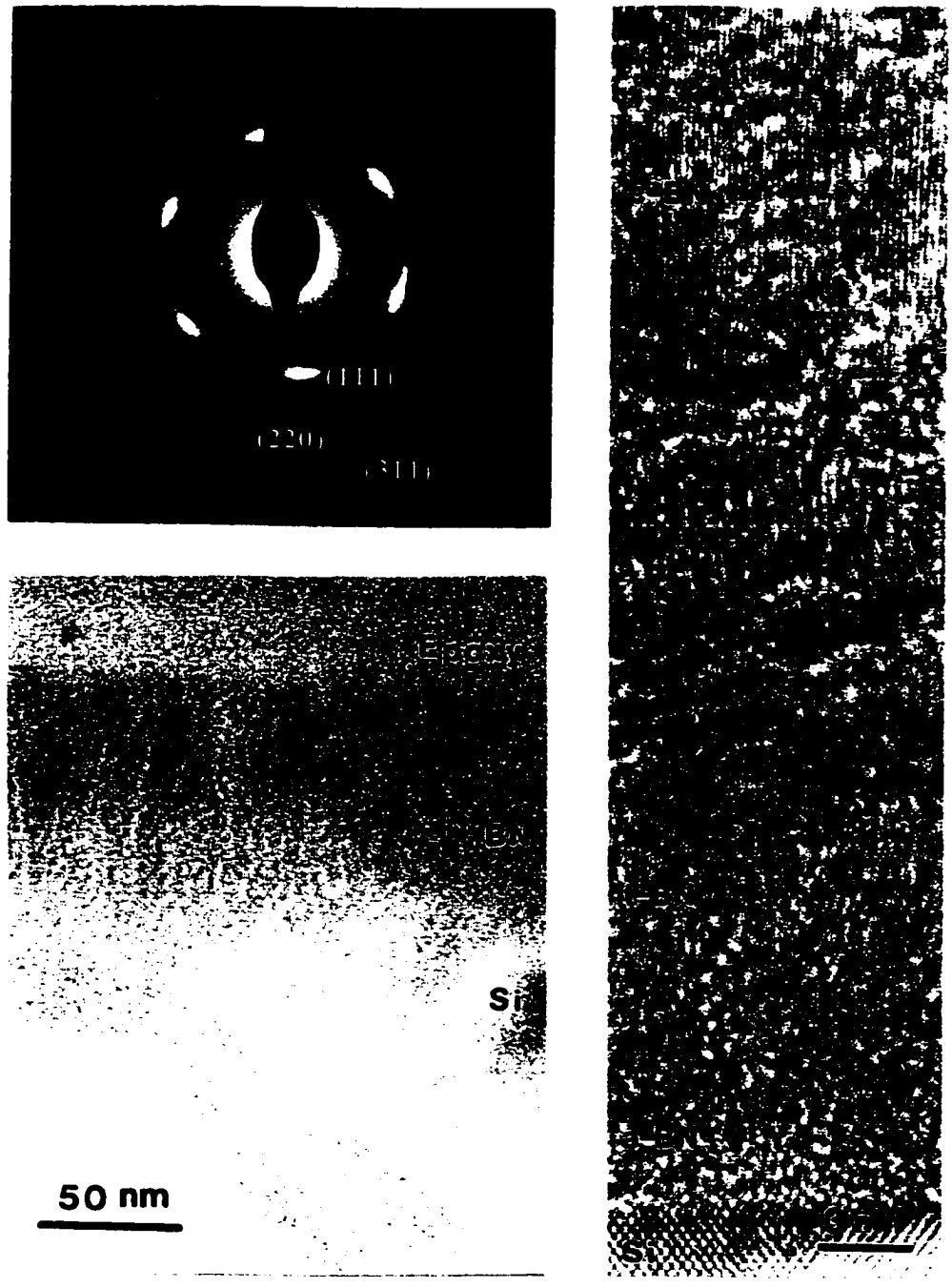

Figure 6-9 The image in the lower left is a low magnification image of the film and the substrate. The image on the right is a HREM image showing the layered growth of BN film. The image inserted in the upper left is a TED pattern taken at the top of the BN film confirming the formation of cubic BN.

450 °C substrate temperature, -120 V substrate bias and substrate target distance d_{ts} = 3 cm.

The high-resolution image in Figure 6-9c, shows that the c-BN phase is grown on the top of a ~30 nm t-BN structure which is formed on a ~ 10 nm amorphous BN layer at the Si interface. The orientation of the t-BN (0002) planes is not necessarily exactly perpendicular to the film/substrate interface. Some of them are at a certain angle to the interface. A low magnification bright field image of the same BN film, in Figure 6-9b, indicates the column growth of the cubic phase. The cubic phase of boron nitride is also confirmed by the diffraction pattern (Figure 6-9a) taken with a selected area aperture covering the cBN film. The diffraction rings are composed of several elongated dots, are indicative of preferential directions in the cubic phase.

6.4 Nucleation of Cubic Boron Nitride

6.4.1. Micro-environments Affecting the Nucleation of the Cubic Phase

In order to understand the nucleation process from a microstructure point of view, TEM was performed for a series of samples deposited with different substrate bias ranging from –50V to –120V (base pressure ~10^{-9} Torr, target power 75 w, substrate temperature 450C, target-substrate separation distance 3 cm). High-resolution images were taken using a CM 200 Phillips microscope operating at 200 kV. Transmission electron diffraction (TED) patterns were taken using a Hitachi HF-2000 microscope operating at 200 kV. Film (a) was grown at the deposition conditions described above using a substrate bias of –120 V. The maximum thickness of film (a) before

delamination is 100 nm. The internal stress of the film (a) (100 nm film thickness) is measured at ~11 GPa (Obtained by measuring the curvature of the sample). XPS proves that the BN film is stoichiometric. Film (b) was grown at the same deposition conditions as for film (a), but with a substrate bias of –50V. The maximum thickness of film (b) before delamination is 500 nm. The internal stress of film (b) (500 nm film thickness) is measured at ~4.5 GPa.

Figure 6-10 a shows a FTIR spectrum of a film (a). The peak at 1070 cm^{-1} corresponds to the cubic BN phase, while the two peaks at 1370 and 780 cm^{-1} correspond to the hexagonal BN phase. The cBN fraction is calculated to be 81% in a conventional way [P. B. Mirkarimi et al., 1994]. Figure 6-10 b shows a FTIR spectrum of a film (b). The peak corresponding to the cBN phase moves to a wavenumber of 1055 cm^{-1} due to the reduced stress. The cBN fraction of film (b) is calculated to be 63%.

Figure 6-11a and b are low magnification XTEM images of film (a) and film (b), respectively. Both images show layered contrast in the BN film.

Figure 6-12 shows EELS spectra of the films using a Gatan GIF 200 attached to a CM 200 microscope. Areas where the EELS spectra are taken are marked on the image in Figure 6-11. The probe size of the electron beam is about 10 nm, which is deliberately larger to avoid severe irradiation damage (the smallest e-beam size can be controlled at ~2nm).

The near-edge structure of the B K-edge spectra consists of a sharp π^* peak, a broad σ^* peak, and an additional sharp peak. The spectrum from area 1 has a strong π^*

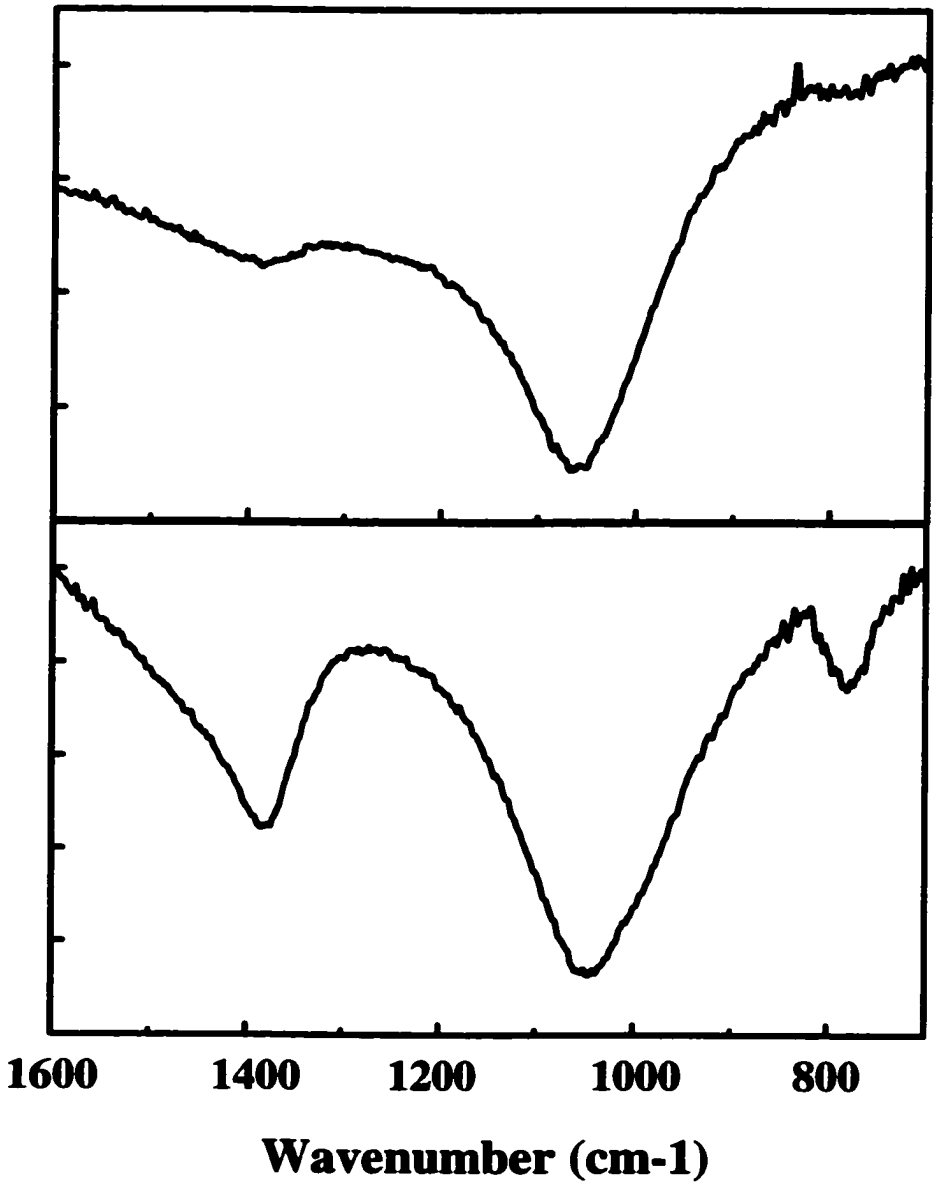

Figure 6-10 FTIR spectra of two BN films deposited using a power of 75 W on a substrate held at 450°C. Film (a) (100 nm thickness) was deposited using a substrate bias of –120 V; Film (b) (500 nm thickness) was deposited using a substrate bias of -50 V.

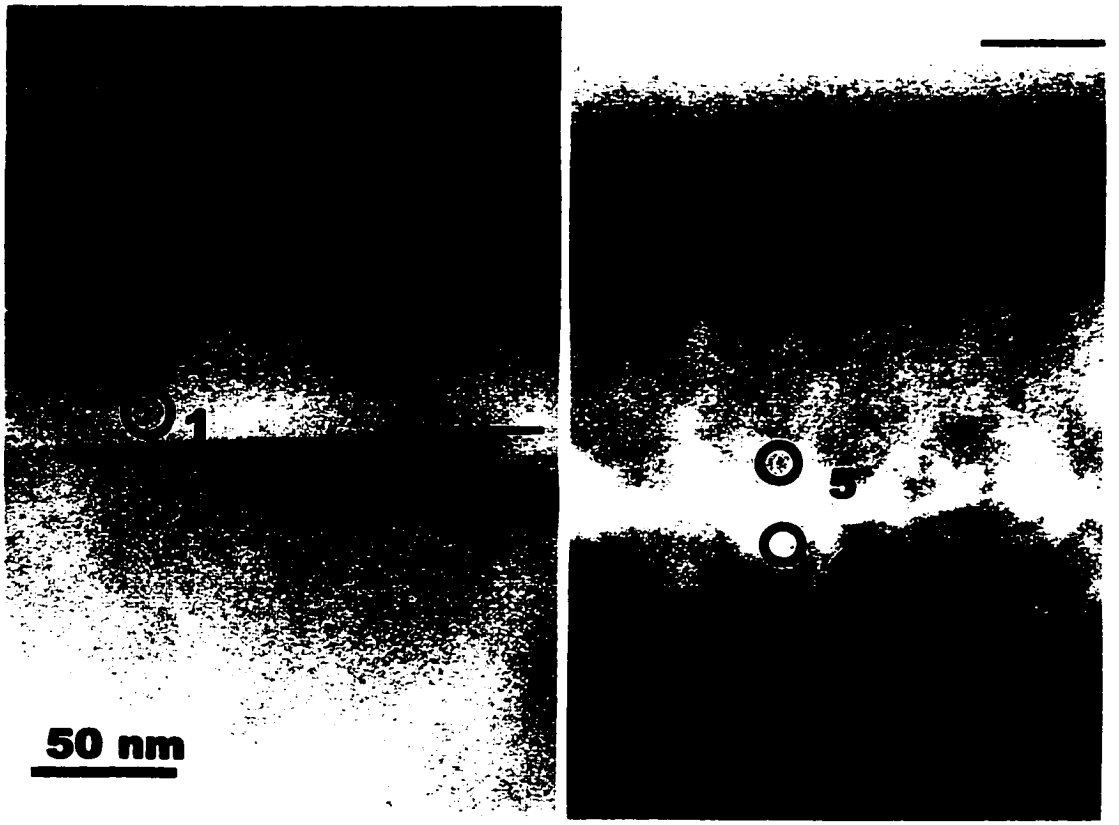

Figure 6-11 Low magnification TEM images of films (a) and (b).

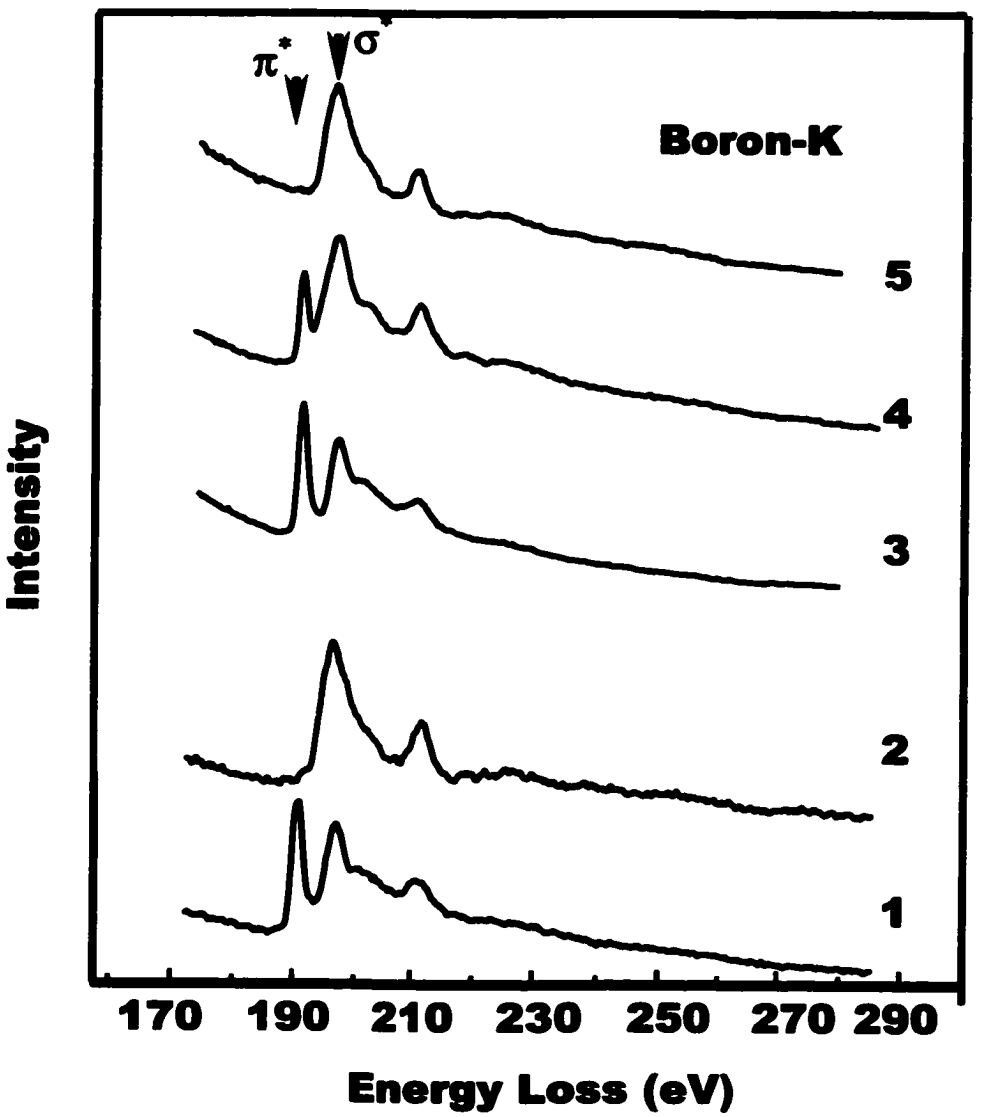

Figure 6-12 EELS spectra of films (a) and (b) taken from different areas of each film. The numbers of the spectra correspond to the areas marked in figure 6-11.

peak at 191 eV due to sp^2 bonded BN. The π^* peak in the spectrum from area 2 and above is absent, and an additional sharp peak appears next to the σ^* peak. This indicates that the BN phase in film (a) above area 2 is ~100% cBN. Area 3 and below also give a strong π^* peak due to sp^2 bonded BN. Area 4 gives a similar spectrum to that taken from area 3, but with a reduced relative intensity of the π^* peak. The spectra from area 5 and above are similar to that taken from area 2 in film (a), indicating that the BN phase in film (b) above area 5 is ~100% cBN.

Figure 6-13 shows a TED pattern taken at the interface of film (a) and the substrate with the electron beam along the Si [110] direction. The TEM results of film (a) are similar to those reported in the literature [D. R. McKenzie et al., 1991; D. J. Kester et al., 1993; P. B. Mirkarimi et al., 1997]. For comparison with the data of film (b), TEM results of film (a) are briefly described. The tBN (0002) diffraction spots are measured to be 90 degree away from the Si (002) diffractions. Instead of uniform ring patterns, three incomplete rings consist of several elongated spots corresponding to cBN (111), (220) and (331) diffraction, respectively. The diffraction pattern of film (a) indicates preferential orientations in both tBN and cBN phases.

The preferential orientation of tBN and cBN are further confirmed by the high-resolution images taken at both the BN/Si interface as well as the cBN/tBN interface with electron beam along the Si (110) zone axis. Figure 6-14 shows that an amorphous BN layer is first formed on the Si substrate, followed by an oriented tBN layer, with its (0002) planes perpendicular to the Si surface.

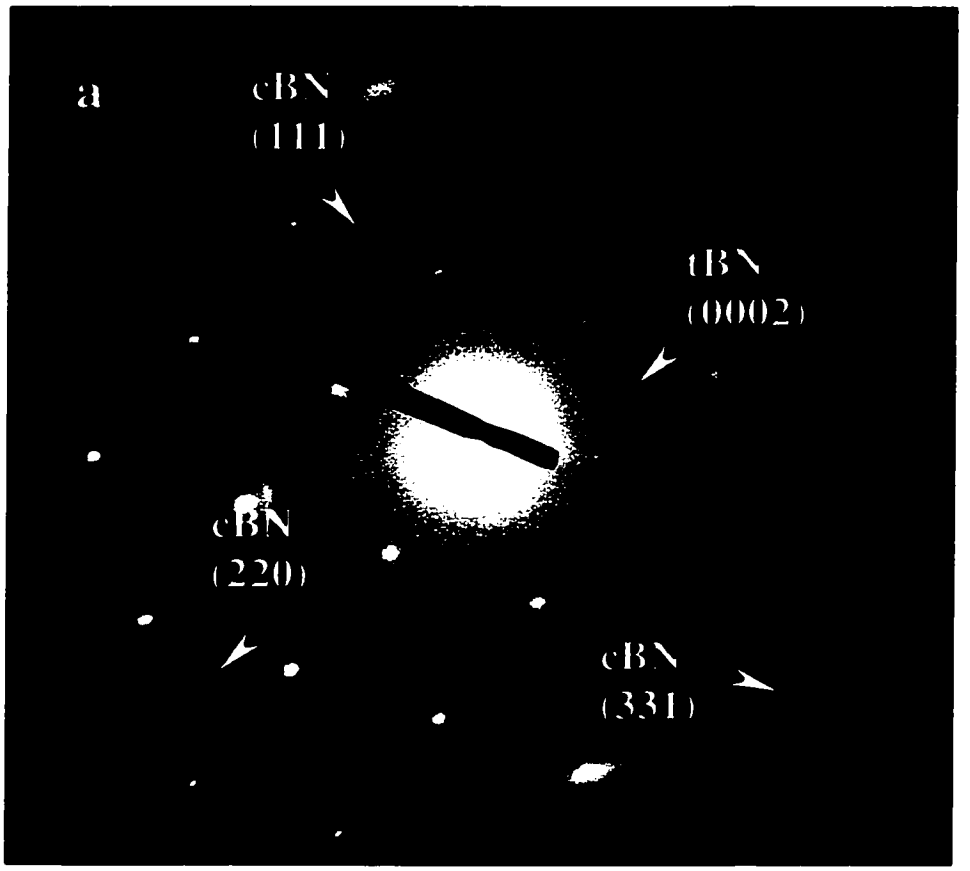

Figure 6-13 TED pattern of film (a). The two tBN (0002) diffraction spots are perpendicular to the Si (002) spot; the incomplete diffraction ring of cBN indicates that the c-BN crystallites are preferentially oriented.

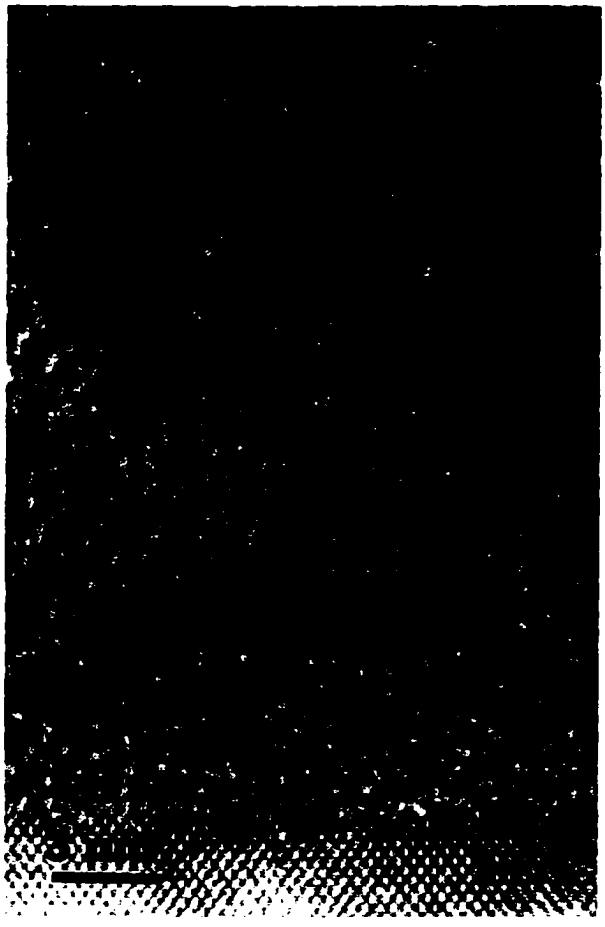

Figure 6-14 High-resolution TEM image of film (a) taken at the interface of the BN film and the silicon substrate with the electron beam along the Si [110] direction.

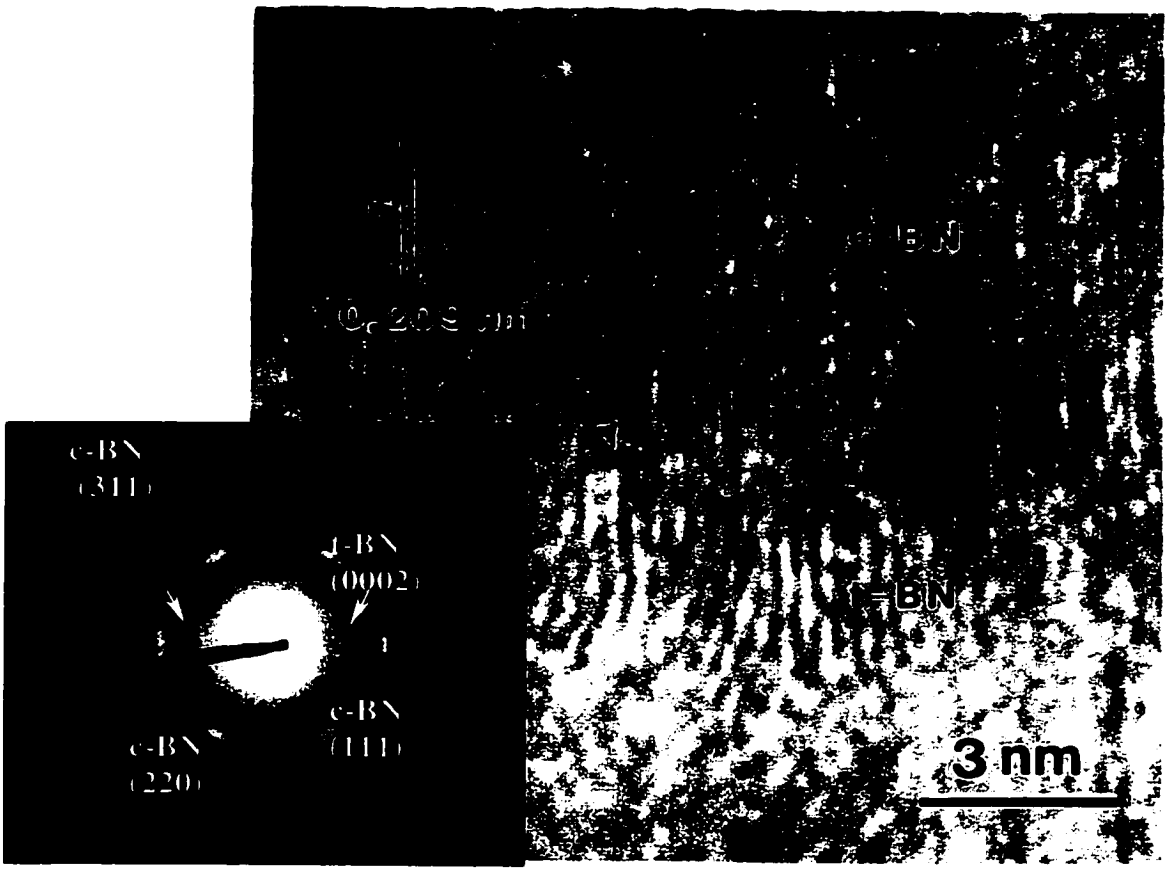

Figure 6-15 High-resolution TEM images of film (a) taken at the tBN/cBN interface.

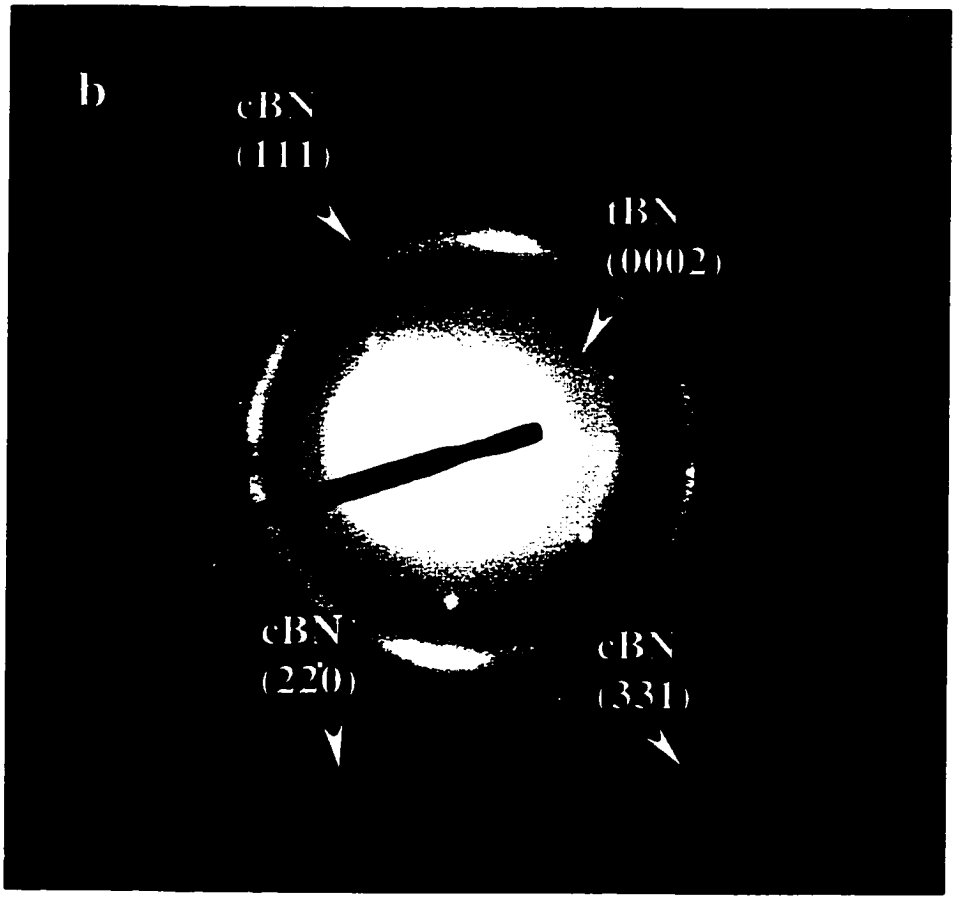

Figure 6-16 TED pattern of BN film (b).Diffraction spots from tBN (0002) planes form a ring-like pattern; the diffraction ring of cBN is more uniform than that of film (a).

Figure 6-15 shows that cBN nucleates on the edge of tBN (0002) planes and further grows with its (111) planes parallel to the tBN (0002) planes. A 3:2 (cBN:tBN) lattice match is maintained locally.

The microstructure of film (b) is quite different from that of film (a). Figure 6-16 shows the TED pattern taken at the interface of the film (b) and the substrate. Diffraction from tBN (0002) planes forms arc-like pattern, almost close up to a ring, which indicates that the preferential orientation in the tBN layer of film (a) diminishes to a large extent. The three relatively uniform rings correspond to the cBN indicate that the orientations of the cBN crystallites are not as textured as those in film (a).

The randomization of the tBN is further confirmed by high-resolution images taken at the BN/Si interface with electron beam along the Si (110) zone axis. Figure 6-17 shows that curved (0002) planes of the tBN layer on top of aBN are randomly oriented. The edges of the tBN (0002) planes are no longer exposed along the growth direction.

Figure 6-18 is a high-resolution image taken at the interface of tBN and cBN. A curled (0002) plane of tBN is exposed along the growth direction and cBN is observed to nucleate on the curved tBN plane and grow further. The (111) planes of cBN are no longer parallel to the tBN (0002) planes due to the curved nature of the tBN planes.

Two other samples, film (x1) and film (x2), have been deposited using substrate biases of –100V and –80 V, with other deposition parameters kept the same as in film (a) and (b). Table 6-2 summarizes the variations of the film properties with substrate bias within a range –120 to –50 V. As the substrate bias changes from –120V to –50V, the internal stress of the film decreases from ~11 GPa to ~4.5 GPa, and the maximum film

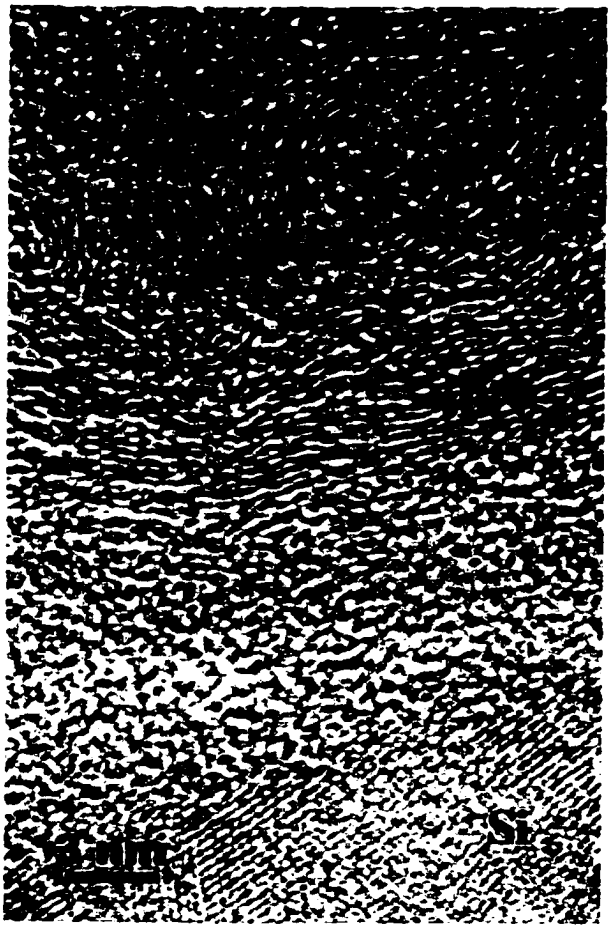

Figure 6-17 High-resolution TEM images of film (b) taken at the interface of the BN film and the silicon substrate with the electron beam along the Si [110] direction.

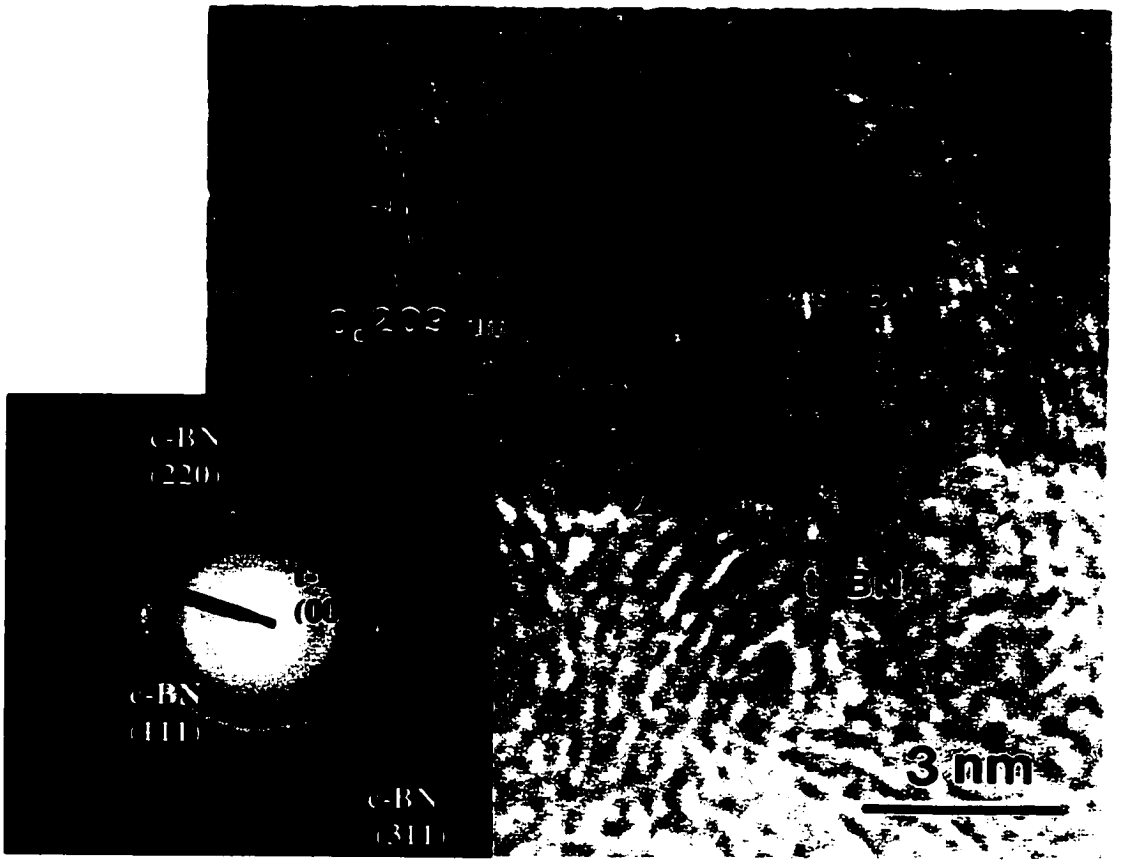

Figure 6-18 High-resolution TEM images of film (b) taken at the tBN/cBN interface.

thickness before delamination increases from 100 nm to 500 nm. The thickness of the tBN layer increases from ~25 nm to ~150 nm as the substrate bias decreases. This explains the increase in tBN faction of the film as a whole, while the cBN layer on top of it remains ~100% purity. Both types of cBN nucleation environments, i.e. "edge nucleation" (type A) and "curvature nucleation" (type B), are observed for all these films. The fraction of type B nucleation, however, increases from ~0% to ~30% as the substrate bias decreases. XPS showed that the B/N ratio remains close to unity for all these films.

Table 6-2 Variations of the film properties with substrate bias

	Substrate Bias (V)	Internal stress of the film (GPa)	Total film thickness at delamination (nm)	tBN layer thickness (nm)	Fraction of the type B tBN/cBN environment (%)
Film (a)	-120	~11	~100	~25	<1
Film (x1)	-100	~9	~150	~40	~3
Film (x2)	-80	~6	~300	~100	~15
Film (b)	-50	~4.5	~500	~150	~30

6.4.2. Reactivity of Different tBN Environments

6.4.2.1 Modeling of tBN Microstructures for Further Reactions Based on TEM Studies

The TEM study shows that there are three types of tBN environment in the BN films deposited using rf magnetron sputtering, which is a physical vapor deposition (PVD) method. Figure 6-19a shows the type I tBN growth, i.e., tBN grows with its (0002) planes perpendicular to the substrate surface. The edges of its (0002) planes are

exposed to the growth direction. A structural model is built for this type of tBN growth using a $B_{18}N_{18}$ cluster. The edges of the tBN (0002) planes are not saturated by hydrogen in order to serve as further reaction sites (Figure 6-19b). In experimental observations, the tBN (0002) planes may not be perfectly normal to the substrate surface; some of them are tilted at certain angles. Type I tBN growth mode represents all these possibilities as long as the edges of the tBN (0002) planes are exposed along the growth direction, these can serve as further reaction sites. Type II tBN growth is shown in Figure 6-20a. The tBN (0002) planes are parallel to the substrate surface; no edge is exposed to the film growth direction. A structural model of this type of tBN growth is shown in Figure 6-20b, the BN cluster used is $B_{18}N_{18}H_{16}$; the edges of the tBN (0002) planes are saturated by hydrogen in order to maintain a stable configuration.

Type (III) tBN growth is quite different from the previous two. The (0002) tBN planes do not have fixed orientations, but are randomized in different directions. Figure 6-21a and 6-22a show the curved tBN (0002) planes with small and large curvatures, respectively. The curved planes are exposed to the growth direction. Corresponding structural models are $B_{18}N_{18}H_{16}$ and $B_{14}N_{14}H_{12}$ as shown in figure 6-21b and 6-22b, respectively. Similar results have been obtained from BN films deposited by dc plasma jet using a mixture of BF_3, H_2 and Ar [Zhang et al., 2000], which is mainly a chemical vapor deposition (CVD) method. These indicate that the three types of tBN growth is a general phenomenon.

6.4.2.2 Theoretical Approaches

It is known that the overlap between the highest occupied molecular orbital (HOMO) of one molecule and the lowest unoccupied molecular orbital (LUMO) of another (also known as electron delocalization) would determine the nature of chemical reactions between the two molecules [Hoffmann, 1988]. The energy difference between the HOMO of the electron donor and the LUMO of the electron acceptor is referred as the HOMO-LUMO difference of the reacting system. A small HOMO-LUMO difference indicates a favorable reaction. In this work, the frontier orbitals of different reactants are determined using the Hartree-Fock (HF) approach. Such an approach has been successfully applied to the studies of silicon substrate pretreatment for cBN deposition [Zhang et al., 2000], the selectivity of hydrogen etching in diamond and boron nitride deposition [Zhang et al., 2000], and the formation mechanism of silicon nanostructures [Zhang et al., 2001].

6.4.2.3 Reactivity of tBN with different microstructures

The reactivity of different tBN environments for further reactions can be analyzed by comparing the HOMO-LUMO energy difference of the tBN and the reactant in the gas atmosphere (Figure 6-23). In the case of B, which is normally treated as an electron acceptor, the energy difference is obtained by comparing the HOMO level of B and the LUMO level of tBN. As N is usually treated as electron donor, the energy difference is thus obtained by comparing the LUMO level of N and the HOMO level of tBN. For the same reactant (B and N in the gas atmosphere), the type of tBN with the lowest LUMO (react with B) and the highest HOMO (react with N) levels would be the most reactive one. Calculations show that type I tBN is the most reactive, and type II tBN the least

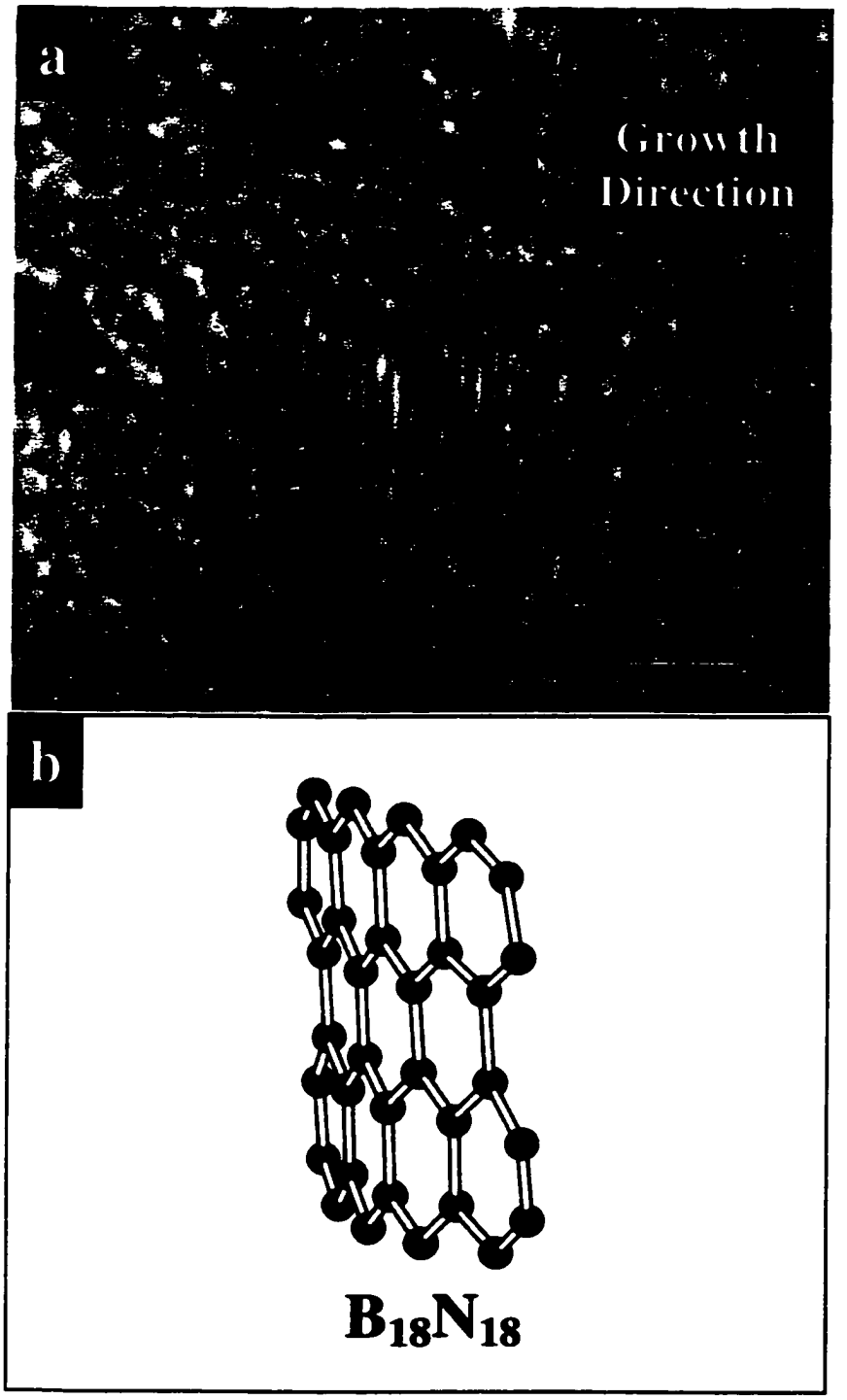

Figure 6-19 (a) High-resolution TEM image of type I tBN growth. (b) Corresponding structural model of tBN shown in (a).

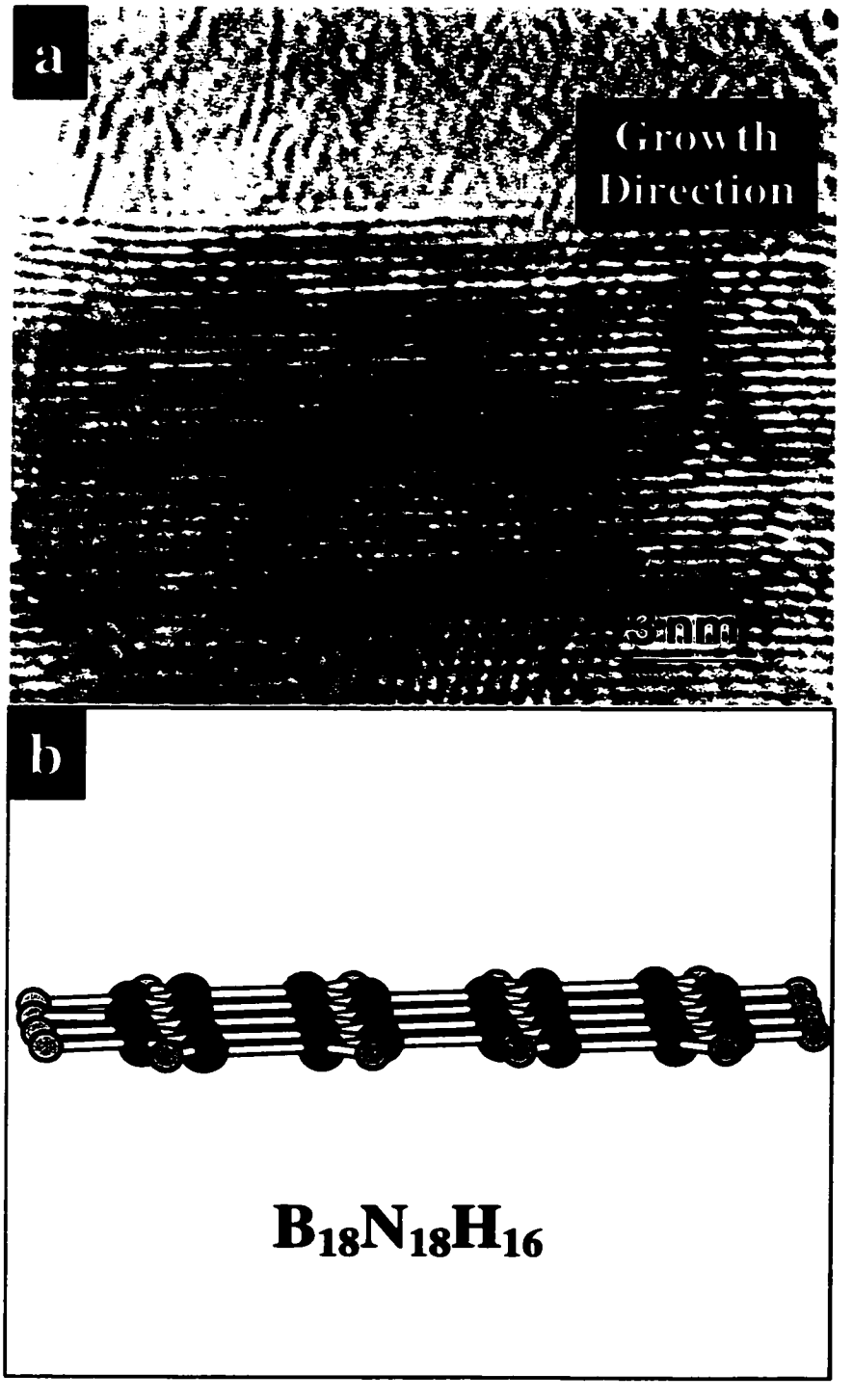

Figure 6-20 (a) High-resolution TEM image of type II tBN growth. (b) Corresponding structural model of tBN shown in (a).

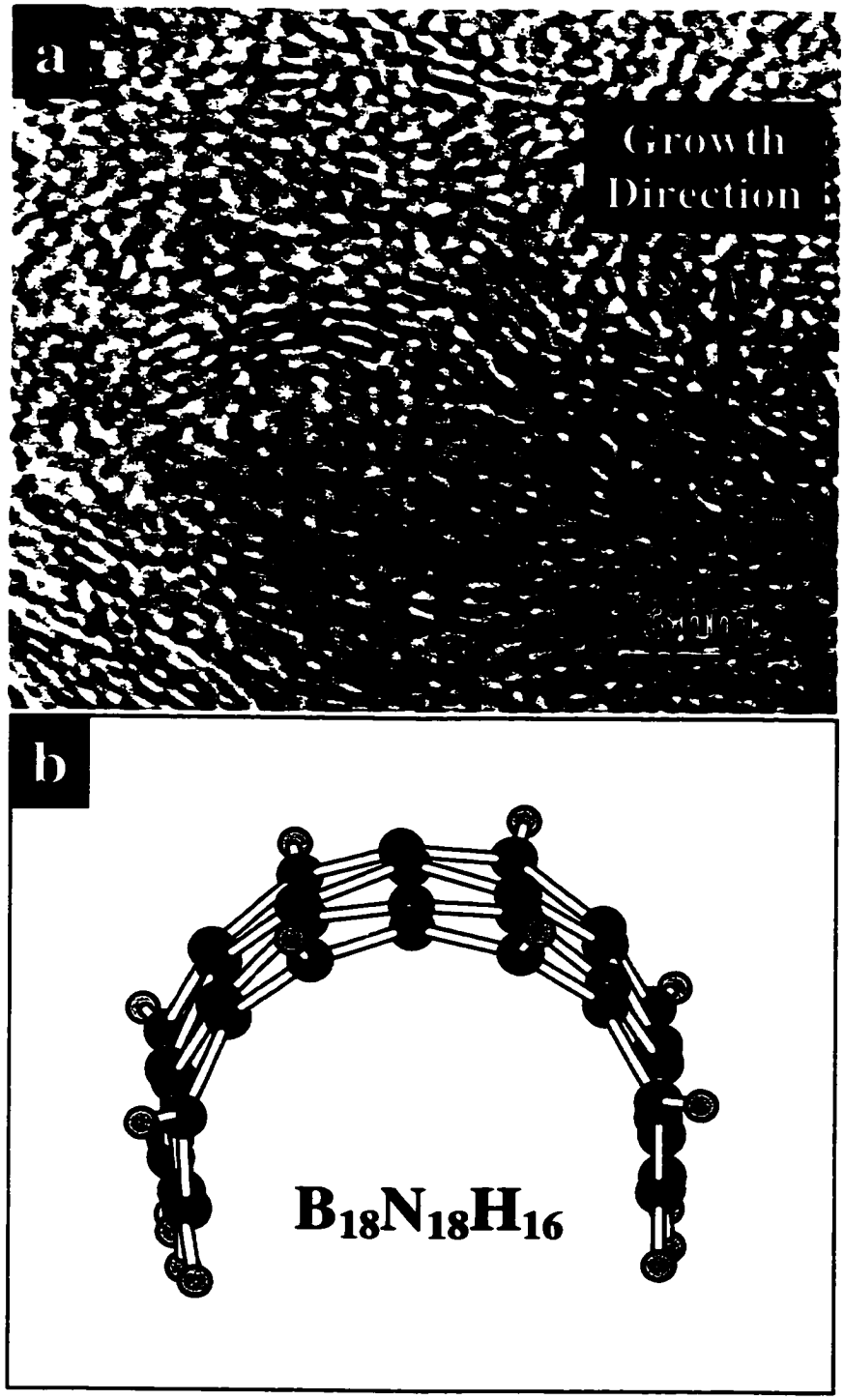

Figure 6-21 (a) High-resolution TEM image of type III tBN growth with its (0002) planes forming large curvatures. (b) Corresponding structural model of tBN shown in (a).

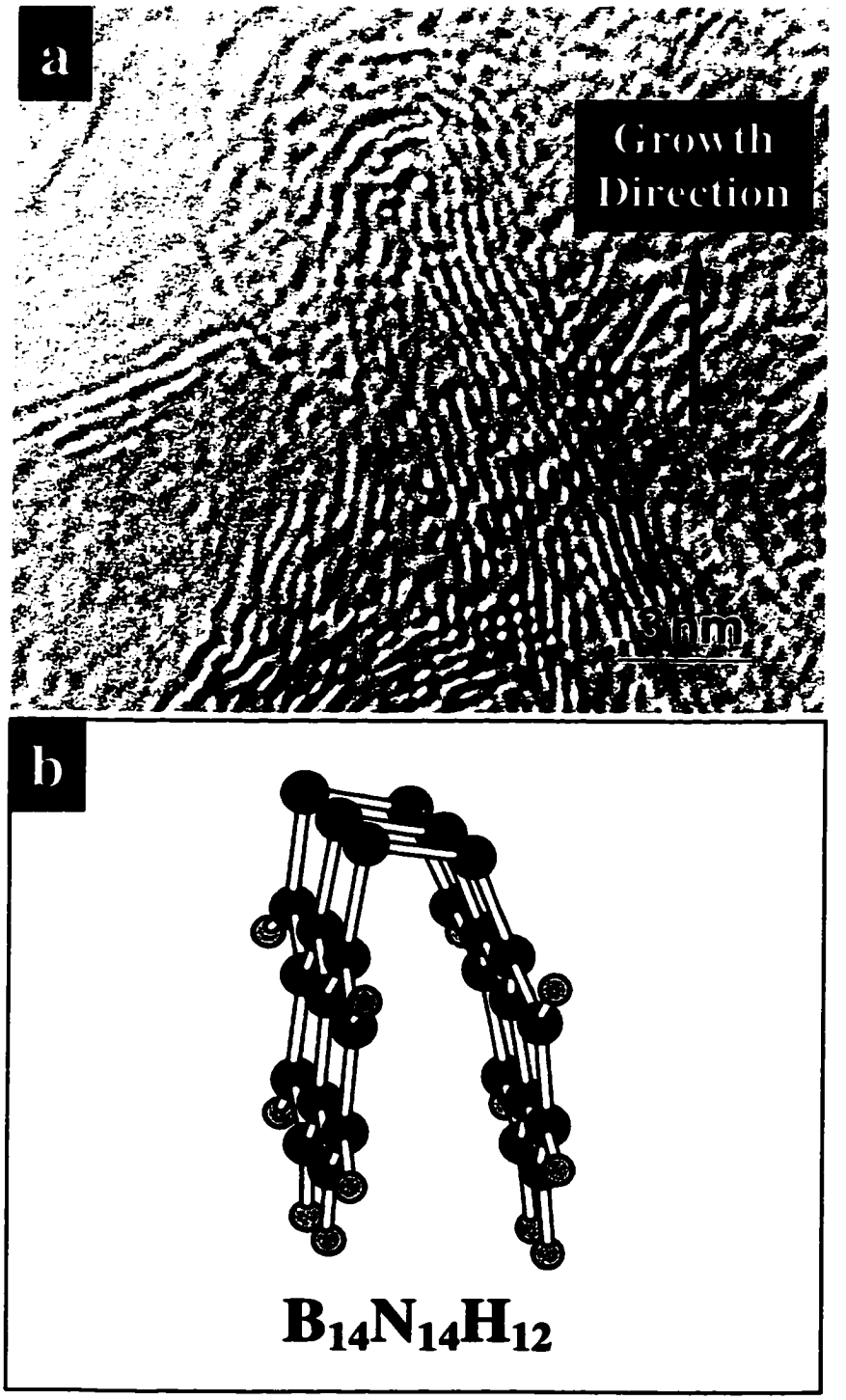

Figure 6-22 (a) High-resolution TEM image of type I tBN growth with its (0002) planes forming small curvatures. (b) Corresponding structural model of tBN shown in (a).

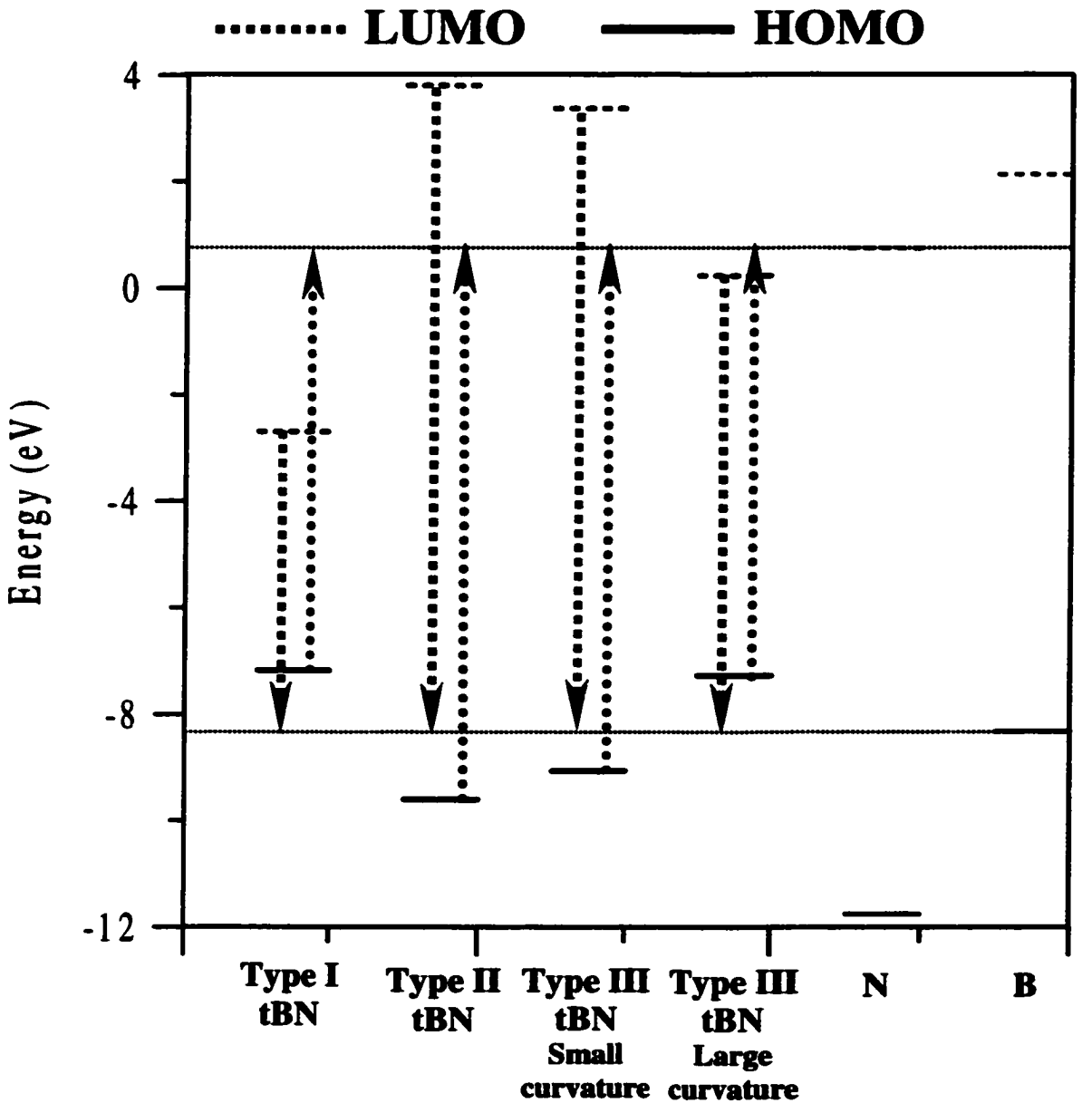

Figure 6-23 HOMO (solid lines) and LUMO (dashed lines) energy levels of different tBN environments (thick lines) and the energy levels of B and N atoms (thin lines).

during BN film growth. The reactivity of type III tBN with large curvatures of its (0002) planes is more reactive than the ones with small curvatures, but still less reactive than that of type I tBN.

The calculations are in good accord with the experimental observations. Type I tBN growth is dominant in BN films deposited with intensive bombardment of energetic species, and associates with high internal stress. The layer thickness of tBN associated with type I growth is small, usually in the range of 5-30 nm. This type of tBN growth has been widely observed to serve as cBN nucleation site in most of the cBN films studied. The edges of the tBN (0002) planes are always aligned to the film growth direction. These edges are in an extremely unsaturated state, thus become very active in further reactions.

BN films deposited with intensive ion-bombardment contain nearly no type II tBN growth, while some type II tBN growth is found in samples deposited with less ion-bombardment in the current study. Type II tBN is the most inert one according to the calculation. In fact, type II tBN growth has not been specifically discussed in previous literatures of cBN films deposition and has never been reported to serve as cBN nucleation sites. Possible explanation is that the chemical bonds of this type of tBN are fully saturated in the sp^2 configuration, leave little chance for further reactions. In other words, further chemical bonding formations on the flat tBN (0002) planes require breaking the existed bonding, thus create higher energy barriers.

Type III tBN growth is observed for samples deposited with medium and low ion bombardment. The amount of this type of tBN increases as the ion bombardment

decreases. The layer thickness associated with this type of tBN growth is usually thick (over 100 nm) compared to that of the type I tBN dominant layer. The curvature of the (0002) tBN planes makes the type III tBN more active than the type II tBN. Collazo-Davila et al. [1997, 2000] found out that the bending of the B-N-B bonds in BN nanoarches led to partially sp^3 hybridized states of the composition atoms, and suggested that these nanoarches may serve as cBN nucleation sites. In fact, the cBN nucleation on the curved tBN (0002) planes has been observed, as described in 6.4.1. Intuitively, the bending of the B-N-B or N-B-N bonds changes the electron distribution of the composition atoms by distorting the planar triangle sp^2 configuration, which makes the B-N bonding deviates from the fully saturated bonding state.

The calculation also indicates that tBN (0002) planes with larger curvature are more reactive than those with smaller curvatures. According to Collazo-Davila et al [1997, 2000]., a 1nm diameter tube consisted of B-N bond would give a B-N-B bending angle about 12° as projected along the tube axis, which is significant fraction of the corresponding value of 54.7° for the projected angle for pure sp^3 bonds. Larger curvature of the (0002) tBN planes would lead to greater B-N bond bending angles, which result in stronger sp^3 character of the bonds, thus have greater possibility to serve as further cBN nucleation sites.

6.4.3. Discussion of cBN Nucleation Mechanisms

Many mechanisms have been proposed to explain the cBN nucleation and growth on tBN in the previous literatures. However, most of mechanisms can only explain some of the experimental results. Indeed, cBN nucleation is a complicated process. Several

factors contribute to the nucleation process. The growth of cBN involves several distinct stages, in each of which different mechanisms occur. These stages include (1) aBN formation, (2) tBN formation, (3) cBN nucleation, (4) cBN growth (and re-nucleation).

For BN film deposited at substrate bias, the transition from the first to the second stage of the growth may be explained by two ways: (i) the stress model, (ii) the preferential displacement model. The stress argument claims that the preferred orientation in the tBN layer is considered to result from the compressive stress induced by the ion bombardment. McKenzie et al. [1994] consider the thermodynamics of the system and find that the preferred orientation with the tBN basal planes arranged in the mist compressible way (c axis parallel to the surface along the biaxial stress direction) has the lowest Gibbs free energy. Cardinale et al. [1994] claim that the plastic deformation of the BN, rather than the minimum elastic strain energy contributes to the observed orientation of the tBN basal planes, as their energy calculation shows that the most favorable orientation would be a 45° tilt of the tBN basal planes from the substrate surface. Lifshitz et al. [1987, 1990] suggested an alternative explanation for the ion-induced orientation of carbon films: preferential displacement of atoms in the direction perpendicular to the basal planes (C-C bond energy ~0.8 eV) with respect to the displacements in the plane (bond energy 7.4 eV). It is interesting to point out that Kulik, Lifshitz et al. [2000] indeed found a compression in oriented graphitic layers grown at elevated substrate temperatures (the spacing between the planes is smaller by 5% with respect to graphite), in accord with a stress induced mechanism. For BN films deposited at lower bias (lower ion energy), the formation of curled tBN planes with random

orientation maybe due to a smaller displacement or reorganization to the minimal Gibbs free energy state (as suggested by Cardinale et al. [1994]). However, in both cases it is unclear whether the significant stress observed in the films already exists in the tBN layer or only evolves later in the subsequent cBN layer.

Until now only the formation of the tBN layer has been dealt with. The next growth stage of our films is the nucleation of cBN crystallites on the top of tBN layers. In the high bias case, experimental observation suggests that the edges of the (0002) planes provide nucleation sites for the formation of the cubic phase. The orientation relation between the two is associated with the local geometrical similarity and the close 2:3 match between the tBN (0002) spacing (3.33Å) and the cBN (111) spacing (2.06Å). Lambrecht et al [1993] showed that the interface between the cBN (cubic diamond) crystallites and hBN (graphite) with that specific geometric configuration is energetically favorable. Both the matching of the tBN (0002) and cBN (111) layers and the energetically favorable configuration of the interface between those layers indicate that tBN can serve as a nucleation site for cBN growth. In the lower bias case, another type of nucleation site, i.e. curved (0002) planes, is observed in the present work. It is generally understood that planar tBN (0002) planes do not allow cBN nucleation, as explained in 6.4.2.3. The bending of the tBN planes changes the electron distribution outside the atomic shell, and makes it possible to serve as a nucleation site for the cubic phase.

The next stage is the growth of cBN nuclei on the nucleation sites and the further growth of the cBN films. The conditions necessary for the formation of critical cubic

nuclei (cBN or cubic diamond) on a specific nucleation site are still unclear and the different mechanisms suggested (sputter, stress, thermal spike, subplantation) are still speculative and need further substantiation. The new nucleation environment (curled tBN) leads to a randomly oriented growth of the cBN with respect to the tBN layers or the initial substrate, contrary to the oriented cBN growth on the edge of the tBN (0002) planes. The oriented cBN growth on top of the tBN (0002) plane edges is in accord with the match between these planes. This oriented cBN growth is associated with a significant stress buildup. It is unclear at present whether the oriented growth is stabilized by the stress (similar to the oriented tBN growth) or it is a pure geometrical effect. The stress itself could be resulting from the oriented growth rather than the origin of the oriented growth. The lack of orientation between the curled tBN sites and the cBN sites may be the result of the lack of a geometrical match between the tBN and cBN for this new nucleation environment allowing a non-oriented cBN growth. The association of the stress buildup to the oriented cBN growth rather than the ion impact indicates that the non-oriented cBN growth would lead to low stress levels if any.

The gradual change of the bias during BN growth enabled the control of the relative amount of the two types of nucleation (type A – (0002) tBN plane edges, type B– curled (0002) tBN planes) within the range of ~0-30% relative amount of type B. The experimental evidence presented in table 6-2 suggests that the stress buildup in cBN films is associated with the growth of oriented cBN layers on the oriented (0002) tBN edges. Reduction of the amount of type A cBN decreases the stress generated in the films so that thicker cBN films can be deposited without delamination. Until now the films deposited

in the current work contains a mixture of cBN crystallites grown on the two type of nucleation sites with a maximal fraction of the second type of ~30%. This means that the films still contain a significant amount of stress originating from the large component of type A cBN. The fraction of type B nucleation indeed increases as the substrate bias drops. Although a thicker tBN layer growth is associated with the bias decrease, the cBN layer on top of it remains ~100% pure, thus guarantee the film quality.

The experimental observations together with the reactivity calculation suggest that other than the energy and momentum needed for the cBN nucleation, the availability of possible nucleation sites with high reactivity can be an important factor as well. Due to the fact that type III tBN environment has great possibility to serve as further reaction site, and the existence of type B cBN nucleation, it is reasonable to assume that by optimizing the deposition conditions to acquire only the type B cBN crystallites, we may remove the stress generated in cBN layers and be able to deposit thick cBN films.

6.5 Possible cBN Nucleation and Growth at Reduced Stress Levels---a Promising Future

One major source of the compressive stress is generally understood as ion bombardment during the deposition process. The ion energy is mainly responsible for the compressive stress build-up in the films. However, in the case of magnetron sputtering, two other types of particle bombardment contribute to the stress built-up as well. The first source of particle bombarding a growing film surface is back-scattered atoms. If the atomic mass of the sputtering gas and the mass of the target material differs much, back-scattered gas atoms will bombard the film. The second source is sputtered particles

themselves, which are ejected from the target with average energies of the order of 20-40 eV [Thompson, 1968]. This may result in energies high enough to create compressive stress in the film. Therefore, conventional magnetron sputter deposition may not be an ideal method to obtain low stress or stress-free cBN films.

On the other hand, ion bombardment is needed for cBN formation. Both the literature and the current study indicate that a certain threshold of the ion energy exists to enable cBN nucleation. Nevertheless, deposition operated at high ion-to-atom ratio may compensate for the low ion energy. Therefore, the preferable system for thick cBN deposition should be able to provide large ion to atom ratio value at relatively low ion energy.

Direct ion beam deposition, especially mass selected ion beam is one choice, as it can provide finely controlled ion mass, ion energy, ion dose, ion incident angle etc. with narrow distributions. The fact that all these parameters can be varied independently makes it simple to study the effects of individual deposition parameters. In fact, Hoffsass et al. [1997] have successfully synthesized nearly pure cBN using the mass selected ion beam deposition. However, the films still suffer from delamination at larger thickness.

Another choice is a CVD method—dc plasma jet [Zhang and Matsumoto, 2000, 2001]. They used mixtures of BF_3, H_2 and Ar as the reactive gases and synthesized high purity cBN at ~1200C substrate temperature with low substrate bias (-50V). They were able to produce cBN films (over 90% cubic phase purity) up to 10 microns without delamination. The internal stress of films is as low as 1.5 GPa. According to Matsumoto [2001, ICMCTF], the tBN environment prior to cBN nucleation is similar to type III tBN

growth, as described in 6.4.2.3 (Figure 6-24). However, due to the difficulty of making TEM sample good enough for large area high-resolution study, the nucleation relationship between the cBN and tBN was not obtained.

6.5.1. Evidence of Thick cBN Film Growth

Figure 6-25 shows a bright field image of a BN film deposited by Zhang et al. [2000] as described above, deposited using a two-step method, i.e. using –50V substrate bias in the first half of the deposition, and –30V bias in the second half of the deposition. The Film is ~5 micron thick, well adhered to the silicon substrate (The lacking of any Si substrate in TEM image is due to the sample preparation process). The TEM image shows columned growth of the film. The sudden enlargement of the column lateral size can be explained by the change of substrate bias [Zhang et al., 2001].

6.5.2. Large cBN Crystal Size

The grain size of cBN crystallites by this deposition method is large compared to those in the literature. Figure 6-26 shows a low magnification plan-view TEM image taken from cBN sample deposited with a constant substrate bias of –50V. The average gain size in this sample is in the range of ~200 nm. However, as shown in Figure 6-25, the cBN film deposited using two-step method has grain size as large as 1 micron. In side each grain, stacking faults or twins as always observed. (Figure 6-27).

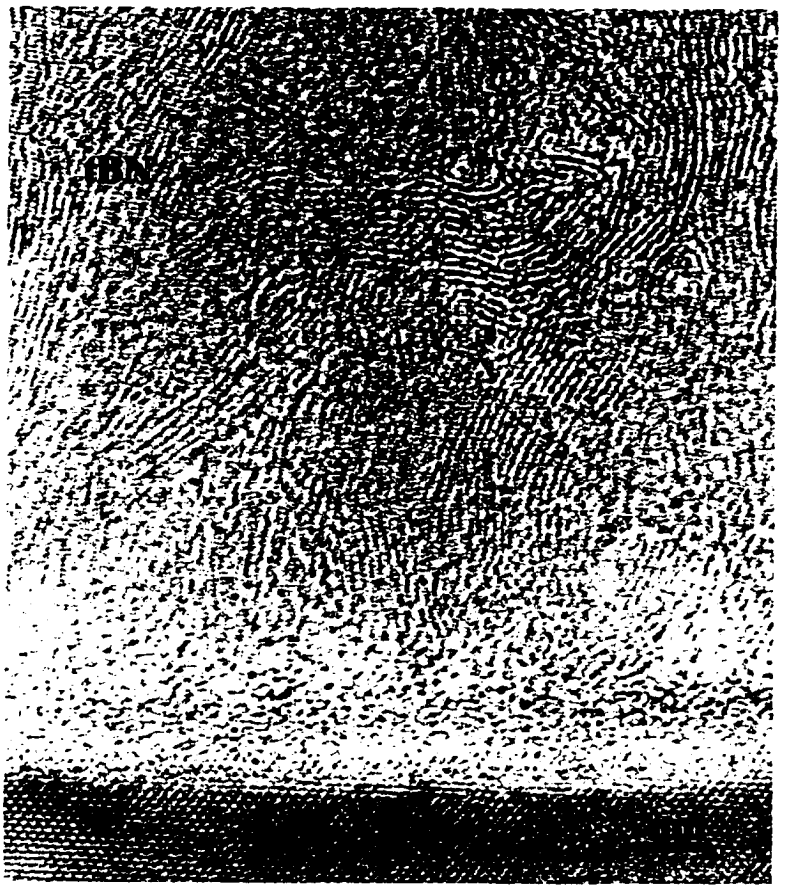

Figure 6-24 High-resolution image of BN sample deposited using dc plasma jet, showing the tBN layer growth prior to the cBN layer. (Courtesy from Matsumoto et al.)

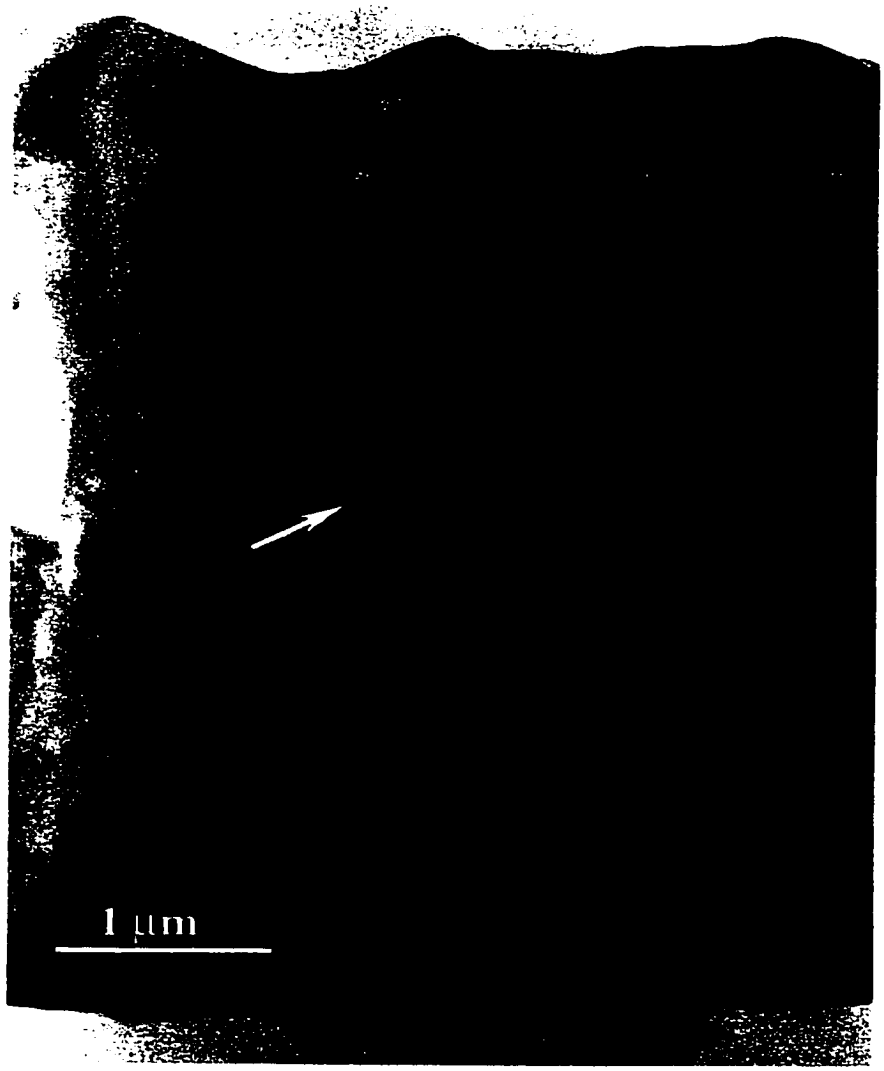

Figure 6-25 Bright field XTEM image taken from a ~5 micron thick cBN film. The film exhibits a column growth. The lateral size of the column near the film surface is about 1 micron

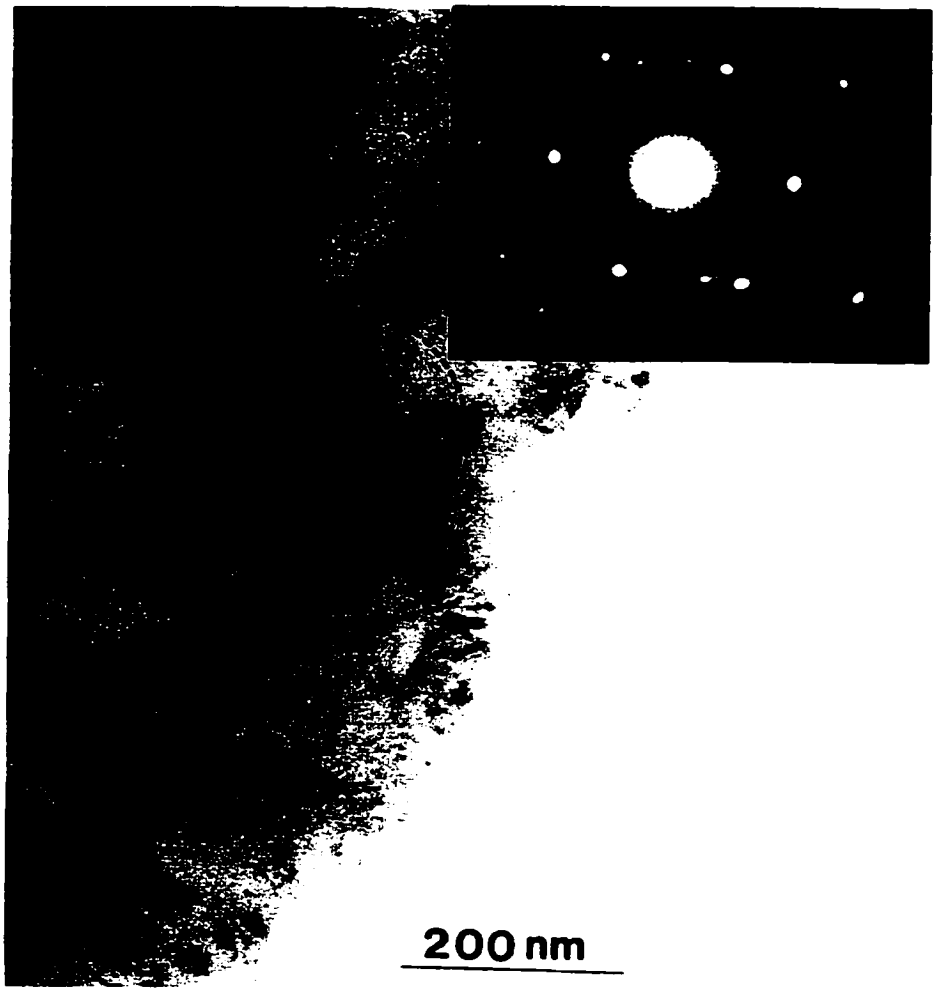

Figure 6-26 Bright field plan-view image of cBN film. The size of the cBN crystal is about 200nm. SAD pattern taken from the circled area indicated that it is a single crystal.

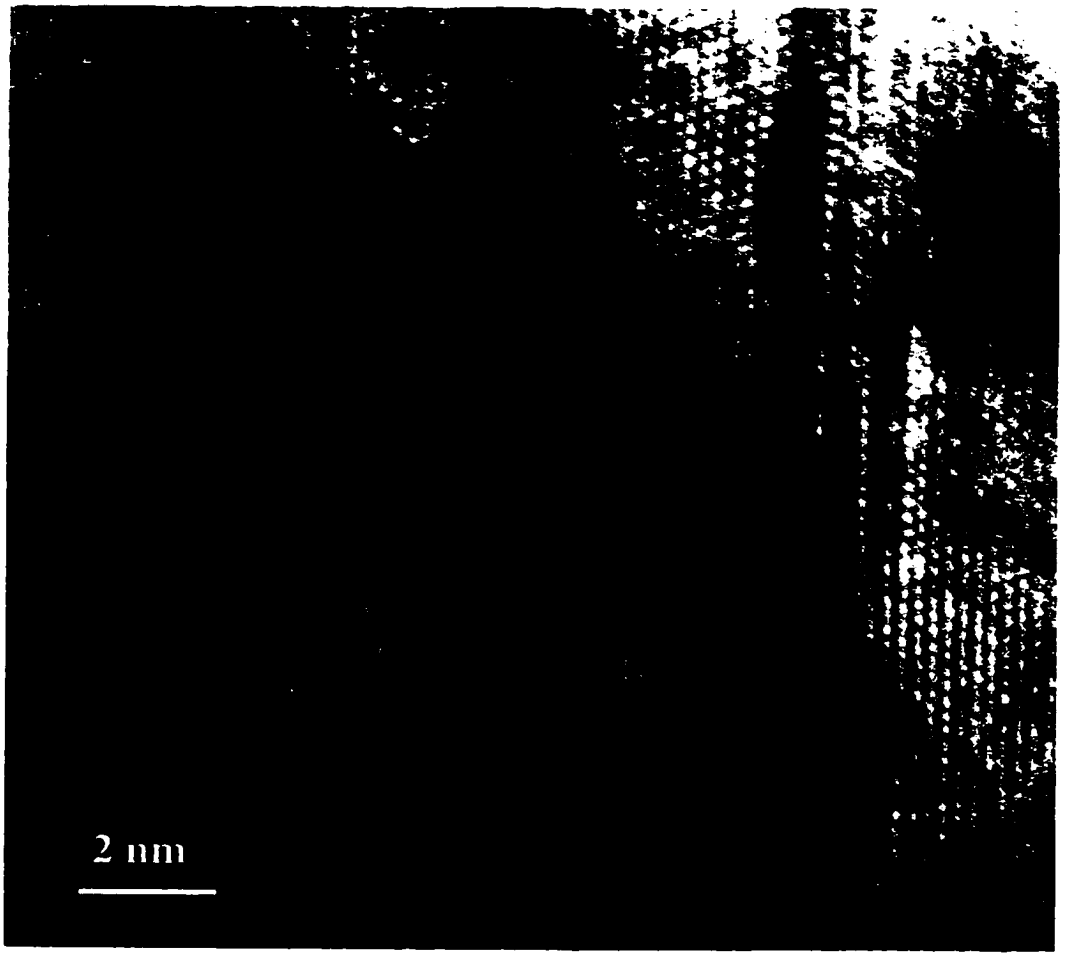

Figure 6-27 HREM image taken from the top region of cBN crystal shown in Figure 6-24 with electron beam along the crystal [110] zone axis. A fairly intact cubic structure is shown with some stacking faults and twins.

6.6 Conclusions

BN films containing cubic phase were synthesized using conventional rf magnetron sputter deposition. The cubic phase formation is sensitive to the deposition parameters, including pre-deposition vacuum, substrate temperature, substrate bias and the separation distance between the target and the substrate. Ion bombardment plays an important role in the cBN nucleation and growth process. Sharp threshold exists for the cubic phase formation in terms of ion mass, ion energy, ion flux and deposition flux.

All BN films containing the cubic phase follow a layered growth sequence, i.e., amorphous BN is first grown on the substrate, followed a layer of tBN, after which the cBN starts to nucleate and grow. Three types of tBN growth are observed in cBN film growth. The tBN (0002) planes are perpendicular to the substrate surface in type I tBN growth, and parallel to the substrate surface in type II tBN growth. Type III tBN is characterized by curved (0002) planes with different curvature radius in random directions. Theoretical study using frontier orbital theory based on ab initio Hartree-Fock calculations shows that type I tBN is the most reactive environment for further reactions, and type II tBN the least. The reactivity of type III tBN with large curvatures of its (0002) planes is more reactive than the ones with small curvatures.

Different types of tBN growth create different nucleation environments for the cubic phase. Under high substrate bias conditions, type I tBN growth is most commonly observed in the BN films. cBN nucleates on the edges of the tBN (0002) planes and further grows with its (111) planes parallel to the tBN (0002) planes. This type of tBN and associated cBN growth results in large internal stress in the films. Under relatively

low bias conditions, all three types of tBN growth are observed. Type II tBN growth is never observed to serve as the cBN nucleation site. However, type III tBN serves as a different nucleation environment for cBN, i.e., cBN nucleates on the curved planes of tBN and further grow without any specific orientation to the tBN, contrary to the cBN nucleation and oriented growth on type I tBN. Non-oriented growth of tBN and cBN results in low stress levels and thus facilitates the production of thicker films. These tBN/cBN environments can be controlled and varied by changing the substrate bias during film deposition. Recently, Matsumoto's group in Japan demonstrates thick cBN film growth without delamination using dc plasma jet. TEM characterization of their samples shows that cBN films up to 10 μm can be deposited onto the silicon substrate without delamination. The films exhibit columnar growth, and the largest grain size of the cBN crystal is ~1 μm. According to Matsumoto's work, the tBN environment prior to cBN nucleation is similar to the type III tBN growth presented in this study, which strongly supports the "low-stress level nucleation of cBN" argument.

CHAPTER 7. EPITAXIAL NUCLEATION OF DIAMOND ON SILICON

7.1 Synthesis of Diamond and Its Nucleation Mechanisms

Diamond and cubic born nitride have a lot in common. Their similar structures result in similar chemical and physical properties, including high hardness, high thermal conductivity, etc. Both of them are not easy to grow at room temperature and pressure, and the common methods to obtain these materials in bulk form require high temperature/high pressure techniques. Chapter 6 has demonstrated that cBN films can be synthesized using the PVD method—ion-assisted (biasing) magnetron sputtering, in which ion-bombardment plays an important role in cBN formation. However, PVD methods to synthesize diamond are not very satisfying. Instead, chemical vapor deposition of diamond can be done routinely and is well developed. Nevertheless, the initial stage of diamond growth (nucleation) is not well understood. Bias-enhanced nucleation (BEN) [Yugo et al., 1991] has been the most common process to nucleate diamond on non-diamond substrates for years, simply due to its capability of achieving a high nucleation density ($\sim 10^{11}/cm^2$), and oriented diamond films after further CVD growth under appropriate conditions [Stoner et al., 1992; Jiang et al., 1992; Yang et al, 1994; Stubhan et al, 1995].

Different mechanisms have been proposed to explain the bias-enhanced nucleation process. Lifshitz et al. [1991] have suggested that subplantation of C-containing species into subsurface sites forms a stress-induced sp^3 cluster, which serves as a precursor to the diamond nucleus formation. Lambrecht et al. [1993] have proposed that oriented graphite planes, which are created during the BEN process, may serve as

nucleation sites, due to the geometrical similarities between the graphite (0001) planes and the diamond (111) planes. Other models include the formation of diamond nuclei in an epitaxial SiC layer deposited on Si [Stockel et al., 1997], and the induction of plasma chemistry changes by biasing [Stockel et al., 1997]. Most recently, Lee et al. [2000] have observed the heteroepitaxial nucleation of diamond on a silicon step using BEN by a hot filament CVD process. A "surface step confinement" effect has been proposed to explain the good epitaxial relationship between the diamond nuclei and silicon.

In spite of all previous studies, the BEN process remains complicated to be thoroughly understood, as it involves not only ion-solid interaction, but plasma chemistry as well. Moreover, the BEN process is very sensitive and difficult to achieve quality diamond films. As indicated in both Chapter 5 and 6, ion-bombardment is important in obtaining metastable phases. One attempt to simplify the diamond nucleation process is to exclude the plasma surface chemistry and focus on the ion-solid interaction. This can be realized by direct ion beam deposition. The present study in this chapter shows that direct ion beam deposition using a Kaufman gas ion source is capable of nucleating diamond. Heteroepitaxial diamond nucleation on silicon can be achieved under appropriate conditions. Acetylene, hydrogen and argon with different ratios are used as the reactive gases to investigate the different ion species/solid interactions and possible reactions. Experimental observations suggest that several competing nucleation mechanisms exist, and the leading mechanism changes as with deposition parameters.

7.2 Diamond Nucleation Using Direct Ion Beam Deposition

Depositions were performed in a high vacuum chamber (Figure 7-1) equipped with a 3 cm diameter Kaufman ion source (3.0-1500-1000, Ion Tech, Inc. USA) facing the substrate holder. The base pressure is ~10^{8} Torr. During deposition, the ion energy and the ion current were maintained at 200eV and 40 mA, respectively. Acetylene, argon and hydrogen were chosen as the reactive gases. A series of films were deposited with C_2H_2/H_2 ratio range from 0.9% to 29%. The gas ratios for the three representative samples were C_2H_2/ Ar / H_2 = (a) 1:30:105 (C_2H_2/H_2 =0.95%), (b) 1:4:14 (C_2H_2/H_2 =7%),) and (c) 1:1:3.5 (C_2H_2/H_2 =29%),), respectively. The total pressure was kept at $5x10^{-4}$ Torr during deposition. Argon was introduced in order to stabilize the ion source. The gas mixtures were decomposed into different ion species inside the ion-source and then accelerated, after which they were directed to the substrate with the incident beam direction along the substrate surface normal. Mirror-polished Si (100) wafers were used as the substrates. They were first ultrasonically cleaned in acetone and methanol, and then etched by 5% hydrofluoric acid to remove the native oxide. The substrate temperature was kept at 700C during deposition. The deposition time for all the samples was 90 minutes.

7.3 Diamond Nucleation at Different Hydrocarbon Concentrations

7.3.1 Processing Gas Effect

Figure 7-2(a)-(c) are SEM images obtained from as-deposited films. Figure 7-2(a) shows a rough film surface. The white spots suggest the existence of strong secondary electron emitters. Film (b) and (c) have similar surface morphology. Clusters

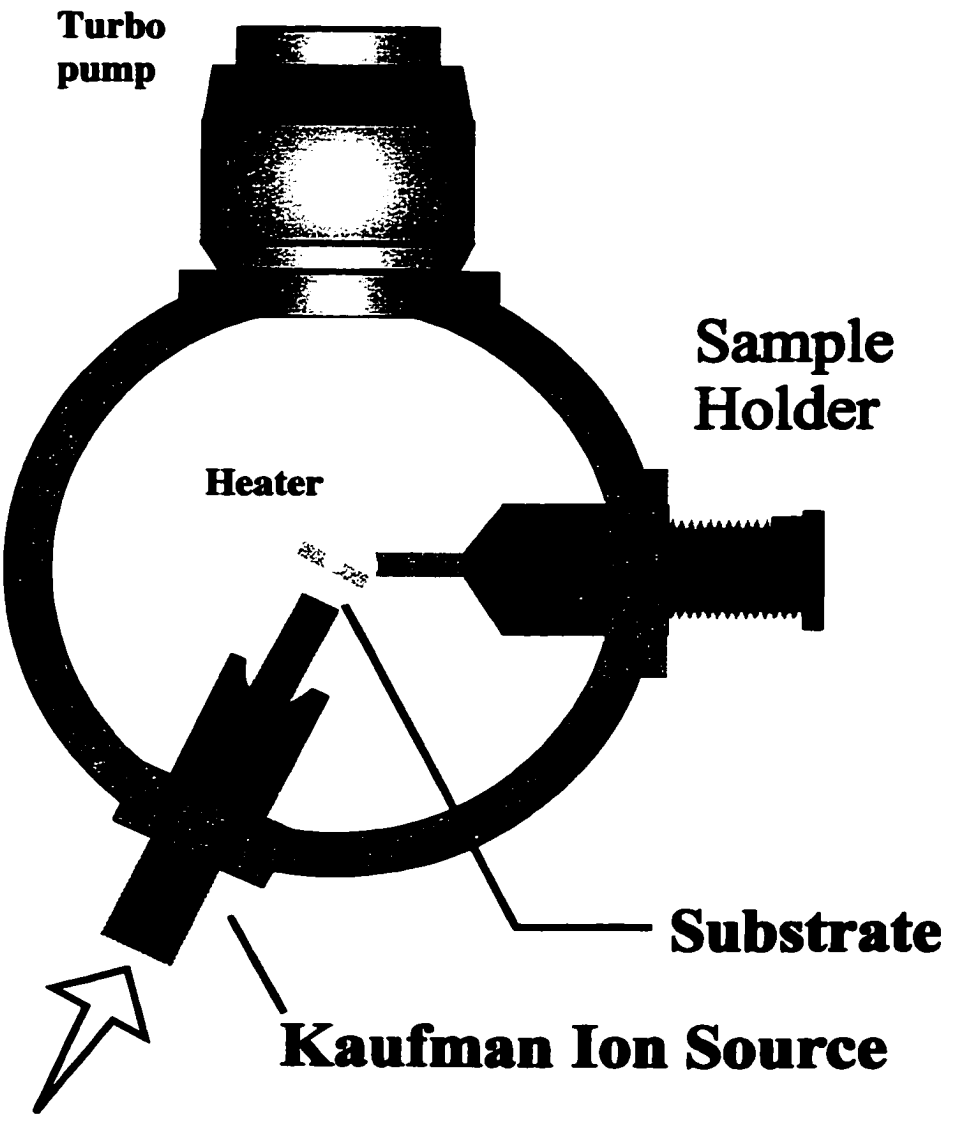

Figure 7-1 Schematic of the ion-beam deposition system for diamond.

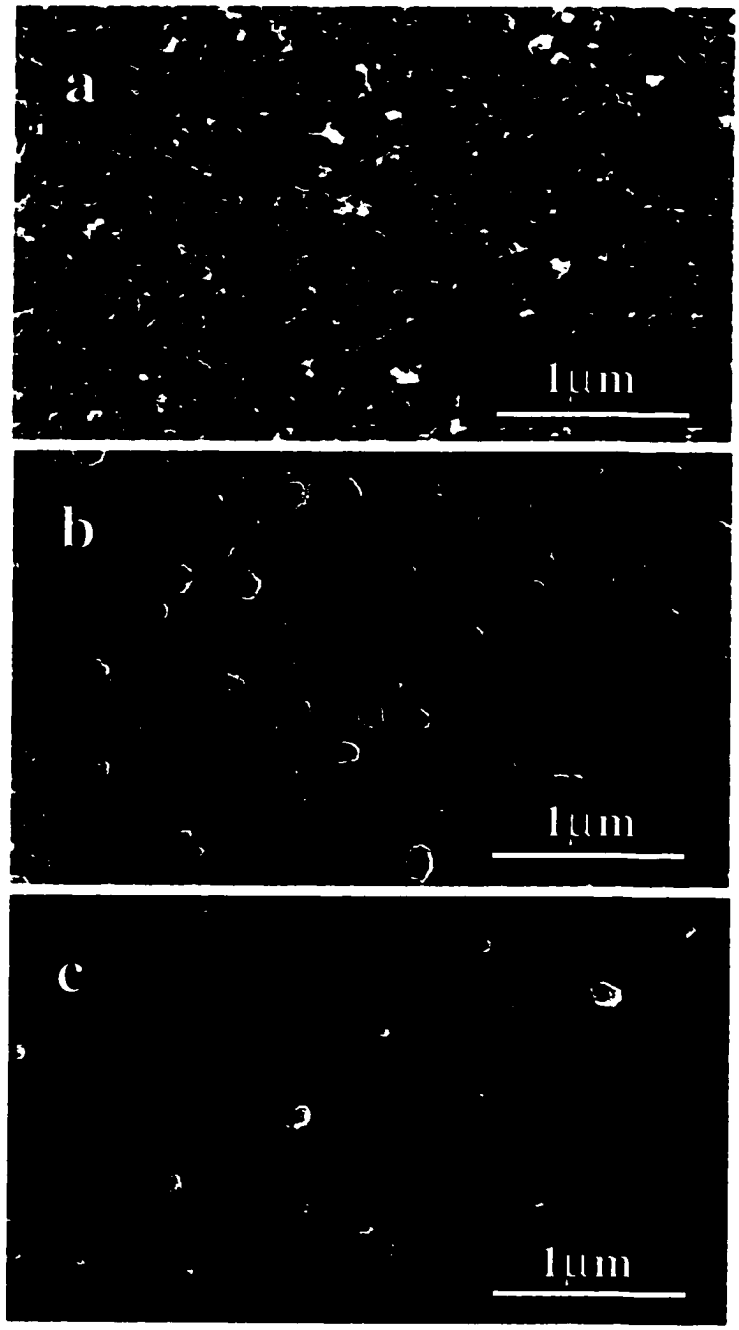

Figure 7-2 SEM images of as-deposited films. . The three films were deposited with 200 eV ion energy, 700C substrate temperature, but different C_2H_2/Ar/H_2 gas ratios: 1:30:105 for film (a), 1:4:14 for film (b) and 1:1:3.5 for film (c).

are embedded in an amorphous-like matrix. The surface of film (b) is much smoother than that of film (a), but rougher compared to that of film (c).

Figure 7-3(a)-(c) are Raman spectra obtained from the three corresponding films. Only two peaks at 820 and 980 are observed for film (a), characteristic of SiC and Si, respectively. A broad signal centered at ~1470 cm^{-1} suggests the existence of amorphous carbon. Dominant peaks at 1358 cm^{-1} and 1558 cm^{-1} are observed for both film (b) and (c). They are characteristic of carbon D band and G band respectively, which reveal the amorphous nature and of film (b) and (c). The Si peak at 980 cm^{-1} is still visible for film (b), but disappears for film (c). This may simply be a result of film (c) being thicker than film (b).

Low magnification TEM bright-field images and transmission electron diffraction (TED) patterns are shown in Figure 7-4. They are listed in the order of a, b and c, corresponding to film (a), (b), and (c), respectively. The silicon surface of film (a) is severely damaged, and hillocks are formed. Particles with size of ~20 nm appear on the slope of the hillocks, showing different contrast from the silicon substrate. These particles are proven to be diamond nuclei later by HREM. The film above the silicon surface appears to be discontinuous, which is consistent with the SEM observation. Electron diffraction from the same region shows three sets of diffraction spots, i.e., from the silicon, SiC, and diamond. A clear epitaxial relationship among silicon, SiC and diamond are suggested by the diffraction pattern. Surface features of film (b) and (c) are similar. Voids are formed in the silicon substrate close to the film/substrate interface,

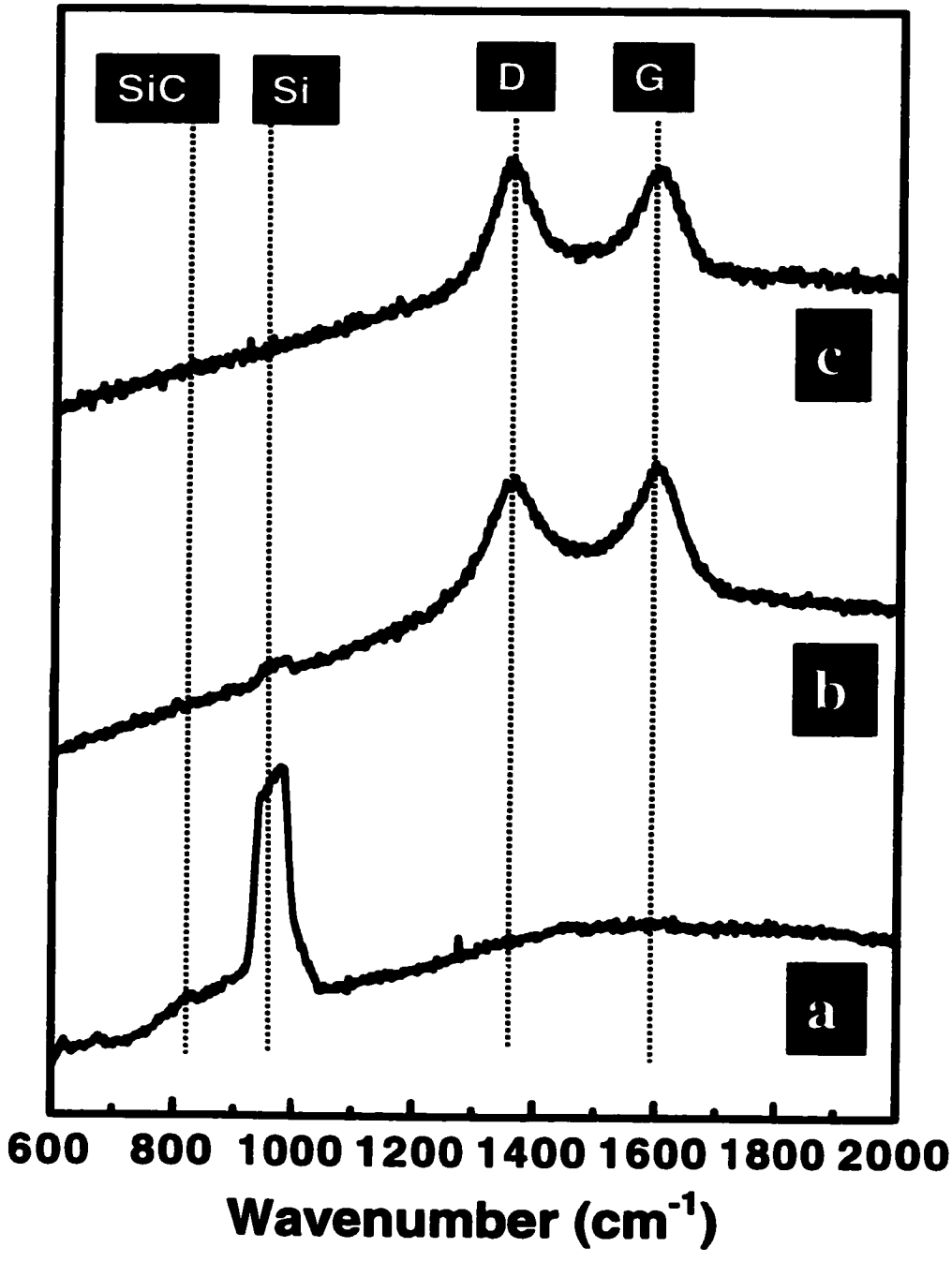

Figure 7-3 Raman spectra obtained from the three films shown in Fig. 7-2.

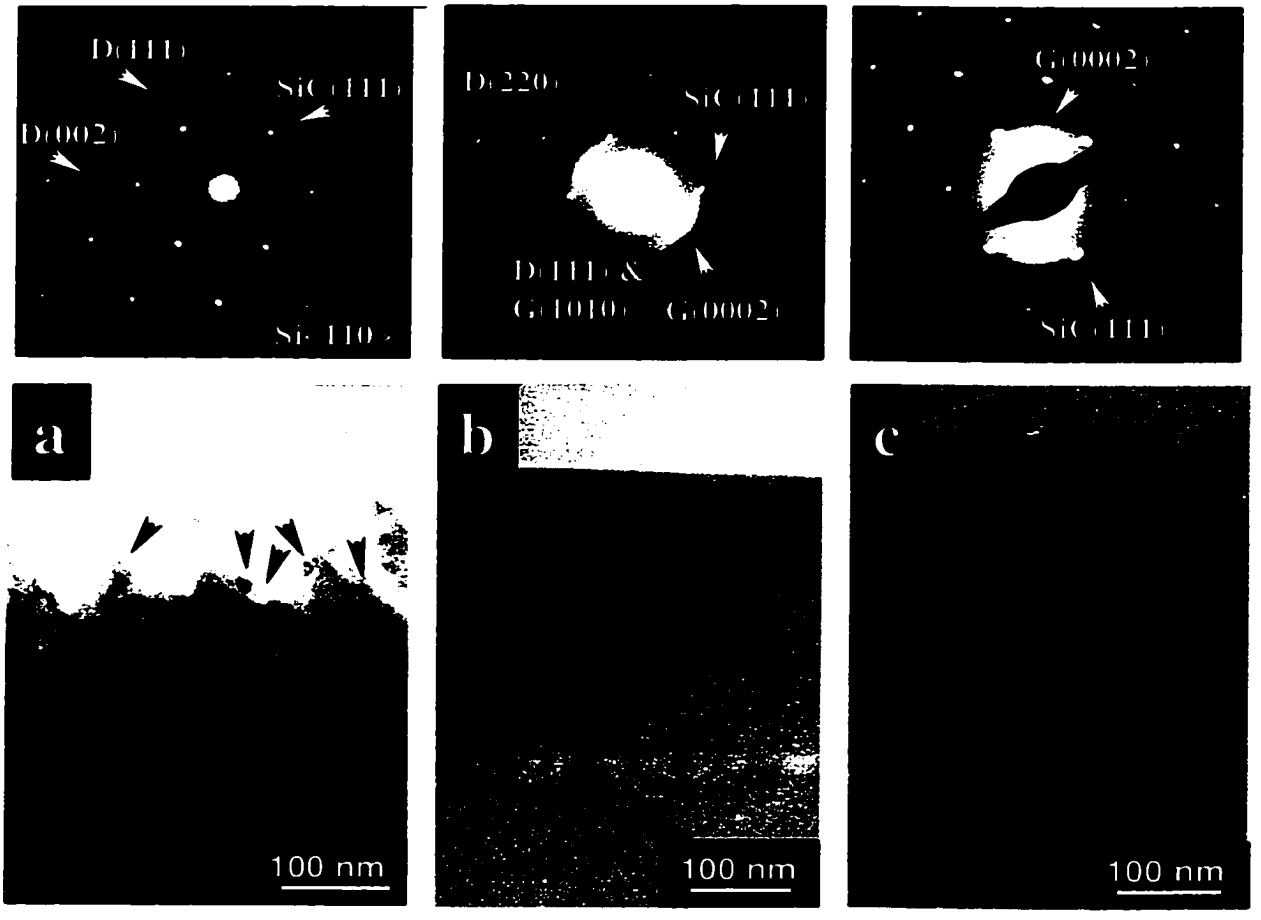

Figure 7-4 Low magnification TEM images and TED patterns of film (a), (b) and (c). The TED patterns are taken with the electron beam along the Si [110] zone axis.

followed by a layer of material showing different contrast from both the main carbon film and the silicon substrate. TED patterns of the two films, however, appear to be different. The one taken from film (b) suggests the existence of four types of materials, i.e., silicon, SiC, graphite and diamond. SiC in both film (b) and (c) appears to have an epitaxial relationship (allowing some orientation spread) with the silicon substrate. The half graphitic rings in the diffraction pattern for both films suggest a preferential orientation of the graphitic planes in the films, i.e., $(001)_{graphite}$ perpendicular to $(001)_{Si}$. Ring patterns in TED (b) indicate the existence of randomly oriented diamond with relatively small crystal size. This is not observed in TED (c). The film thickness increases from (a) to (c), although their deposition times are the same. This is consistent with the Raman result.

The epitaxial relationship between SiC and Si is further confirmed by HREM study. Figure 7-5 is a high-resolution image of film (a) taken at the film/substrate interface with the electron beam along the Si [110] direction. The same epitaxial relationships are observed for all films deposited. Nevertheless, only small patches of SiC are found on the Si hillocks when the acetylene/hydrogen ratio is low. Epitaxial SiC layers appear, and the layer thickness does not increase with the acetylene/hydrogen ratio.

Figure 7-6 is a high-resolution image taken at film (a)/substrate interface. The d-spacing of the particle above the silicon surface is measured to be 2.09 Å, which corresponds to that of diamond. The diamond nucleus grows directly from the silicon substrate, forming excellent epitaxial relationships with the silicon, i.e., $(\bar{1}11)_{Dia}//(\bar{1}11)_{Si}$;

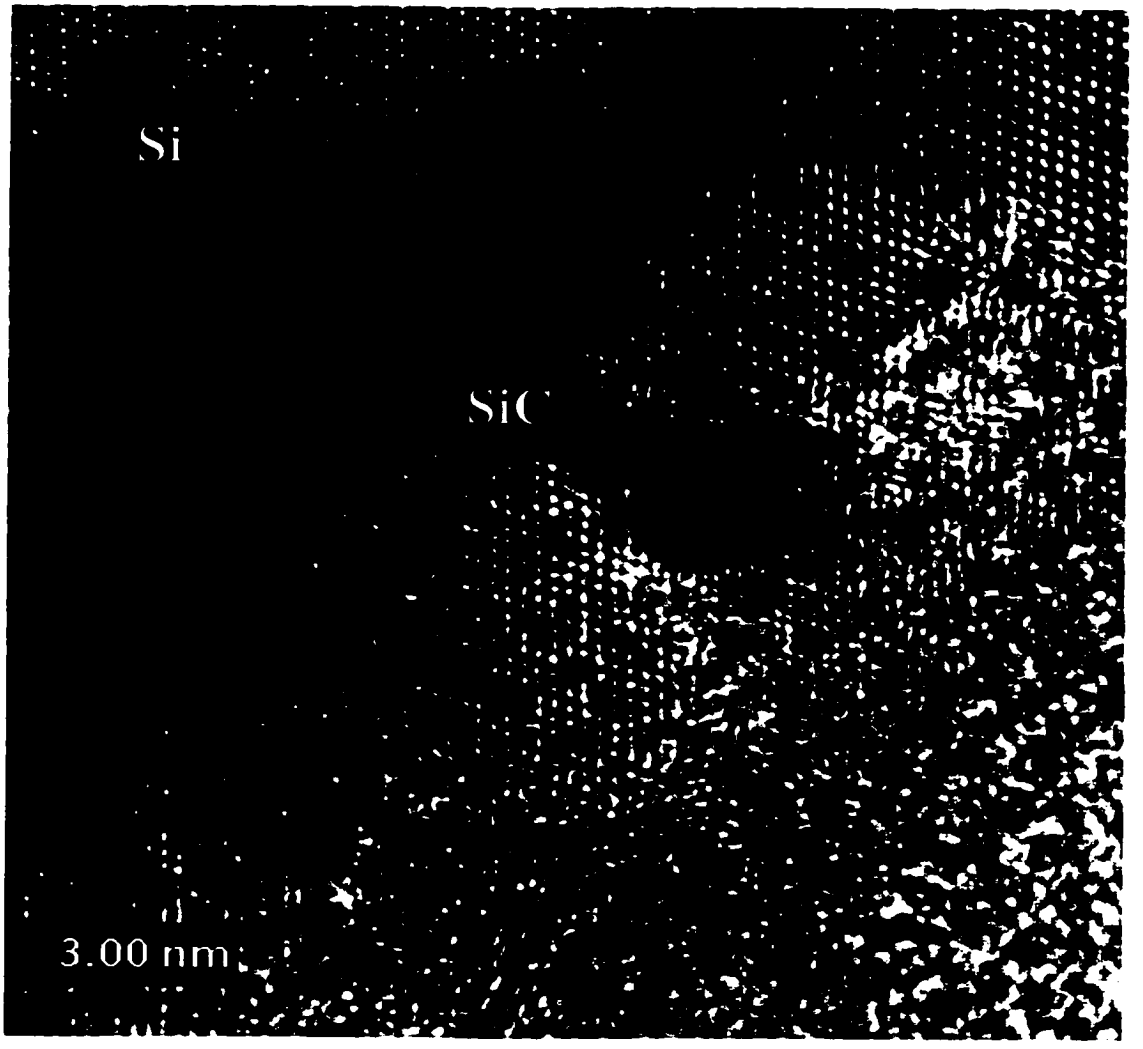

Figure 7-5 A high-resolution image taken at the interface of film (a) and the Si substrate, with electron beam along the Si [110] direction. The SiC particle is observed to be epitaxially grown on Si.

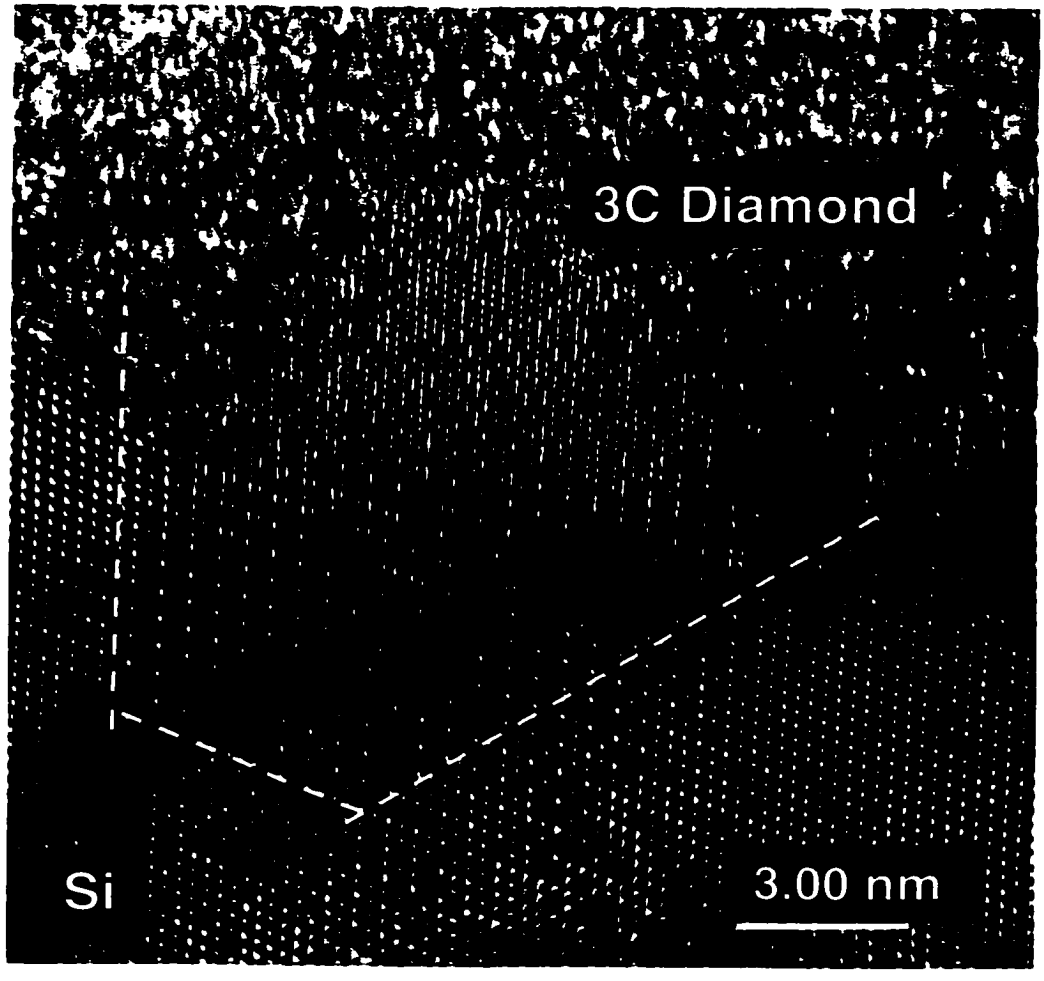

Figure 7-6 A high-resolution image taken at the interface of film (a) and the Si substrate, with electron beam along the Si [110] direction. An epitaxial diamond nucleus is observed on the silicon substrate, with part of the crystallite "buried inside" the Si.

$(1\bar{1}1)_{Dia}//(1\bar{1}1)_{Si}$; and $(002)_{Dia}//(002)_{Si}$. Moiré fringes appear at the film/substrate interface, which is caused by the overlapping of the diamond crystallite and the silicon substrate. There are some diamond nuclei embedded in the discontinuous amorphous carbon film above silicon as well. However, the number of such nuclei is few.

No epitaxially nucleated diamond crystallites is found on silicon in either film (b) or (c). Nevertheless, we observe that diamond particles are embedded in an amorphous carbon matrix with random orientation for film (b) (Figure 7-7). The sizes of the crystallites are in the range of 2-10 nm. This is consistent with the TED result in Figure 3b. No diamond nucleation is found for film (c).

The above data demonstrate that ion beam deposition can nucleate diamond over a large range of acetylene/hydrogen concentrations. However, the nuclei appear to be different. Epitaxial nucleation of diamond on silicon is achieved at low acetylene/hydrogen ratios. Only a few non-epitaxial nuclei exist in the amorphous carbon matrix. As the acetylene/hydrogen ratio increases, epitaxial nucleation of diamond diminishes, and the amount of non-epitaxial diamond nuclei in the amorphous carbon films first increases, then decreases to zero with further increase in the acetylene/hydrogen ratio. The overall trend is similar to that observed in conventional CVD diamond deposition. It is well known that atomic hydrogen or hydrogen ions from hydrogen-rich reactive gases can preferentially etch the non-diamond phase, terminate the carbon dangling bonds with a sp^3 configuration, and stabilize the surface [Angus et al., 1968; Frenklach et al., 1989; Hsu et al., 1988; Saito et al., 1988; Liou et al., 1990]. The carbon species originate from the hydrocarbon gas. They contribute to the formation

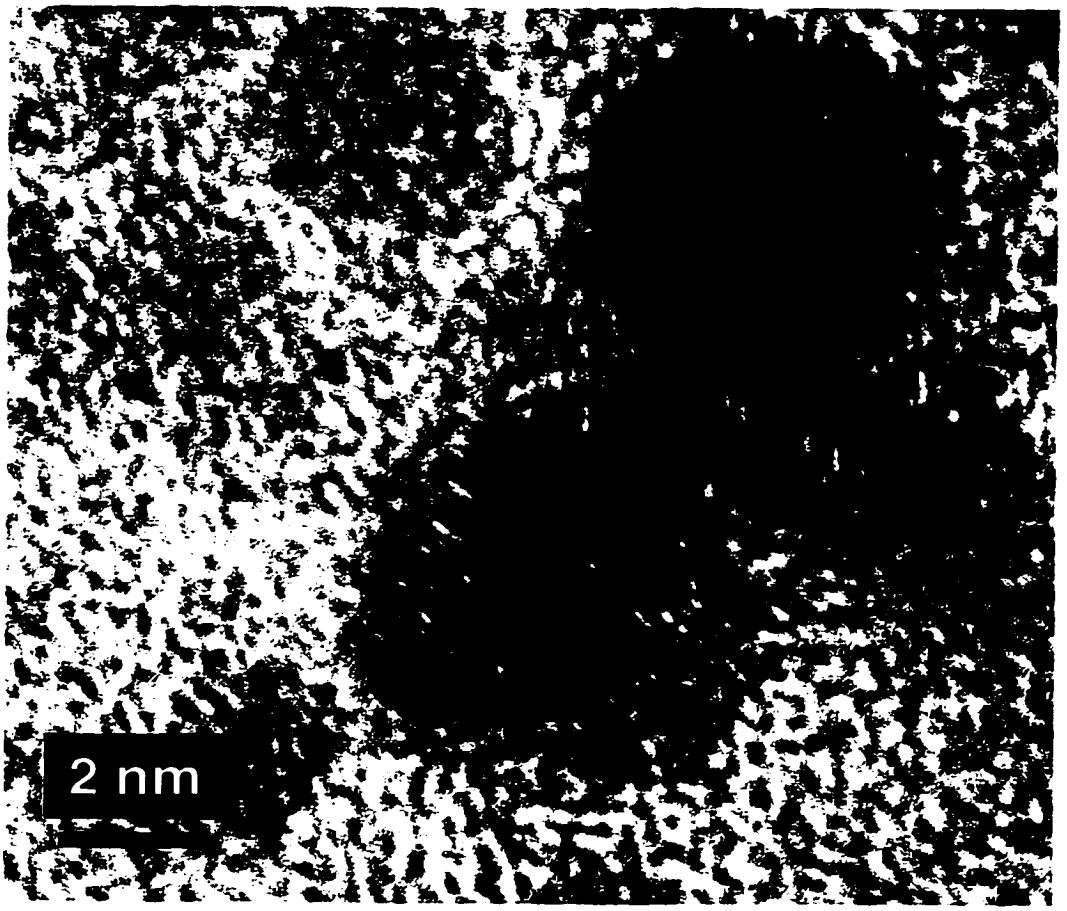

Figure 7-7 A high-resolution image of film (b) showing non-epitaxial diamond crystallites in the amorphous carbon matrix.

of diamond nuclei, graphite, and amorphous carbon films, and chemically react with silicon to form silicon carbide. At the same time, they also cause densification and local stress due to their penetration and momentum transfer. Reducing the hydrogen to carbon ratio leads to non-diamond phase growth, even no diamond growth. Moreover, atomic H can etch the silicon substrate and create silicon steps, which then serve as the sites for epitaxial diamond nucleation. The surface steps are believed to be important in deciding the epitaxial diamond nucleation, as they create boundary conditions by at least two Si surface on the evolution of the C phase [Lee et al. 2000]. Most of the epitaxial diamond nuclei are found to be "buried inside" the silicon substrate. As the acetylene/hydrogen ratio increases, this type of nucleation site becomes unavailable (Figure 7-4b and 7-4c), which may contribute to the disappearance of the epitaxial diamond nuclei.

7.3.2 Epitaxial Diamond Nucleation on Silicon

7.3.2.1. Nucleation Mechanisms

Although plasma chemistry is not a process factor, the direct ion beam nucleation process remains complicated. Several nucleation mechanisms exist and compete with one another, including the "subplantation" model suggested by Lifshitz et al. [1991], nucleation of diamond on the graphitic edges [Lambrecht et al., 1993], on the SiC layer [Gerber et al. 1996] and on the Si steps [Lee et al., 2000]. In direct ion beam deposition, energetic atomic species from the gas ion-source collide with the sample surface, penetrating to the subsurface layers and being trapped there, a typical subplantation process [Lifshitz et al., 1991]. At low acetylene/hydrogen concentrations, the epitaxially nucleated diamond nuclei are always found to form more than one interface with the

silicon substrate, which suggest that the silicon step may be an important factor in the epitaxial nucleation. Although the TED pattern of film (a) suggests a good epitaxial relationship among the silicon, SiC and diamond, the diamond nuclei do not form the epitaxial relationship with the silicon via a silicon carbide interlayer. Instead, they are epitaxially grown directly from the silicon substrate. As the acetylene/hydrogen ratio increases, graphitic edges with preferential orientations appear in the film, as indicated by the TED in Figure 7-4b and 7-4c. These graphitic edges may serve as diamond nucleation sites, as suggested by Lambrecht et al. [1993]. However, this type of nucleation site has not been observed in the current study.

7.3.2.2. Formation of SiC and the Competition between SiC and Diamond

Figure 7-8 is taken with the same sample as shown in Figure 7-6, but in a different region. Other than the epitaxially nucleated diamond crystallite, SiC is also observed. Instead of forming in between the diamond nucleus and the silicon substrate, the SiC grows parallel to the diamond nucleus. SiC is grown from the Si substrate forming the same epitaxial relationship as diamond.

The facts that (i) SiC grows epitaxially on silicon; (ii) voids form in the silicon substrate close to the film/substrate interface at higher hydrocarbon concentrations, and SiC exists above these voids and under the carbon film; and (iii) the SiC layer thickness does not increase with the acetylene/hydrogen ratio suggest that the formation of SiC involves an inter-diffusion process between the silicon substrate and the carbon films. Therefore, any deposition parameter that controls the diffusion process, such as substrate temperature, also controls the SiC growth. This indicates that the optimum condition to

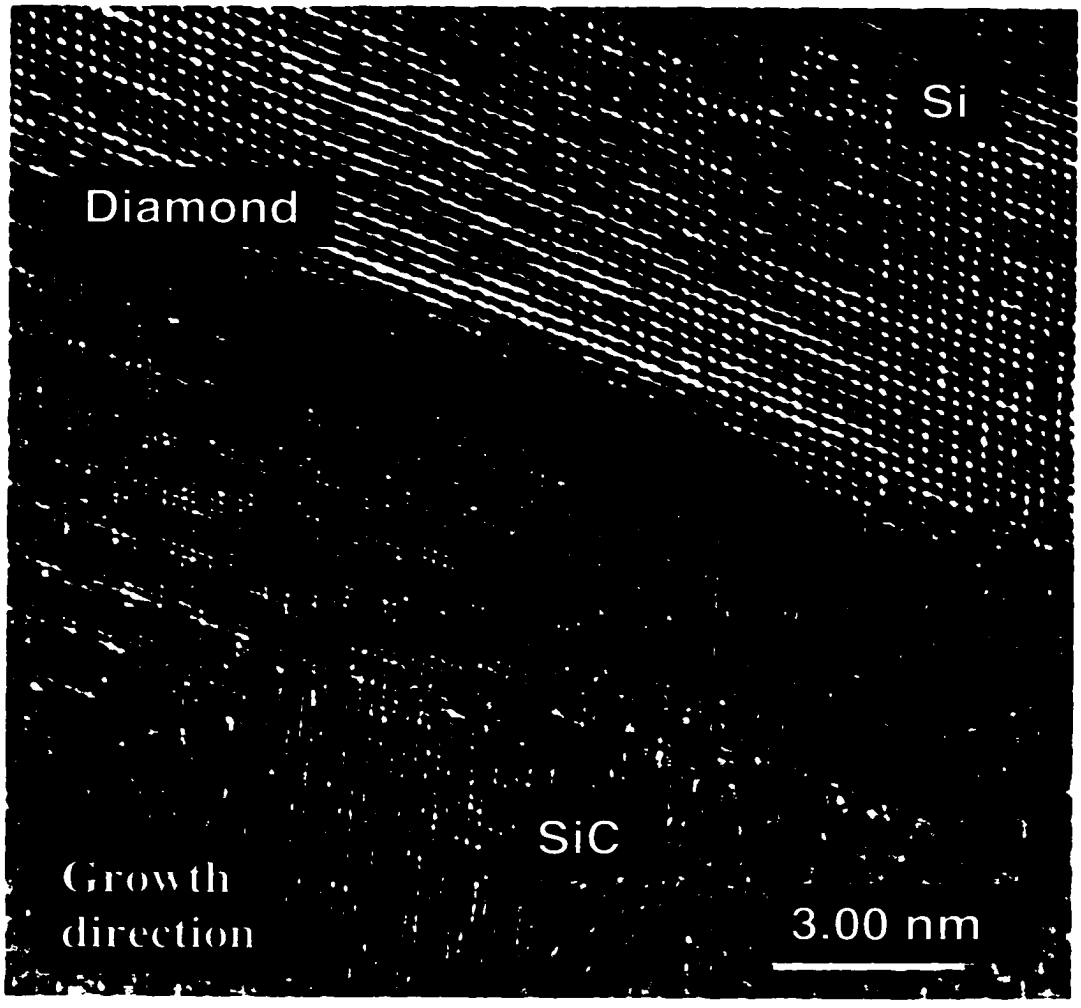

Figure 7-8 A high-resolution image taken at the interface of film (a) and the Si substrate, with electron beam along the Si [110] direction. Other than the epitaxial diamond nucleus on the silicon substrate, SiC is also found to form the same epitaxial relationship with the Si in the nearby region.

achieve SiC and epitaxial diamond nuclei can be different. This gives us a way to optimize diamond nucleation, while reducing, or possibly eliminating SiC formation. On the other hand, as described above, SiC and diamond compete with each other for nucleation sites during the deposition process. Further investigations are needed to understand this competition process.

7.4 Formation of Diamond Polytypes and Their Epitaxial Relationships with Silicon

7.4.1 Diamond Polytypes—An Introduction

Polytypism is a special kind of one-dimensional polymorphism exhibited by certain closed-packed and layer structures such SiC and ZnS [Verma et al. 1966; Hartmann et al. 1982]. All polytypes are built up by stacking identical unit layers of structure, and differ only in the stacking sequence of these layers. Unit cell dimensions of these polytypes are constant in a plane parallel to the stacked layers, and differ only in the direction perpendicular to these layers.

The study of diamond polytypism goes back to early 60's [Wyckoff et al., 1963]. Cubic diamond and lonsdaleite (2H) are two well known polytypes. Both contain only sp^3-type carbons, and each structure can be described in terms of identical packed hexagonal layers of these sp^3 carbon atoms. Figure 7-9 shows the structures of these two forms of diamond. The hexagonal layers of carbons lie parallel to the 3C cubic diamond (111) planes and 2H hexagonal diamond (001) planes. The hexagonal rings of these carbons are all in a chair configuration. The six-membered carbon rings also form between the two layers in the stacking direction. For the 3C diamond, these rings remain in the chair configuration. In the case of 2H diamond, the rings in the stacking direction

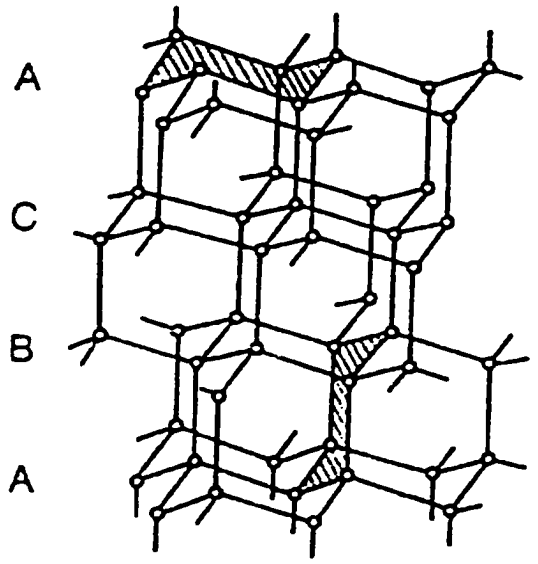

3C Diamond

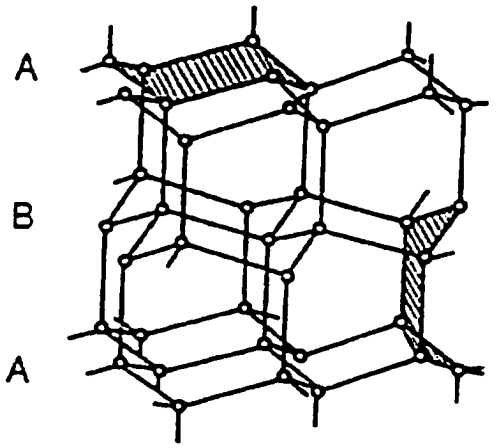

2H Diamond

Figure 7-9 Atomic arrangements for 3C and 2H diamond [Spear, 1989]

exhibit a boat configuration. Therefore, the repeating layer stacking sequence in 3C diamond is typically defined as ABCABC..., and ABAB...in 2H diamond.

Based on experimental results and theoretical deductions, a series of diamond polytype structures have been postulated [Spear et al., 1990]. Other than the regular 3C diamond and the possible hexagonal diamond polytypes, including 2H, 4H, 6H, 8H, etc., the rhombohedral diamond (15R and 21R) is also predicted [Phelps et al., 1989].

7.4.2. 3C Diamond

Figure 7-10 shows a 3C cubic diamond crystallite nucleated on the silicon step. The epitaxial relationship between silicon and diamond is:

$[1\bar{1}1]_{3C}//[1\bar{1}1]_{Si}$; $[\bar{1}11]_{3C}//[\bar{1}11]_{Si}$; and $[002]_{3C}//[002]_{Si}$.

The interface between silicon and diamond is not always sharp. At sharp interfaces, a 2:3 lattice match is observed between silicon and diamond, as shown in Figure 7-8.

Not all diamond nuclei sit in the silicon confinement as obvious as that in Figure 7-10. Moiré fringes are commonly observed at the silicon/diamond interface, indicating the overlapping of two structures (Figure 7-6, 7-11). This result suggests that the surface steps are randomly created on the silicon surface. Diamond nucleates on these steps with no preference.

7.4.3. 9R Diamond

Although the rhombohedral structure of diamond including 15R and 21R has been predicted long time ago, surprisingly, nobody has ever observed the rhombohedral structure 9R until recently. Duan et al. [2001] first reported the 9R diamond by ion-beam

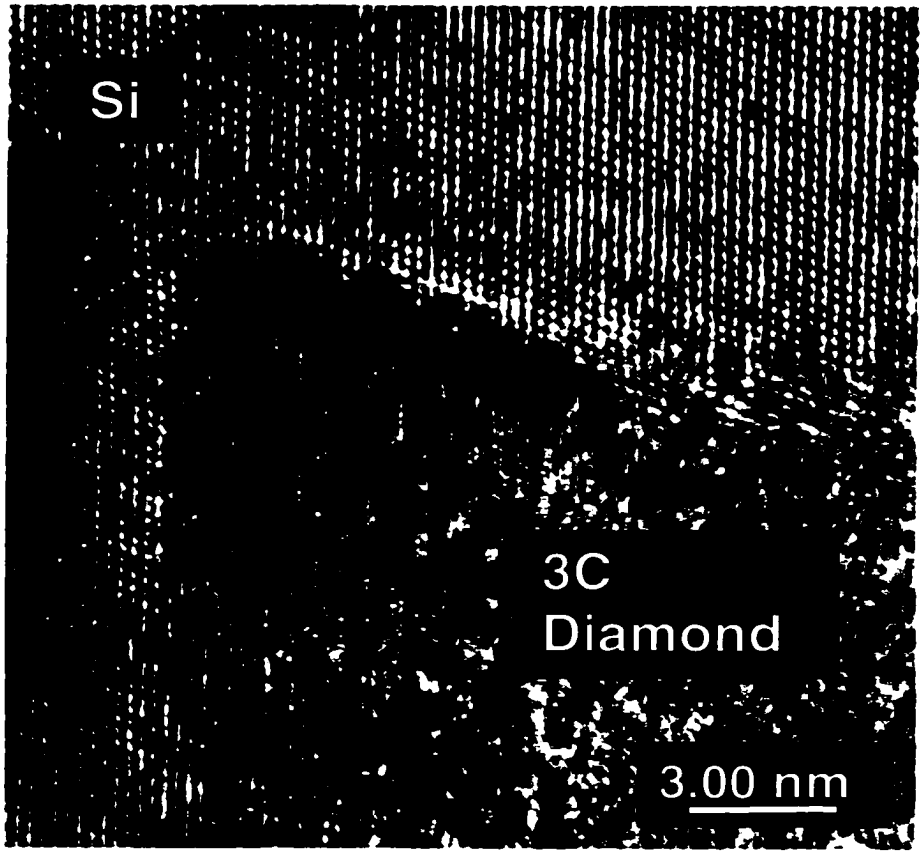

Figure 7-10 A high resolution image taken with electron beam along the silicon [110] zone axis from a 3C cubic diamond crystallite heteroepitaxially nucleated on the silicon step.

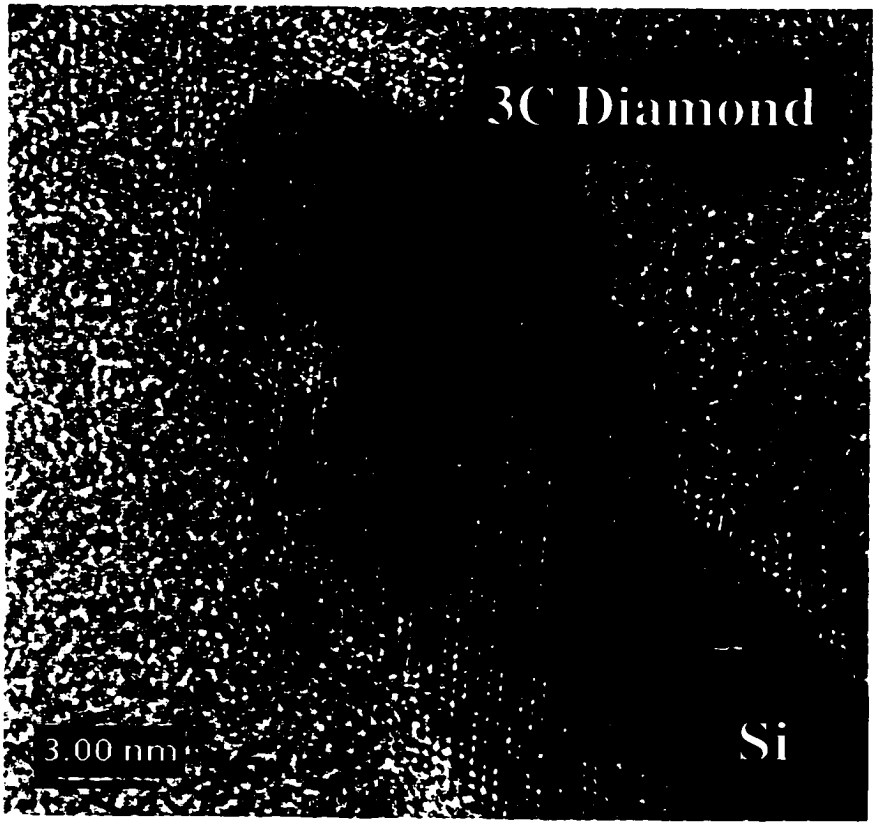

Figure 7-11 A high-resolution image of a diamond crystallite grown on silicon, taken with electron beam along the silicon [110] zone axis. Note that the diamond-silicon interface is not sharp.

deposition using CH_4, Ar and H_2 as the reactive gases. The same structure is observed in the current study using C_2H_2 instead of CH_4. In fact, the deposition parameters of the two studies differ not only in the reactive gas, but in ion energy and deposition temperature as well [Duan et al., 2001]. Figure 7-12 shows the detailed structure of a large 9R diamond crystallite. A filtered image is inserted in the upper right corner in Figure 7-12.

A clear structure definition for the 9R diamond has been given by Duan et al. [2001]. The 9R diamond starts with the first three cubic diamond layers ABC, then A is missing and again three diamond layers BCA are stacked, then B is missing and the next three diamond layer are CAB. The nine layers sequence ABCBCACAB repeats itself periodically (Figure 7-13).

Figure 7-14 shows that 9R diamond is hetero-epitaxially nucleated on silicon substrate. The epitaxial relationship between silicon and 9R diamond is the same as that between silicon and 3C diamond, presented in the rhombohedral unit cell:

$[001]_{9R}//[\bar{1}\,11]_{Si}$, $[100]_{9R}//[110]_{Si}$, $[010]_{9R}//[0\bar{1}\,1]_{Si}$

As all the diamond polytypes have the same close-packed plane parallel to the stacking direction, a 2:3 lattice match also exists between silicon and the 9R diamond

7.4.4. 2H Diamond

Another diamond polytype, 2H hexagonal diamond, is also obtained by ion beam deposition. Figure 7-15 shows diamond nuclei growing on a silicon step. The epitaxial relationship between silicon and 2H diamond is:

$[001]_{2H}//[\bar{1}\,11]_{Si}$, $[100]_{2H}//[110]_{Si}$, $[010]_{2H}//[0\bar{1}\,1]_{Si}$

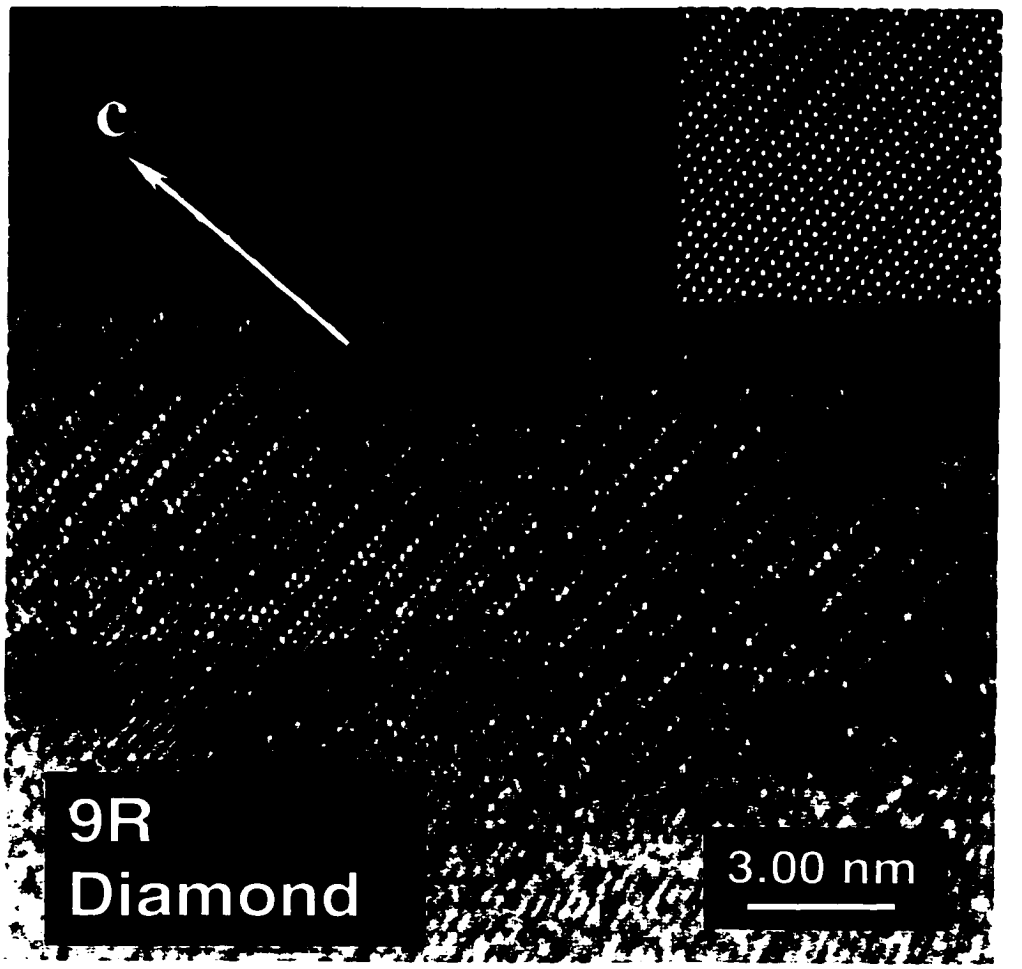

Figure 7-12 High-resolution image taken from a 50 nm 9R diamond crystallite.

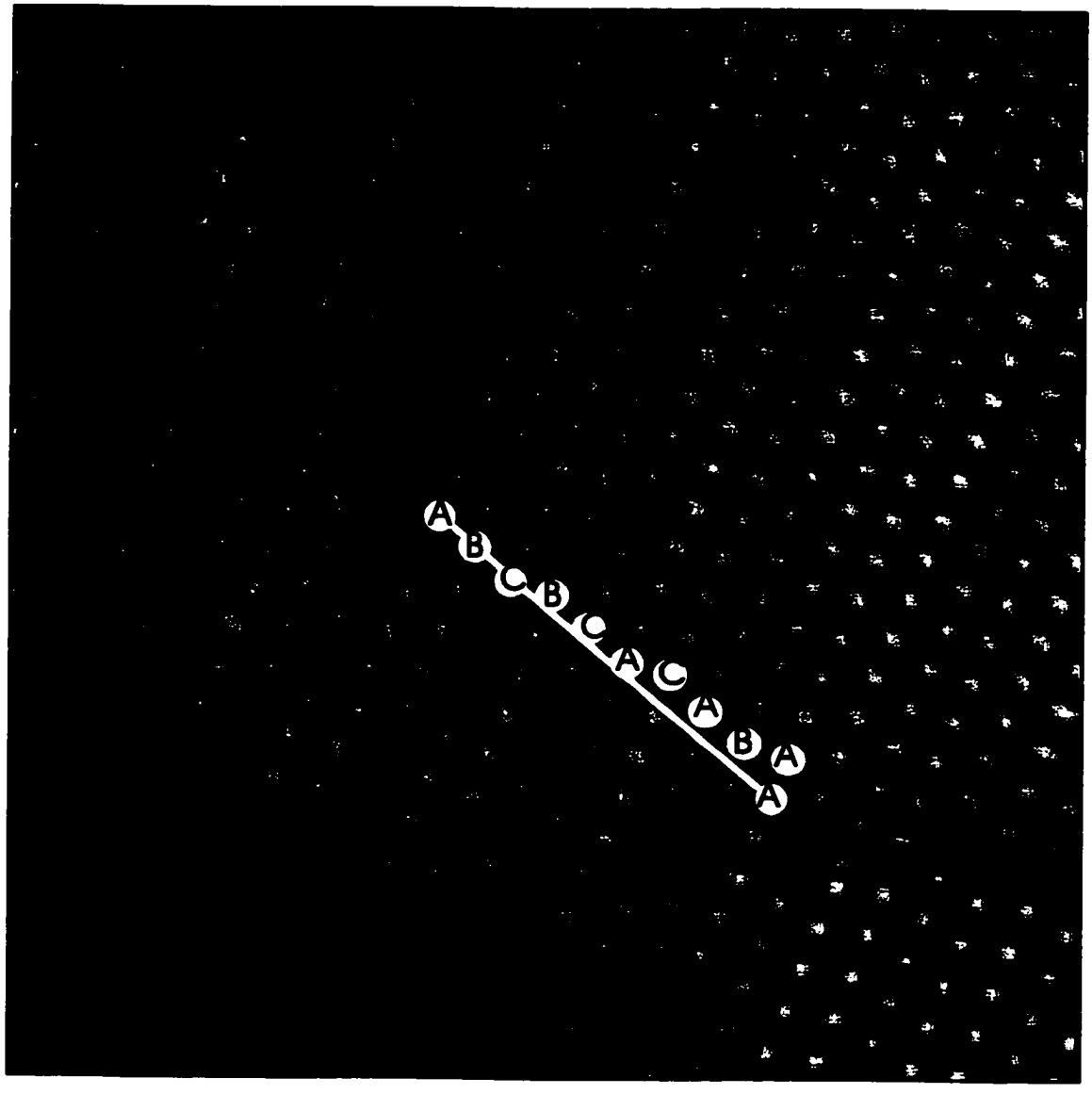

Figure 7-13 Stacking sequence of 9R diamond. (Courtesy from X. F. Duan)

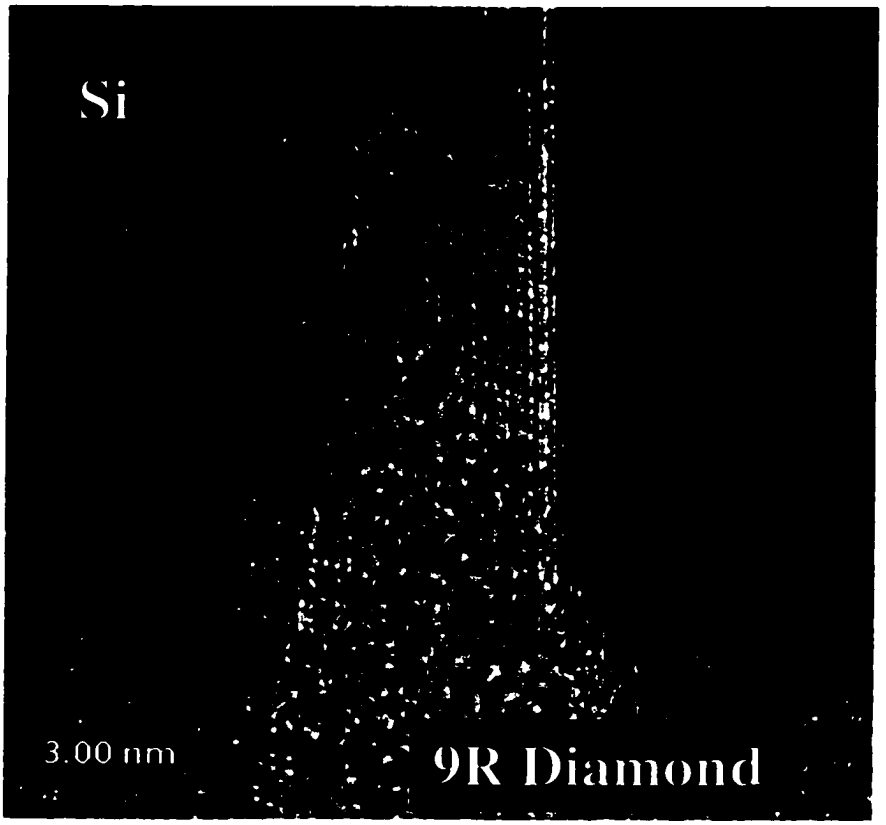

Figure 7-14 High-resolution images taken with electron beam along the silicon [110] zone axis. A 9R rohbomhedtral diamond is epitaxially nucleated on silicon substrate.

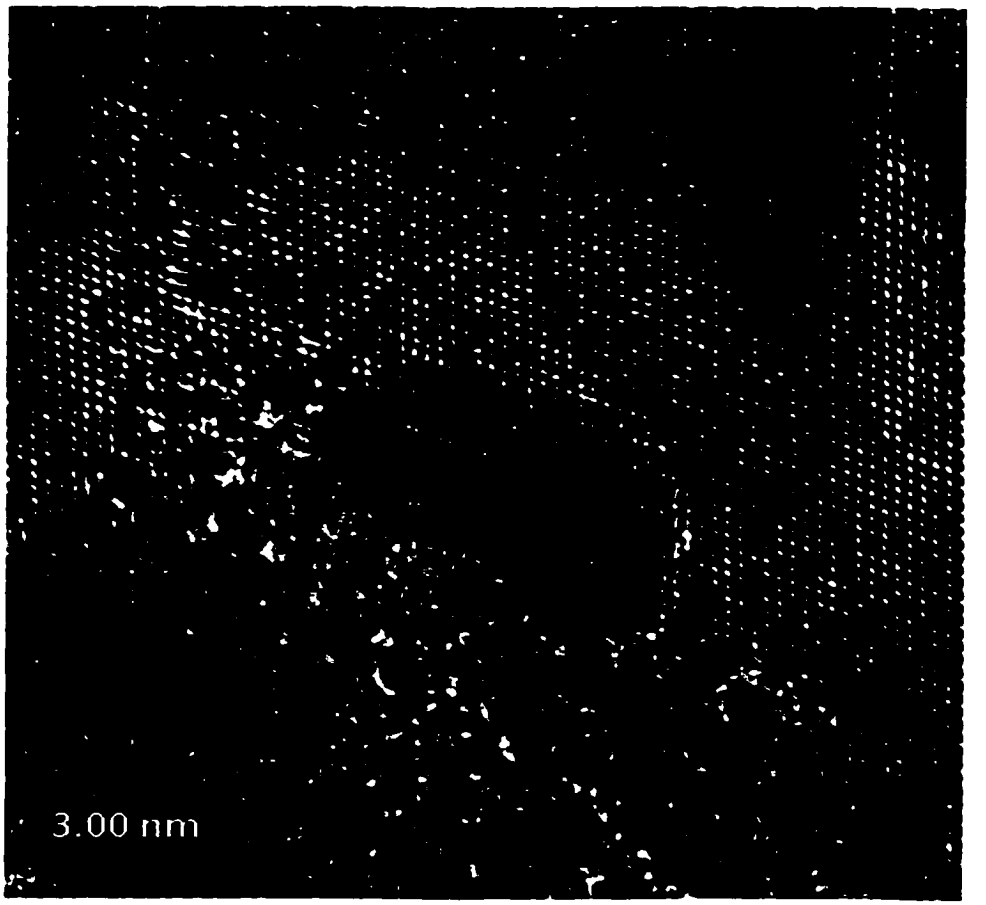

Figure 7-15 High-resolution image taken with electron beam alone the silicon [110] zone axis.

Interestingly, other than forming the regular epitaxial relationship with silicon like 3C and 9R, the 2H diamond is observed to form another type of epitaxial relationship with the silicon (Figure 7-16):

$[2\bar{1}0]_{2H}$// $[1\bar{1}1]_{Si}$; $[010]_{2H}$// $[110]_{Si}$; $[0\bar{1}1]_{2H}$//$[011]_{Si}$

substrate with electron beam along the silicon [110] zone axis

This type of nucleation may be due to the similar d-spacing along the 2H [001] (d001 = 2.06 Å) and [120] (d010 = 2.18 Å) direction. However, the detailed mechanism for this type of nucleation is not clear.

7.4.5. Coexistence of Diamond Polytypes in Individual Diamond Nucleus

Knowing that all the diamond polytypes have the same close packed planes perpendicular to the stacking direction, it is natural to suspect that for diamond growth under appropriate conditions, it may be possible for two or more polytypes to coexist in one crystallite, as they can be developed simply by stacking faults. Figure 7-17 demonstrates the existence of multiple polytypes. The structure in area a is the same as that in area c—9R diamond structure. However, the structure in area b turns out to be different. It is a 2H structure lasting for only several atomic layers.

Although polytype structures may be initiated by the occurrence of stacking faults, the formation of polytypes with size larger than one unit cell, i.e., the close-packed planes stack in a specific sequence and repeat in certain periodicity, is far more complicated. Both thermodynamics of the polytype structures and their growth kinetics contribute to the determination of the final structures [Fissel et al., 2000]. The detailed mechanisms are not clear owing to the lack of experimental data.

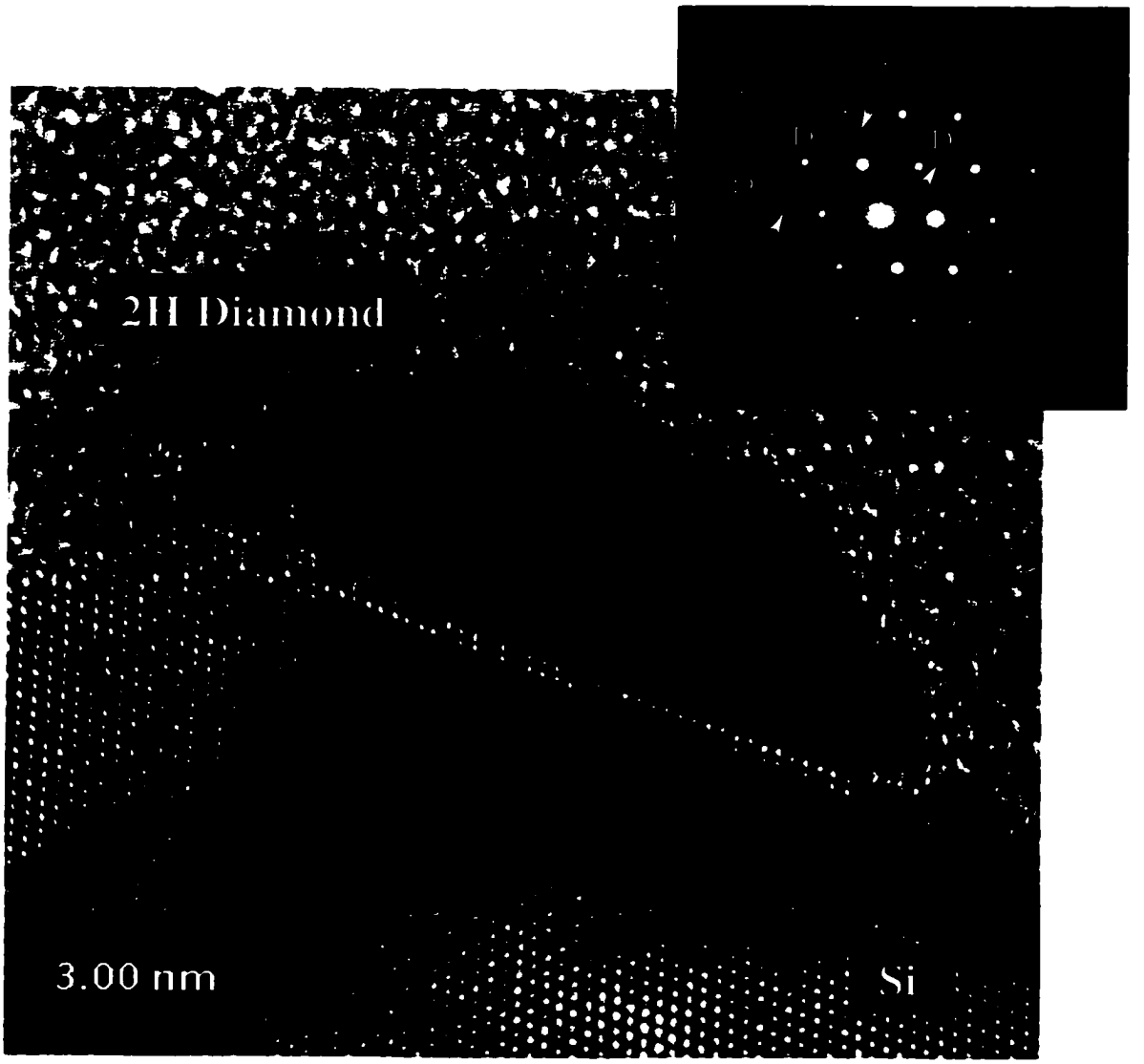

Figure 7-16 High-resolution image taken from a 2H diamond nucleated on silicon

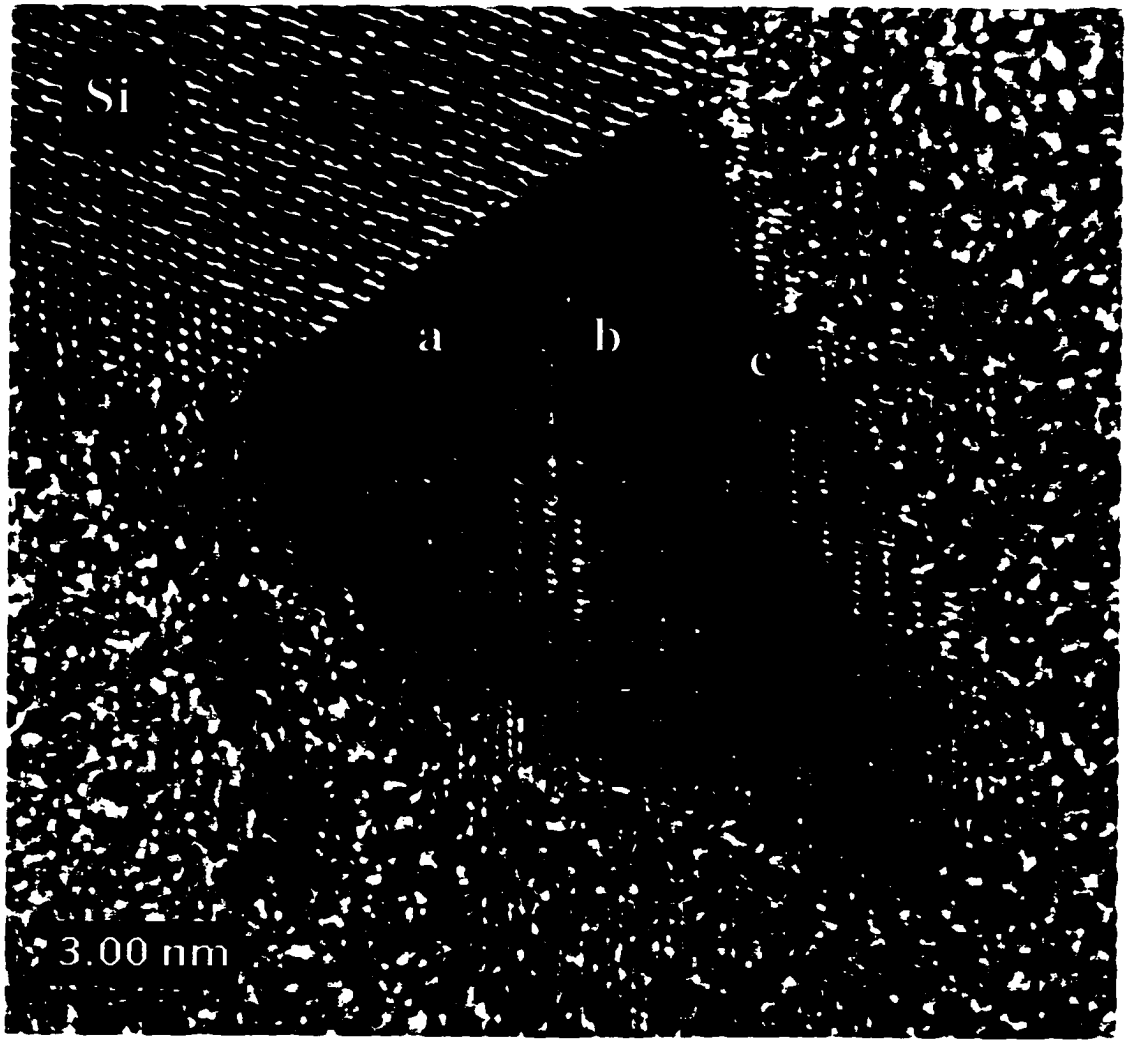

Figure 7-17 High-resolution image taken with electron beam alone the silicon [110] zone axis. A 9R-2H-9R sandwich structure is observed

7.5 Conclusions

Direct ion-beam deposition is capable of nucleating diamond over a large range of acetylene/hydrogen concentrations. Epitaxial nucleation of diamond directly on silicon is achieved using low acetylene/hydrogen concentrations, which is commonly considered to be inadequate for diamond nucleation. The silicon surface is severely damaged by ion etching, and surface steps are created to serve as the epitaxial nucleation sites for diamond. No SiC interlayer is found between the diamond nucleus and the silicon substrate. As the acetylene/hydrogen ratio increases, non-epitaxial nucleation of diamond takes the place of the epitaxial nucleation. No diamond nucleation is achieved when the acetylene/hydrogen ratio increases to 29%. These experimental results can be explained by the role of H played in diamond deposition, as it bombards the sample surface, etches the non-diamond phase, and terminates the carbon dangling bonds with an sp^3 configuration. The formation of epitaxial SiC layer is believed to involve an inter-diffusion process between silicon and the carbon film deposited on top of it. The nucleation of diamond by direct ion-beam deposition remains complicated. Several competing mechanisms exist. The most plausible mechanisms are the "subplantation" model and the "surface step" model.

Diamond polytypes 3C, 2H, and 9R are observed using this deposition method. All of the nuclei are epitaxially nucleated on the silicon step. The epitaxial relationship between silicon and the polytypes are as following

3C diamond: $[1\bar{1}1]_{3C}//[1\bar{1}1]_{Si}$; $[\bar{1}11]_{3C}//[\bar{1}11]_{Si}$; and $[002]_{3C}//[002]_{Si}$.

9R diamond: $[001]_{9R}//[\bar{1}11]_{Si}$, $[100]_{9R}//[110]_{Si}$, $[010]_{9R}//[0\bar{1}1]_{Si}$

2H diamond: $[001]_{2H}//[\bar{1}\,1\,1]_{Si}$, $[100]_{2H}//[1\,1\,0]_{Si}$, $[010]_{2H}//[0\,\bar{1}\,1]_{Si}$

$[2\,\bar{1}\,0]_{2H}//[1\,\bar{1}\,1]_{Si}$; $[010]_{2H}//[1\,1\,0]_{Si}$; $[0\,\bar{1}\,1]_{2H}//[0\,1\,1]_{Si}$

The three diamond polytypes have the same close-packed planes perpendicular to the stacking direction. Coexistence of two different structures in one diamond nucleus was observed, which may be explained by the changes in stacking sequences via stacking faults.

CHAPTER 8. RECOMMENDATION FOR FUTURE RESEARCH

8.1 Phases of Crystalline Aluminum Oxide

The existences of multiple phases in the synthesis of alumina thin films makes it difficult for both selective phase deposition and specific phase identification after deposition. The above-presented studies demonstrate the deposition of crystalline alumina (especially α-alumina) at a record low temperature of 250C. However, we were not able to make specific phase identification and composition analysis of the film from XRD data, due to stress induced peak shifting and the film texture. Careful XRD simulations of different alumina phases considering the stress in the films may be able to correlate the experimental XRD peaks to the specific phases. It is also important to point out that other metastable phases of alumina such as delta alumina should be considered, as it may be introduced by the non-equilibrium deposition process. It will also be interesting to further explore the effects of different deposition parameters on the differentiation of various alumina phases.

8.2 Cubic Boron Nitride

One of the most serious problems with cBN is the large internal stress, which causes the film to delaminate. The current study points out that type II cBN nucleation may be the solution to low-stress cBN film synthesis. Nevertheless, it fails to suggest specific deposition parameter requirements other than low substrate bias, which would induce this type of cBN nucleation. A systematic study investigating more deposition parameters using various deposition methods is needed, in order to further understand this

type of cBN nucleation and develop feasible deposition techniques for thick cBN film growth.

It is also indicated by the current study that the compressive stress in the films does not necessarily scales with ion bombardment (ion energy). In fact, it is inappropriate to relate the internal stress of the as-deposited BN films to ion bombardment (different ion energy) without considering other factors. The current work shows that changing the ion bombardment also changes the microstructure of the BN films. The internal stresses of the films with different microstructures are not comparable. It is therefore interesting to design a series of experiments, which can produce only amorphous BN using different substrate bias. This may isolate the ion bombardment contribution to the film internal stress.

Another suggestion to the future research is inspired by the other problem of cBN film fabrication, i.e., the presence of an amorphous layer prior to tBN and later cBN nucleation. In order to understand the origin of the amorphous layer and its effect on the BN film growth, we need to first find out whether this layer of material is really amorphous BN, as most people take for granted. EELS will be the most effective tool in determining the chemical composition and the bonding state of the amorphous layer.

REFERENCES

Ambacher O, J. Phys. 31 (1998) 2653

Angus JC, Will HA, and Stanko WS, J. Appl. Phys., 39 (1968) 2915

Areshkin AG, Vasiljeva LI, Fedorov DL, and Markov LS, J. Opt. Soc. Am. B 15 (1998) 41

Ballal AK, Salamanca-Riba L, Doll GL, TaylorII C A, Clarke R, J. Mater. Res. 7 (1992) 1618.

Banhart F, Rep. Prog. Phys. 62 (1999) 1181

Bello I, Notes of "Thin Film Technology" City University of Hong Kong 2000

Bengu E, "Experimental and computational study of surfaces, interfaces and thin films" PhD thesis, Northwestern University, 2000

Bundy FP, Wentorf RH, J. Chem. Phys. 38 (1963) 1144

Cardinale GF, Mirkarimi PB, McCarty KF, Klaus EJ, Medlin DL, Clift WM and Howitt DG, Thin Solid Films 253 (1994) 130

Chayahara A, Yokoyama H, Imura T, Osaka Y, Jpn. J. Appl. Phys. 26 (1987) L1435.

Chelikowsky JR, Phys. Rev. B 35 (1987) 1174

Christian JW, Olson GB and Cohen M, Journal De Physique IV, Vol. 5, Dec. 1995

Christensen NE and Gorczyca I, Phys. Rev. B 50 (1994) 4397

Cohen M, Olson GB, and Clapp PC, Presented at ICOMAT-79, MIT, Cambridge, MA, 24-29 June 1979

Collazo-Davila C, Bengu E, Leslie C, and Marks LD, Appl. Phys. Lett. 72 (1997) 314

Collazo-Davila C, Bengu E, Marks LD, and Kirk M, Diamond Relat. Mater. 8 (1999) 1091

Cullity BD, "Elements of x-ray diffraction" second edition, Addison-wesley publishing company, Inc. 1978

Deshpandey C and Holland L, Thin Solid Films 96 (1982) 265

Engstrom C, Berlind T, Birch J, Hultman L, Ivanov IP, Kirkpatrick SR and Rohde S, Vacuum 56 (2000) 107

Fair RB, J. Appl. Phys. 42 (1971) 3176

Fissel A, J. Cryt. Growth, 212 (2000) 438-450

Frenklach M, J. Appl. Phys. 65 (1989) 5124

Friedmann TA, Mirkarimi PB, Medlin DL, McCarty KF, Klaus EJ, Boehme D, Jonsen HA, Mills MJ, Ottesen DK, J. Appl. Phys. 76 (1994) 3088.

Gaβmann P, Boysen J, Schmitz G, Bartolucci F and Franchy R, Solid State Comm. 97 (1996) 1

Gerber J, J. Appl. Phys. 79 (1996) 4388

Gibbs JW, "The Collected works of J. W. Gibbs", Vol. I. Longmans Green, London, New York and Toronto, 1928

Hackenberger LB, Philione LJ, Messier R, Lamaze GP, J. Vac. Sci. Technol. A 12 (1994) 1569.

Hahn J, Richter F, Pintaske R, Roder M, Schneider E, Welzel T, Surf. Coat. Technol. 92 (1996) 129

Hartmann H, Mach R, and Selle B, Current topics in materials science, edited by E. Kaldis (North Holland, Amsterdam, 1982)

Hirsch P, Howie A, Nicholson R, Pashley DW, Whelan MJ, " Electron Microscopy of Thin Crystals" Krieger Publishing Company, Malabar, Florida 1965

Hirschauer B, Soderholm S, Chiaia G, Karlsson UO, Thin Solid Films 305 (1997) 243

Hirth JP, Pound GM "Condensation and evaporation; Nucleation and growth kinetics" Pergamon, London 1963

Hirth JP, Moazed KL, "Physics of Thin Films" (G. Hass and R. E. Thun, eds), Vol. 4, p97. Academics Press, New York 1967

Hoffmann R. Rev. Mod. Phys., 60 (1988) 601

Holleck H, J. Vac. Sci. Technol. A 4 (1986) 2661

Hsu WL, J. Vac. Sci. Technol. 6, (1988) 1803

Ikeda T, Kawate Y., Hirai Y, J. Vac. Sci. Technol. A 8 (1990) 3168.

Ikeda T, Appl. Phys. Lett. 61 (1992) 786.

Inagawa K, Watanabe K, Ohsone H, Saitoh K, Itoh A, J. Vac. Sci. Technol. A 5 (1987) 2696.

Jena AK, and Chaturvedi MC, "Phase Transformations in Materials" 1992

Jiang X and Klages C –P, Diamond Relat. Mater. 1 (1992) 195

Johansson MP, Ivanoz I, Hultman L, Munger P, Schutze A, J. Vac. Sci. Technol. A 14 (1996) 3100.

Kester DJ, Ailey KS, Davis RF, More KL, J. Mater. Res. 8 (1993) 1213.

Kester DJ, Messier R, J. Appl. Phys. 72 (1992) 504.

Kidner S, Taylor II CA, Clarke R, Appl. Phys. Lett. 64 (1994) 1859.

Konuma M, "Film Deposition by Plasma Techniques" Spring-Verlag Berlin Heidelberg. 1992

Kulikovsky VY, Shaginyan LR, Vereschaka VM, Hatyento NG, Diamond Relat. Mater. 4 (1995) 113.

Lambrecht WRL, Lee CH, Segall B, Angus JC, Li Z, Sunkara M, Nature 364 (1993) 607

Lee ST, Peng HY, Zhou XT, Wang N, Lee CS, Bello I, Lifshitz Y, Science 287 (2000) 104

Leonard-Jones JE, Physica 4 (1937) 941

Lewis B, Campbell DS, J. Vac. Sci. Technol. 4 (1967) 209

Lewis B, J. App. Phys. 41 (1970) 30

Lewis B, Sur. Sci. 21 (1970) 289

Lewis B, "Crystal growth" (B. R. Pamplin, eds), p. 12 Pergamon, Oxford and New York 1974

Lifshitz Y, Kasi SR, Rabalais JW, and Eckstein W, Phys. Rev. B 41 (1990) 10468

Liou Y, Inspector A, Weimer R, Knight D, and Messier R, J. Mater. Res., 5, (1990) 2305
London F, Z. Phys. 63 (1930) 245

London F, Z. Phys. Chem. 11 (1930) 222

Lothe J and Pound GM, J. Chem. Phys. 36 (1962) 2080

Ma E, Liu BX, Chen X, and Li HD, Thin Solid Films 147 (1987) 49

Madan A, Kim IW, and Barnett SA, Unpublished (1996)

Madan A, Kim IW, Cheng SC, Yashar P, Dravid VP, and Barnett SA, Phys. Rev. Lett. 78 (1997) 1743

Malengreau F, Hagege S, Sporken R, Vermeersch M, and Caudano R, J. Euro. Ceramic Soc. 17 (1997) 1807

Matsumoto S, Zhang WJ, Jpn. J Appl. Phys. 39 (2000) L442

Matsumoto S, Presented at "International Conference on Metallurgical coatings and Thin Films (ICMCTF)" 2001, San Diego, CA

McCaffrey J P, J. Hulse, Micron 29 (2-3) (1998) 139

McCaffrey JP "Development of Transmission Electron Microscopy Techniques for the Study of Thin Films" Ph. D. Thesis, Linkoping 2000

McKenzie DR, Cockayne DJH., Muller DA, Murakawa M, Miyake S, Wantanabe S, Fallon P, J. Appl. Phys. 70 (1991) 3007.

Medlin DL, Friedmann TA, Mirkarimi PB, Cardinale GF, and McCarty KF, J. Appl. Phys. 79 (1996) 3567

Meng WJ, Sell JA, Perry TA, Rehn LE and Baldo PM, J. Appl. Phys. 75 (7), (1994) 3446

Meyer K, Schuller IK, Falco CM, J Appl. Phys. 52 (1981) 5803

Mieno M, Yoshida T, Jpn. J. Appl. Phys. 29 (1990) L1175.

Mirkarimi PB, Shinn M, and Barnett SA, J. Vac. Sci. Technol. A 10 (1992) 1618

Mirkarimi PB, Medlin DL, McCarty KF, Barbour JC, Appl. Phys. Lett. 66 (1995) 2813

Mirkarimi PB, Medlin DL, McCarty KF, Dibble DC, Clift WM, Knapp JA, Barbour JC, J. Appl. Phys. 82 (1997) 1617.

Mirkarimi PB, McCarty KF, Medlin DL, Mater. Sci. Eng. R21 (1997) 47.

Moore JF, Strongin DR, Comita PB, Ruckman MW and Strongin M, Appl. Phys. Lett. 65 (1994) 368

Moulder JF, Stickle WF, Sobol PE, Bomben KD, Handbook of X-ray Photoelectron Spectroscopy, Physical Electronics Inc.,1992, 1995, USA, p38 and p42.

Nakai H, Shinohara J, Sassa T, Ikegami Y, Nuclear Instruments and Methods in Physics Research B 121 (1997) 125

Ohring M, "The Materials Science of Thin Films" Academic Press, Inc. 1992

Okamato M, Yokoyama H, Osaka Y, Jpn. J. Appl. Phys. 29 (1990) 930.

Petrov I, Mojab E, Powell RC, Greene JE, Hultman L, Sundgren JE, Appl. Phys. Lett. 60 (20) (1992) 2491

Petrov I, Adibi F, Greene JE, Sproul WD and Munz WD, J. Vac. Sci. Technol. A10 (1992) 3283

Pharr GM and Oliver WC, MRS Bull. 17 (1992) 28

Pound GM, Simnad MT, Yang L, J. Chem. Phys. 22 (1954) 1215

Reinke S, Kuhr M, Kulisch W, and Kassing R, Diamond Relat. Mater. 4 (1995) 272

Schneider JM, Sproul WD, Voevodin AA and Matthews A, J. Vac. Sci. Technol. A 15 (1997) 1

Saito Y, Sato K, Tanaka H, Fujita K, and Matsuda S, J. Mater. Sci., 23 (1988) 842

Schulz H and Thiemann K, Solid State Commun. 23 (1977) 815

Seitz F, Koehler JS, Solid State Phys. 2 (1956) 305

Solozhenko VL, Thermochimica Acta 218 (1993) 221

Spear KE, J Am. Ceram. Soc., 72 (2) (1989) 171

Spear KE, Phleps AW, White WB, J. Mat. Res. Vol. 5, No. 11 (1990) 2277

Spence JC, "Experimental High-resolution Electron Microscopy" second edition, Oxford University Press 1988

Sproul WD, Surf. & Coat. Technol. 33 (1987) 73

Sproul WD, Graham ME, Wong MS, Lopez S, Li D and Scholl RA, J. Vac. Sci. Technol A 13 (1995) 1188

Stockel R, J. Appl. Phys. 83 (1998) 531

Stoner BR and Glass JT, Appl. Phys. Lett. 60 (1992) 698

Stubhan F, Ferguson M, Fusser HJ, and Behm RJ, Appl. Phys. Lett. 66 (1995) 1900

Thompson MW, Philos. Mag. 18 (1968) 377

Van Camp PE, Van Doren VE, and Devreese JT, Phys. Rev. B 44 (1991) 9056

Vel L, Demazeau G, Etourneau J, Mater. Sci. Engin. B 10 (1991) 149

Verma AR and Krishna P, Polyporphism and Polytypism in Crystals (Wiley, New York, 1966)

Vossen JL, Kern W, "Thin Film Processes" Academic Press, Inc.

Wado H, Shimizu T, and Ishida M, Appl. Phys. Lett. 67 (1995) 2200

Walton D, Phil. Mag. 7 (1962) 1671

Walton D, J. Chem. Phys. 37 (1962) 2182

Wasa K, Hayakawa S, "Handbook of Sputter Deposition Technology" Noyes Publications 1992

Watanabe S, Miyake S, Zhou W, Ikuhara Y, Suzuki T, and Murakawa M, Appl. Phys. Lett.66 (1995) 1478

Wong MS, Chia WJ, Yashar P, Schneider JM, Sproul WD, and Barnett SA, Surface and Coating Technology 86-87 (1996) 381

Yang J, Lin Z, Wang LX, Jin S, and Zhang Z, Appl. Phys. Lett. 65 (1994) 3203

Yashar P, Chu X, Barnett SA, Rechner J, Wang YY, Wong MS, Sproul WD, Appl. Phys. Lett. 72 (8) (1998) 987

Yugo S, Kanai T, Kimura T, and Muto T, Appl. Phys. Lett. 58 (1991) 1036

Yokoyama H, Okamoto M, Osaka Y, Jpn. J. Appl. Phys. 30 (1991) 344.

Yoshida T, Diamond Relat. Mater. 5 (1996) 501

Zhang RQ, Wong NB, Lee ST, Zhu RS, and Han KL, Chem. Phys. Lett., 319 (2000) 213

Zhang RQ, Lee CS and Lee ST, J. Chem. Phys., 112(19) (2000) 8614

Zhang RQ, Chu TS, Bello I, and Lee ST, Diamond Relat. Mater. 9 (2000) 596

Zhang RQ, Chu TS, Lee CS, and Lee ST, J. Phys. Chem. B, 104 (2000) 6761

Zhang RQ, Chan KS, Zhu RS, and Han KL, Phys. Rev. B, 63 (2001). 85419

Zhang RQ, Chu TS, Cheung HF, Wang N and Lee ST, Phys. Rev. B, to be published.

Zhang W, Someno Y, Sasaki M and Hirai T, J. Cryt. Growth 130 (1993) 308

Zhou ZF, Bello I, Lei MK, Li KY, Lee CS, Lee ST, Surf. Coat. Technol.128-129 (2000) 334.

Zinsmeister G, "Basic problems in thin film physics" (R. Niedermayer and H. Mayer, eds), p33. Vandenhoeck and Ruprecht, Gottingen. (English translation; Vacuum 16, 529)